Western University
Scholarship@Western

1987

Dynamic Analysis Of Offshore Structures

Hisham Mohammed Mitwally

Follow this and additional works at: https://ir.lib.uwo.ca/digitizedtheses

CANADIAN THESES

THÈSES CANADIENNES

NOTICE

The quality of this microfiche is heavily dependent upon the quality of the original thesis submitted for microfilming. Every effort has been made to ensure the highest quality of reproduction possible.

If pages are missing, contact the university which granted the degree.

Some pages may have indistinct print especially if the original pages were typed with a poor typewriter ribbon or if the university sent us an inferior photocopy.

Previously copyrighted materials (journal articles, published tests, etc.) are not filmed.

Reproduction in full or in part of this film is governed by the Canadian Copyright Act, R.S.C. 1970, c. C-30.

AVIS

La qualité de cette microfiche dépend grandement de la qualité de la thèse soumise au microfilmage. Nous avons tout fait pour assurer une qualité supérieure de reproduction.

S'il manque des pages, veuillez communiquer avec l'université qui a conféré le grade.

La qualité d'impression de certaines pages peut laisser à désirer, surtout si les pages originales ont été dactylographiées à l'aide d'un ruban usé ou si l'université nous a fait parvenir une photocopie de qualité inférieure.

Les documents qui font déjà l'objet d'un droit d'auteur (articles de revue, examens publiés, etc.) ne sont pas microfilmés.

La reproduction, même partielle, de ce microfilm est soumise à la Loi canadienne sur le droit d'auteur, SRC 1970, c. C-30.

THIS DISSERTATION HAS BEEN MICROFILMED EXACTLY AS RECEIVED

LA THÈSE A ÉTÉ MICROFILMÉE TELLE QUE NOUS L'AVONS REÇUE

Canada

NL-339 (r.86/06)

Dynamic Analysis of Offshore Structures

by

Hisham Mohammed Mitwally

Faculty of Engineering Science

Submitted in partial fulfillment
of the requirements for the degree of
Doctor of Philosophy

Faculty of Graduate Studies
The University of Western Ontario
London, Ontario
February, 1987

of offshore structures to environmental loads, which are mainly dynamic. It alters the dynamic properties of the structure and may increase or decrease the response depending on the relationship of the fundamental natural frequency to the dominant exciting frequency. Random wave forces on offshore towers are usually evaluated using the directional spectrum of sea surface elevation. This representation does not take into account the lack of spatial correlation which may be associated with fully developed random waves.

1.2. Objectives of the Study and Organization of the Thesis

This study is divided into two main parts. The first part deals with the pile drivability analysis. The second part is concerned with the response of fixed offshore structures to random wave forces. The objectives of the first part are:

1. To improve on the one dimensional wave equation analysis of pile drivability by accounting, in a rational way, for wave propagation in the soil and by formulating parameters related to standard soil characteristics.

2. To formulate a three dimensional finite element analysis with suitable transmitting boundaries and compare its results to those of the one dimensional analysis in order to illustrate the advantages and limitations of both models.

In the second part of the study, the analysis is limited to the jacket type platforms or towers, and the objectives are:

1. To examine the effect of dynamic pile-soil-pile interaction on the response of fixed offshore towers to random wave forces.

2. To establish an approach for evaluating random wave loads on offshore towers which takes into account the lack of spatial correlation of random waves and allow for directional effects.

Chapter 2 gives a brief review of different types of offshore structures, main sources of environmental loads and the important parameters that govern the behaviour of these structures. In Chapter 3, the one dimensional wave equation

Abstract

This study comprises three main parts:

1. **Pile Driving Analysis**: The conventional one dimensional wave equation analysis of the pile driving problem suffers from the empirical representation of the soil parameters. In this study, an improved one dimensional wave equation model is developed which accounts for wave propagation in the soil mass and thus gives more realistic prediction of the pile displacements. A three dimensional finite element analysis of the problem is also formulated and its results are compared with those of the one dimensional analysis. The finite element analysis is computationally very expensive which is not justified due to its sensitivity to the input parameters.

2. **Modelling of Wave Forces**: Lack of spatial correlation of short crested waves is accounted for using a coherence function model and the wave forces estimated using this model are compared with those estimated using the directional spectrum model. Both models are found to give comparable resultant wave forces and their attenuation with separation if their parameters are properly chosen. The error resulting from assuming a constant water particle velocity along the tributary length is examined and appears to be small.

3. **Response of Fixed Offshore Towers to Random Wave Forces Accounting for Pile-Soil-Pile Interaction**: Dynamic pile-soil-pile interaction under the effect of wave forces is usually neglected in the design of offshore towers. It is examined and found to have a significant effect on the response of the tower to random waves. It is incorporated in the analysis using dynamic interaction factors which consider pile-soil separation. The response of the tower is found to be greatly influenced by pile-soil-pile interaction which is attributed to the increase in flexibility and damping of the tower.

III

Acknowledgements

I would like to express my sincerest gratitude and appreciation to Professor M. Novak for his invaluable support and encouragement throughout the course of this investigation.

I would also like to express my appreciation to my colleagues the graduate students in the Engineering Department of the University of Western Ontario for stimulating discussions and friendship.

Table of Contents

List of Figures

List of Tables

Chapter One
Introduction

1.1. General

Offshore structures are used for several purposes such as oil and gas production, oceanographic research, navigational lighting and radar tracking, however, the vast majority are used for the first application. Dwindling oil supply from onshore locations has accelerated offshore exploration and production activities. Offshore platforms are installed in ever increasing water depths and extremely hostile environments, such as those encountered in the North Sea. These conditions introduce considerable difficulties in design and increase the potential loss in human life and capital in case of a major failure. Accordingly, extensive research programmes have been undertaken during the last four decades to understand all aspects of behaviour of offshore structures.

Two main factors are crucial in assessing the reliability of any structure: strength and loading. The supporting foundation, which consists of piles for most offshore structures, is one of the more important parameters that define the strength of an offshore structure. Prediction of the axial capacity of the supporting piles and assessing their drivability using a certain hammer system are major problems encountered, in offshore piling. Due to adverse weather conditions and the necessity of ordering equipment ahead of time, pile drivability prediction is assigned special importance in offshore construction. The one dimensional wave equation analysis [1] is widely used in studying the pile drivability problem. Yet, offshore piles are extremely expensive and further investigations of their behaviour are needed.

Soil-structure interaction plays an important role in predicting the response

of offshore structures to environmental loads, which are mainly dynamic. It alters the dynamic properties of the structure and may increase or decrease the response depending on the relationship of the fundamental natural frequency to the dominant exciting frequency. Random wave forces on offshore towers are usually evaluated using the directional spectrum of sea surface elevation. This representation does not take into account the lack of spatial correlation which may be associated with fully developed random waves.

1.2. Objectives of the Study and Organization of the Thesis

This study is divided into two main parts. The first part deals with the pile drivability analysis. The second part is concerned with the response of fixed offshore structures to random wave forces. The objectives of the first part are:

1. To improve on the one dimensional wave equation analysis of pile drivability by accounting, in a rational way, for wave propagation in the soil and by formulating parameters related to standard soil characteristics.

2. To formulate a three dimensional finite element analysis with suitable transmitting boundaries and compare its results to those of the one dimensional analysis in order to illustrate the advantages and limitations of both models.

In the second part of the study, the analysis is limited to the jacket type platforms or towers, and the objectives are:

1. To examine the effect of dynamic pile-soil-pile interaction on the response of fixed offshore towers to random wave forces.

2. To establish an approach for evaluating random wave loads on offshore towers which takes into account the lack of spatial correlation of random waves and allow for directional effects.

Chapter 2 gives a brief review of different types of offshore structures, main sources of environmental loads and the important parameters that govern the behaviour of these structures. In Chapter 3, the one dimensional wave equation

analysis of pile driving is reviewed. An improved soil model is developed which employs soil reactions to a harmonic load based on the plane strain assumption. Results obtained using the improved model are compared with those obtained from the traditional wave equation model.

A three dimensional finite element analysis of pile drivability is presented in Chapter 4. The pile-soil interface is modeled using a thin interface element characterized by an elastic-plastic behaviour. Plane strain soil reaction in the axisymmetric radial direction is developed to be used with soil reactions in the other directions as transmitting boundaries. Comparison with the improved one dimensional model is presented.

In Chapter 5, modelling of the tower foundation is discussed. Pile-soil-pile interaction is introduced by employing dynamic interaction factors which are modified to account for pile-soil separation. Effect of pile-soil-pile interaction on the dynamic properties of pile groups is demonstrated. In Chapter 6, a model for evaluating random wave loads on offshore structures is presented which takes into account the lack of spatial correlation associated with such waves. Spectrum of wave forces on offshore towers is formulated for members with general orientation. Wave force spectrum obtained using this model is compared with that obtained using the directional spectrum respresentation of sea surface elevation. The approximation involved by using a constant value of the velocity field over the tributary length is also examined using both models.

Chapter 7 presents the theoretical model used in evaluating the tower response. In Chapter 8, numerical results of the response of the tower are presented and the effects of the different parameters on the response are discussed. In Chapter 9, a summary of the study is given and conclusions are drawn.

Chapter Two
Review of Offshore Structures

2.1. Types of Offshore Structures

Currently, about 20 % of the world oil production is extracted from offshore reservoirs. Most of these reservoirs are located in the continental shelves where the average water depth is about 120 m. The vast majority of the early offshore structures are of the steel jacket (template) type which are installed in water depths less than 100 m. These template structures are fixed at the sea bed and are characterized by having short fundamental periods (or high fundamental frequencies) in the range of 1 to 5 seconds. Their natural periods, thus fall below those of the waves with significant energy content. Under such conditions, the response to extreme waves is mainly static with little dynamic magnification. These waves, typically, have periods ranging from 6 seconds to 25 seconds with the longer period waves having higher energy.

As new resources are discovered in deeper water and more severe environments, extrapolation of the conventional jacket platforms becomes unfeasible for two reasons. First, the required barge capacities for transportation and erection of these towers places a constraint on their size. Secondly and more important is the relationship of the natural periods to the periods of waves with high energy content. The natural period increases with water depth until, for deep water, it lies within the peak wave energy zone which leads to large dynamic magnification. For deep water, an alternative for the fixed platforms are the compliant structures which have fundamental periods well above the highest peak wave periods. In what follows, four main types of offshore structures are briefly described.

4

5
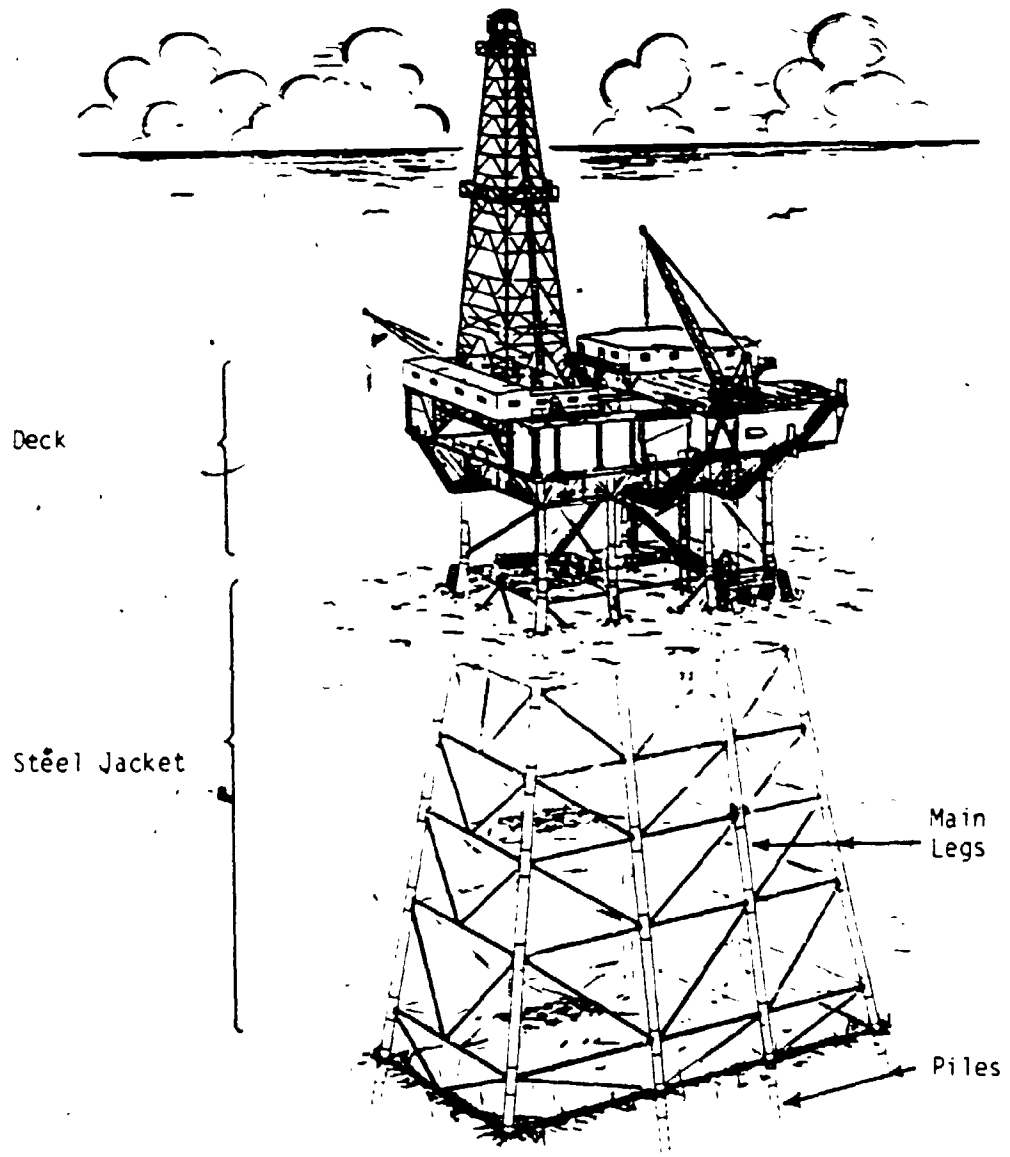
Figure 2-1: Steel Jacket Offshore Platform. Dawson [183]

1)Steel Jacket (Template) Platform: This is a space frame that extends from the sea bottom to above the water surface. Fig. 2.1   Piles are driven through the legs of the jacket into the sea floor.   These transfer vertical loads to the soil and fix the structure in place against lateral loads from wind, waves, currents and collisions with ships or icebergs.   The bending stiffness of the piles contribute to the lateral stiffness of the structure and thus they are rigidly connected to the structure and are placed as far away from each other as possible.   Template type platforms are suitable for water depths up to 300 m. The tallest such structure is the Cognac platform standing in 312 m of water.

2)Tension Leg Platform (TLP): It consists of a floating hull of a large size which is pulled down by highly tensioned vertical tethers. Fig. 2.2.   Some degree of lateral motion is allowed but the hull is pulled down so far that the tethers never go slack even in the trough of extreme waves.   One advantage of the TLP is the relative insensitivity of its cost to water depth.   Tension leg platforms have periods above 20 seconds and appear to be advantageous to other systems for water depths greater than 500 m.   The Hutton platform, constructed in 148 m of water, is the only TLP constructed so far.

The TLP foundation, which may consist of piles or gravity type footings, serves as an anchor to fix the tethers to the bottom of the sea.   In case of piled foundations, a base template is first positioned at the sea bed then piles are driven through sleeves in the template and grouted in these sleeves.   The foundation loading consists of the dead load and a constant tensile force due to buoyancy of the hull in addition to cyclic wave loads.   Experimental studies have shown that cyclic loading can cause significant degradation in the soil transfer capability and a marked decrease in the soil stiffness.

3)Guyed Tower PLatform: It consists of a slender steel tower held

Deck Section

Floating Hull

Tethers

Foundation
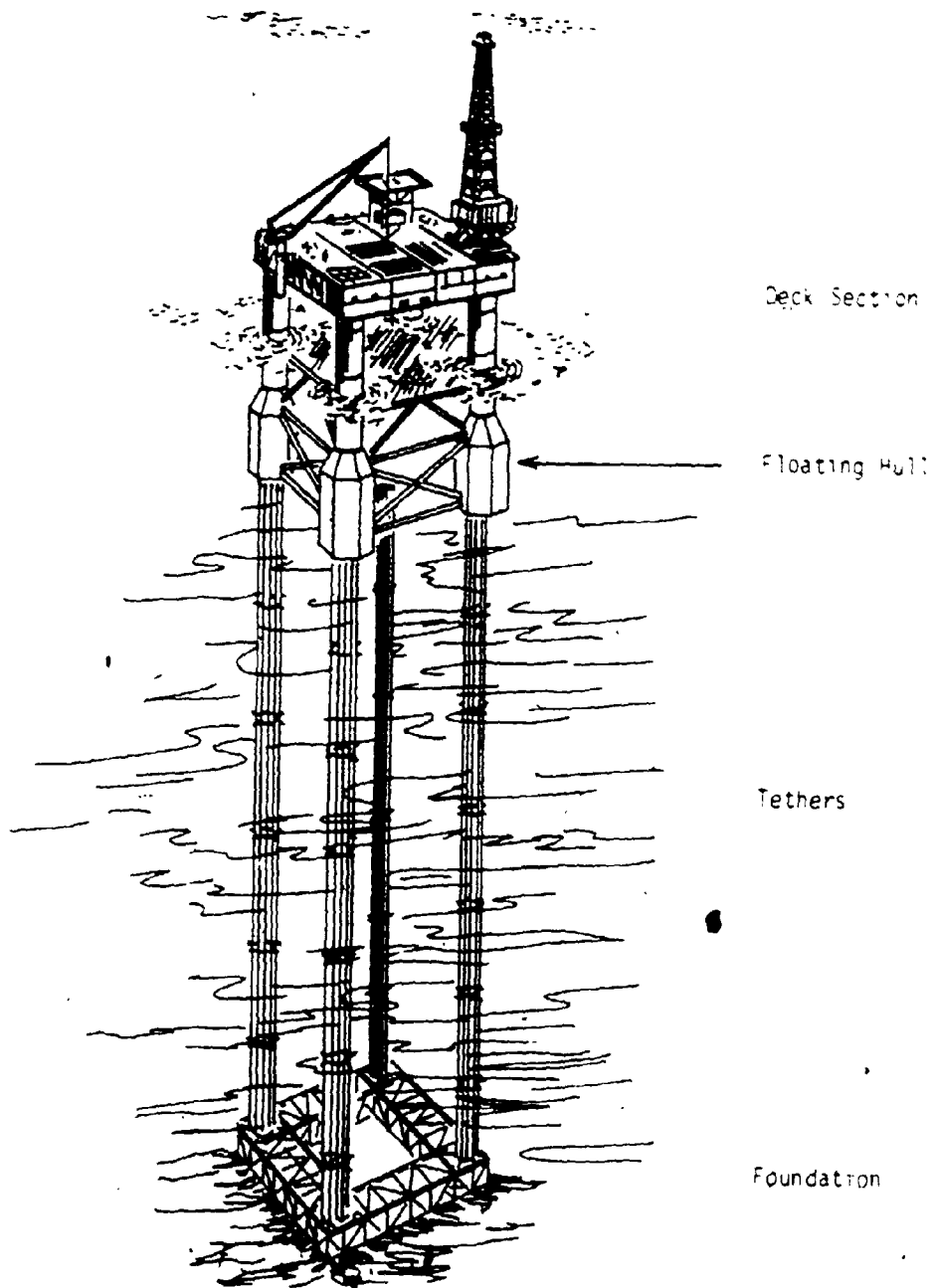
Figure 2-2: Schematic of a Tension Leg Platform, Dawson [183]

upright by anchor cables with clump weights resting on the sea bed. Fig. 2.3 Under extreme waves, these clump weights will gradually lift and allow the tower to tilt. The guyed tower, thus acts as a tower pinned at its base by pile foundations. Since this design uncouples the bending stiffness of the piles from the lateral stiffness of the tower, piles are not rigidly connected to the tower at the base but are pinned.

Lena guyed tower is the only such platform and was installed in 1984 in 305 m of water. Guyed towers, like TLP, are compliant structures with long natural periods and are allowed to moore laterally, thus resisting the wave loads by their inertia rather than their stiffness. It is expected that guyed towers will be cost effective in the range of 350 to 450 m of water [3].

4)Gravity Platforms: These are concrete structures with a large diameter base resting on the sea bed. The base usually consists of cylindrical cells of which only a few extend above mean water level to support the deck section which is made of steel modules, Fig. 2.4. Gravity base structures do not need to be anchored to the sea bed as they are stable under their immense weight. The cylindrical cells are used for the storage of crude oil and deisel fuel. Tankers can load crude oil directly from the platform, thus saving the cost of extending a pipeline to an onshore facility. The largest gravity type structure is the Statfjord B platform which weighs 899,000 ton and is built in 144 m of water.

2.2. Environmental Loads

The main sources of environmental loads on offshore structures are waves, currents, wind, ice, earthquakes and mudslides. Some of these loads are briefly discussed in the following.

1)Wave Loads: These can either be described by deterministic or stochastic methods. In the deterministic approach, a design wave is selected based upon a

Deck Section

Cables

Guyed Tower

Clump
Weight

Piled Foundation
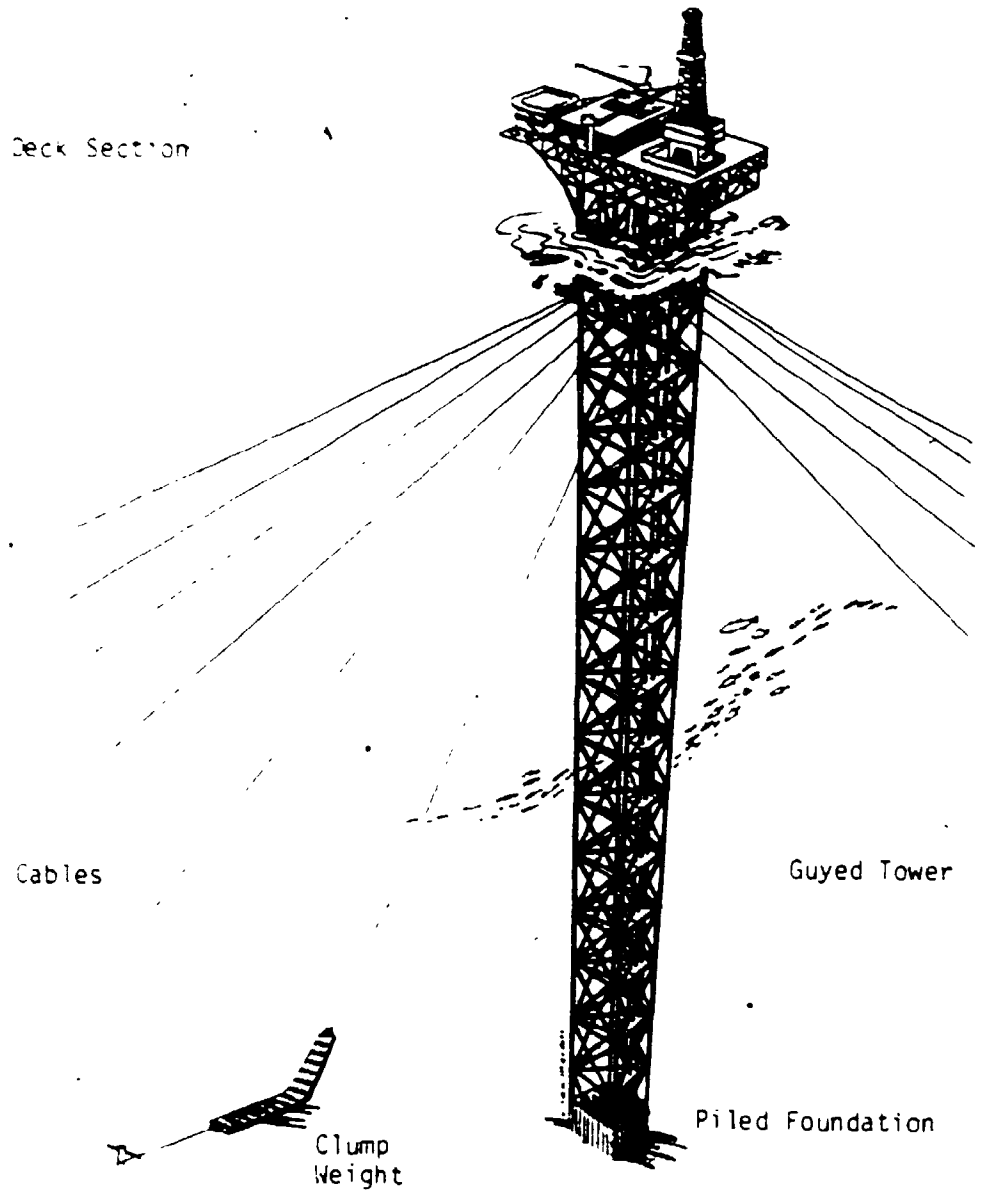
Figure 2-3: Guyed Tower Platform. Dawson [183]

Deck Section

Sea Level

Supporting Columns

Cylindrical
Cells

(-144 m)

Sea Floor
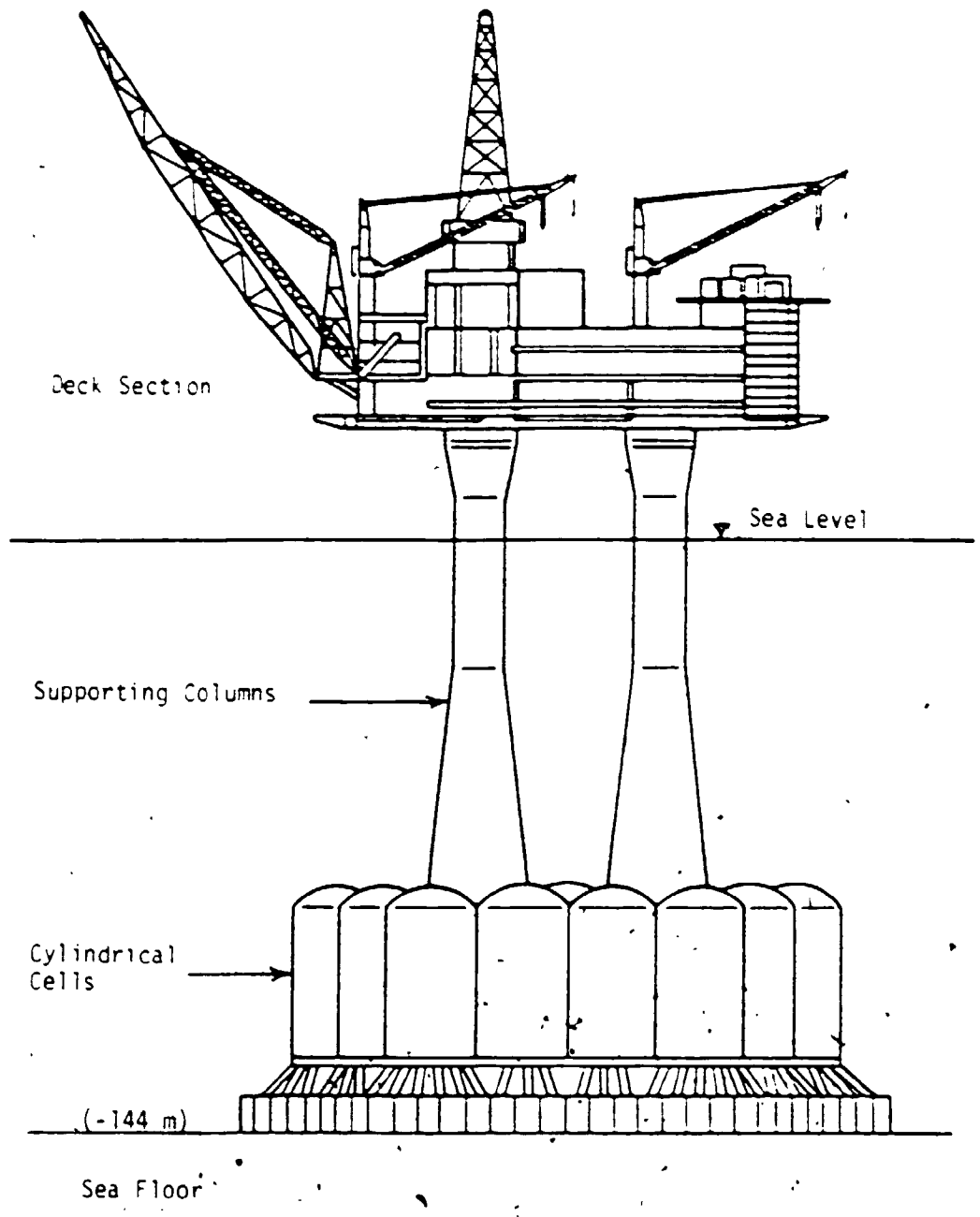
Figure 2-4: Statfjord B Concrete Gravity Platform

certain return period and may be specified by a nonlinear wave theory. In the stochastic approach, the sea surface elevation spectrum, which is related to the mean wind speed, is specified and a spectral analysis is performed

Wave loads are the dominant environmental loads for fixed structures such as the 'emplate and gravity structures. For compliant structures, wind loads may be predominant as their fundamental periods lie outside the peak wave energy periods and are closer to the peak periods of wind spectrum.

Shorter waves with little energy content have periods coincident with the natural periods of fixed offshore structures. Since their number of occurence per year is greater than that for longer waves, jacket type structures are more prone to fatigue damage than are compliant structures.

2)Wind Loads: These will be predominant for compliant structures with fundamental periods greater than approximately 40 seconds [4]. However, experience and data for wind loads on structures with such high natural periods are limited and further research is needed.

3)Ice Forces: These will be predominant in areas subject to severe ice conditions. Ice forces depend on many factors such as the mechanical properties of ice and geometry and type of ice formations [5]. Ice forces on a sloping structure (cone like) are less than those on a vertical structure since the ice sheets are broken by bending in the former case while they are broken by direct compression in the latter case. That is why ice resistant structures often have a conical geometry in the area subjected to ice sheets collision.

Chapter Three
One Dimensional Analysis of Pile Driving

3.1. Introduction

Theoretical prediction and analysis of pile driving records serve two purposes. On one hand, pile drivability and penetration can be assessed by determining the permanent set per blow (blow count) for a certain hammer system. On the other hand, driving records can be used to evaluate the pile bearing capacity.

Early attempts for pile driving analysis resulted in the "Dynamic Pile Formulae" which are used to determine the pile bearing capacity by relating it to certain parameters of the driving process. All of these formulae are empirical and consequently apply only to certain types of piles or soil conditions. These formulae, however can produce misleading results owing to the poor representation of the time dependent aspects of the problem.

Smith [1], in 1960, formulated the pile driving problem in terms of the one dimensional wave equation and introduced a numerical solution to the problem using a finite difference scheme . His solution caught wide attention and received acceptance because it offered the first rational approach for studying the many subtleties of the pile driving process. Smith introduced two non-traditional soil mechanics parameters in his model. These parameters are the quake and a damping constant. The quake is defined as the maximum elastic deformation of the soil adjacent to the pile before plastic deformation occurs. Both of these parameters can not be evaluated from laboratory experiments and have to be determined empirically by correlating the wave equation results with load tests and pile driving records.

Since then, most research has been directed towards refining the solution

Introduced by Smith. Because the method is mathematically sound. as far as wave propagation inside the pile is concerned. such refinements have been limited to suggesting better alternatives of the difference scheme to be used [6] or more sophisticated rheological models [7,8]. The wave equation analysis has also been used to study the influence of pile plugging [9] and residual forces on pile drivability and bearing capacity [10].

Recent research at Case Western Reserve University resulted in the Case Method Bearing Capacity Equation [11]. Using this equation. the bearing capacity of a pile is evaluated by relating it to certain values of the velocity and force time records measured during driving. It is important therefore to obtain a realistic prediction of both ; the permanent set and the time histories of the pertinent quantities. In this chapter. the representation of the soil resistance during driving is improved by accounting explicitly for wave propagation in the soil. This is accomplished using the plane strain soil reactions [12]. These reactions represent the resistance of a soil continuum to the harmonic vibration of an infinitely long rigid cylinder under the plane strain assumption. Soil shear modulus. Poisson's ratio and soil material damping ratio are the only parameters necessary to evaluate the plane strain soil reactions. These three parameters can be evaluated from conventional laboratory experiments. Results of the wave equation analysis obtained using the proposed model are then compared with those obtained using the original Smith model.

3.2. Wave Equation in Pile Driving Analysis

3.2.1. One Dimensional Wave Equation

Isaacs [13]. in 1931. was the first to point out that wave action occurs during pile driving. In 1938. Fox published the first solution to the wave equation applied to pile driving. but due to computation limitations he was compelled to make a number of simplifying assumptions which marred his solution [1].

When an elastic rod is subjected to a suddenly applied axial load, a stress wave is generated which travels away from the point of load application. For a slender rod, the plane stress approximation holds and the wave is considered as a one dimensional stress wave. With the lateral strain and material hysteresis neglected, the governing differential equation is the classical wave equation

$$\frac{\partial^2 u}{\partial t^2} = V_p^{'2} \frac{\partial^2 u}{\partial x^2} \qquad (3.1)$$

where $u = u(x,t)$ is the axial displacement of a particle at time t, whose original position is x, $V_p' = \sqrt{E/\rho}$ is the one dimensional primary wave velocity and E and ρ are the Young's modulus and mass density of the rod material, respectively. The solution to this equation is well known e.g. [14], and is given by

$$u(x,t) = g(V_p' t + x) + h(V_p' t - x) \qquad (3.2)$$

where g and h are arbitrary functions which depend on the initial disturbance. Waves traveling in the positive x-direction are represented by $h(V_p' t - x)$ while those traveling in the negative x-direction are represented by $g(V_p' t + x)$.

During pile driving, the vibrating pile meets soil resistance and an additional term has to be added to the wave equation to represent the soil resistance. The governing equation is then written as

$$\frac{\partial^2 u}{\partial t^2} = V_p^2 \frac{\partial^2 u}{\partial x^2} \pm \frac{R}{\rho A} \qquad (3.3)$$

where R is the soil resistance per unit length of the pile and A is the cross section area of the pile. $\pm R$ indicates that the soil resistance always opposes the motion. The solution of Eq. 3.3 depends on the nature of soil resistance.

Dynamic soil resistance differs from the static one in two main aspects. One is the presence of inertia forces in the vibrating soil mass, the other is the energy dissipation associated with wave propagation in the soil continuum. Soil

resistance can be split into a rate of deformaton independent part (stiffness) and a rate of deformation dependent part (damping). Both parts of soil resistance are nonlinear [7,15] and Eq. 3.3 is thus a second order nonlinear partial differential equation. An analytical solution to such an equation is difficult and numerical methods such as finite elements and finite differences are resorted to. The method suggested by Smith represents a finite difference solution to Eq. 3.3.

3.2.2. Smith Model

Only a brief description of the Smith model is given below as it is described in full detail elsewhere [1,16]. The pile-hammer system consists of the hammer ram, capblock, pile cap, cushion and the pile, Fig. 3.1. The ram and pile cap are idealized as rigid masses while the cap block and cushion are considered as massless springs. The pile is idealized by a set of dicrete elements, each ascribed a weight W'_m and a spring S_m. Soil resistance is assigned to each of these elements and is split into a rate (of deformation) dependent part, idealized as a dashpot and a rate independent part, idealized as a spring.

Under the effect of the hammer blow, the pile elements move and so do the adjacent soil particles. Soil deformation grows elastically up to a certain displacement where slip occurs and the soil offers a constant resistance to the pile elements, Fig. 3.2. On reversal of the direction of velocity, the soil deforms elastically until a full reversal has taken place where slip occurs in the opposite direction. As the pile element reaches the maximum displacement under the effect of the blow, elastic forces of the soil push it upwards and the element vibrates for a while before it settles in a new equilibrium position. The plastic displacement of the pile tip (permanent penetration) is called the set, Fig. 3.3. The spring representing soil stiffness per unit length of pile-soil interface is given by

$$k = R_u/Q \qquad (3.4)$$
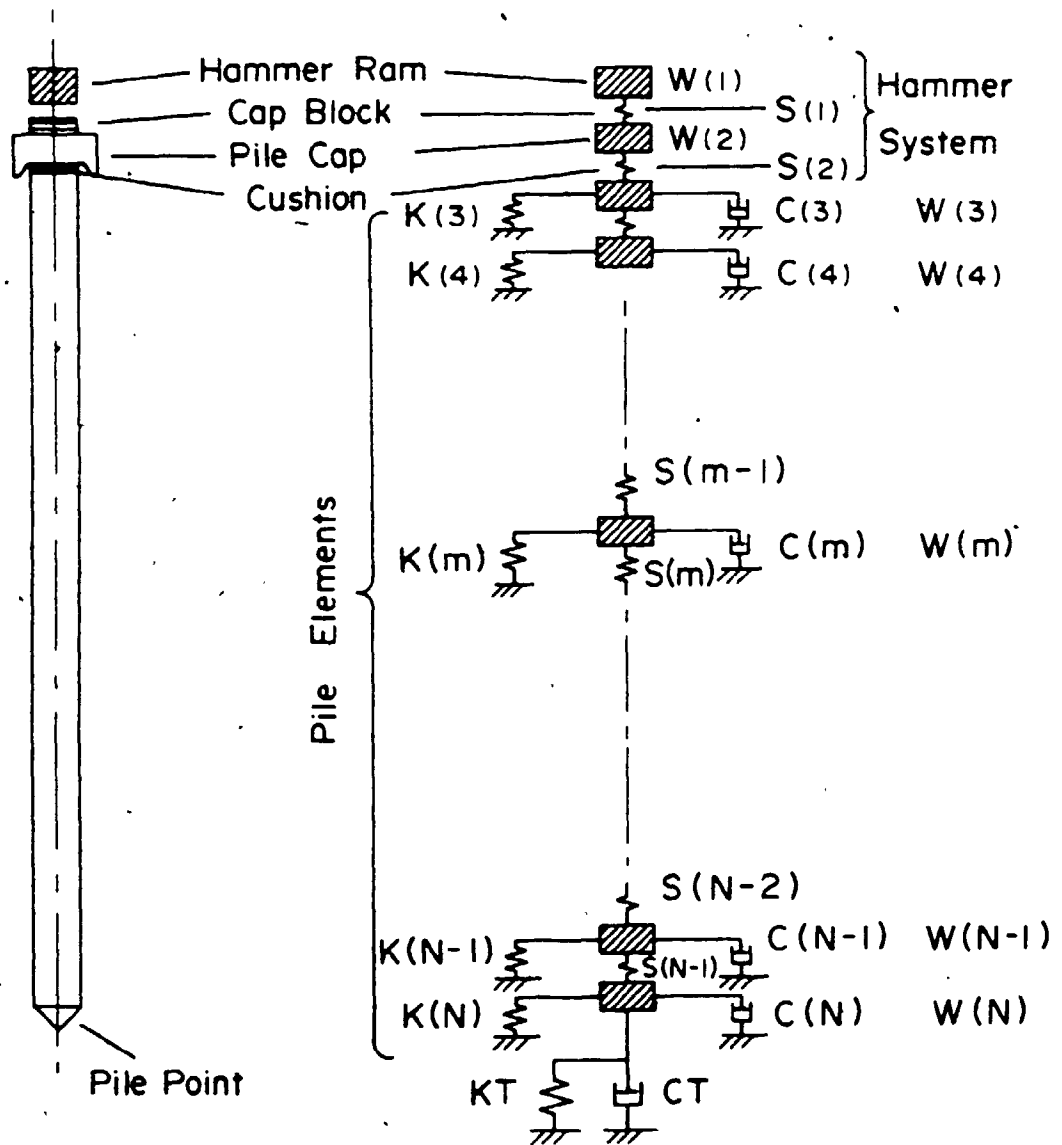
Figure 3-1: One Dimensional Idealization of the Pile Soil System

17
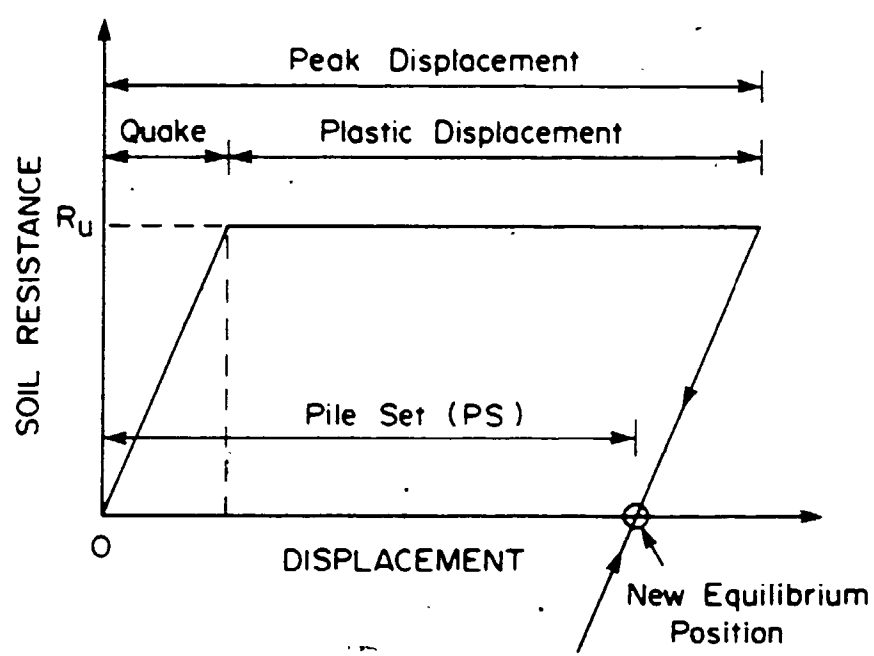
Figure 3-2: Force Displacement Relationship of Soil Spring
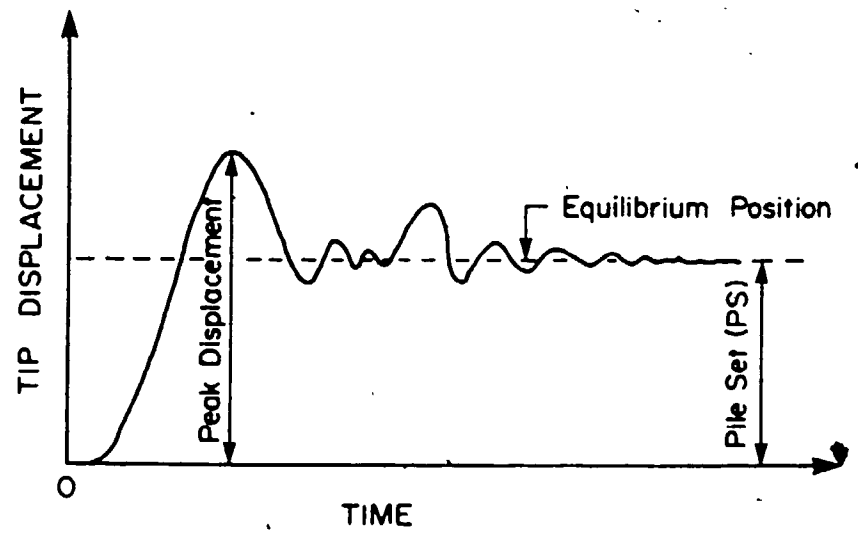
Figure 3-3: Vibration of Pile Tip Around an Equilibrium Position

where R_u is the ultimate static soil resistance per unit length of the interface and Q is the maximum elastic soil displacement, called the quake. For a given displacement of an embedded pile element, the corresponding static soil resistance, R_s, per unit length of the element is:

$$R_s = \begin{cases} kD & D < Q \\ k(D-D_p) & D \geq Q \end{cases} \qquad (3.5)$$

where D is the total displacement of the element and D_p is the plastic displacement of the ground, i.e. displacement in excess of Q.

The damping force, R_d, represents the dynamic part of the resistance and is given by

$$R_d = JR_s V = cV \qquad (3.6)$$

where J is a damping constant, V is the element velocity and c is the constant of equivalent viscous damping. Thus, the total soil resistance R_t is given by

$$R_t = R_d + R_s = R_s(1 + JV) \qquad (3.7)$$

or

$$R_t = \begin{cases} kD(1 + JV) & D < Q \\ k(D-D_p)(1 + JV) & D \geq Q \end{cases} \qquad (3.8)$$

Smith assigned different values for the tip and shaft damping constants J_p and J_s, respectively.

By the application of Newton's second law, Smith derived the following equations of motion

$$D_m^{(n)} = D_m^{(n-1)} + V_m^{(n-1)}\Delta t \qquad (3.9)$$

$$F_m^{(n)} = S_m(D_m^{(n)} - D_{m+1}^{(n)}) \qquad (3.10)$$

$$Z_m^{(n)} = F_{m-1}^{(n)} - F_m^{(n)} - R_m^{(n)} \qquad (3.11)$$

and

$$V_m^{\cdot(n)} = V_m^{\cdot(n-1)} - \frac{Z_m^{(n)}}{W_m^{\cdot}} \Delta t\, g \tag{3.12}$$

where m is the element number and n is the number of the time step. Δt and g are the time interval and gravity acceleration, respectively. $W_m^{\cdot}$, S_m and R_m are the weight, elastic spring constant and soil resistance associated with element m, respectively. Z_m is the net force acting on element m. In Fig. 3.1, S_1 and S_2 are the spring constants representing the cap block and cushion block, respectively, while S_3 to S_{N-1} represent the spring constants of the pile elements. Also in Fig. 3.1, k_t and c_t are the spring and dashpot constants of the pile tip, respectively, and k_3 to k_N and c_3 to c_N are the spring and dashpot constants of the soil resistance, respectively.

Smith showed that Eqs. 3.9 to 3.12 represent a finite difference solution to Eq. 3.3. Thus, in the Smith model, the following assumptions are adopted for soil:

1. An elastic, perfectly plastic soil spring.

2. A linear viscous dashpot whose magnitude is proportional to a fraction of the static soil resistance, i.e.

$$c = JR_s \tag{3.13}$$

The only parameters needed to establish this solution are the quake value Q, the damping constants J_s and J_p and the ultimate static soil resistance R_u. Based upon his personal experience, Smith recommended the following values: $Q = 0.1$ in., $J_s = 0.164$ sec/m and $J_p = 0.492$ sec/m and called for further investigations to study the soil behaviour during pile driving and determine more accurate values for Q and J.

3:3. Soil Resistance During Driving

The major shortcoming of the Smith model stems from the soil parameters. Q and J necessary to carry out the solution. Both parameters are empirical and are not standard soil mechanics parameters. Not much conflict has been reported about the value of the quake and a finite element analysis showed that Q ranged between 2 and 4 mm [17,18] which is in the vicinity of the original assumption of 2.54 mm suggested by Smith. Most troublesome is the damping constant J and considerable research has been devoted to its evaluation [15,19]. Unfortunately, these efforts have met little success. The contradiction reported in both the damping law as well as the value of J are attributed to two reasons. One being that R_d need not be proportional to R_s especially in the nonlinear range. The other is that J is not a standard soil mechanics parameter and the means to standardize it and evaluate it experimentally have not been developed yet. It was pointed out that the damping constant might not be a constant at all and that it might vary with velocity and other parameters [20].

Goble et al. [19] and Rausche et al. [11] used force and velocity field measurements to evaluate the static bearing capacity. For the dynamic resistance, they used an empirical form for the damping for correlation with static load tests to deduce suitable values for the damping constants to be used in similar conditions. However, load tests and field measurements are not always available and their cost might be prohibitive, especially for offshore structures [21]. Thus, the need arises for a better prediction of the time histories of the required quantities which could be used in lieu of field measurements in the process of evaluating the bearing capacity. A three dimensional finite element analysis conducted by I.M. Smith showed that the one dimensional calculations can be used to evaluate the blow count but not the bearing capacity.

During pile driving, the soil around the pile is subjected to elastic stresses which increase until they are equal to the shear strength of the soil causing ultimate failure of the soil in the form of plastic flow. As a result of this flow and plastic deformations, the soil is disturbed and remoulded causing excess pore water pressure to be generated. Consequently, shear strength of the soil around the pile is significantly less than that of the undisturbed soil. This reduction of the shear strength has been recommended by Vijayverglya [22] and reported by Roy et al. [23] based on full scale measurements on instrumented piles in a sensitive clay.

From the previous discussion, the following conclusions are drawn:

1. The Case method for pile driving analysis is suited only for situations where pile instrumentation is possible and can not give predictions for drivability or bearing capacity before the piles are driven in.

2. Although the Smith model introduced a fundamental improvement in understanding the pile driving process, it suffers from the limitation that the necessary parameters are empirical.

3. The need arises to improve the Smith model by introducing parameters based on traditional soil characteristics that can be reliably evaluated.

3.4. Proposed Model for Soil Resistance

In the current study, soil resistance to the vibrating pile is modelled using the plane strain soil reactions. The mathematical model used for formulating and solving the equations of motion is the finite difference model developed by Smith.

3.4.1. Plane Strain Soil Reactions

As the pile vibrates, forces are transfered through the pile-soil interface causing the soil mass around the pile to vibrate as well. During this vibration, energy is dissipated through radiation of elastic waves (geometeric damping) and by conversion into heat due to hysteresis (material damping). A proper

consideration of the soil resistance to the pile motion should consider this energy dissipation as well as the inertia forces of the soil mass and thus treat the soil as a continuum. Soil resistance to a harmonically vibrating rigid cylinder under the plane strain assumption was formulated by Novak et al. [12]. The soil resistance in the vertical direction is expressed in terms of the complex stiffness K_t where

$$K_t = G(S_{t1} + iS_{t2})$$ (3.14)

In Eq. 3.14, G is the soil shear modulus and S_{t1} and S_{t2} are dimensionless parameters that represent the soil stiffness and damping, respectively and depend on frequency. The plane strain soil reactions are discussed in more detail in Section 4.2.

Soil resistance also depends on pile slippage and the resulting nonlinearity. Near the pile, soil behaves nonlinearly while some distance away from the pile, soil acts linearly. To account for this behaviour, an approximate solution was formulated which considers a weakened zone of soil around the pile [24,25]. The weakened zone is assumed to be axisymmetric with radius b and have a shear modulus G_m.

Fig. 3.4 shows the variation in S_{t1} and S_{t2} with dimensionless frequency a_o ($a_o = \omega r_o/V_s$ where ω is the circular frequency, r_o is the cylinder radius and V_s is the soil shear wave velocity). It can be seen that the stiffness of the composite medium is less than that of the homogeneous medium at lower frequencies and is larger at higher frequencies. Damping of the composite medium is less than that of the homogeneous medium and the reduction is more significant at higher frequencies. Larger reductions in S_{t1} and S_{t2} occur for smaller values of G_m/G and r_o/b.
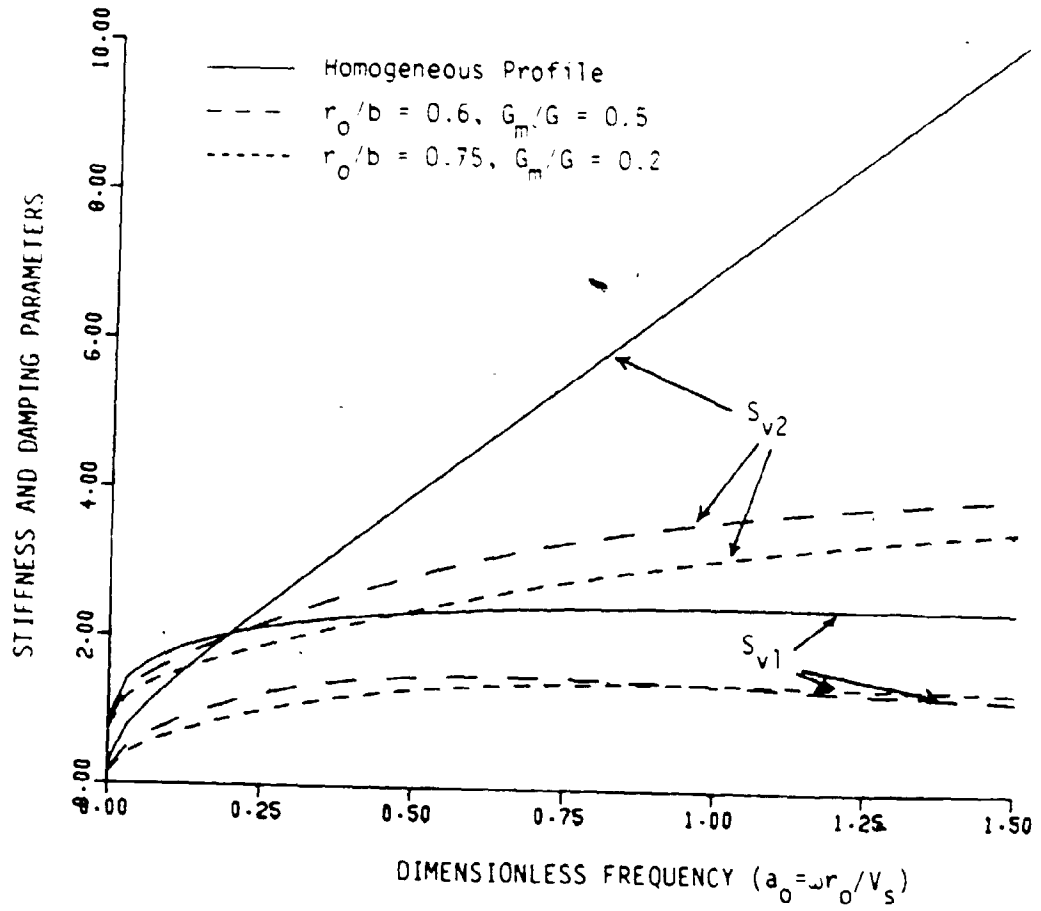
Figure 3-4: Plane Strain Vertical Reactions for the Composite Medium

3.4.2. Soil Stiffness and Damping

In this study. the spring representing soil stiffness along the pile shaft is modelled as

$$k = GS_{v1} \tag{3.15}$$

and that at the pile tip is given by

$$k' = Gr_o C_{v1} \tag{3.16}$$

In Eq. 3.16. C_{v1} is the real part of the viscoelastic half space reaction to a vibrating rigid massless disk [26]. A bilinear soil spring. Fig. 3.2. is also assumed in the proposed model. The elastic limit of the soil resistance may be determined using either of the following criteria

1. Assuming a value for the quake as in the original Smith model. In this case. the ultimate resistance is $R_u = GS_{v1}Q$.

2. Assuming a value for the ultimate resistance R_u. In this case. the quake value is $Q = R_u/GS_{v1}$.

These two criteria are used to analyse the drivability of an example pile and the results are compared in Section 3.5.

The rate dependent part of the resistance is modelled by a viscous dashpot whose magnitude. for the pile shaft, is

$$c = GS_{v2}/\omega \tag{3.17}$$

and for the pile tip is

$$c' = Gr_o C_{v2}/\omega \tag{3.18}$$

In Eq. 3.18. C_{v2} is the imaginary part of the viscoelastic half space reaction to a vibrating rigid massless disc [26].

Before slippage occurs. the pile and the surrounding soil are still in contact and vibration of the soil mass provides radiation damping to the pile motion. Accordingly. the values of the parameters S_{v1} and S_{v2} in Eqs. 3.15 and 3.17. respectively. should be those for a horizontally homogeneous medium. However. the stresses in the soil near the pile are high and the soil around the pile has been

disturbed under the effect of previous hammer blows. Thus, it is reasonable to allow for a weakened zone with a reduced shear modulus around the pile shaft, even before slippage. During plastic deformation (slippage), the bond between the pile and the surrounding soil breaks and each of them moves independently except for the interconnecting frictional force between the two. Radiation damping during slippage thus depends on the velocity of the adjacent soil particles and not that of the pile. Soil resistance to pile motion during slippage would be best modelled by this frictional force if realistic values for the friction can be estimated. Unfortunately, systematic and reliable measurements of this force are not yet available. In this study, the soil stiffness and damping parameters for the pile shaft, S_{t1} and S_{t2}, respectively, are taken to be those of the composite medium before and during slippage. Accordingly, the total soil resistance at the pile shaft is given by

$$R_t = \begin{cases} (GS_{t1})D + (GS_{t2})V & D < Q \\ (GS_{t1})Q + (GS_{t2})V & D \geq Q \end{cases} \qquad (3.19)$$

and for the pile tip is given by

$$R_t' = \begin{cases} (Gr_oC_{t1})D + (Gr_oC_{t2}/\omega)V & D < Q \\ (Gr_oC_{t1})Q + (Gr_oC_{t2}/\omega)V & D \geq Q \end{cases} \qquad (3.20)$$

3.5. Example

The following properties are assumed for the soil-hammer-pile system

Hammer and capblock

Hammer weight	75 KN
Impact velocity	5 m/sec
Capblock diameter	0.72 m
Capblock height	0.18 m
Young's modulus of capblock	3.1×10^9 Pa
Coefficient of restitution of capblock	0.8
Weight of pile cap	31.5 KN

Pile

Outer diameter	1.524 m
Density	7700 kg/m^3

Wall thickness	0.032 m
Total length = embedded length	20 m
Young's modulus	2×10^{11} N/m^2

Soil

J_p	0.492 m/sec
J_s	0.164 m/sec
Density	1800 kg·m^3
Quake	2.5×10^{-3} m
Poisson's ratio	0.25

A numerical study has shown that the system is stable for $\Delta t \leq 2 \times 10^{-4}$ sec. accordingly. Δt was chosen to be 2×10^{-4} sec. For the Smith model, the soil resistance is calculated from Eq. 3.8 and the ultimate static resistance per unit length at the pile shaft is evaluated from

$$R_u = \alpha \pi d C_u \qquad (3.21)$$

and for the pile tip

$$R_u' = \pi \frac{d^2}{4} N_d C_u \qquad (3.22)$$

In Eqs. 3.21 and 3.22, C_u is the soil undrained shear strength. α is a reduction factor to represent the reduction in ultimate soil resistance during driving. d is the pile diameter and N_d is the bearing capacity factor assigned here the numerical value of 9. For the proposed model, the reduction in shear modulus in the weakened zone is taken to be equal to α for the sake of comparison with the Smith model, i.e.

$$G_m/G = \alpha \qquad (3.23)$$

The real part of the viscoelastic half space reaction to a rigid massless disc varies mildly with frequency while C_{v2}/ω is almost frequency independent. The elastic soil properties needed to evaluate the parameters for the proposed model are established from the following relationship

$$E = \lambda C_u \qquad (3.24)$$

where E is the soil Young's modulus and λ ranges between 500 and 1000.

Fig. 3.5 shows the time history of the tip displacement evaluated using both models and assuming $C_u = 100$ KPa, $\alpha = 0.5$, $r_o/b = 0.3$, $a_o = 0.5$ and $\lambda = 500$. It can be seen that the first peak is very close for both models but that the proposed model gives a more damped response. It is noticed that the less damped vibration resulting from the Smith model has a distinct period of vibration. This period can be used to establish the value of a_o at which the parameters of the proposed model are evaluated. However, it was recognized by a number of authors that the lightly damped oscillations characteristic of the Smith model are unrealistic.

Fig. 3.6 shows the time history of the tip displacement calculated using both models for $C_u = 100$ KPa, $\alpha = 0.5$, $r_o/b = 0.65$, $a_o = \dfrac{2\pi r_o}{T V_s}$ and $\lambda = 500$ where T is the vibration period shown in Fig. 3.5. Also shown in Fig. 3.6 is the pile tip displacement evaluated assuming $Q = \dfrac{\alpha \pi d C_u}{G S_{vl}}$. While the three models predict almost the same value for the first peak, model A gives a larger set as it has a smaller value of the quake. Fig. 3.7 shows the pile tip displacements calculated using the proposed model and Smith model for $\alpha = 0.2$ and $\alpha = 1.0$. It can be seen that the proposed model gives a smaller value for the set in both cases. These results are qualitative rather than quantitative since the pile tip displacements and all other quantities are sensitive to both r_o/b and a_o. If the value of a_o is chosen on the basis of the dominant period of the undamped pile as suggested, it remains to evaluate the proper value of r_o/b. For the pile studied in the present example, a value of $r_o/b=0.65$ gives a good agreement with the pile set from the Smith model. The actual value of r_o/b is believed to be random in nature and should be established from comparison with a large number of pile driving records and load test results. This point needs further investigation.
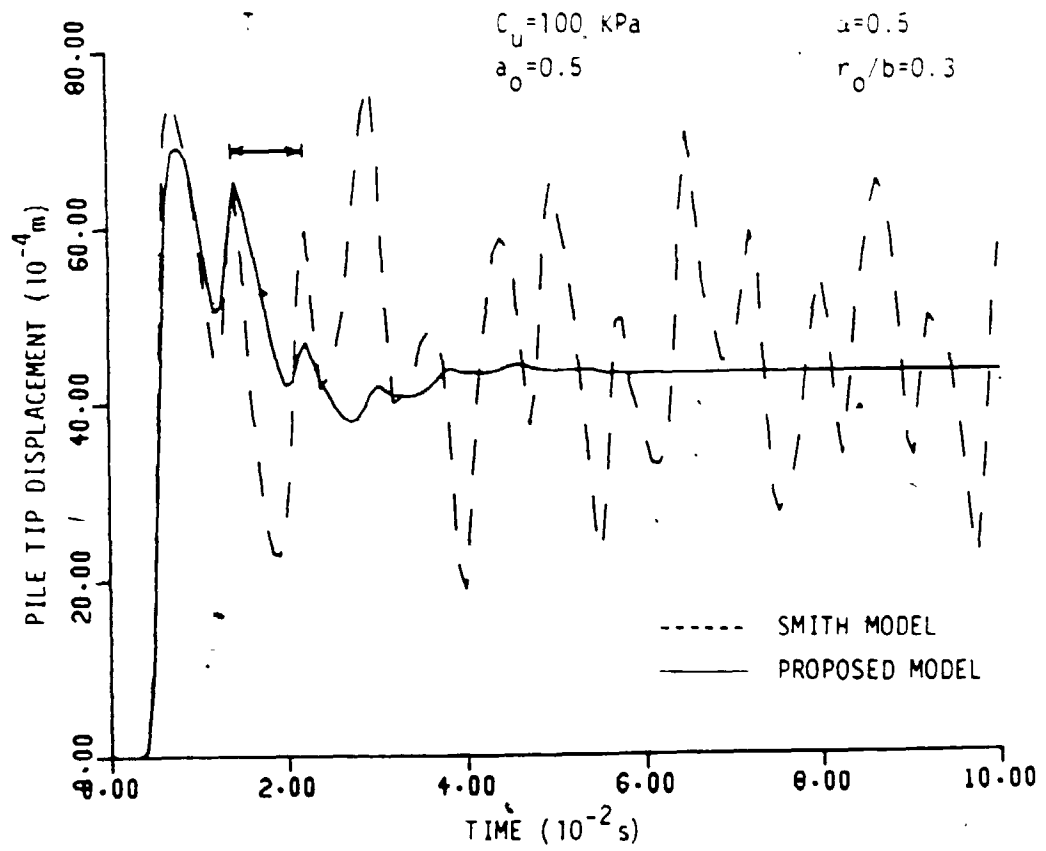
Figure 3-5: Comparison of Pile Tip Displacements for Two Models
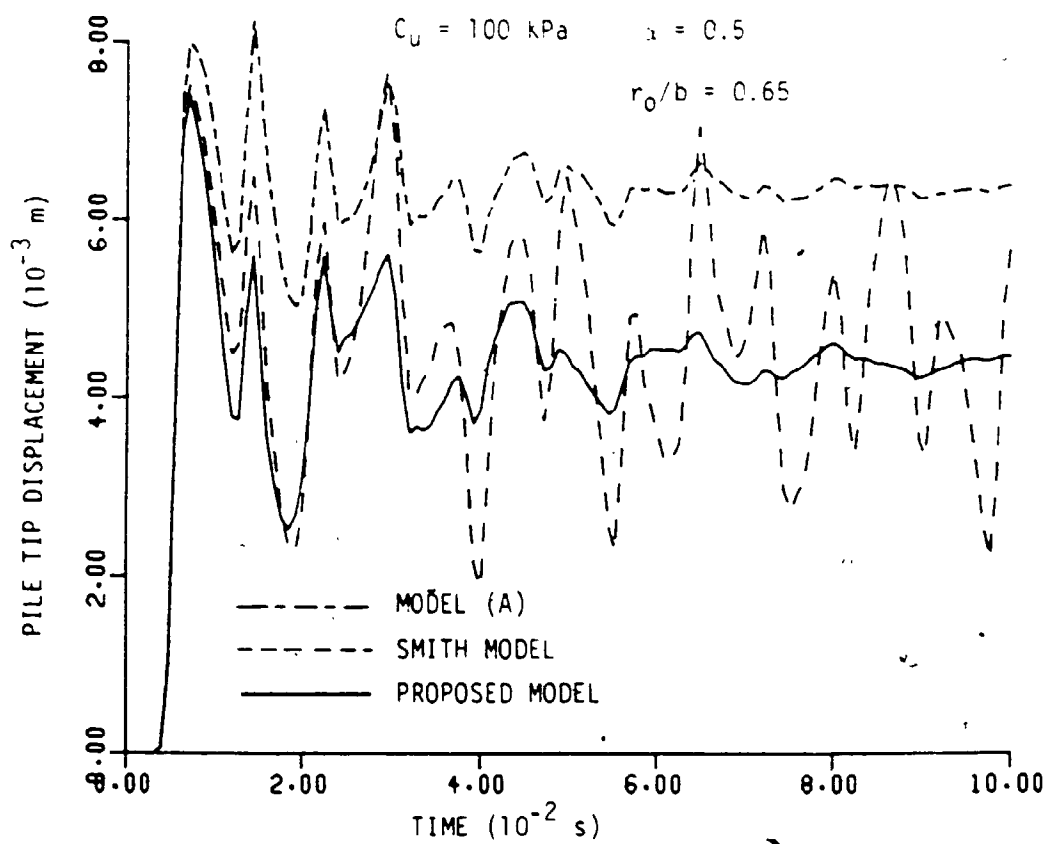
Figure 3-6: Comparison of Pile Tip Displacements for Three Models
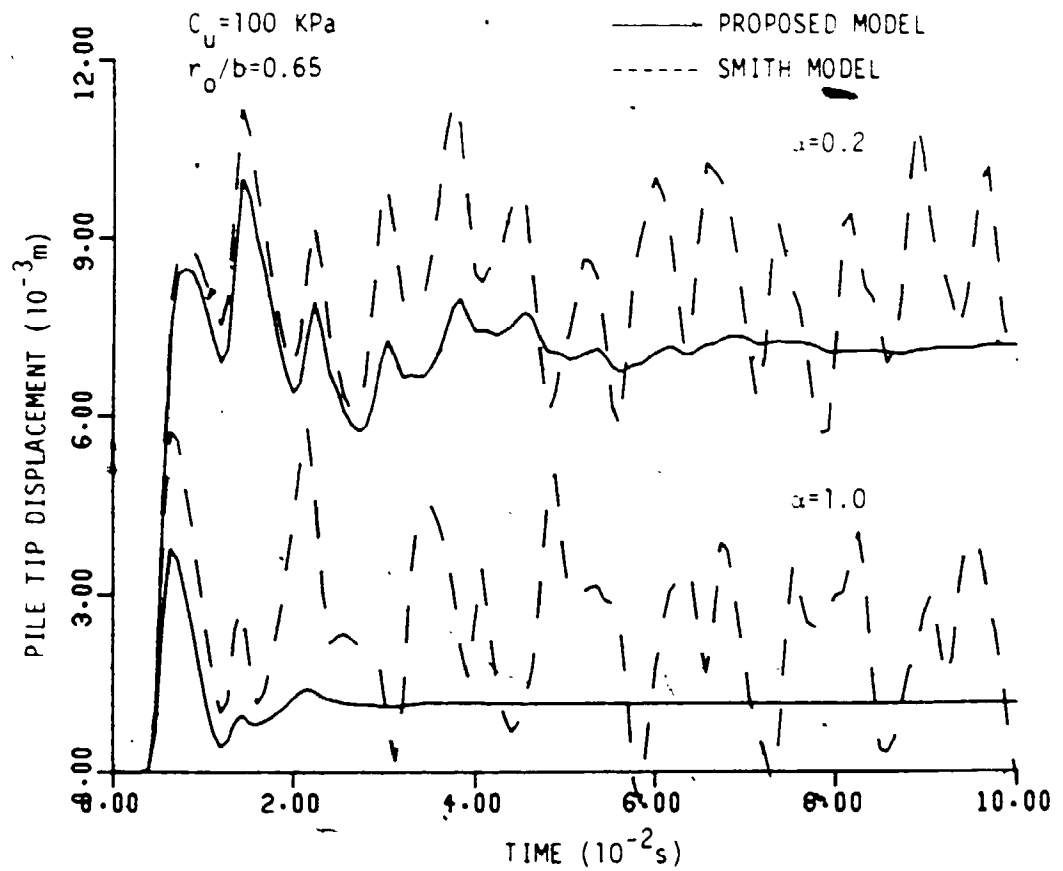
Figure 3-7: Pile Tip Displacements for Two Interface Conditions

Figs. 3.8 and 3.9 show the velocity and force time histories, respectively, for both models calculated assuming $\alpha = 0.5$ and $C_u = 100$ KPa. It is noticed that the two models give equal values for the first two peaks of velocity and force, which are usually used for bearing capacity evaluation. The time records for velocity and force at the pile top for both models evaluated assuming $\alpha = 0.5$ and $C_u = 300$ KPa, are shown in Figs. 3.10 and 3.11, respectively. Although the first two peaks of the force are equal, those of the velocity differ substantially which may lead to significant differences in the bearing capacity prediction.

The proposed model is applied to evaluate the pile tip displacements resulting from a number of blows applied at several stages of the driving process for a pile with somewhat different properties than the example pile. Fig. 3.12 shows the pile tip displacements for 10 hammer blows as the embedded length of the pile increases from $L/10$ to L. As the embedded length of the pile increases, the set decreases indicating an increased blow count and the response becomes more damped.

The static bearing capacity R_s of the example pile is evaluated using the Case Method Bearing Capacity Equation [11] which is written as

$$R_s = \frac{1}{2}(1 - j_c)\{F(t_m) + MV_p V(t_m)/L\} \tag{3.25}$$
$$+ \frac{1}{2}(1 + j_c)\{F(t_m + 2L/V_p) - MV_p V(t_m + 2L/V_p)/L\}$$

In Eq. 3.25, F and V are the force and velocity at the pile top, respectively. M, V_p and L are the mass, primary wave velocity and length of the pile, respectively. t_m is the time at which the first velocity peak occurs and j_c is a dimensionless damping constant. The bearing capacity is calculated for different values of the embedded length assuming a value of $j_c = 0.4$ which is characteristic of silty clay as recommended in [11]. Fig. 3.13 shows the increase in bearing capacity and blow count as the embedded length of the pile increases.
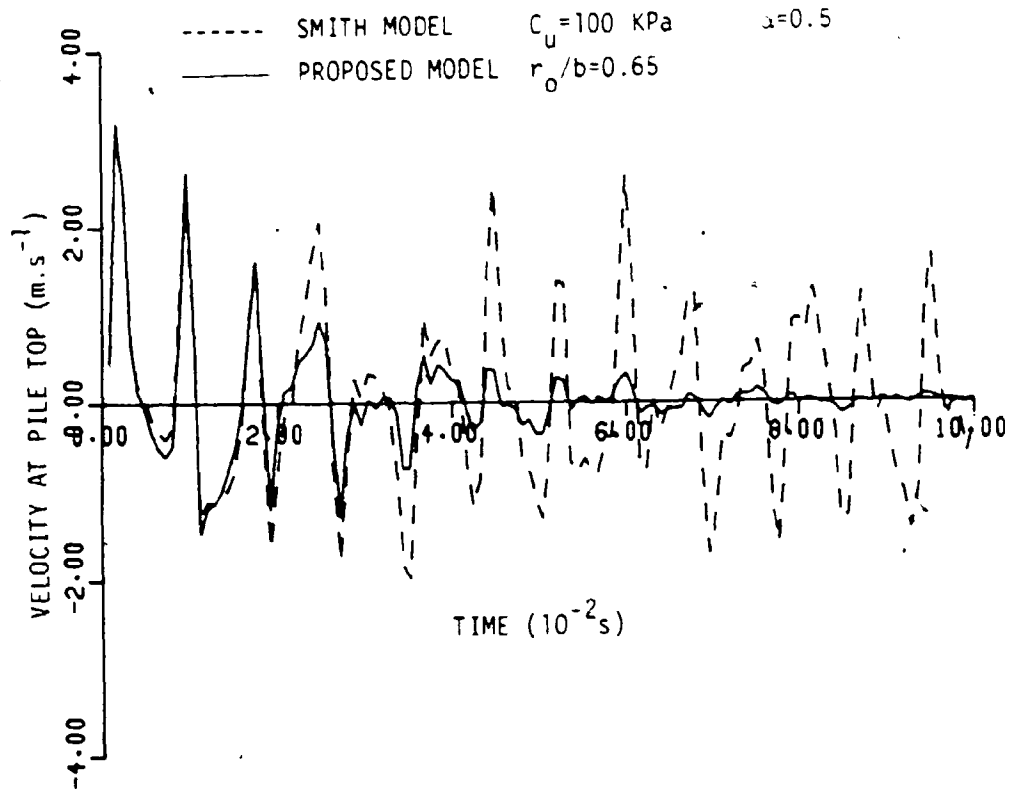
Figure 3-8: Time History of Velocity at Pile Top ($\alpha=0.5$ and $C_u = 100$ KPa)
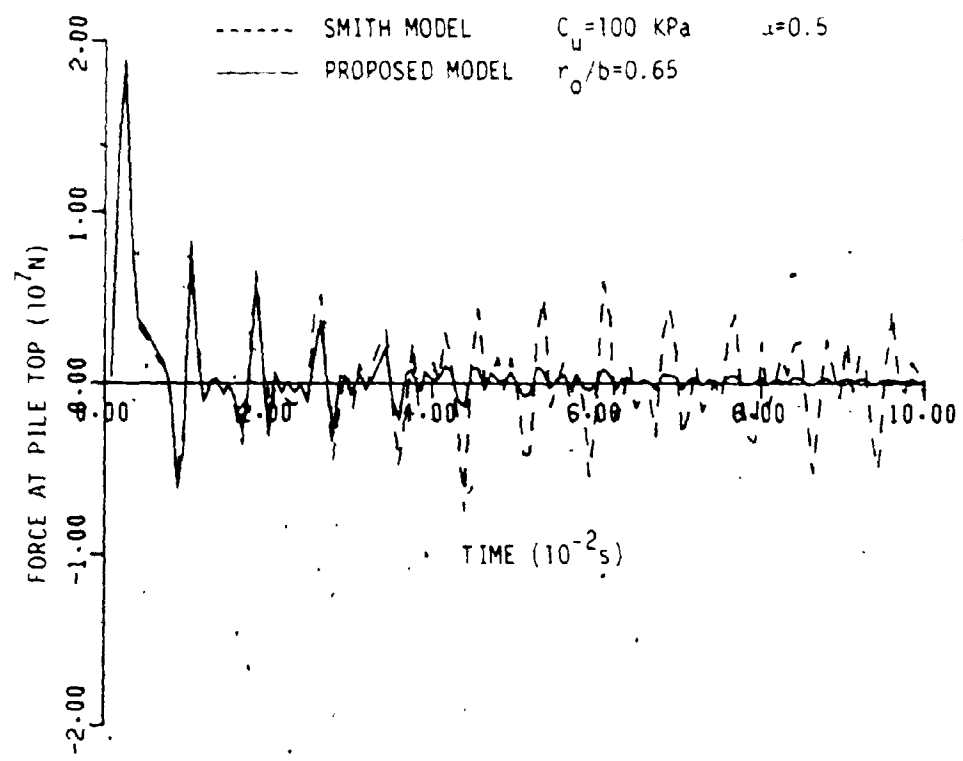
Figure 3-9: Time History of Force at Pile Top ($\alpha = 0.5$ and $C_u = 100$ KPa)

34
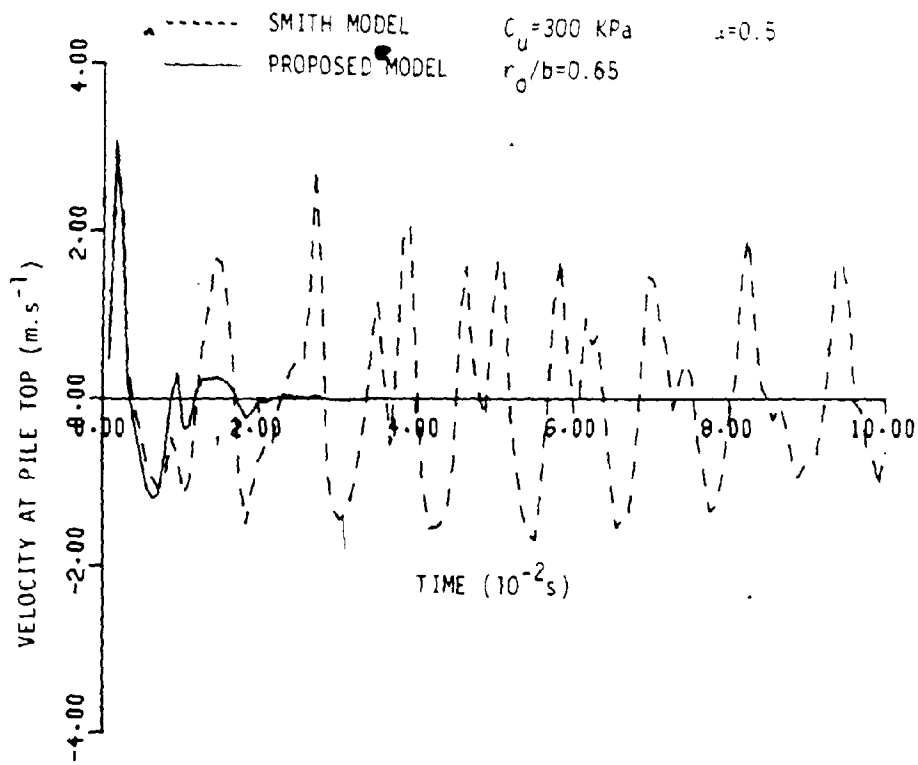
Figure 3-10: Time History of Velocity at Pile Top ($\alpha = 0.5$ and $C_u = 300$ KPa)
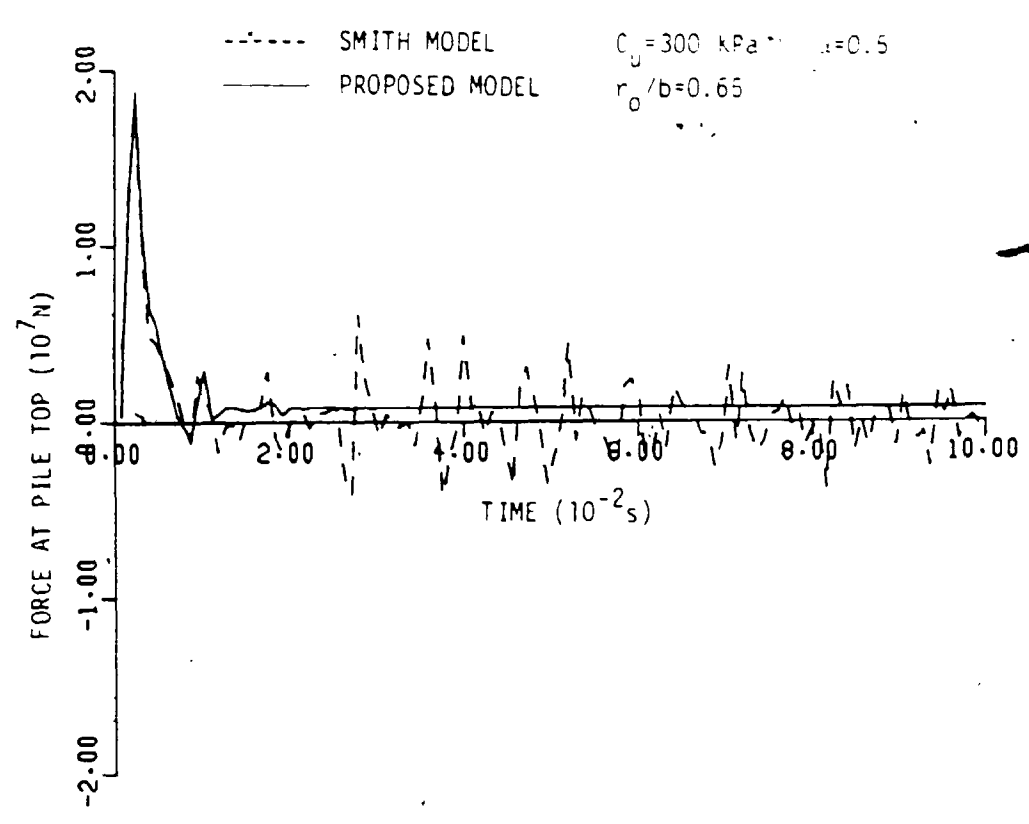
Figure 3-11: Time History of Force at Pile Top ($\alpha = 0.5$ and $C_u = 300$ KPa)
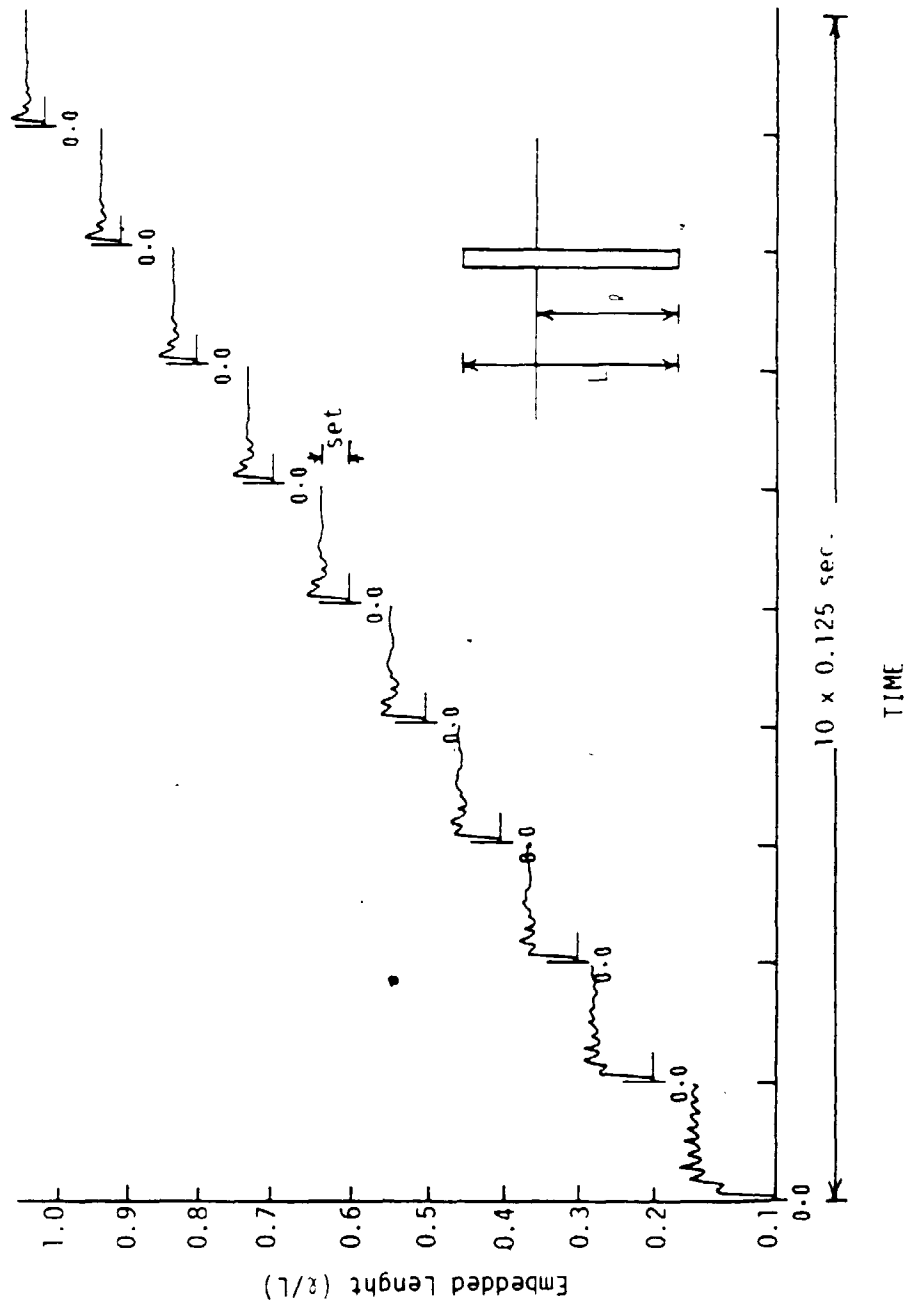
Figure 3-12: Pile Tip Displacements for Different Embedded Lengths
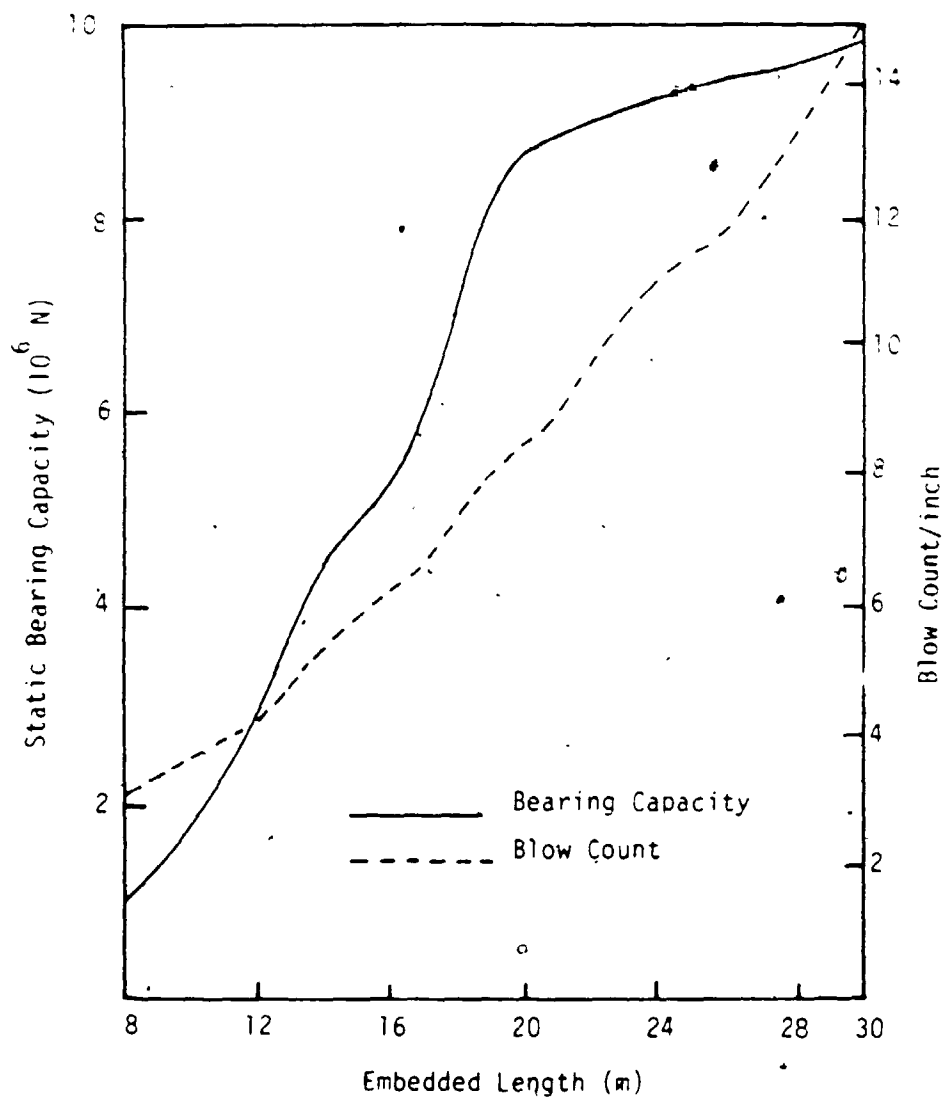
Figure 3-13: Bearing Capacity and Blow Count for Different Embedded Lengths

3.6. Conclusions

Pile driving analysis is used to assess the drivability as well as predict the pile bearing capacity. The conventional one dimensional wave equation analysis represents the soil resistance using empirical constants which might affect its reliability. In this study, soil resistance is derived from the plane strain soil reactions which are based on fundamental soil properties. This model takes into account the inertial effects of the surrounding soil medium and the nonlinearity of the soil zone adjacent to the pile in an approximate fashion. Results obtained using this model are compared with those of the conventional analysis and the following conclusions are drawn:

1. The new soil model gives a more damped response than that obtained from the conventional model, which is closer to reality and might affect the velocity and force time records and consequently the evaluation of the bearing capacity.

2. The pile tip displacement obtained using the new soil model is sensitive to the extent of the weakened zone around the pile which should be estimated from comparisons with field data.

3. The new soil model is based on fundamental soil properties which makes it more reliable.

Chapter Four
Three Dimensional Analysis
of Pile Driving

4.1. Introduction

The one dimensional wave equation idealization is increasingly in use for pile drivability analysis, e.g. [27,28,29]. Recent advances in pile instrumentation and measurement techniques made it possible to extend the applicability of the wave equation analysis to predict the static pile bearing capacity [30,31,11]. Due to the high costs involved with test driving piles, especially in the offshore environment [21], the need arose for a method which enables the accurate prediction of pile driving records. Although this can readily be done using the one dimensional model, the main weakness of this approach is the use of non standard soil characteristics as pointed out in Chapter 3. Some researchers have even recommended to abandon the use of the quake value Q and the damping constants J_s and J_p and to use a constant value for the shaft friction [32].

Smith et al. [17,33] and Chow et al. [18] conducted a three dimensional finite element analysis of the pile driving problem in an attempt to model the soil inertia and geometric damping more realistically. In their analysis, Smith et al. used an interface element to account for slippage between the pile and surrounding soil and a viscous boundary to absorb elastic waves at the boundaries of the finite element mesh. They concluded that while the one dimensional model closely estimates the pile set, it does not accurately predict the displacement, velocity and force time records. More recently, Wu et al. [20] used the finite element method to model the shaft resistance during driving and correlate the quake and damping constant with the soil shear modulus and yield strain.

In this chapter, a finite element analysis of the pile-soil system is developed to examine the applicability of the finite element analysis to the pile driving problem. Results of this analysis are compared with the results of the model developed in Chapter 3 to assess the behaviour of both models. A new transmitting boundary for vibration in the radial direction is developed for use in the finite element mesh.

4.2. Transmitting Boundaries

4.2.1. General

In the finite element method, a finite region of the unbounded soil domain is represented and discretized into finite elements, Fig. 4.1. A vibrating body in an elastic medium causes the propagation of elastic waves in the continuum. These waves are reflected back inside the mesh if either a free or a fixed boundary is used. To alleviate this problem, Luco and Hadjian [34] tried to determine the amount of material damping which would account for energy radiation that otherwise takes place in the semi infinite medium and several artificial boundaries have been proposed as a means of absorbing the radiated energy.

Lysmer et al. [35] and Kuhlemeyer [36] introduced the viscous boundary which relies on the fact that the normal stress in an elastic rod is proportional to the particle velocity at the same point taking on the character of viscous damping. An artificial boundary is thus formed by imposing a viscous boundary along the mesh periphery. When used in a continuum, the accuracy of the viscous boundary deteriorates with the obliqueness of the incident waves. White et al. [37,38] attempted to improve on the viscous boundary and to include soil anisotropy. They minimized the unabsorbed energy with respect to the viscous dashpots. Lysmer and Drake [39], introduced a consistent boundary that is especially designed to absorb Rayleigh or Love waves in layered media. Other artificial boundaries were also suggested by different researchers, e.g. [40,41].
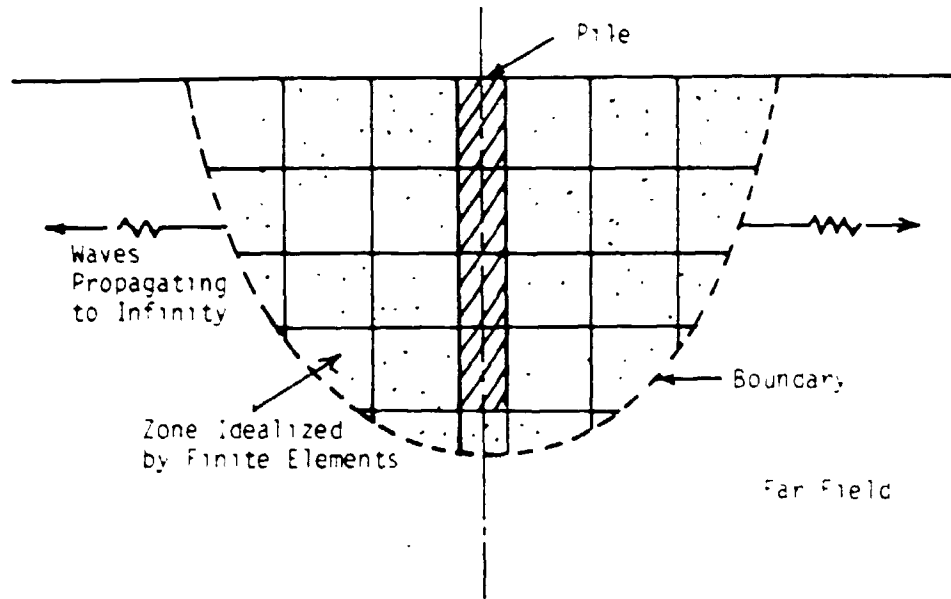
Figure 4-1: Finite Element Modelling of a Continuum Problem
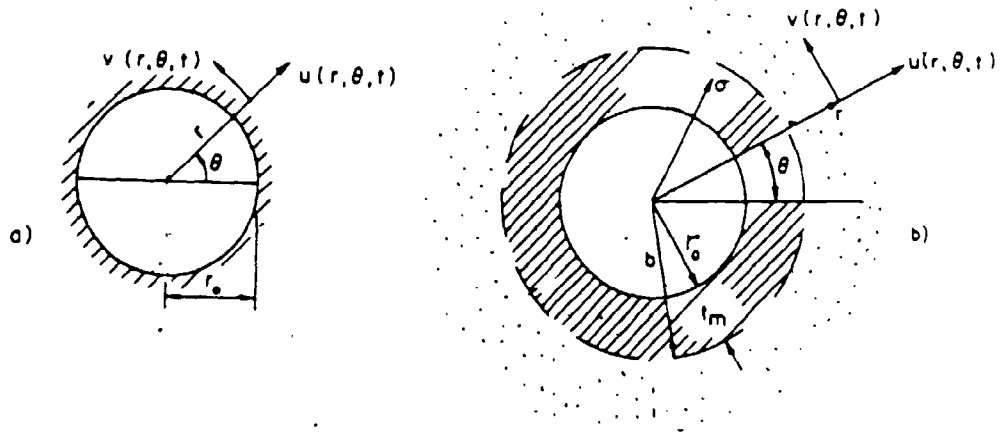
Figure 4-2: Displacement Components in the Cylindrical Coordinates

Among the several artificial boundaries developed by various investigators, the standard viscous boundary is most popular due to its simplicity and suitability for time domain analysis. However, for pile driving analysis this boundary is defficient in that it lacks the stiffness (in phase) part which may result in further errors.

4.2.2. Plane Strain Transmitting Boundary

In this study, a new transmitting boundary is formulated which applies to the sides of the finite element mesh. This new boundary is based on the plane strain soil reactions [12] and is best suited for frequency domain analysis. Soil resistance to harmonic vibration of an infinitely long rigid cylinder was investigated by Novak et al. for all vibration modes except for the radial axisymmetric vibration which is investigated in this study. The following assumptions are adopted:

1. The cylinder is rigid, massless and infinitely long.

2. Perfect bond occurs between the cylinder and soil medium.

3. The soil medium is isotropic and viscoelastic with frequency independent material damping and is either homogeneous as in Fig. 4.2a or has an inner weakened zone as in Fig. 4.2b.

4. The displacements are small and the vibration is harmonic.

Under these assumptions, the equations of motion of a viscoelastic continuum in the cylindrical coordinates, Fig. 4.2, are written as [12]

$$(1 + \imath 2\beta) \; \{(\lambda + 2G)\frac{\partial \Delta}{\partial r} - \frac{2G}{r}\frac{\partial \omega_z}{\partial \theta} + 2G\frac{\partial \omega_\theta}{\partial \omega_z}\} = \rho \frac{\partial^2 u}{\partial t^2} ; \qquad (4.1)$$

$$(1 + \imath 2\beta) \{(\lambda + 2G)\frac{\partial \Delta}{r\partial \theta} - \frac{2G}{r}\frac{\partial \omega_r}{\partial \theta} + 2G\frac{\partial \omega_z}{\partial r}\} = \rho \frac{\partial^2 v}{\partial t^2}$$

$$(1 + \imath 2\beta) \{(\lambda + 2G)\frac{\partial \Delta}{\partial z} - \frac{2G}{r}\frac{\partial (r\omega_\theta)}{\partial r} + 2G\frac{\partial \omega_r}{r\partial \theta}\} = \rho \frac{\partial^2 w}{\partial t^2}$$

The relative volume change Δ is given by

$$\Delta = \frac{\partial(ru)}{r\partial r} + \frac{\partial v}{r\partial \theta} + \frac{\partial u}{\partial z} \qquad (4.2)$$

and the components of the rotation vector are given by

$$\omega_r = \frac{1}{2}\left(\frac{\partial u}{r\partial \theta} - \frac{\partial v}{\partial z}\right) \qquad (4.3)$$

$$\omega_\theta = \frac{1}{2}\left(\frac{\partial u}{\partial z} - \frac{\partial u}{\partial r}\right)$$

$$\omega_z = \frac{1}{2}\left(\frac{\partial(rv)}{r\partial r} - \frac{\partial u}{r\partial \theta}\right)$$

In Eqs. 4.1 to 4.3. u, v and u are the components of displacement at a point whose coordinates are r, θ and z at time t. λ and G are the bulk and shear modulii of the soil, respectively and β is the soil material damping ratio.

4.2.3. Homogeneous Medium

Vertical Vibration: The complex soil stiffness per unit length of the cylinder associated with a unit vertical displacement follows from Eq. 4.1 as

$$K_v = 2\pi G(1 + i2\beta)a_o \cdot \frac{K_1(a_o^*)}{K_0(a_o^*)} \qquad (4.4)$$

$$= G(S_{v1} + iS_{v2})$$

where K_1 and K_0 are the modified Bessel functions of orders 1 and zero, respectively.

$$a_o^* = a_o / \sqrt{1 + i2\beta} \qquad (4.5)$$

and

$$a_o = \omega r_o / V_s \qquad (4.6)$$

where V_s is the soil shear wave velocity and r_o is the cylinder radius.

Axisymmetric Radial Vibration: In this case, the displacements v and u vanish and the equations of motion of the viscoelastic continuum, Eq. 4.1, reduce to

$$(\lambda + 2G)(1 + i2\beta)\frac{\partial}{\partial r}\left(\frac{\partial u}{\partial r} + \frac{u}{r}\right) = \rho\frac{\partial^2 u}{\partial t^2} \qquad (4.7)$$

For the solution in the form of $u(r,t)=U(r)e^{i-t}$, Eq. 4.7 becomes

$$\frac{d^2U}{dq^2} + \frac{dU}{qdq} - (1+\frac{1}{q^2})U = 0 \tag{4.8}$$

where $q=sr$ and

$$s = \frac{1}{V_s\sqrt{1+i2\beta}}\cdot\sqrt{(1-2\nu)/2(1-\nu)} \tag{4.9}$$

Eq. 4.8 is the modified Bessel Equation of the first order whose solution is given by

$$U(r) = A\,I_1(sr) + B\,K_1(sr) \tag{4.10}$$

In Eq. 4.10 K_1 and I_1 are the modified Bessel functions of the first order and A and B are constants to be determined from the following boundary conditions

1. $U(r)=1$ at $r=r_o$

2. $U(r)=0$ at $r\to\infty$

Applying these two boundary conditions give $A=0$ and $B=\frac{1}{K_1(sr_o)}$. The normal stress in the radial direction is given by

$$\sigma_r = \lambda\Delta + 2G\epsilon_r \tag{4.11}$$

where ϵ_r is the radial strain given by

$$\epsilon_r = \frac{\partial u}{\partial r} \tag{4.12}$$

From Eqs. 4.10 to 4.12, the radial normal stress is

$$\sigma_r = -\frac{G}{r_o}\{2(1+i2\beta)[\frac{(1-\nu)}{(1-2\nu)}(\frac{K_o(sr_o)sr_o}{K_1(sr_o)})+1]\} \tag{4.13}$$

Accordingly, the complex radial soil reaction per unit area of contact between the cylinder and soil medium associated with a unit radial displacement is written as

$$K_r = -\sigma_r = \frac{G}{r_o}(S_{r1}+iS_{r2}) \tag{4.14}$$

4.2.4. Nonhomogeneous Medium

When the cylinder experiences large displacement amplitudes, slip might occur between the cylinder and the soil. Near the cylinder, the soil behaves nonlinearly. As the strain increases, the shear modulus decreases, material damping increases and the affected zone around the pile can be regarded as a weakened zone. An approximate approach was formulated which considers the soil zone with large deformations around the pile, Fig. 4.2b, as a zone with reduced shear modulus [25]. Soil resistance is then calculated approximately assuming that the pile is surrounded by a medium consisting of an inner soft layer and an outer harder one.

Vertical Vibration: Novak and Sheta [25] considered the inner layer to be massless and the complex stiffness of the composite medium follows as:

$$K_v = \frac{2\pi(G_m/G)}{-\ln(r_o/b) + (G_m/G) K_0(sb)/sbK_1(sb)}$$ (4.15)

$$= G(S_{v1} + iS_{v2})$$

where s is given by

$$s = \frac{i\omega}{V_s\sqrt{1 + i2\beta}}$$ (4.16)

This solution was used in Eq. 3.19 for the one dimensional model.

Veletsos and Dotson [42] formulated the solution for the vertical direction considering the mass of the inner zone and concluded that the differences introduced due to neglecting it may be substantial at high dimensionless frequencies. Lakshmanan and Minai [43] considered the shear modulus to vary linearly with distance in the weakened zone and accounted for the mass of the inner zone.

Radial Axisymmetric Vibration: In this chapter, the complex stiffness of

the composite medium for the case of radial axisymmetric vibration is formulated considering the mass of the inner zone. As in the case of the homogeneous medium, the displacements are expressed in terms of the modified Bessel functions, i.e.

$$u(r) = AI_1(s_i r) + BK_1(s_i r) \qquad\qquad r_o \le r < b \qquad (4.17)$$
$$u(r) = CI_1(s_o r) + DK_0(s_o r) \qquad\qquad r \ge b$$

where s_i and s_o are the parameters s, defined by Eq. 4.9 of the inner and outer zones, respectively. The constants A, B, C and D are determined from the following boundary conditions

1. $U'(r) = 0$ at $r \to \infty$.

2. $U'(r) = 1$ at $r = r_o$.

3. The displacements of both media are equal at $r = b$.

4. The normal stresses of both media are equal at $r = b$.

Application of these boundary conditions yields $C = 0$ and, after rather lengthy manipulations, the following values for A, B and D:

$$A = \{\alpha\gamma[s_i r_o \frac{K_0(s_i b)}{K_1(s_i r_o)} + \frac{K_1(s_i b)}{b/r_o K_1(s_i r_o)}] + \delta \frac{1}{b/r_o}(1-\alpha)\frac{K_1(s_i b)}{K_1(s_i r_o)} \qquad (4.18)$$

$$-\gamma[s_o r_o \frac{K_0(s_o b)K_1(s_i b)}{K_1 s_i r_o K_1(s_o b)} + \frac{K_1(s_o b)}{b/r_o K_1(s_i r_o)} \cdot \frac{K_1(s_i b)}{K_1(s_o b)}]\} /$$

$$\{\alpha\gamma[s_i r_o I_0(s_i b) + \frac{I_1(s_i r_o)}{K_1(s_i r_o)} s_i r_o K_0(s_i b)]$$

$$+ \gamma[(\frac{I_1(s_i r_o)K_1(s_i b)}{K_1(s_i r_o) b/r_o} - \frac{I_1(s_i b)}{b/r_o})(\alpha - 1) + \frac{I_1(s_i b)}{K_1(s_o b)} s_o r_o K_0(s_o b)$$

$$- \frac{I_1(s_i r_o)K_1(s_i b)}{K_1(s_i r_o) K_1(s_o b)} s_o r_o K_0(s_o b)]$$

$$- \frac{\delta}{b/r_o}(1-\alpha)[I_1(s_i b) - \frac{I_1(s_i r_o)}{K_1(s_i r_o)} K_1(s_i b)]\}$$

and

$$(4.19)$$

$$B = \frac{1}{K_1(s_1 r_o)} - A \frac{I_1(s_1 r_o)}{K_1(s_1 r_o)}$$

$$D = A' \frac{I_1(s_1 b)}{K_1(s_o b)} - \frac{I_1(s_1 r_o)}{K_1(s_1 r_o)} \frac{K_1(s_1 b)}{K_1(s_o b)}$$

$$(4.20)$$

$$- \frac{K_1(s_1 b)}{K_1(s_o b) K_1(s_1 r_o)}$$

The normal stress in the radial direction is given by Eq. 4.11 and at $r = r_o$ is given by

$$\sigma_r = -2 \frac{G_m}{r_o} (1 + i2\beta_m)(\gamma\{A[s_1 r_o I_0(s_1 r_o) - I_1(s_1 r_o)]$$

$$- B[s_1 r_o K_0(s_1 r_o) + K_1(s_1 r_o)]\} + \delta[A I_1(s_1 r_o + B K_1(s_1 r_o)])$$

$$(4.21)$$

Hence, the complex soil reaction of the composite medium per unit area of contact between the cylinder and the soil associated with a unit displacement in the radial direction is given by

$$K_r = -\sigma_r = \frac{G_m}{r_o}(S_{r1} + i S_{r2})$$

$$(4.22)$$

In Eqs. 4.18 and 4.21

$$\alpha = \frac{G_m}{G} \frac{(1 + i2\beta_m)}{(1 + i2\beta)}$$

$$(4.23)$$

$$\gamma = \frac{(1-\nu)}{(1-2\nu)}$$

$$(4.24)$$

and

$$\delta = \frac{\nu}{(1-2\nu)}$$

$$(4.25)$$

Fig. 4.3 shows the variation in S_{r1} and S_{r2} with a_o for the homogeneous medium. Static stiffness is obtained at $a_o = 0$, then the stiffness parameter S_{r1} decreases with the increase in a_o, at a higher rate with higher Poisson's ratios. Damping is derived solely from material damping at $a_o = 0$, then S_{r2} increases
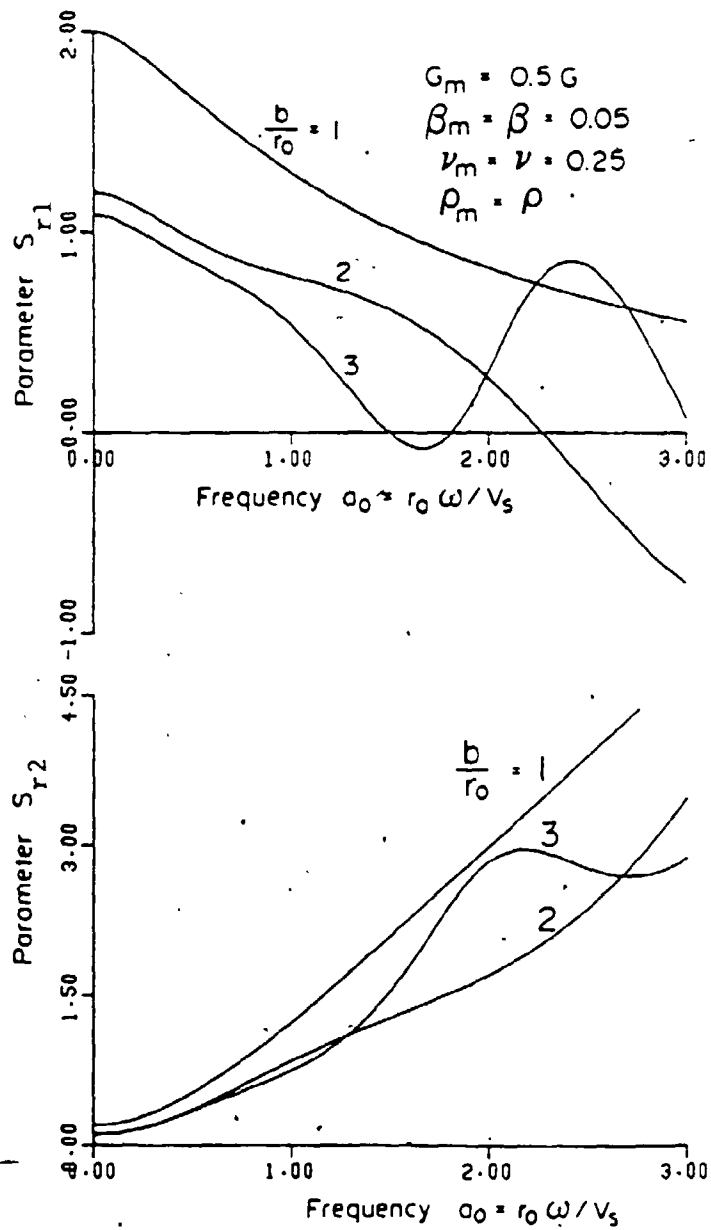
Figure 4-3: Plane Strain Axisymmetric Radial Stiffness and Damping for a Homogeneous Medium

almost linearly with frequency. Shown in Fig. 4.4 is the variation in S_{r1} and S_{r2} with a_o for the composite medium for different b/r_o ratios. The stiffness and damping are mostly reduced for all frequencies due to the presence of the weakened zone. Both the real and imaginary parts oscillate at higher b/r_o ratios. This boundary with weakened zone can be particularly useful in problems involving cavity expansions, i.e. soil deformation at pile tip, explosions, etc.

4.3. Implementation of the Plane Strain Transmitting Boundary

4.3.1. Finite Element Formulation

The cylindrical axisymmetric element used by Kuhlemeyer [36] is used in this study to model the pile and the soil (Fig. 4.5). However, the stiffness matrix given in [36] has a few errors, and the correct expressions could not be found in the literature. Thus the stiffness matrix was derived from first principles in this study. The displacement field $\{\delta\}$ is expressed as

$$\{\delta\} = [N]\{u\}_e \tag{4.26}$$

where $[N]$, is the shape functions matrix and $\{u\}_e$ is the element nodal displacements. The element strain vector $\{\epsilon\}_e$ is related to the element nodal displacements by

$$\{\epsilon\}_e = [B]\{u\}_e \tag{4.27}$$

and the stress strain relationship follows from

$$\{\sigma\}_e = [D]\{\epsilon\}_e \tag{4.28}$$

where $\{\sigma\}_e$ is the element stress vector and $[D]$ is the elasticity matrix. Applying the theory of virtual work yields the following expression for the stiffness matrix

$$[K] = \int\int\int_V [B]^T[D][B]\ dV \tag{4.29}$$

The matrix of shape functions used in Eqs. 4.26 to 4.29 is the same one given in [36]. The stiffness matrix derived using this procedure is given in Appendix A.
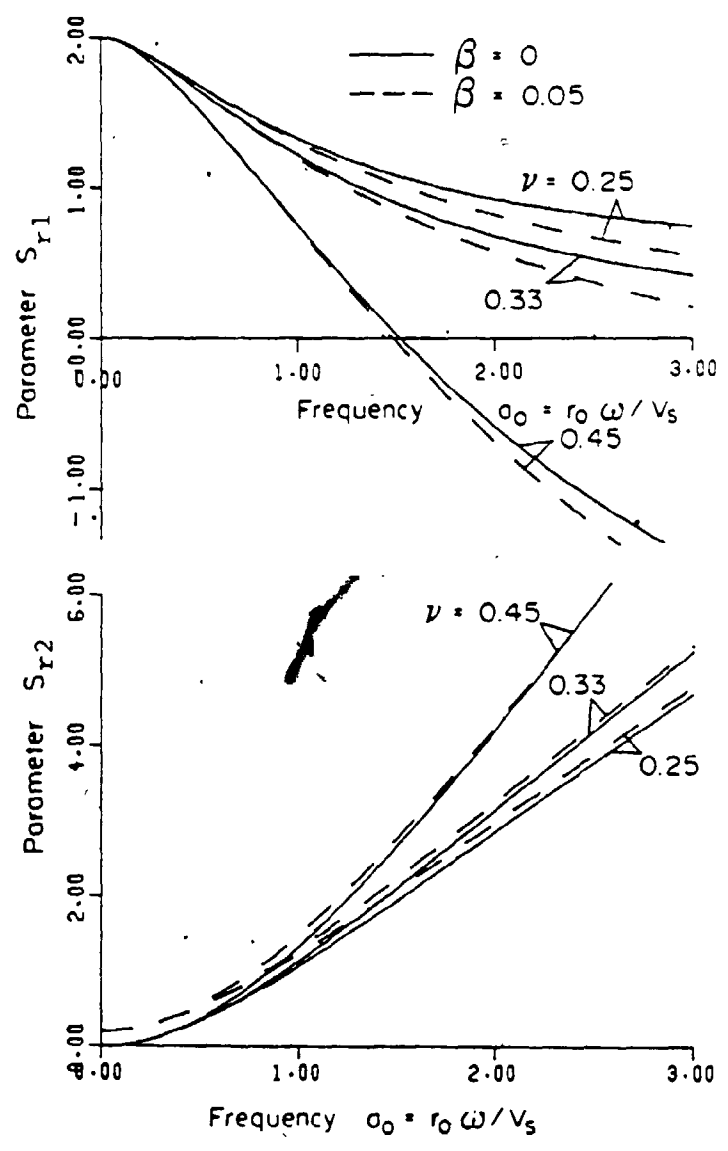
Figure 4-4: Plane Strain Axisymmetric Radial Stiffness and Damping for a Composite Soil Medium
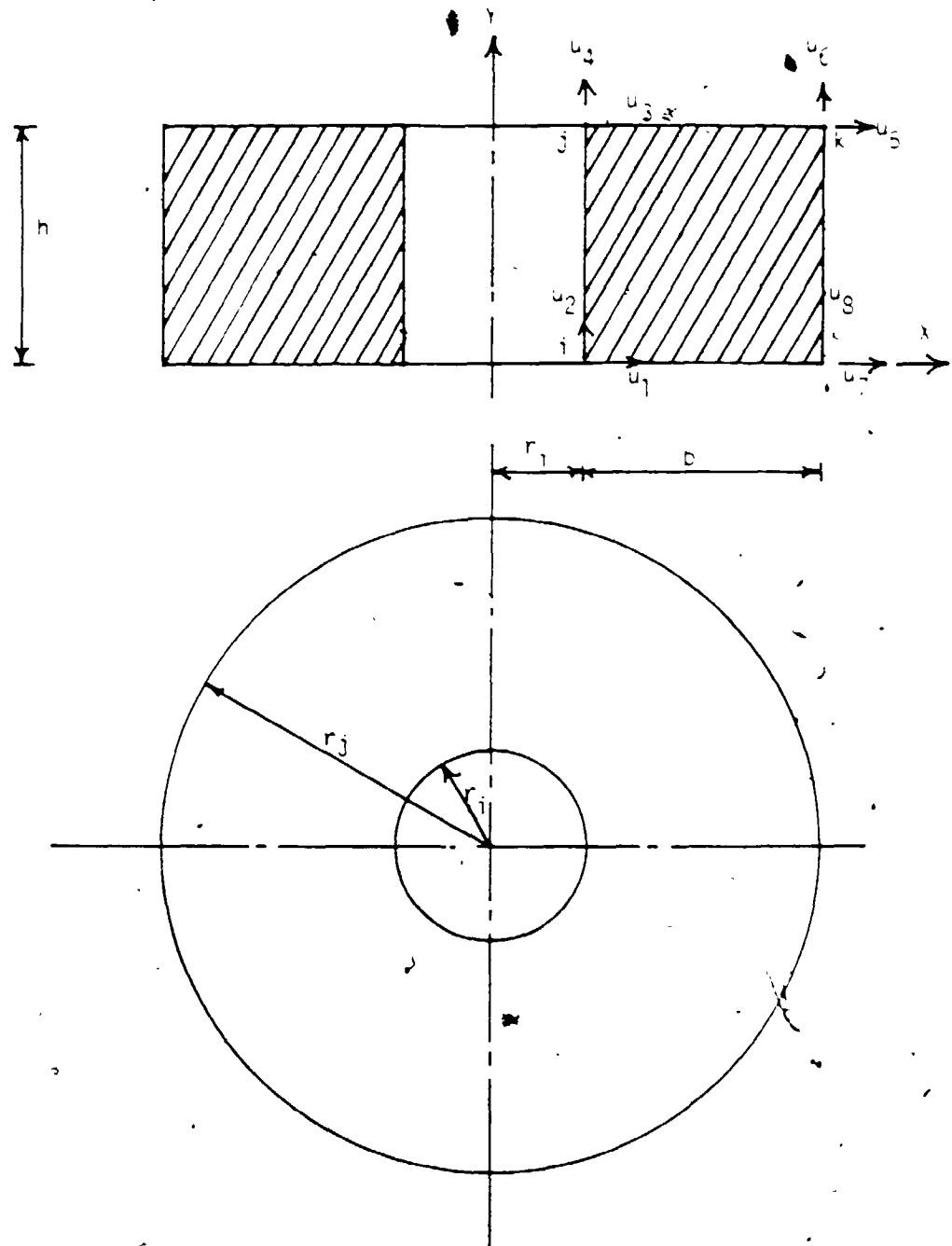
Figure 4-5: Three Dimensional Axisymmetric Element

Equations of motion of the system are written in matrix form as

$$[M]\{\ddot{u}\} + [C]\{\dot{u}\} + [K]\{u\} = \{P\}$$ (4.30)

where $[M]$, $[C]$ and $[K]$ are the global mass, damping and stiffness matrices, respectively. $\{\ddot{u}\}$, $\{\dot{u}\}$ and $\{u\}$ are the vectors of accelerations, velocities and displacements, respectively, and $\{P\}$ is the vector of external loads.

Eq. 4.30 can be solved by three different methods depending on the nature of the problem

1. Time domain analysis (step by step numerical integration) is suitable for transient and nonlinear problems and systems with frequency independent parameters.

2. Complex frequency response is suitable for either transient or steady state response as long as the system parameters are frequency dependent and the system is linear.

3. Modal superposition is suitable for systems that decouple easily and when the first few modes are sufficient to express the response.

4.3.2. Boundary Stiffness and Damping Matrices

When surface tractions are applied to one of the elements, the resulting vector of element nodal loads $\{P\}_e$ is given by

$$\{P_e\} = \int\int_S [N]^T\{q\}dS$$ (4.31)

where $\{q\}$ is the vector of surface tractions and S denotes a surface integral. Imposition of the proper boundary conditions at the mesh boundaries corresponds to applying the proper soil reactions in the form of surface tractions to the elements falling on the boundaries.

Let $\{q\}_b$ be the vector of soil reactions applied to the boundary elements which can be written as

$$\{q\}_b = [-\tau \quad -\sigma]^T = -[BD]\{\dot{u}\}_s - [BS]\{u\}_s$$ (4.32)

In Eq. 4.32, $[BD]$ and $[BS]$ are the damping and stiffness matrices corresponding

to the soil reactions to be applied at the mesh boundaries and the subscript s indicates that the velocities and displacements are at the element surface   The vectors $\{u\}_n$ and $\{u\}_s$ are given by

$$\{u\}_n = N\{u\}_c \qquad\qquad 4.33$$

and

$$\{u\}_s = N\{u\}_c \qquad\qquad 4.34$$

where $\{u\}_c$ is the vector of element velocities. From Eqs 4.31 to 4.34.

$$\{P\}_c = \left\{\int\int_s N^T BD_c N\, dS\right\}\{u\}_{c,} \qquad\qquad 4.35$$

$$-\left\{\int\int_s N^T BS_c N\, dS\right\}\{u\}_c$$

$$= -CB_c\{u\}_c - KB_c\{u\}_c$$

where CB_c and KB_c are the element boundary damping and stiffness matrices, respectively, which can be included into the global boundary damping and stiffness matrices CB and KB, respectively. Hence. Eq 4.30 is rewritten as

$$M\{u\} + (C + CB)\{u\} + (K + KB)\{u\} = \{P\} \qquad (4.36)$$

The viscous boundary does not have a real part or stiffnes, i e $BS = 0$. For a horizontal boundary with radial and vertical displacements $[r\ v]^T$, the element boundary damping matrix is defined as

$$BD_H = \begin{bmatrix} \rho V_s & 0 \\ 0 & \rho V_p \end{bmatrix} \qquad\qquad (4.37)$$

where V_p is the primary wave velocity $(V_p = \sqrt{(2G + \lambda)/\rho})$ The element boundary damping matrix for a vertical boundary is given by

$$BD_V = \begin{bmatrix} 0 & \rho V_s \\ \rho V_p & 0 \end{bmatrix} \qquad\qquad (4.38)$$

Proposed Boundary: It is assumed that the stresses at a point on a vertical boundary (sides of the mesh) are equal to the plane strain soil reactions for the radial and vertical vibrations described earlier. Accordingly, for the vertical boundary, the element boundary stiffness matrix is defined by

$$BS_{\lambda} = \begin{bmatrix} 0 & GS_{r1} \, r_b \\ GS_{r1}/r_b & 0 \end{bmatrix}$$

where r_b is the radius of the vertical mesh boundary, and the element boundary damping matrix is given by

$$BD_{\lambda} = \begin{bmatrix} 0 & GS_{r2} \, 2\pi \omega r_b \\ GS_{r2} \, \omega r_b & 0 \end{bmatrix} \qquad 4\ 40$$

For a horizontal boundary, the normal vertical stresses are assumed to be equal to the viscoelastic half space reactions to a vibrating rigid massless disc [26] which are expressed as

$$R_1 = K_{11}(C_{11} + ia_o C_{12}) \qquad 4\ 41$$

where K_{11} is the vertical static stiffness of the disc given by

$$K_{11} = \frac{4Gr_o}{(1 - \nu)} \qquad 4\ 42$$

and C_{11} and C_{12} are dimensionless stiffness and damping parameters, respectively. Accordingly, for the horizontal boundary, the element boundary stiffness matrix is given by

$$BS_{H} = \begin{bmatrix} GS_{r1}/r_e & 0 \\ 0 & K_{11}C_{11}/\pi r_b^2 \end{bmatrix} \qquad (4\ 43$$

where r_e is the average radius of the element under consideration and the element boundary damping matrix is given by

$$BD_{H} = \begin{bmatrix} GS_{r2}/\omega r_e & 0 \\ 0 & K_{11}a_o C_{12}/\pi \omega r_b^2 \end{bmatrix} \qquad (4\ 44$$

where $a_o = \omega r_b/V_s$. The horizontal soil reactions at the base of the mesh are taken as equal to the radial normal stress at the same point as an approximation although other values could also be used. A numerical study was performed which showed that the results for the vertical vibration are not sensitive to the

horizontal soil reactions at the mesh base because the horizontal displacements at the base are very small and could even be neglected.

The parameters $S_{,1}$, $S_{,2}$, S_{r1} and S_{r2} in Eqs. 4.39 to 4.44 are those for the homogeneous medium as it is assumed that the soil outside the finite element mesh remains elastic. It can be seen from Fig. 4.6 that the parameters $S_{,1}$, $S_{,2} \sim$ and $S_{r2} \sim$ for the homogeneous medium vary only slowly with frequency and so does the parameter $C_{,2}$. The stiffness parameters S_{r1} and $C_{,1}$ vary mildly with frequency. Accordingly, a time domain analysis, desirable for the nonlinear problem of pile driving, can be performed using the proposed boundary if the soil reactions are evaluated at a frequency close to the dominant excitation frequency.

4.4. Verification of the Plane Strain Transmitting Boundary

A finite element computer program is developed in this study to analyse the pile driving problem. A few examples are analysed to examine the performance of both the viscous and plane strain boundaries in both the frequency and time domains. To evaluate the response in the time domain, the Newmark-β method is used for numerical integration of the equations of motion. In the frequency domain, the complex frequency response method is used. In the latter approach, both the exciting force and response are harmonic and are written as

$$\{P(t)\} = \{P_o\}e^{i\omega t} \tag{4.45}$$

and

$$\{u(t)\} = \{u_c\}e^{i\omega t} \tag{4.46}$$

where $\{u_c\}$ is a vector of complex response amplitudes. By substituting Eqs. 4.45 and 4.46 into Eq. 4.30, one gets

$$[([K] - \omega^2[M]) + i\omega[C]]\{u_c\} = \{P_o\} \tag{4.47}$$

which can also be written as

$$[K_c]\{u_c\} = \{P_o\} \tag{4.48}$$
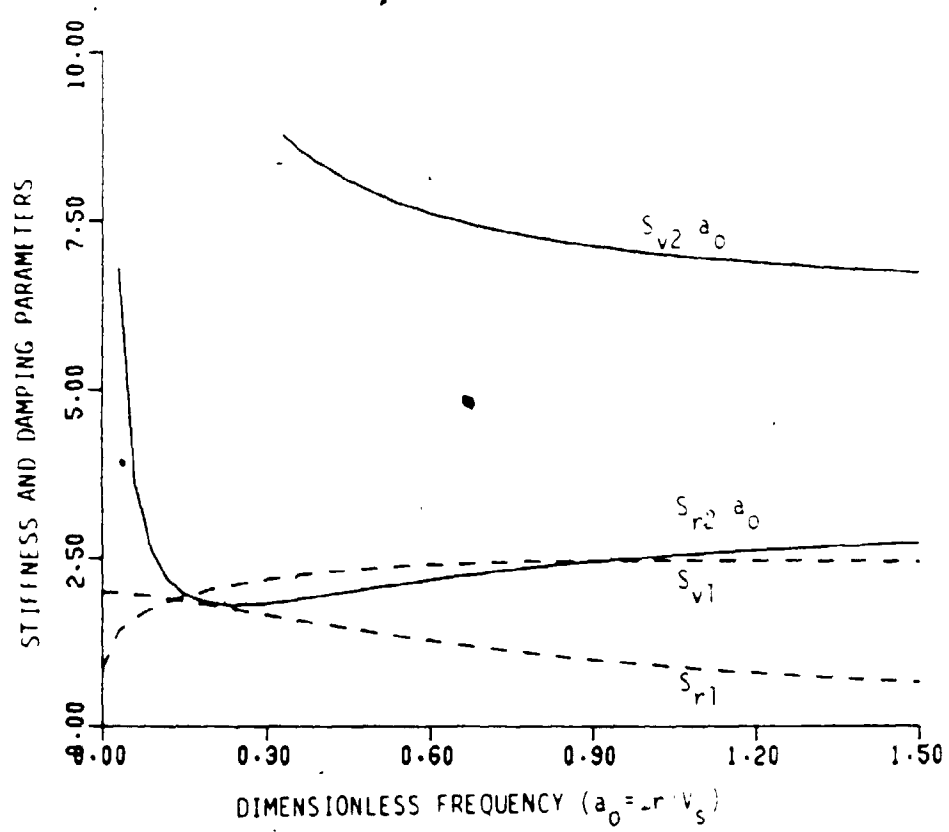
Figure 4-6: Variation in the Transmitting Boundary Parameters, S_{v1}, S_{v2}/a_o and S_{r2}/a_o, with Frequency

where $[K_c]$ is a complex, frequency dependent stiffness matrix. Material damping is considered to be of the hysteretic frequency independent type and is included in the analysis by expressing it in terms of the equivalent viscous damping ,i e

$$[C_{eq}] = \frac{2\beta}{\omega}[K]$$

(4 49)

where β is the material damping ratio. In this case, the complex stiffness matrix is given by

$$[K_c] = ([K] - \omega^2 [M]) + i\omega ([C] + \frac{2\beta}{\omega}[K])$$

(4 50)

The examples considered for the verification are the vertical vibration of an elastic bar, an embedded pile and a surface foundation.

Vertical Vibration of an Elastic Bar

The simple case of a semi infinite elastic bar is chosen to illustrate the effects of the viscous boundary. The bar is assumed to be purely elastic and material damping is neglected. Only a finite length of the bar can be modeled by finite elements. The load is applied at one end of the bar and at the other end, either a fixed or a viscous boundary is specified. The bar axial stiffness is EA/L where E , A and L are the Young's modulus, cross section area and length of the bar, respectively.

The response of the bar (axial displacement of the point of load application) to a suddenly applied constant force $P(t) = P_o$ is evaluated for both types of boundaries and the results are shown in Fig. 4.7. The exact displacement at the bar top is also shown in Fig. 4.7 and is given by

$$u_t = \frac{P_o V_p}{EA} t$$

(4.51)

where V_p is the one dimensional primary wave velocity defined in Eq 3 1 Arbitrary values are assigned to P_o, E, A and V_p such that $P_o V_p / EA = 1$ m/s, hence, $u(t) = t$. It can be seen that the application of the fixed boundary leads to
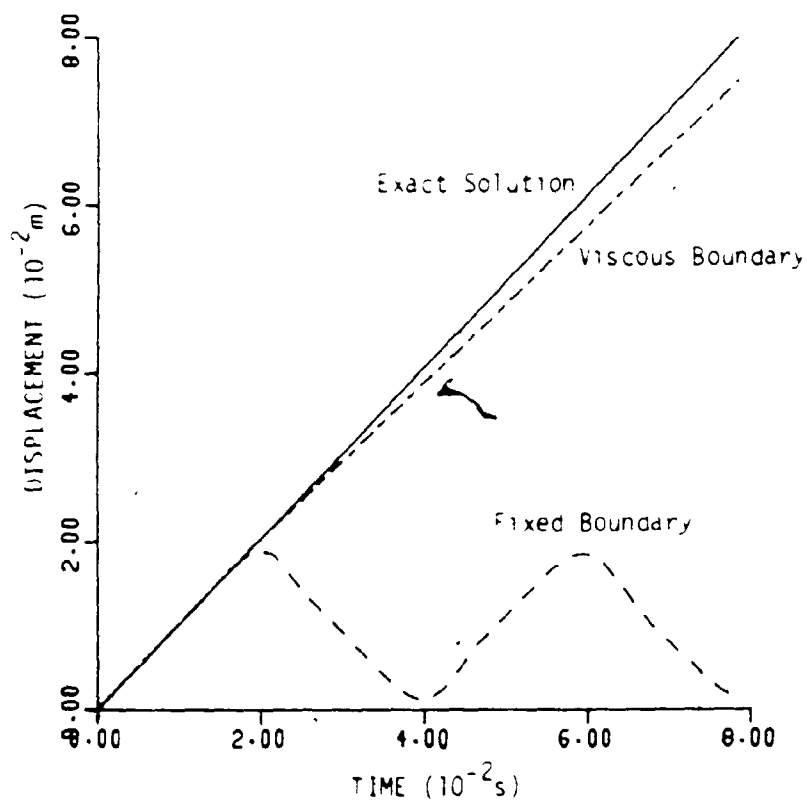
Figure 4-7: Displacement of a Semi Infinite Elastic Bar Subjected to a Constant Load ($P_o V_p / EA = 1$ m/s)

an oscillatory response whereas the application of the viscous boundary gives a linear displacement that increases with time and is very close to the exact solution. Fig. 4.8 shows the axial stresses inside the bar calculated at time $t = 3L/2V_p$ for both boundaries as well as the exact solution $\sigma = P_o/A$. The values chosen for P_o and A are such that the resulting stress is unity. At time $t = 3L/2V_p$, the stress wave will have enough time to cover a distance of $3L/2$. While the viscous boundary absorbs the outgoing stress wave leading to the correct results, the fixed boundary reflects the stress wave back inside the modeled zone yielding distorted results. Fig. 4.9 shows the response of the bar to a harmonic excitation given by $P(t) = P_o \cos \omega t$, for both boundaries. For this case, P_o/EA is chosen to be equal to 0.002 and the period T of the harmonic load is 0.1 s. The response evaluated using the viscous boundary is oscillatory around a non zero constant value which is attributed to the absence of a real part or stiffness in the viscous boundary. Using a fixed boundary, however, yields a symmetric harmonic oscillation.

Vertical Vibration of an Embedded Pile

The vertical vibration of a single pile is analysed in the frequency domain as well as the time domain. Both, the static and dynamic stiffnesses in the vertical direction are evaluated and compared to other finite element and analytical solutions.

In the frequency domain, the complex springs representing the boundaries, shown in Fig. 4.10, are evaluated at the excitation frequency and the resulting damping and stiffness boundary matrices are assembled in the global complex stiffness matrix $[K_c]$. Eq. 4.48 is used to evaluate the complex stiffness of a single pile by specifying a unit vertical displacement at the pile top. The vertical complex stiffness of a single pile is written as
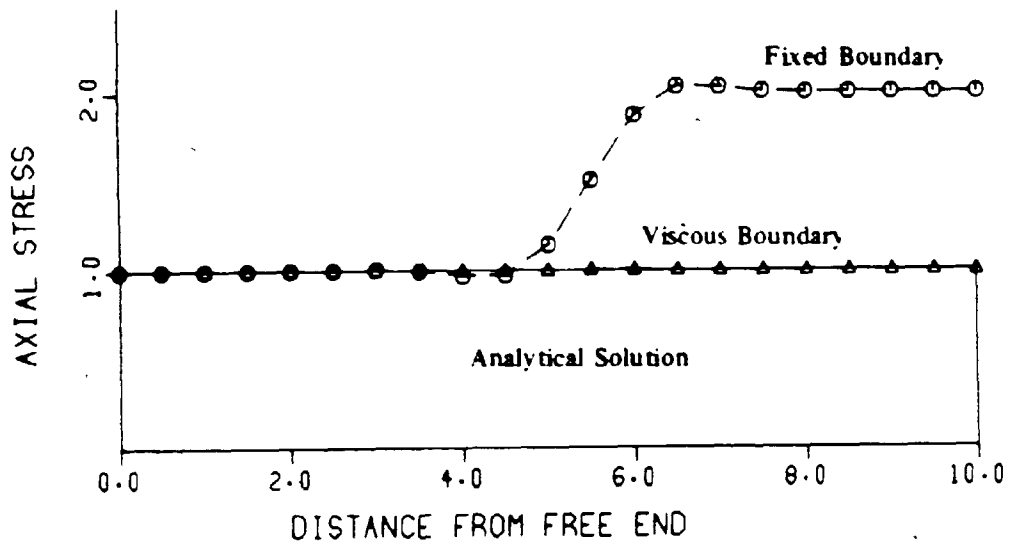
Figure 4-8: Normal Stress Distribution Along an Elastic Bar Subjected
to a Constant Load (at time $t = 3L/2V_p$)
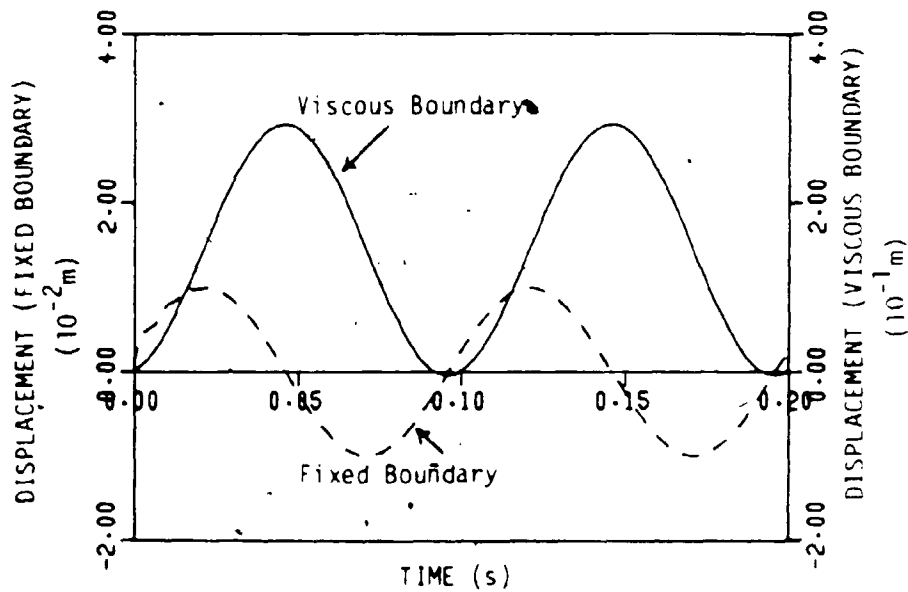
Figure 4-9: Displacement of an Elastic Bar Subjected to a Harmonic
Load ($P_o/EA = 0.002$, $T = 0.1$ s)
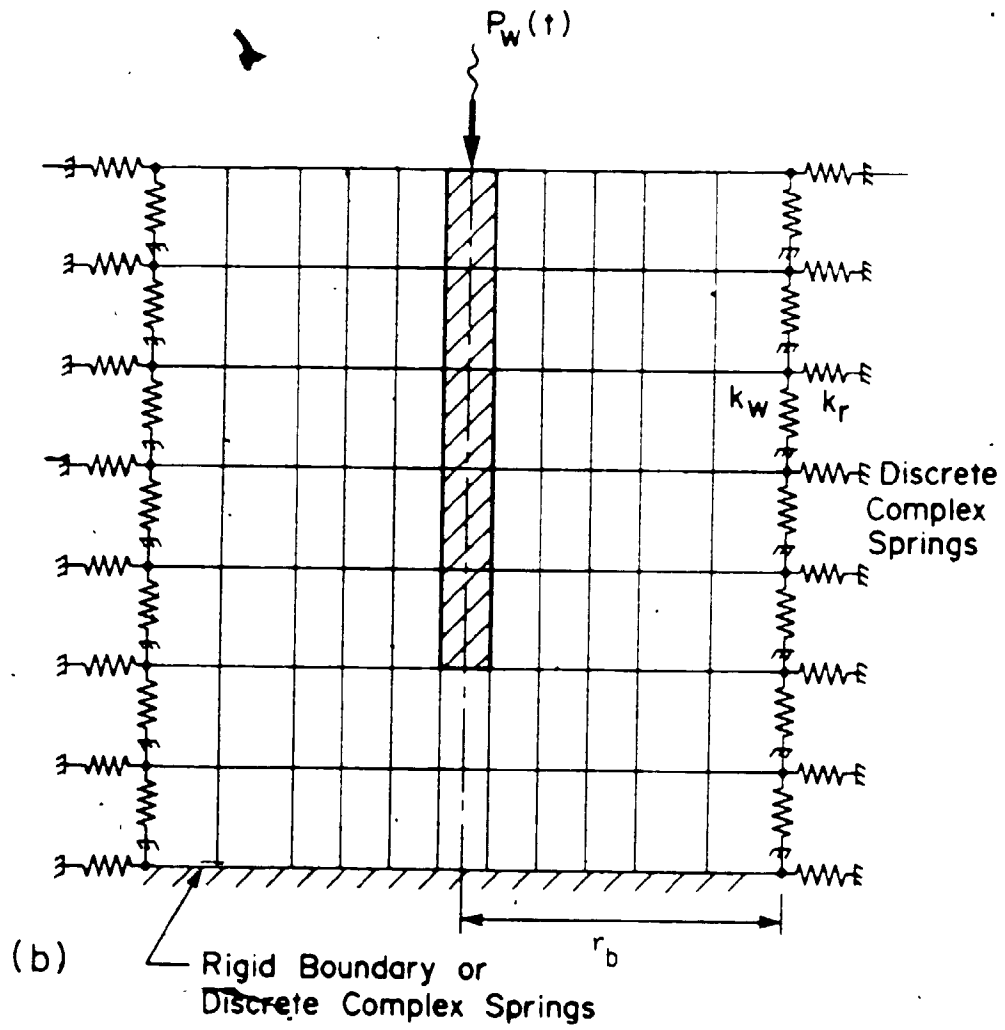
Figure 4-10: Finite Element Mesh with Transmitting Boundary.

$$K = K_1 + iK_2 \qquad (4.52)$$

The dimensionless parameters f_{t1} and f_{t2} which represent the vertical stiffness and damping, respectively, of a single pile are evaluated in order to compare the results with Novak's solution [46]. These parameters are defined as

$$f_{t1} = \frac{K_1 r_o}{E_p A_p} \qquad (4.53)$$

and

$$f_{t2} = \frac{K_2 \, r_o}{a_o E_p A_p} \qquad 4.54$$

where E_p, A_p and r_o are the pile Young's modulus, cross section area and radius, respectively.

First, the static stiffness is evaluated using the proposed boundary and the results are compared with Poulos solution [47] in Fig. 4.11 for 3 different stiffness ratios (E_p/E_s, where E_s is the soil Young's modulus). Both solutions agree quite well especially at higher E_p/E_s ratios. The dimensionless parameters f_{t1} and f_{t2} are evaluated for a vertical floating pile using the proposed boundary and are shown in Fig. 4.12. Also shown in Fig. 4.12 are f_{t1} and f_{t2} evaluated using the viscous boundary as well as those obtained by Novak. It can be seen that the results obtained using the proposed boundary are closer to Novak's solution than those obtained using the viscous boundary. Fig. 4.13 shows the vertical stiffness and damping of a floating pile calculated using the proposed boundary compared to those obtained by Ostadan [48] using a finite element analysis. A good agreement between the two solutions is observed except at lower dimensionless frequencies where the damping calculated using the proposed boundary exceeds that obtained by Ostadan.

To check the proposed boundary in the time domain, a vertical floating pile
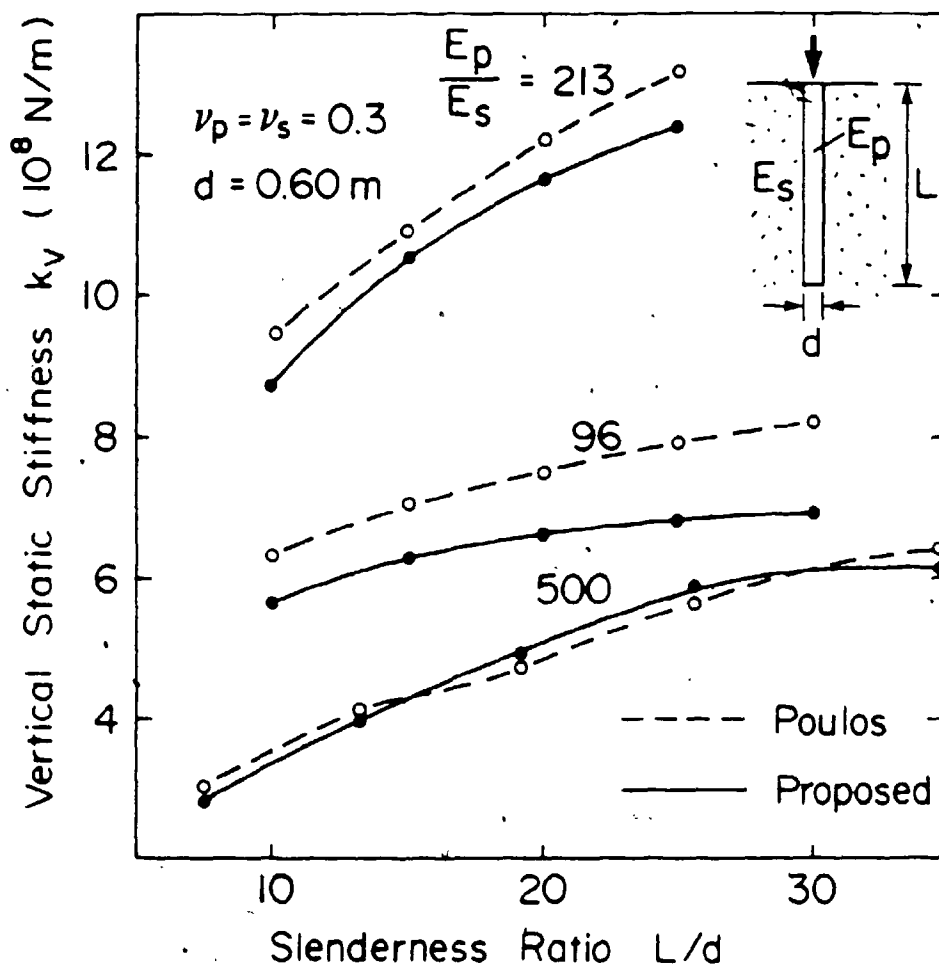
Figure 4-11: Vertical Static Stiffness of a Single Pile (Poulos
Solution Compared with Present Solution)
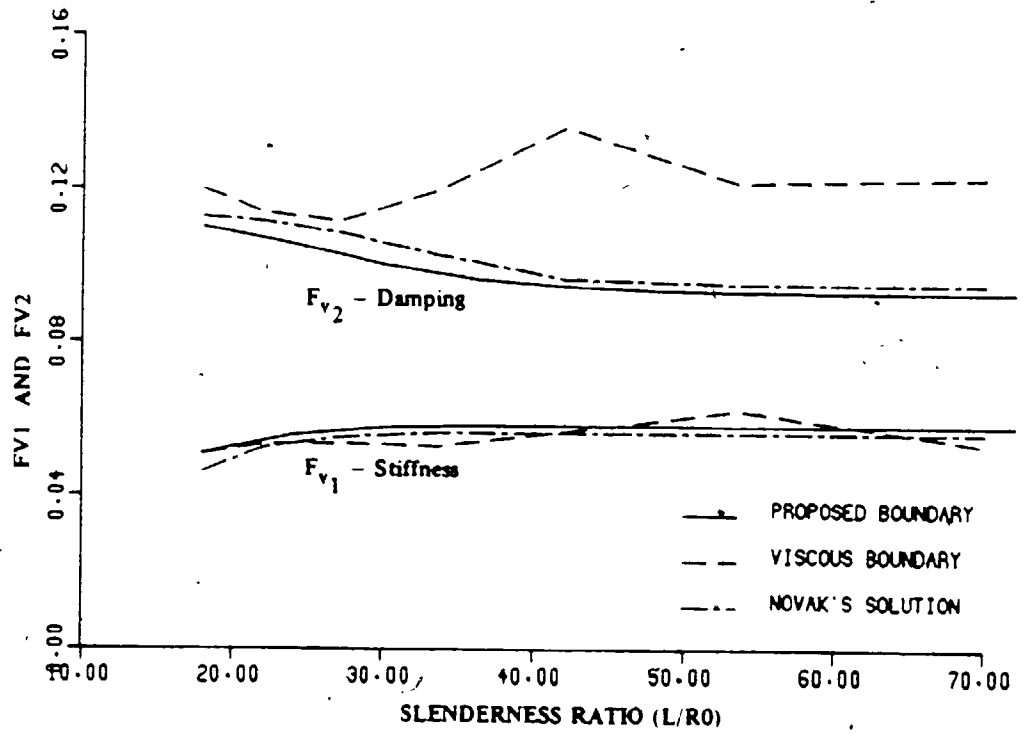
Figure 4-12: Vertical Dynamic Stiffness and Damping of a Single
Pile (Viscous Boundary Compared with Plane Strain Boundary,
$a_o = 0.3$)
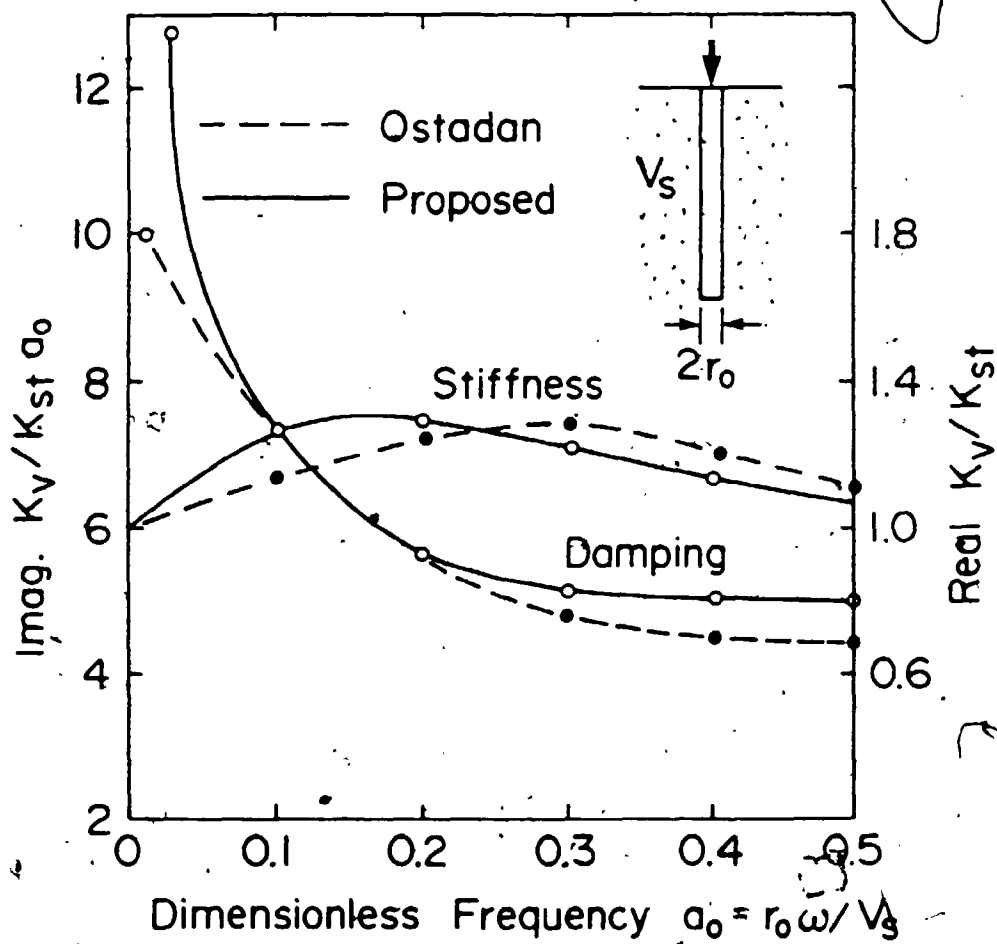
Figure 4-13: Vertical Stiffness and Damping of a Single Pile (Finite Element Solution by Ostadan Compared with Present Solution. $L/r_o = 30$)

is subjected to a vertical harmonic excitation and the response is evaluated in the time domain. Fig. 4.14 shows the displacement of the pile tip calculated using the viscous boundary and the proposed boundary. A shift in the datum about which the harmonic oscillation occurs is noticed in the response evaluated using the viscous boundary which confirms a similar observation for the case of the semi infinite bar. A similar shift in the time domain response of a vertically loaded pile was obtained by Zaman et al. [49] who also used the viscous boundary. Wu [50] also presented results for a harmonic vibration of a pile segment which exhibits a shift around a non zero equilibrium position. Fig. 4.15. However, if the proposed boundary is used, a symmetric harmonic oscillation is obtained due to the presence of an in-phase component of the stiffness. The viscous boundary is mathematically accurate for a one dimensional rod but only approximate for three dimensional situations. The lack of the stiffness part may result in spurious static sets and distort the results where such sets are important. This is the case of pile driving

Vertical Vibration of a Surface Foundation

Stiffness and damping of a rigid massless disc vibrating on a viscoelastic half space are evaluated using the proposed model and compared with the solution by Veletsos [26]. Fig. 4.16 shows C_{v1} and C_{v2}, defined in Eq. 4.41, evaluated using the two solutions. A reasonable agreement is obtained and it can be improved by refining the mesh and extending it.

4.5. Interface Element

4.5.1. General

In pile driving analysis, the use of an interface element at the pile-soil interface is essential to allow for the pile penetration inside the soil. Interface behaviour is quite crucial in many applications and hence, interface elements are widely used in both static and dynamic analyses. A comprehensive review on
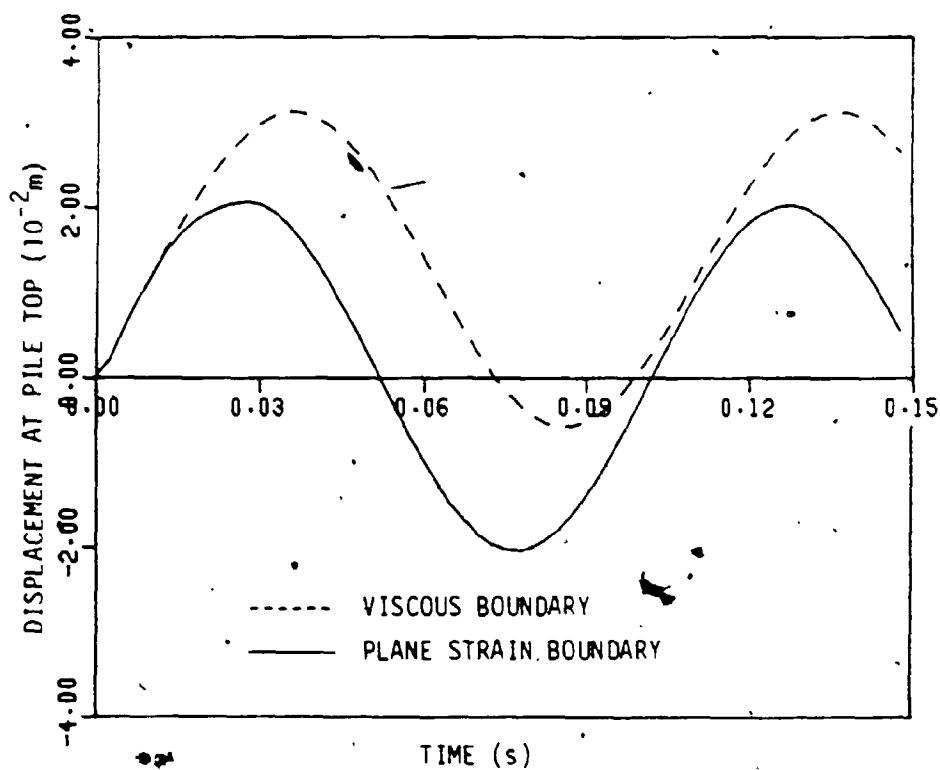
Figure 4-14: Displacement of Pile Tip Subjected to a Harmonic Load
(Comparison Between Viscous and Plane Strain Boundaries
based on a time domain analysis); $a_o=0.05$ and $L/r_o=24$
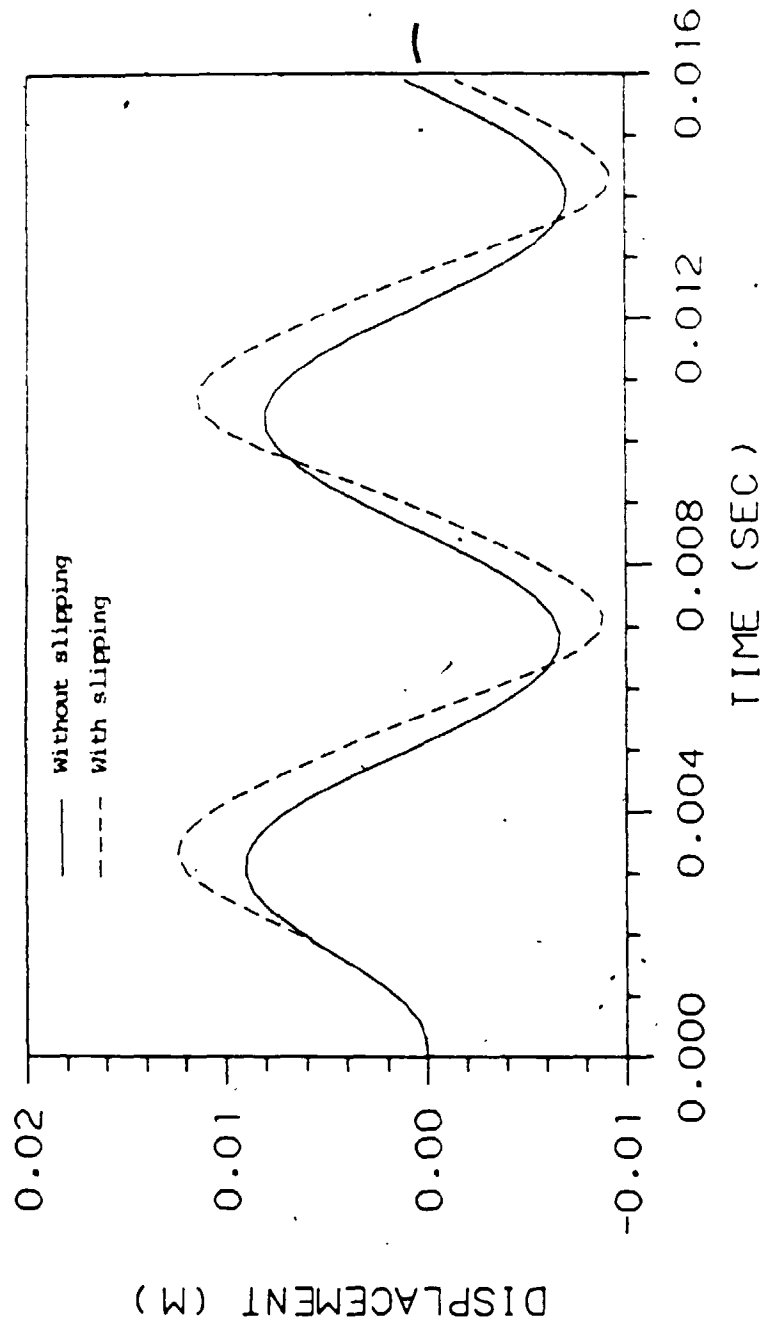
Figure 4-15: Displacement of a Pile Segment Subjected to a Harmonic Load (Wu [50])
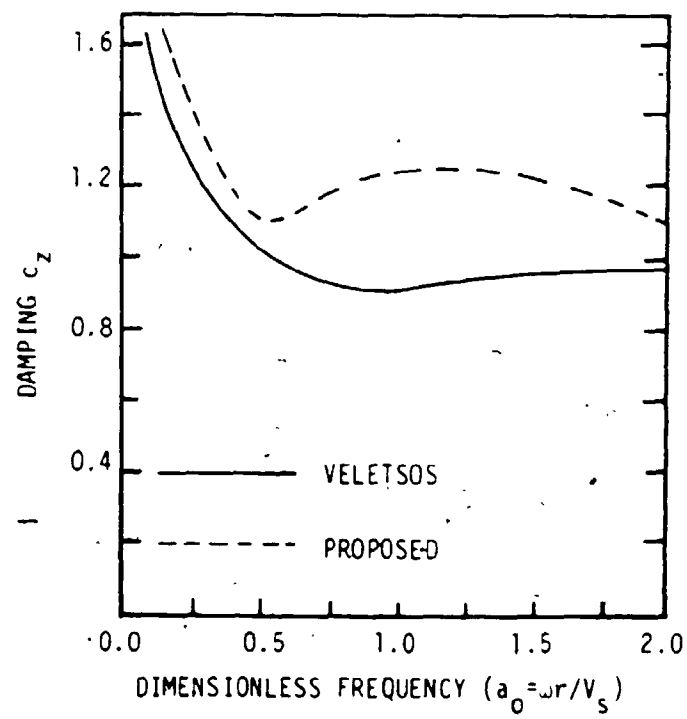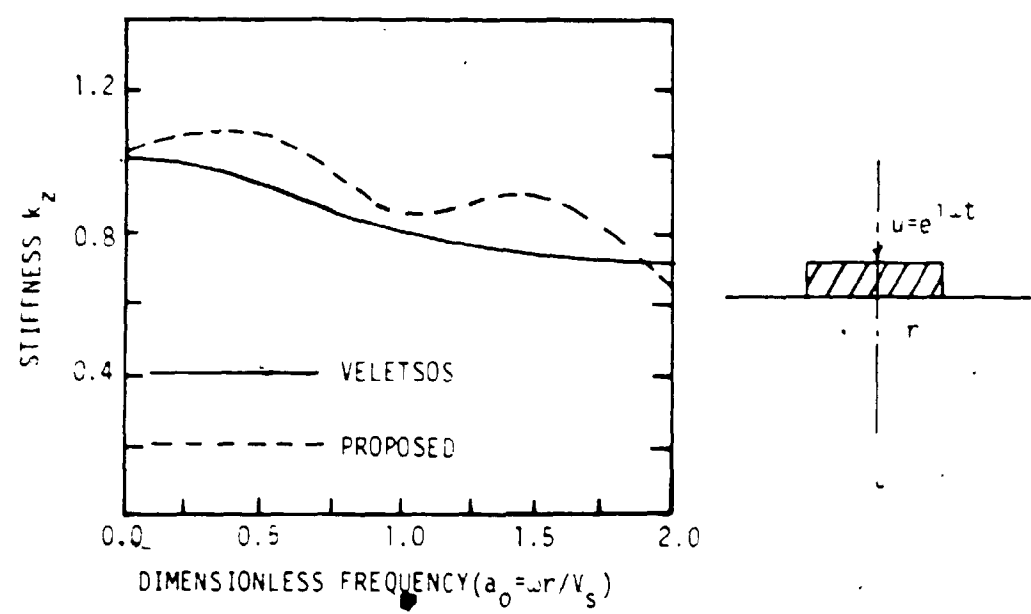
Figure 4-16: Vertical Dynamic Stiffness and Damping of a Rigid
Massless Disc on Halfspace

interface behaviour is found in [51]. Goodman et al [52] developed a two dimensional zero thickness rectangular element for use in the static analysis of rock joints. In their formulation, the element stiffness is expressed in terms of the normal and shear stiffness of the joint. Clough and Duncan [53] used the same element for the analysis of retaining walls. Zienkiewicz et al. [54] used a similar joint element in an isoparametric formulation Ghaboussi et al [55] developed an element similar to that of Goodman where the element was considered to have non zero "thin" thickness and used the relative displacements at the interface as independent degrees of freedom.

The effect of interface behaviour on dynamic response of structures was studied by Toki et al. [56] who used the element developed by Goodman and considered the separation and sliding modes during strong earthquakes Desai [57,58] and Drumm and Desai [59,60] conducted experiments to develop constitutive models for interface behaviour during cyclic loading. These constitutive models were implemented in static and dynamic analyses by Zaman et al. who used a thin interface element and considered various deformation modes such as no slip, slip, debonding and rebonding [61]. In the present study, the thin interface element developed by Ghaboussi et al. [55] is used.

4.5.2. Formulation

The interface element used in this study is vertical cylindrical axisymmetric, with eight degrees of freedom, Fig. 4.17. The following assumptions are adopted for derivation of the stiffness matrix

1. Only the normal stress in the radial direction σ_r and longitudinal shear stress τ_{rz} are considered in the analysis together with the corresponding strains ϵ_r and γ_{rz}.

2. Strains are constant along the radial direction and vary linearly in the vertical direction.
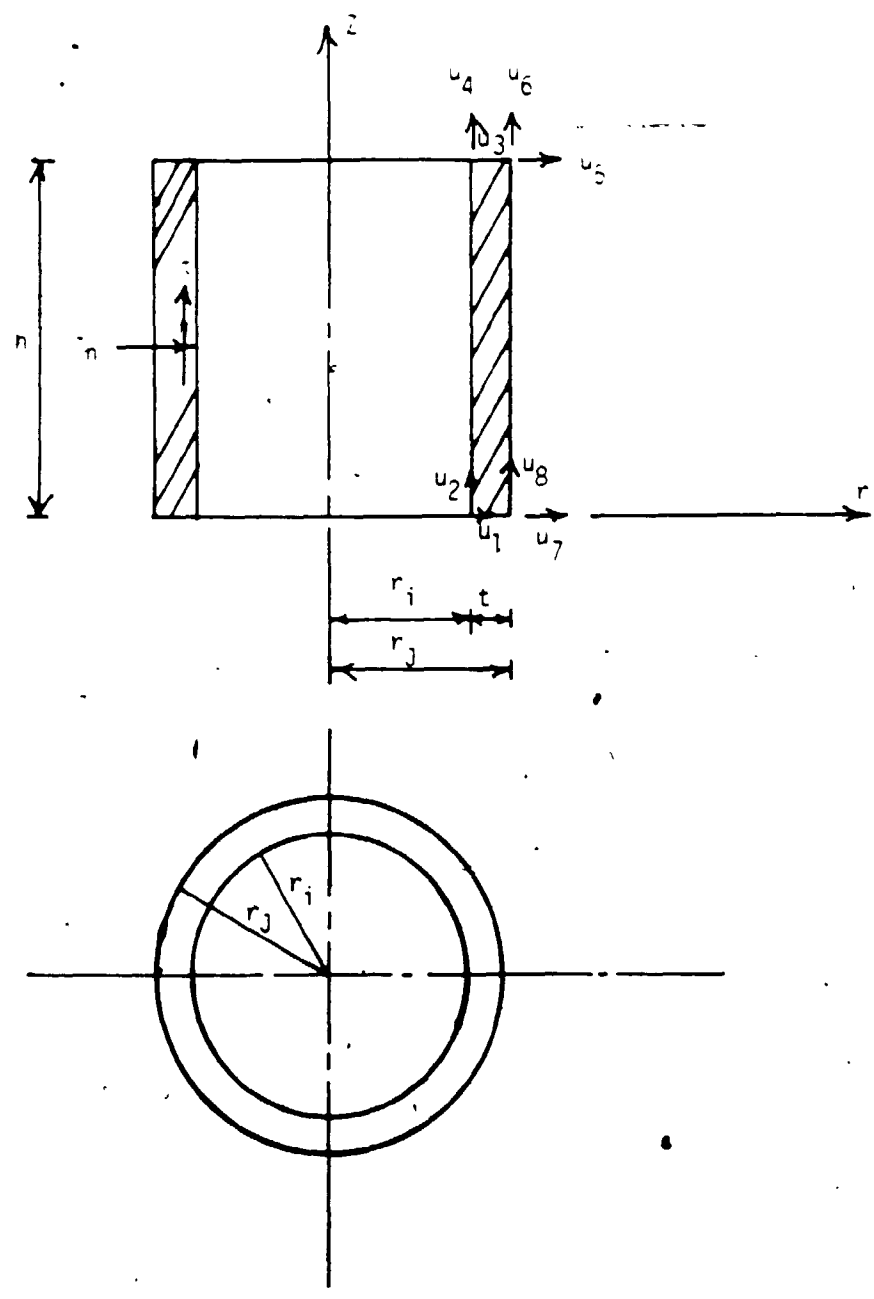
Figure 4-17: Thin Interface Element

3. Shear and normal displacements are uncoupled. i.e. non dilatant behaviour of the interface is assumed.

Because the element is very thin, the contribution to the internal virtual work during deformation from the vertical and circumferential stresses, σ_z and σ_θ, respectively, can be neglected which justifies the first assumption. Although the regular axisymmetric element is assumed to have linear strains in both directions, due to the small thickness of the element, it can be assumed that $\frac{\partial u}{\partial r} \approx \frac{\Delta u}{\Delta r}$ without loss of accuracy.

A Mohr-Coulomb yield criterion is assumed where the shear stress increases linearly until it is equal to the yield stress where the element offers constant resistance during further deformation until the shear stress is reduced again due to negative stress increments, Fig. 4.18. The yield stress τ_y is given by

(4.55)

$$\tau_y = \alpha C_u + \sigma_n \tan \phi$$

where C_u and ϕ are the undrained cohesive strength of the soil and the angle of friction between the pile material and soil, respectively and α is a reduction factor for driving conditions. In Eq. 4.55, σ_n is the radial normal stress at the pile soil interface, given by

$$\sigma_n = |\sigma - \sigma_v'| K_o$$

(4.56)

where σ is the radial normal stress inside the interface element that results from the driving process and σ_v' and K_o are the effective overburden pressure and the coefficient of lateral earth pressure at rest, respectively. Three modes of deformation are considered

A)Stick Mode: identified by

$\sigma_n < 0$ and $\tau < \tau_y$.

During this mode, the interface behaves elastically and the soil remains in contact with the pile.

B)Slip or Sliding Mode: identified by

$$\tau_y = \alpha C_u + \sigma_n \tan \phi$$
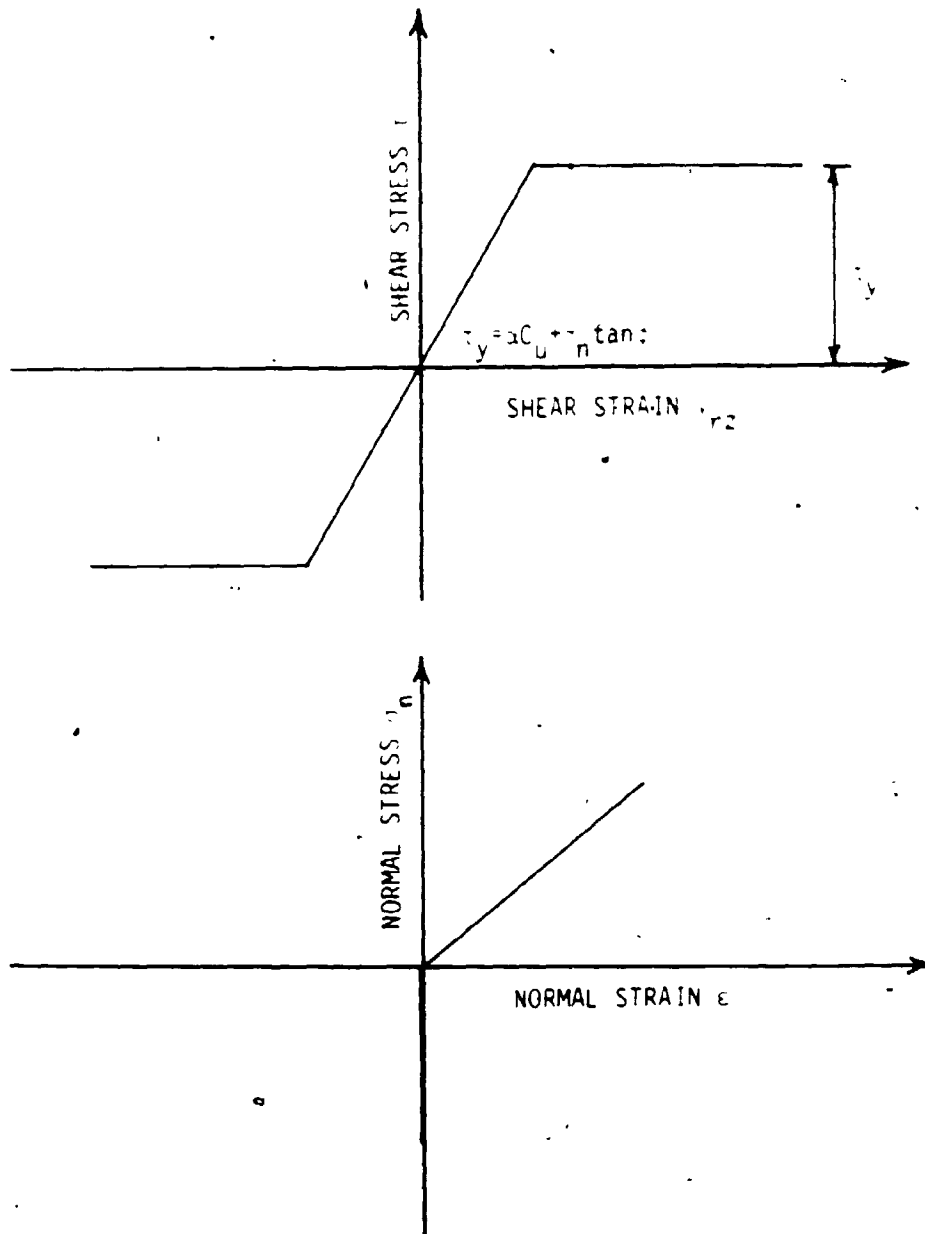
Figure 4-18: Stress Strain Relationship for Interface Behaviour

$$\sigma_n < 0 \quad \text{and} \quad \tau = \tau_y$$

In this mode, the shear stress exceeds the yield shear stress and the excess stresses are redistributed iteratively until the shear stress is adjusted to be equal to the yield stress.

Separation Mode: Identified by

$$\sigma_n > 0$$

When σ_n tends to exceed zero (tensile stresses), separation between the soil and pile is assumed and in this mode, both the normal stresses and shear stresses have to be iteratively adjusted to zero. This means that the element offers no resistance and is assumed to be non existent.

In some of the previous studies, the Young's modulus of the interface element was assigned arbitrarily high values [55,62] to prevent interpenetration between the soil and the pile. However, the experiments conducted by Desai et al. [51] indicate that the normal properties of the interface should be based on the normal properties of the soil. In the present study, the elastic properties of the interface are assumed to be the same as those of the soil. A parametric study by Desai et al. indicated that the best results are obtained when the thickness of the interface element is beetween 0.1 and 0.01 of that of the neighbouring elements [51].

The Newmark β method for time integration is used in this study together with the initial stress method for nonlinear finite element problems [63]. In this method, the global stiffness matrix is assembled only once, at the beginning of calculations, assuming elastic properties for all the elements. During the solution process, the nonlinear behaviour of the interface elements is represented by their internal resistance. At any time t, the solution quantities are known and so are the internal resistance forces. From the incremental equations of equilibrium at

time $t + \Delta t$, the incremental displacements are evaluated and so are the total stresses inside all the elasto plastic elements.

If the yield stress has been exceeded in any of the elasto plastic elements, the stress value is adjusted to the yield stress and an iteration is performed by applying the excess forces at the corresponding nodes and solving for the incremental displacements. This process is repeated within each time step until convergence is achieved.

The incremental equations of equilibrium at time $t + \Delta t$ are written as [45]

$$[M]\ddot{U}^{(k)}_{t+\Delta t} + [C]\dot{U}^{(k)}_{t+\Delta t} + [K]\Delta U^{(k)} = R_{t+\Delta t} - F^{(k-1)}_{t+\Delta t} \tag{4.57}$$

where k denotes the iteration number, t is time, Δt is the time step and ΔU is the vector of incremental displacements. $R_{t+\Delta t}$ and $F_{t+\Delta t}$ are the vectors of external and internal forces, respectively. The following incremental relationship holds [45]

$$U^{(k)}_{t+\Delta t} = U^{(k-1)}_{t+\Delta t} + \Delta U^{(k)} \tag{4.58}$$

with the initial conditions

$$U^{(0)}_{t+\Delta t} = U_t \tag{4.59}$$

and

$$F^{(0)}_{t+\Delta t} = F_t \tag{4.60}$$

By using the linear acceleration assumption and after some manipulation, Eq. 4.57 is written as

$$([K] + \frac{4}{\Delta t^2}[M] + \frac{2}{\Delta t}[C])\Delta U^{(k)} = R_{t+\Delta t} - F^{(k-1)}_{t+\Delta t} \tag{4.61}$$

$$+ [M][\frac{4}{\Delta t^2}(U_t - U^{(k-1)}_{t+\Delta t}) + \frac{4}{\Delta t}\dot{U}_t + \ddot{U}_t]$$

$$+ [C][\frac{2}{\Delta t}(U_t - U^{(k-1)}_{t+\Delta t}) + \dot{U}_t]$$

where the unbracketed variables are understood to be vectors. Iterations are repeated until convergence is achieved according to the following criterion

$$(4.62)$$

$$\frac{\|\Delta U^{(k)}\|_2}{\|U^k_{t-\Delta t}\|_2} \le \epsilon_D$$

where ϵ_D is a displacement tolerance and the vector norm $\|\cdot\|_2$ is defined by

$$\|U\|_2 = (\sum_{i=1}^{N} |U_i|^2)^{1/2}$$ 4.63

When convergence is achieved, the accelerations and velocities at time $t+\Delta t$ are calculated from

$$\ddot{U}_{t+\Delta t} = \frac{4}{\Delta t^2} U^{(k)}_{t+\Delta t} - U_t - \frac{4}{\Delta t} \dot{U}_t - \ddot{U}_t$$ 4.64

and

$$\dot{U}_{t+\Delta t} = \frac{2}{\Delta t} [U^{(k)}_{t+\Delta t} - U_t] - \dot{U}_t$$ $$(4.65)$$

Although plastic flow and nonlinearity might occur in the soil zone near the pile, a true nonlinear dynamic analysis is prohibitively expensive. An alternative is a quasi linear analysis where the shear modulus of each element is adjusted after each time step according to the level of strain inside it. In the present study, nonlinearity is confined to the interface and the rest of the soil elements are assumed to remain elastic. However, to allow the pile to penetrate the soil, the soil element just underneath the pile tip is assumed to be elastic perfectly plastic. The vertical compressive normal stress grows linearly with strain until it reaches a yield stress σ_y where it remains constant during further strains or decreases due to a stress increment opposite in sign.

The internal resistance force vector $F^{(k)}_{t+\Delta t}$ is written as

$$\{F^{(k)}\} = \{F_e^{(k)}\} + \{F_i^{(k)}\} + \{F_p^{(k)}\}$$ $$(4.66)$$

where $\{F_e^{(k)}\}$, $\{F_i^{(k)}\}$ and $\{F_p^{(k)}\}$ are the vectors of internal forces of the elastic

elements, interface elements and the plastic element underneath the pile tip, respectively. The subscript $t+\Delta t$ is dropped from the variables in Eq 4.66 for brevity. The vectors of internal forces are calculated as outlined below.

1)Forces in Elastic Elements:

$$\{F_e^{(k)}\} = [K_e]\{U_{t-\Delta t}^{(k)}\} \tag{4.67}$$

where $[K_e]$ is a global elastic stiffness matrix with only the stiffness matrix of the elastic elements assembled in it.

2)Forces in the Interface Elements:

$$\{F_I^{(k)}\} = \sum_{j=1}^{N_I} \{F_j^{(k)}\}_I \tag{4.68}$$

where N_I is the number of interface elements and $\{F_j^{(k)}\}_I$ is given by

$$\{F_j^{(k)}\} = \frac{V}{2t}\{-\sigma_o \quad -\tau_o \quad -\sigma_o \quad -\tau_o \quad \sigma_o \quad \tau_o \quad \sigma_o \quad \tau_o\}^{(k)} \tag{4.69}$$

In Eq. 4.69, V and t are the volume and thickness of the jth interface element. $\sigma_o^{(k)}$ and $\tau_o^{(k)}$ are the average adjusted total stresses inside the element which are evaluated from

$$\sigma_o^{(k)} = \begin{cases} \sigma^{(k)} & (\sigma^{(k)} - \sigma'_t K_o) < 0 \\ \\ 0 & (\sigma^{(k)} - \sigma'_t K_o) > 0 \end{cases} \tag{4.70}$$

where the normal stress before adjustment $\sigma^{(k)}$ is given by

$$\sigma^{(k)} = \sigma^{(k-1)} + \Delta\sigma^{(k)} \tag{4.71}$$

and

$$\tau_o^{(k)} = \begin{cases} \tau^{(k)} & |\tau^{(k)}| < \tau_y \\ \tau_y\dfrac{\tau^{(k)}}{|\tau^{(k)}|} & |\tau^{(k)}| > \tau_y \end{cases} \sigma^{(k)} < 0 \\ 0 & \sigma^{(k)} > 0 \end{cases} \tag{4.72}$$

and the total shear stress before adjustment is given by

$$\tau^{(k)} = \tau^{(k-1)} + \Delta\tau^{(k)} \tag{4.73}$$

The stress increments are given by

$$\Delta\sigma^{(k)} = \frac{E}{2t}(\Delta U_7 + \Delta U_5 - \Delta U_3 - \Delta U_1)^{(k)} \tag{4.74}$$

and

$$\Delta\tau^{(k)} = \frac{G}{2t}(\Delta U_8 + \Delta U_6 - \Delta U_4 - \Delta U_2)^{(k)} \tag{4.75}$$

3) Forces in the Plastic Elements

$$\{F_p^{(k)}\} = \int_V [B]^T \{\sigma_o^{(k)}\} dV \tag{4.76}$$

where $[B]^T$ is the strain displacement matrix and $\{\sigma_o^{(k)}\}$ is the vector of average

stresses inside the plastic element, i.e.

$$\{\sigma_o^{(k)}\}^T = \{\sigma_{r_o} \quad \sigma_{z_o} \quad \sigma_{\theta_o} \quad \tau_o\}^{(k)} \tag{4.77}$$

The vector of average stresses is evaluated from

$$\{\sigma_o^{(k)}\} = \{\sigma_o^{(k-1)}\} + \{\Delta\sigma_o^{(k)}\} \tag{4.78}$$

and the vector of average stress increments is given by

$$\{\Delta\sigma_o^{(k)}\} = (\frac{1}{V}\int_V [D][B]dV)\{\Delta U^{(k)}\} \tag{4.79}$$

The following constraint is applied for the vertical stress so that it is always less

than or equal to the yield stress underneath the pile

$$\sigma_{z_o}^{(k)} = \begin{cases} \sigma_{z_o}^{(k)} & |\sigma_{z_o}^{(k)}| < \sigma_y \\ \sigma_y |\sigma_{z_o}^{(k)}|/\sigma_{z_o}^{(k)} & |\sigma_{z_o}^{(k)}| > \sigma_y \end{cases} \tag{4.80}$$

In Eq. 4.80, σ_y is the vertical yield stress underneath the pile. The value of σ_y is

taken to be $N_d C_u$ where N_d is the bearing capacity factor for the pile tip and is

assigned a value of 9 which is the common practice in soil mechanics.

To check the performance of the interface element, the response of a

vertically loaded pile subjected to harmonic load is evaluated in the time domain

with and without the interface element. The plane strain transmitting boundary is used in this example and the thickness of the interface element is taken as 0.1 of that of the neighbouring elements. The yield shear stress τ_y is assumed to be half the undrained cohesive strength of the soil. Young's modulus of the soil is evaluated as 500 C_u. Fig. 4.18 shows the pile top response for both cases. It is seen that the presence of the interface element increases the response of the pile.

4.6. Example

Due to the high computing costs of the finite element analysis, a shorter pile than that of Chapter 2 is used in this example. The following properties are assumed

Hammer and Capblock

	Hammer mass	5000 Kg
	Cushion stiffness	8E8 N/m
	Impact Velocity of the hammer	5.0 m/s

Pile

	Outer diameter	0.4 m
	Wall thickness	0.04 m
	Density	7700 Kg/m^3
	Total length=penetration length	12.0 m
	Young's modulus	2×10^{11} Pa
	Poisson ratio	0.2
	Material damping ratio	0.01

Soil

	Undrained cohesive strength	2×10^5 Pa
	Density	1700 Kg/m^3
	Poisson ratio	0.25
	τ_y	8×10^4 Pa
	σ_y	9×10^5 Pa

The impact of the hammer on the pile is expressed as a pulse force evaluated as explained in [64] and is given by

$$F(t) = k \frac{V_h}{\omega_d} e^{-\xi t} \sin \omega_d t \qquad (4.81)$$

where k is the cushion stiffness. V_h is the hammer impact velocity, ω_d is the damped natural frequency given by

2

MICROCOPY RESOLUTION TEST CHART
NBS 1010a
(ANSI and ISO TEST CHART No. 2)
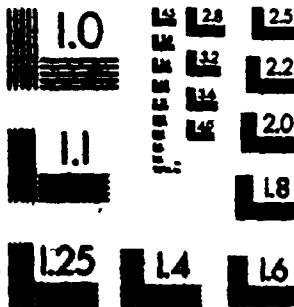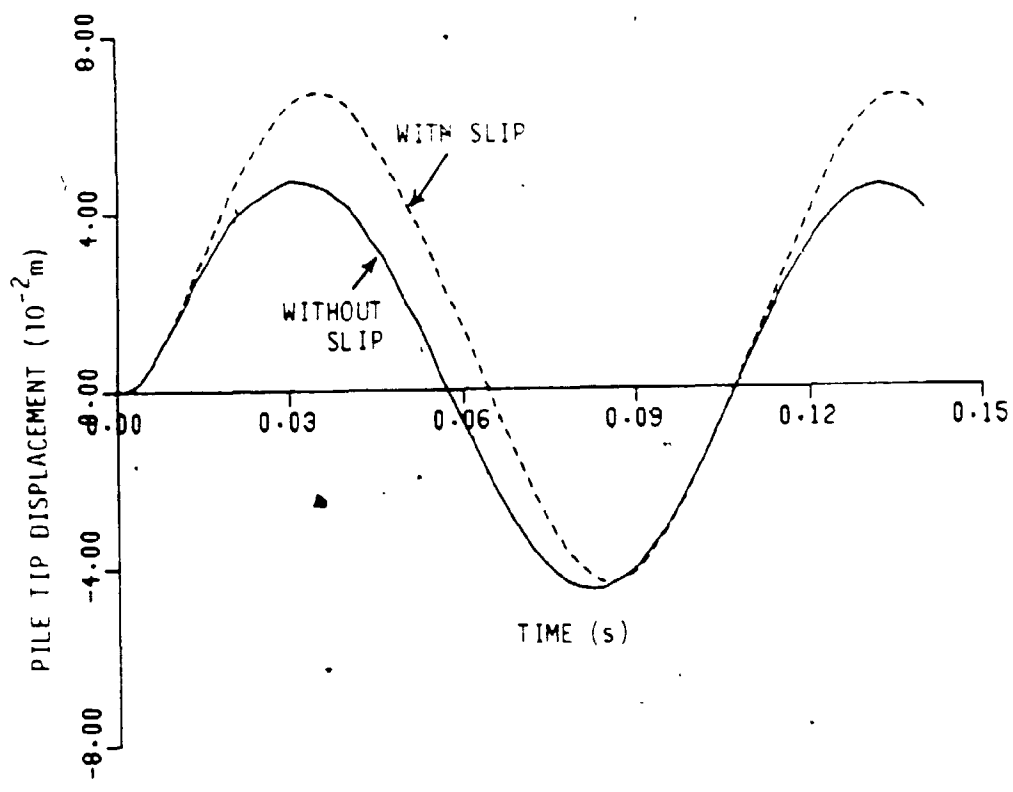
Figure 4-19: Pile Top Displacement With and Without Pile Soil Slip ($a_o=0.06$ and $L/r_o=24$)

$$-_d = \sqrt{k \cdot m(1 - \xi^2)} \qquad (4.82)$$

In Eq. 4.82, m is the hammer mass and ξ is a damping ratio given by

$$\xi = \frac{kc}{2 \cdot AE} \qquad (4.83)$$

where c is the one dimensional primary wave velocity of the the pile material; A and E are the cross section and Young's modulus of the pile material. respectively. The same pile subjected to the same hammer blow is analysed using the proposed model of the one dimensional analysis formulated in Chapter 3. In the one dimensional analysis, the following values are used: $\alpha = 0.4$, $\beta = 500$, $C_u = 2 \times 10^5$ and $r_o/b = 0.65$.

Fig. 4.20 shows the pile tip displacement for both models for a period of 0.06 seconds. The finite element results show a more damped response and a smaller value for the set than the one dimensional analysis. The smaller value of the set may be attributed to the fact that the soil behaviour is assumed to be linear except for the interface elements and the plastic soil element underneath the pile tip. It seems that a more realistic analysis is needed which takes into account the plastic behaviour of the soil around the pile. The analysis is not pursued further because of the high computing cost, thus the results shown are limited to the elastic behaviour of the soil medium.

4.7. Conclusions

A finite element model is developed to examine the pile driving problem. The model incorporated the slip at the pile soil interface by employing an interface element and a plastic soil element underneath the pile tip. Energy absorbing boundaries are placed at the boundaries of the finite element mesh which are based on the plane strain soil reactions. The soil continuum, except for the interface element and a plastic element underneath the pile, is assumed to be
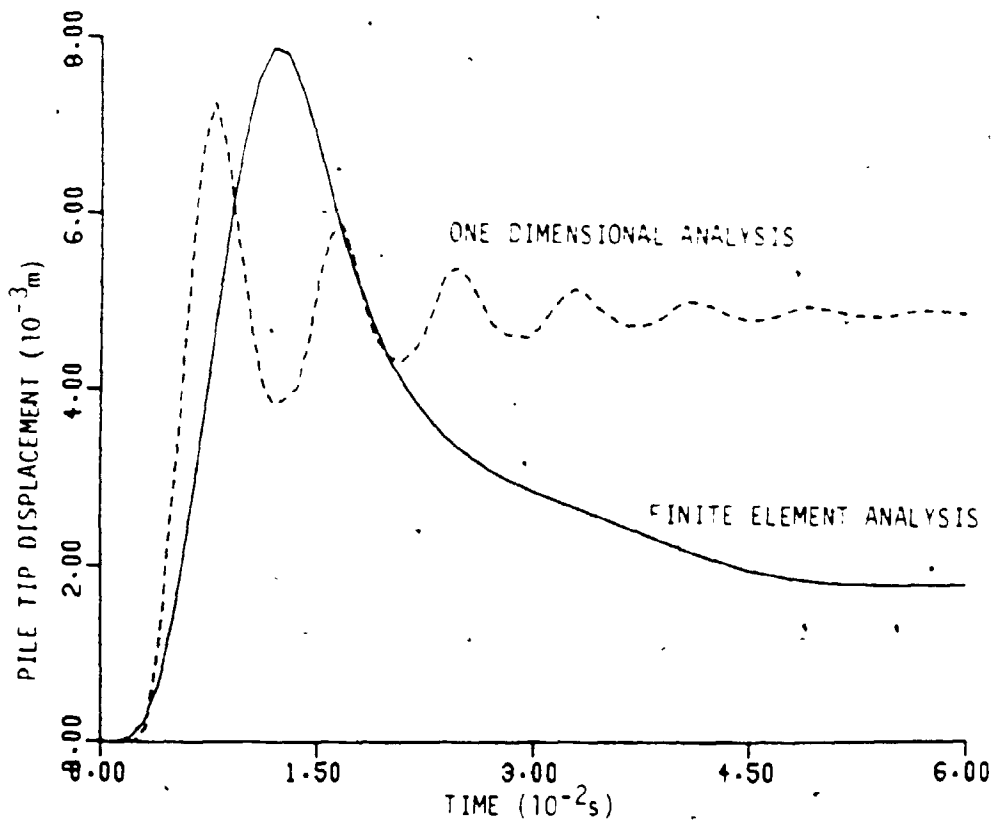
Figure 4-20: Comparison of Pile Tip Displacement for the 1-D and 3-D Analyses

linearly elastic. The applicability of the plane strain and the viscous boundaries to the pile driving problem are examined and the following conclusions emerge

1. The transmitting boundary developed in this study which is based on the plane strain soil reactions can be used for static as well as dynamic analyses. Due to the relative insensitivity of its parameters to frequency, it can also be used for time domain analysis. This boundary appears superior to the standard viscous boundary

2. Pile response to a harmonic load obtained using the viscous boundary experiences a shift in the equilibrium position which might affect the value of the pile set if such a boundary is used for pile driving analysis.

3. The soil model used in this chapter is not suitable for pile driving analysis and a more realistic model should include the soil plasticity in the analysis.

4. Finite element analysis of pile driving is very costly and at least 2 orders of magnitude more expensive than a one dimensional analysis. A true time domain analysis for large offshore piles that would take the plastic behaviour of the soil into account would indeed be prohibitively expensive. Given the physical uncertainties involved, this cost can hardly be justified. If such analysis were to be conducted, the transmitting boundary formulated herein is adequate.

Chapter Five
Foundation Model For Fixed ,
Offshore Towers

5.1. Introduction

Soil-structure interaction occurs when the foundation is flexible, under earthquake excitation it occurs when the footing displacements differ from those of the far field. This interaction is more significant for soft soils. Inclusion of soil-structure interaction in the dynamic analysis of offshore towers is essential as it affects the free vibration characteristics which have a direct bearing on the response prediction. Typically, considering the foundation flexibility in the analysis modifies the natural frequencies and mode shapes and accounts for radiation damping [65.66.67]. These modifications are extremely important, specially for narrow band processes such as wave loads, since a shift in the fundamental frequency may bring it closer to the peak frequency of the load spectrum. Furthermore, in a seismic event, the tower with its foundation will interact with the surrounding soil leading to a modification in the input seismic signal at the base of the structure [68] known as kinematic interaction.

For pile supported towers, the flexibility of single piles is routinely accounted for in both static [69.70.71] and dynamic [66.72.73] analyses. The inclusion of interaction between individual piles, known as pile-soil-pile interaction, is standard practice in static analysis [74-77]. Pile-soil-pile interaction in static analysis may significantly increase the settlement and lateral deflection of the superstructure [76] and reduce the bearing capacity of a pile group. On the other hand, the influence of dynamic pile-soil-pile interaction on the tower response has not been fully appreciated.

84

Nonlinear behaviour of single piles is commonly considered in static analysis based on the p-y curves but is less common for dynamic analysis [78,79]. Very few attempts were made to incorporate nonlinearity into pile-soil-pile interaction analysis [76,80,81]. The degradation of soil stiffness due to cyclic loading has been considered by Anagnostopoulos [78] and Kagawa [65] for earthquake loading and by Angelides [73] for wave loading.

In this chapter, the inclusion of dynamic pile-soil-pile interaction in the foundation stiffness matrix is outlined. This is achieved using frequency dependent dynamic interaction factors. The effect of soil-pile separation on dynamic interaction factors is studied using an idealization of a system of two piles with free lengths. Pile group impedance functions are formulated for all modes of vibration and incorporated in a computer based analysis of pile groups with rigid or flexible caps. Typical offshore pile clusters are analysed to demonstrate the effect of dynamic pile-soil-pile interaction on pile group properties. The analysis performed in this study is linear but it is assumed that nonlinearity can be accounted for by using the equivalent linearization technique and iteratively adjusting the soil properties to the level of strain.

5.2. Impedance Functions of Single Piles

In the absence of a computer program for direct dynamic analysis of pile groups, the basic elements necessary to evaluate the pile group stiffness are the impedance functions of single piles and interaction factors.

5.2.1. Stiffness Matrix of a Single Pile

A pile head can undergo three translations u, v and w in directions X, Y and Z, respectively and three rotations ξ, η and ζ about the same 3 axes. Fig. 5.1. These displacements form the vector

$$\{\Delta\} = \{u \ v \ w \ \xi \ \eta \ \zeta\}^T \quad (5.1)$$

Impedance functions are frequency dependent complex numbers, i.e.
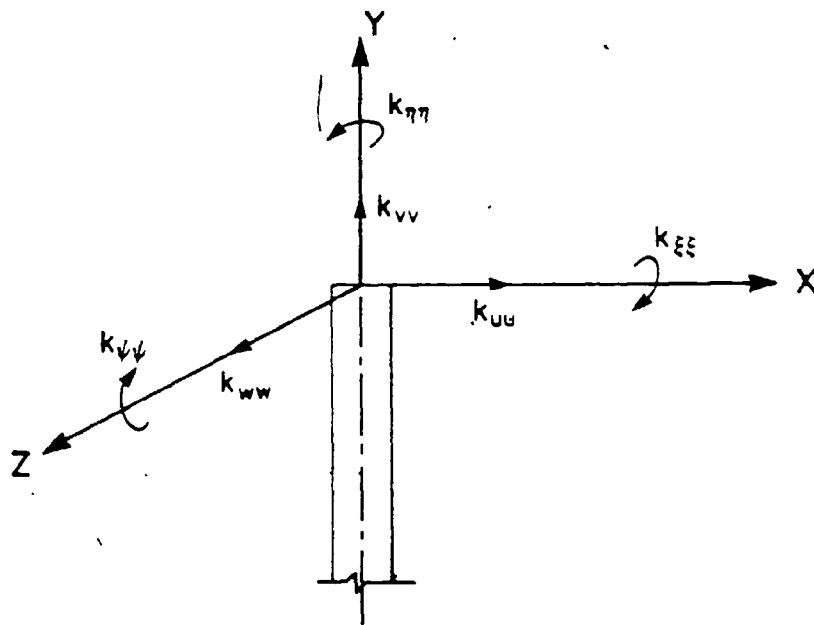
Figure 5-1: Notation for Pile Head Stiffness Constants
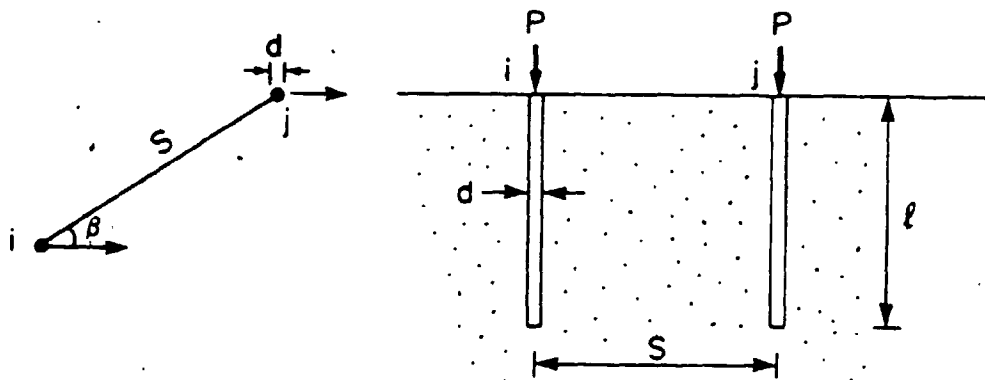
Figure 5-2: Two Identical and Equally Loaded Piles

Interaction factors with those evaluated using a direct analysis was reported by El Sharnouby and Novak [102]. They showed that the interaction factor approach is adequate except for short end bearing piles under vertical loads. Dynamic group stiffness constants evaluated using interaction factors were also shown to be quite satisfactory by Kaynia and Kausel [103].

Poulos [104] evaluated the static interaction factors for 2 rigid vertically loaded piles floating in an elastic half space. He later extended his solution to the horizontal case [105] and to vertically loaded end bearing piles [106]. Butterfield and Banerjee used the boundary element method for a group of piles with the pile cap connected to the ground [107].

Dynamic behaviour of pile groups has been studied by Wolf et al. [108,109] who used the finite element method. Nogami [110,111] analysed the vertical vibration of pile groups using the displacement field based on his earlier work on single piles. Sheta and Novak [112] analysed vertical pile groups using the displacement field obtained from the plane strain solution. Kaynia and Kausel [103] studied the behaviour of pile groups in a layered viscoelastic halfspace using Green's function for buried dynamic barrel loads to evaluate the soil flexibility matrix. They directly evaluated the group stiffness by imposing the boundary conditions and also evaluated the dynamic interaction factors. Ostadan [48] developed special elements for pile groups which incorporated the use of a beam element for the pile and an inter-pile element which models the soil between the piles for a general configuration of piles. El Sharnouby [113] implemented an efficient scheme to evaluate the group stiffness and the interaction factors for static loading using the displacement field based on Mindlin's Equation.

For vertical piles with circular cross sections. the horizontal. rocking and cross stiffnesses in both directions are equal. I.e. $k_{uu}=k_{u'u'}$, $k_{u\nu}=k_{u'\zeta}$ and $k_{\nu\nu}=k_{\zeta\zeta}$. The same holds for damping coefficients. Also, the vertical translation and torsional rotation are uncoupled from the other displacements.

5.2.2. Review of Existing Solutions for Impedance Functions

For piles with two planes of symmetry. such as circular piles, available solutions for evaluating the dynamic stiffness constants of a single pile can be categorized into lumped mass models [82-85]. continuum models [86-90]. finite element models [48,91-94] and boundary element models [95].

Lumped Mass Models: the pile mass is lumped into a set of discrete stations and the soil resistance is prescribed to these stations in the form of springs and dashpots. The main advantage of this model is its ability to handle nonlinearity because the springs and dashpots can be made nonlinear as desired. This method encounters some difficulty in choosing the appropriate nonlinear springs and dashpots properties. However. some success has been achieved in modelling the nonlinear spring characteristics from full scale tests by Matlock et al. [85]. The lumped mass model was employed by Penzien et al. [82,84] who used the static displacement field resulting from a single force applied at an interior point of a homogeneous half space (Mindlin's equation) to obtain the soil resistance at a point along the pile shaft. The basic disadvantage of this model is its inability to account for interaction between individual piles in its present form.

Continuum Models: these models basically employ the equations of motion of a linear viscoelastic medium to obtain the soil resistance to the pile motion. Tajimi [86] considered a frequency dependent viscous damping (Kelvin-Voigt model) and solved the horizontal response of a fixed head pile with a pinned tip.

Nogami and Novak [87,88] studied an elastic end bearing pile undergoing harmonic vibration in both the vertical and horizontal directions. The soil is assumed to be a viscoelastic homogeneous medium with frequency independent material damping. For the vertical response, horizontal displacements are assumed to be negligibly small and so are the vertical displacements for the horizontal response. Displacements and local soil resistance are expressed as the sum of contributions from an infinite number of wave modes. 'Below the resonant frequency (of a specific mode) the stiffness depends heavily on the mode number, no progressive wave propagates in the layer and damping is all derived from material damping.

This solution agrees well with the static stiffness by Poulos and with the dynamic plane strain solution [89] for slender piles, soft soils 'and frequencies above the first natural frequency of the soil layer. It also agrees well with Tajimi's solution for the horizontal case, if the difference in the definition of material damping is accounted for. The main drawback of this solution is the assumption of soil homogeneity and its limitation to end bearing piles.

Kobori et al. [90] studied the vibration of an elastic pile in a viscoelastic soil stratum overlying a bedrock subjected to a concentrated external excitation and to uniformly distributed bed rock motion. A simpler approach than that of Nogami and Novak, based on soil reactions calculated under the assumption of plane strain, was introduced by Novak [89] who derived the dynamic soil springs from Baranov's equations [96].

The assumption of plane strain is accurate for an infinitely long rigid pile undergoing uniform harmonic vibration in an infinite homogeneous layer. The soil layer is assumed to be composed of independent infinitesimally thin layers extending horizontally to infinity. In horizontal response no strain occurs in the vertical direction and waves propagate only in the horizontal direction.

The solution was first formulated in terms of linear elasticity for an end bearing pile in a homogeneous layer [89]. It was later extended to include floating piles vibrating vertically [97] and the effect of material damping. For a viscoelastic half space, material damping can be incorporated by the application of the correspondance principle [98]. This is done by complimenting the real shear modulus G with its imaginary counterpart G' such that

$$G^* = G - iG' = G(1 + i\tan\delta)$$ 5.6

where $\tan\delta = G'/G$ and δ is the loss angle; $\tan\delta =$ twice the damping ratio.

Finite Element Models: only a finite region of the unbounded soil domain is modeled by finite elements and a suitable boundary is applied to account for energy radiation and prevent wave reflection inside the modeled zone. The main advantage of this model is its ability to handle nonhomogeneity and nonlinearity. It has been successfully employed by Kuhlemeyer who used a rectangular axisymmetric element and a viscous boundary to analyze vertical and lateral vibration of a single pile [91,92]. The results obtained by Kuhlemeyer compare well with Poulos' results for the static case and with Novak's plane strain solution for the dynamic case.

Blaney at al. [93] used a toroidal element with 3 degrees of freedom per node. The far field is represented by a semi analytic energy transmitting boundary, which is an extension of the work done by Kausel et al. [40,99]. The transmitting boundary comprises a consistent boundary matrix which relates the displacements of the boundary to the corresponding reactions and unlike a Winkler's medium, couples all the boundary nodes. Use of finite elements can be avoided by modelling the pile by beam elements and moving the transmitting boundary to the pile. The method is general and variation of the soil properties in the horizontal direction can be accounted for by extending the modeled zone for a few elements

away from the pile   This solution was compared with Novak's plane strain solution and was found to be in good agreement '93', with Novak's results being higher by 10% for stiffness and 20 % for damping. An even better agreement was recently reported in '100'.

Angelides '30' extended this solution for a floating pile experiencing vertical vibration and incorporated soil nonlinearity in an approximate manner. He adopted an iterative linear procedure in which the shear modulus in each element is adjusted to the level of strain after each cycle. Ostadan '48' used the modified axisymmetric element employed by Kuhlemeyer 92 together with the consistent boundary developed by Kausel 40 .

Boundary Element Models: only the boundaries of the region being analysed are discretized which results in much smaller systems of equations 95 .

5.2.3. Plane Strain Impedance Functions

The validity of the plane strain solution for the basic case of a homogeneous layer overlying bedrock has been checked by comparing it with the more rigorous approach by Nogami and Novak '87.88'. For dimensionless frequencies $A_o \rightarrow 0$. the approximate stiffness diminishes while the more rigorous approach gives an almost constant stiffness which is equal to the static stiffness. As frequency increases, the approximate solution approaches the more rigorous one. At lower frequencies, the complex stiffness can approximately be taken as constant and equal to that calculated at a suitable dimensionless frequency such as $A_o = 0.3$.

At large displacement amplitudes, the soil adjacent to the pile behaves nonlinearly. An approximate approach was formulated where the pile is surrounded by a composite, linear viscoelastic medium comprising two parts, an outer infinite region and an inner cylindrical zone which is weakened by the effect of nonlinearity and lack of bond [25].

Using a finite element idealization of the pile, Novak and Aboul Ella [98] extended the solution to the case of a layered medium where shear modulus can vary with depth in any desired fashion and even complete separation can be accounted for. In this study, the plane strain impedance functions are employed and are evaluated using the computer program PILAY2 [101] developed by Novak et al.

5.2.4. Nonlinearity

The analysis conducted in this investigation is limited to the linear case (small strains). However, the analysis can be easily extended for extreme waves, where nonlinearity of the foundation behaviour is important, using the equivalent linearization technique. This is achieved by dividing the soil surrounding the pile into several layers and calculating the pile displacements and associated soil strains that result from the linear analysis. Soil shear modulus in each layer is then adjusted to the level of strain. The adjusted shear modulus may be extended radially to infinity or confined to a weakened zone around the pile. The foundation stiffness is then recalculated and the analysis is repeated to re-evaluate the tower and foundation responses. The new values of the foundation displacements are taken as input for the next cycle of calculations and the analysis is repeated until convergence is achieved.

5.3. Pile Group Behaviour

Pile-soil-pile interaction is the displacement of one pile due to its presence in the displacement field of a neighbouring loaded pile. Thus, pile-soil-pile interaction increases the settlement of pile groups, redistributes the loads on individual piles and modifies the group stiffness as well as damping. Pile group effects can be accounted for either by direct analysis of the whole group or by employing the interaction factors.

A detailed comparison of static group stiffness constants evaluated using

Interaction factors with those evaluated using a direct analysis was reported by El Sharnouby and Novak [102]. They showed that the interaction factor approach is adequate except for short end bearing piles under vertical loads. Dynamic group stiffness constants evaluated using interaction factors were also shown to be quite satisfactory by Kaynia and Kausel [103].

Poulos [104] evaluated the static interaction factors for 2 rigid vertically loaded piles floating in an elastic half space. He later extended his solution to the horizontal case [105] and to vertically loaded end bearing piles [106]. Butterfield and Banerjee used the boundary element method for a group of piles with the pile cap connected to the ground [107].

Dynamic behaviour of pile groups has been studied by Wolf et al. [108,109] who used the finite element method. Nogami [110,111] analysed the vertical vibration of pile groups using the displacement field based on his earlier work on single piles. Sheta and Novak [112] analysed vertical pile groups using the displacement field obtained from the plane strain solution. Kaynia and Kausel [103] studied the behaviour of pile groups in a layered viscoelastic halfspace using Green's function for buried dynamic barrel loads to evaluate the soil flexibility matrix. They directly evaluated the group stiffness by imposing the boundary conditions and also evaluated the dynamic interaction factors. Ostadan [48] developed special elements for pile groups which incorporated the use of a beam element for the pile and an inter-pile element which models the soil between the piles for a general configuration of piles. El Sharnouby [113] implemented an efficient scheme to evaluate the group stiffness and the interaction factors for static loading using the displacement field based on Mindlin's Equation.

5.4. Interaction Factors

An interaction factor is the dimensionless (normalized) displacement of one pile due to the load on a neighbouring pile. For two identical and equally loaded piles, i and j, Fig. 5.2, the static interaction factor α_{ij} is usually defined as

$$\alpha_{ij} = \frac{\text{displacement of pile } i \text{ due to load on pile } j}{\text{displacement of pile } i \text{ due to its own load}}$$

and the dynamic interaction factor is defined as

$$\alpha_{ij} = \frac{\text{dynamic displacement of pile } i \text{ due to load on pile } j}{\text{static displacement of pile } i \text{ due to its own load}}$$

For a vertical pile, the vertical translation is assumed to be independent of the horizontal translation and rotation in a vertical plane and only four different types of interaction factors need be considered. These are α_{vv} and α_{uu} for the vertical and horizontal translations, respectively, $\alpha_{\iota\tau}$ for rotation in a vertical plane and $\alpha_{u\psi}$ for the coupling between the horizontal translation and rotation.

5.4.1. Dynamic Interaction Factors

To account for the effects of both stiffness and damping, dynamic interaction factors are employed. The dynamic interaction factors are frequency dependent complex numbers, i.e.

$$\alpha_{ij} = \alpha_{ij}(1) + i\alpha_{ij}(2) \tag{5.7}$$

and depend on L/d, ρ_p/ρ_s, E_p/E_s, A_o and S/d where E_p, ρ_p, L and d are the pile Young's modulus, density, length and diameter, respectively, ρ_s and E_s are the soil density and Young's modulus, respectively, and A_o is dimensionless frequency defined as

$$A_o = \omega d / V_s \tag{5.8}$$

where V_s is the soil shear wave velocity. The horizontal and rotational interaction factors depend also on the angle β, Fig. 5.2, between the direction of the horizontal displacement and the line joining the two piles. Interaction factors are usually evaluated for the 2 limiting cases, $\beta = 0°$ and $\beta = 90°$. For intermediate angles, Randolph and Poulos [11], suggested the following relationship

$$(5.9)$$

$$\alpha_{ij}(\beta) = \alpha_{ij}(0^\circ)\cos^2\beta + \alpha_{ij}(90^\circ)\sin^2\beta$$

In this study, the dynamic interaction factors produced by Kaynia and Kausel [103] are employed. These interaction factors are presented in the form of charts and give dynamic displacements normalized by the static displacements of the reference pile under its own load. For inclusion in the computer program, the dynamic interaction factors were fitted with analytical expressions using the Chebychev polynomials. Accordingly, an interaction factor $\alpha_{ij}(A_o)$ is expressed as a Chebychev series, i.e.

$$\alpha_{ij}(A_o) = 0.5 A_1 T_0(\overline{A}_o) + \sum_{i=1}^{N} A_{i+1} T_i(\overline{A}_o) \qquad (5.10)$$

where T_i is the Chebychev polynomial of the first kind of degree i, A_i are the coefficients of the Chebychev series and $\overline{A}_o$ is a normalized variable given by

$$\overline{A}_o = \frac{((A_o - A_{\alpha(min)}) - (A_{\alpha(max)} - A_o))}{(A_{\alpha(max)} - A_{\alpha(min)})} \qquad (5.11)$$

where $A_{\alpha(min)}$ and $A_{\alpha(max)}$ are the minimum and maximum values, respectively, in the interpolation interval. In this study, $A_{\alpha(min)}=0.0$ and $A_{\alpha(max)}=0.5$.

The interaction factors in [103] are given for $E_s/E_p = 10^{-3}$, $L/d = 15$, $\rho_s/\rho_p = 0.7$, three different values of S/d, i.e. $S/d = 2$, 5 and 10 and A_o in the range of 0 - 1.0. To obtain the interaction factors at intermediate values of S/d and A_o, a two step interpolation is employed; first interpolating for the dimensionless frequency A_o and then for the spacing ratio S/d. The Chebychev polynomials established in this way provide perfect fit with the given charts. Interaction factors for $S/d > 10$ are neglected as they become very small.

Because the interaction factors obtained in this manner are valid only for

specific values of E_s/E_p, ρ_s/ρ_p, and L/d, their applicability for other values of these parameters has to be assessed. El Sharnouby and Novak [102] have shown that the slenderness ratio L/d has little effect on the interaction factors for $L/d > 10$ and that the soil profile is of minor importance. Similarly, the effect of ρ_s/ρ_p on interaction factors is very small for low dimensionless frequencies. Finally, the ratio $E_s/E_p = 10^{-3}$ is representative of the ratios encountered offshore. However, to reduce possible errors, the interaction factors obtained from the interpolation scheme are multiplied by the ratio of the static interaction factors to the dynamic interaction factors at $A_o = 0$.

5.4.2. Static Interaction Factors

. These depend on L/d, E_s/E_p and S/d. The vertical static interaction factors produced by Poulus [47] are used together with an interpolation scheme similar to the one described earlier. The horizontal interaction factors used in this study are those presented by Novak and El Sharnouby [114] in the form of simple analytical expressions, i.e.

$$\alpha_{ij} = A(E_p/E_s)^B (d/S)^C \qquad (5.12)$$

where A, B and C are tabulated constants. The last correction to be incorporated involves the effect of pile separation.

5.4.3. Effect of Pile Separation on Interaction Factors

Monitoring of the natural frequencies of existing offshore towers indicate that during a heavy storm, the natural frequencies may drop significantly but during a subsequent calm period, they may return to the original values [115,116]. This is attributed primarily to pile loosening due to large displacements that results in pile separation from the soil (gapping) followed by "healing" in the course of time. This separation affects not only the the stiffness of single piles but also the interaction between piles. In this study, it was desired to account for the effect of pile separation on interaction factors.

To evaluate the effect of gapping on dynamic interaction factors, a system of two piles with equal free lengths, e, is considered. The pile separation is represented by the free lengths of the two piles, Fig. 5.3. and idealized by beam elements. The composite medium, comprising the soil with the embedded parts of the two piles is represented by a complex spring connecting the lower ends of the two free lengths. A global stiffness matrix for the idealized system is first constructed. While the stiffness matrices for elements (1) and (2) are those of the standard beam elements, that of element (3) is obtained as the inverse of the flexibility matrix $[F]$ defined as

$$[F] = \begin{bmatrix} [K_{H}]^{-1} & [f_{H}] \\ [f_{H}] & [K_{H}]^{-1} \end{bmatrix}$$

(5.13)

where $[K_{H}]$ is the complex dynamic stiffness matrix of a single pile for the horizontal translation and rotation (rocking) given by

$$[K_{H}] = \begin{bmatrix} K_{uu} & K_{uv} \\ K_{vu} & K_{vv} \end{bmatrix}$$

(5.14)

where

$$K_{ij} = k_{ij} + i\omega c_{ij}$$

(5.15)

The complex flexibility matrix $[f_{H}]$ represents the interaction matrix between the horizontal displacements and rotations of the two piles. i.e.

$$[f_{H}] = \begin{bmatrix} f_{uu} & f_{uv} \\ f_{vu} & f_{vv} \end{bmatrix}$$

(5.16)

In which the dynamic flexibility coefficients f_{ij} represent the interaction between

(a) Pile with free length   (b) Model of system
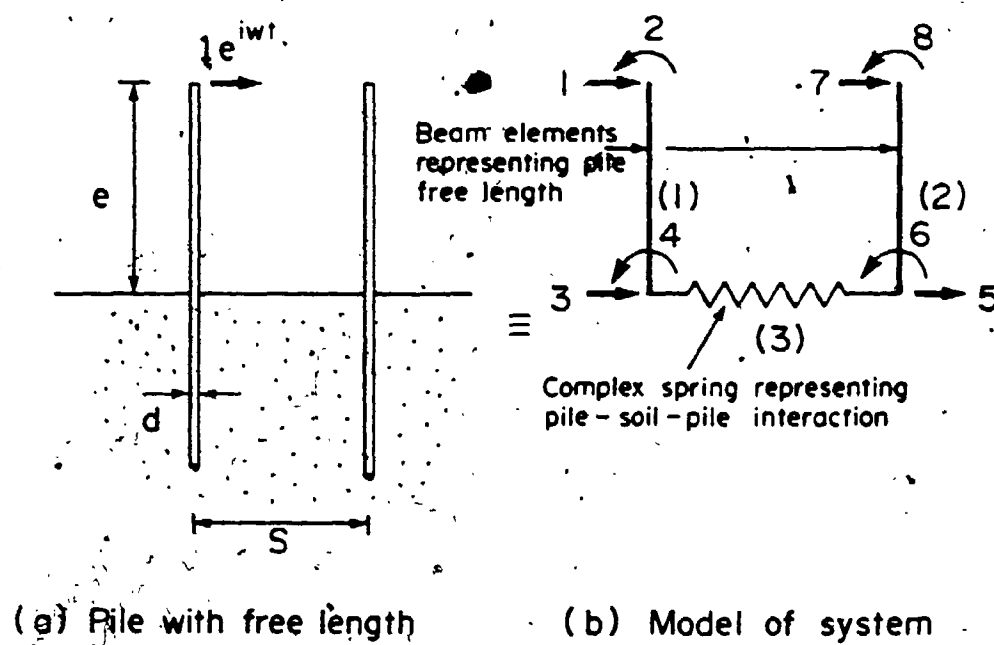
Figure 5-3: Model Used to Account for Effect of Pile Separation on Interaction Factors

the two piles and are expressed in terms of static flexibility coefficients T_{ij} and complex dynamic interaction factors

$$f_{ij} = T_{ij} \alpha_{ij} \qquad (5.17)$$

Once the global stiffness matrix (8×8) is assembled, a unit harmonic horizontal load and moment are applied, at different frequencies, at d.o.f. 1 and 2. The corresponding displacements at d.o.f. 7 and 8, normalized by the static flexibility of the pile with free length, are the interaction factors. The dynamic interaction factors of Kaynia and Kausel [103] are substituted for α_{ij} in Eq. 5.17. An interpolation scheme similar to the one described earlier is employed to evaluate the interaction factors for a free length at intermediate values of A_o and S/d.

Figs. 5.4 and 5.5 show the variation in the interaction factors α_{uu}, $\alpha_{u\iota}$ and $\alpha_{\iota\iota}$ with frequency for $\beta = 0°$ and $90°$, $S/d = 2$ and three different values of e/d. The variations in the same interaction factors with the spacing ratio S/d is shown in Figs. 5.6 and 5.7. It can be seen from Figs. 5.4 to 5.7 that the absolute values of both the real and imaginary parts of the interaction factors are reduced by the presence of a free length. This reduction increases with the increase in the pile separation ratio e/d. For the real part, the reduction is largest at $A_o = 0$, and for the imaginary part, the reduction increases with dimensionless frequency A_o. In Figs. 5.6 and 5.7, the variations in the interaction factors with the spacing ratio show a drooping trend; however, for higher frequencies these variations may show an oscillatory trend [112]. While the presence of a free length increases the single pile flexibility, it decreases the interaction factors. These two effects counteract and the net effect of pile separation on the pile group may be smaller than its effect on a single pile.
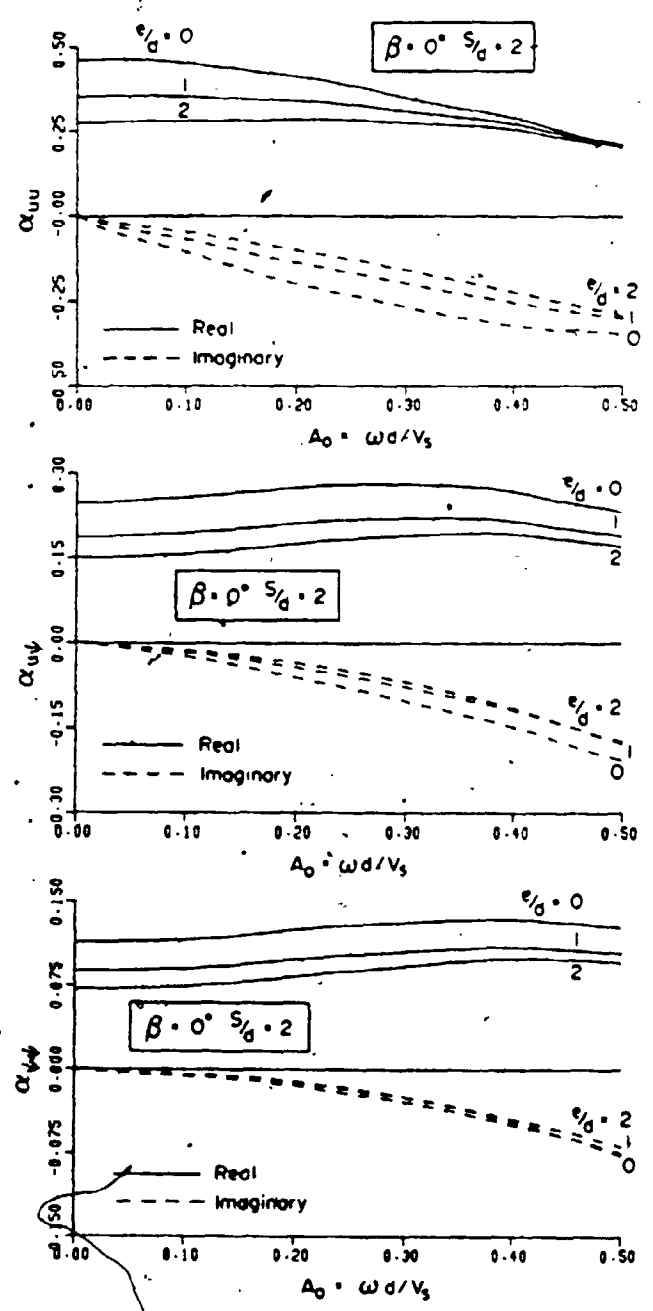
Figure 5-4: Variation in Interaction Factors α_{uu}, α_{uv} and α_{vv} with Pile Separation Ratio (e/d) and Dimensionless Frequency (A_o) for $S/d=2$ and $\beta=0°$

Figure 5-5: Variation in Interaction Factors α_{uu}, $\alpha_{u\psi}$ and $\alpha_{\psi\psi}$ with Pile Separation Ratio (e/d) and Dimensionless Frequency (A_0) for $S/d=2$ and $\beta=90°$
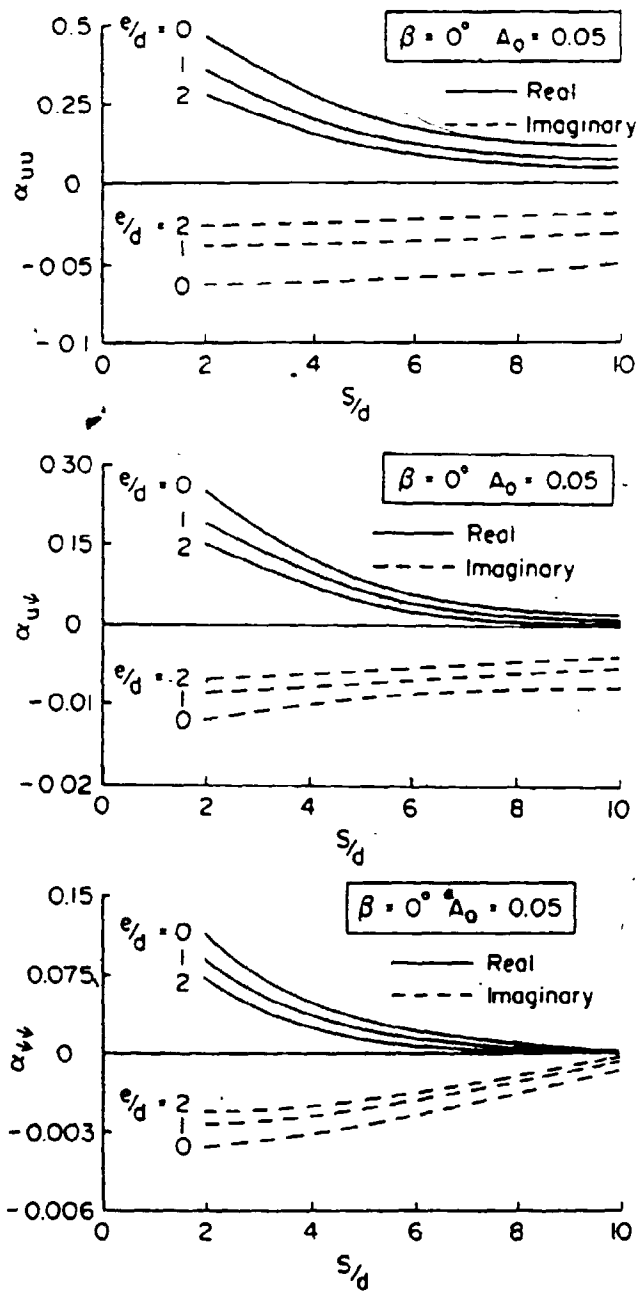
Figure 5-6: Variation in Interaction Factors α_{uu}, $\alpha_{u\psi}$ and $\alpha_{\psi\psi}$ with Pile Spacing Ratio (S/d) and Separation Ratio (e/d) for $\beta = 0°$ and $A_o = 0.05$
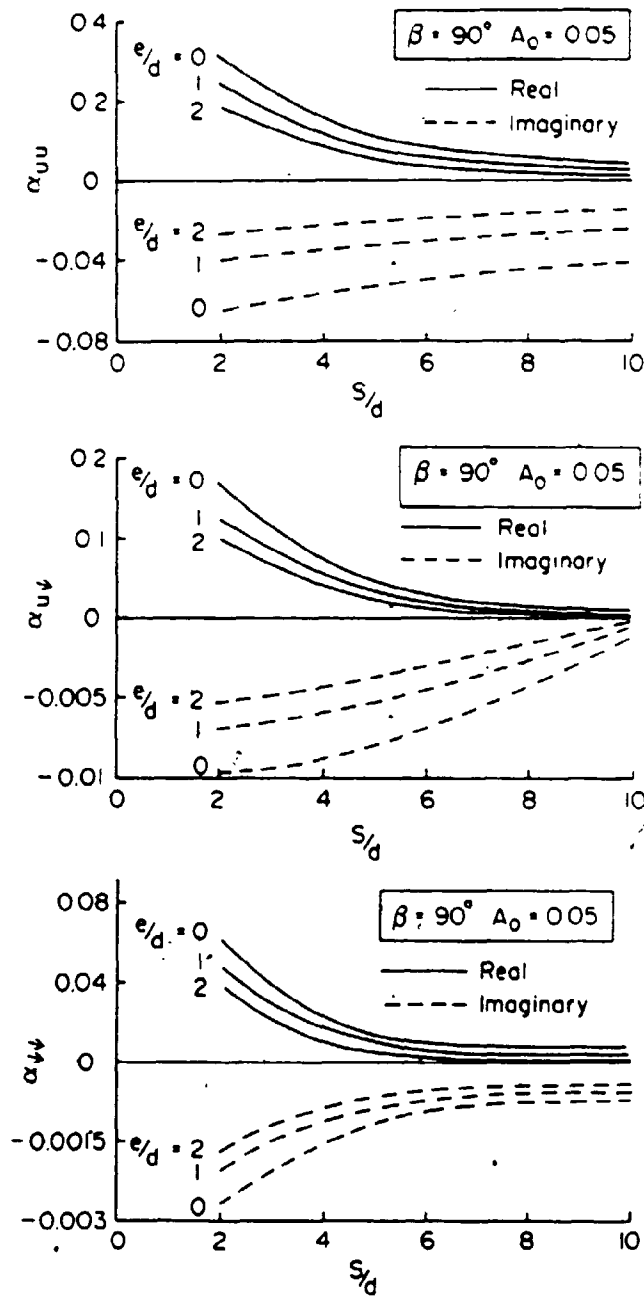
Figure 5-7: Variation in Interaction Factors α_{uu}, α_{uv}, and α_{vv} with Pile Spacing Ratio (S/d) and Separation Ratio (e/d) for $\beta=90°$ and $A_o=0.05$

5.5. Foundation Stiffness Matrix

The complex foundation stiffness matrix $[K_b]$ is obtained as the inverse of the complex foundation flexibility matrix $[F_b]$, i.e.

$$[K_b] = [F_b]^{-1} \qquad 5.18$$

For a group of n piles, the foundation flexibility matrix is a symmetric $6n \times 6n$ matrix

$$
5.19
$$

$$
[F_b] = \begin{bmatrix} [f]_{11} & [f]_{1i} & [f]_{1n} \\ [f]_{i1} & [f]_{ii} & [f]_{in} \\ [f]_{n1} & [f]_{ni} & [f]_{nn} \end{bmatrix}
$$

where each of the diagonal submatrices $[f]_{ii}$ is the inverse of the single pile 6×6 complex stiffness matrix, Eq. 5.3. The off diagonal submatrices $[f]_{ij}$ represent the interaction between the degrees of freedom at the heads of piles i and j, i.e.

$$
(5.20)
$$

$$
[f]_{ij} = \begin{bmatrix} & u & v & w & \zeta & \eta & v \\ \alpha_{uu}T_{uu} & & & & & \alpha_{uv}T_{uv} \\ & \alpha_{vv}T_{vv} & & & & \\ & & \alpha_{ww}T_{ww} & \alpha_{w\zeta}T_{w\zeta} & & \\ & & \alpha_{\zeta w}T_{\zeta w} & \alpha_{\zeta\zeta}T_{\zeta\zeta} & & \\ & & & & \alpha_{\eta\eta}T_{\eta\eta} & \\ \alpha_{vu}T_{vu} & & & & & \alpha_{vv}T_{vv} \end{bmatrix}
$$

In Eq. 5.20, α_{ij}-s are the complex dynamic interaction factors and T_{ij}-s are the static flexibility coefficients. The interaction factor $\alpha_{\eta\eta}$ which accounts for pile twisting is usually very small and is neglected. In standard solutions, pile-soil-pile interaction is neglected and consequently the off diagonal submatrices given by Eq. 5.20 are absent from Eq. 5.19.

Each of the tower main legs is supported either by a large diameter single pile, Fig. 5.8, or by a pile cluster, Fig. 5.9. When each of the main legs is supported by a single pile, the foundation system is a flexible one where the displacements of pile heads vary from one pile to another. On the other hand, when each of the r. legs is supported by a pile cluster, piles of the same cluster are connected by a rigid cap which controls the displacements of all pile heads. In this case, each pile cluster is represented as one node in the space frame model, and the stiffness constants of such a cluster are evaluated by imposing the proper boundary conditions. In both cases, after evaluating the stiffness constants of the supporting foundation for each main leg, the interaction between these supporting foundations should be accounted for.

5.6. Pile Group Impedance Functions

With the foundation flexibility matrix established, Eq. 5.19, the group impedance functions for n piles connected by a rigid cap can be formulated by imposing the proper boundary conditions for each displacement mode.

5.6.1. Vertical Group Stiffness

For vertical circular piles, vertical displacements are uncoupled from horizontal displacements and rotations in a vertical plane. Thus it is computationally more efficient to assemble the group vertical flexibility matrix separately from that of the horizontal displacements and rotations. The compatibility equations are written as

$$T_{i \dashv} [f]_V \{P\}_V = \{v\}$$ (5.21)

where $\{P\}_V$ and $\{v\}$ are the vectors of vertical forces and displacements at individual pile heads, respectively, $[f]_V$ is the interaction matrix of the vertical displacements, written as
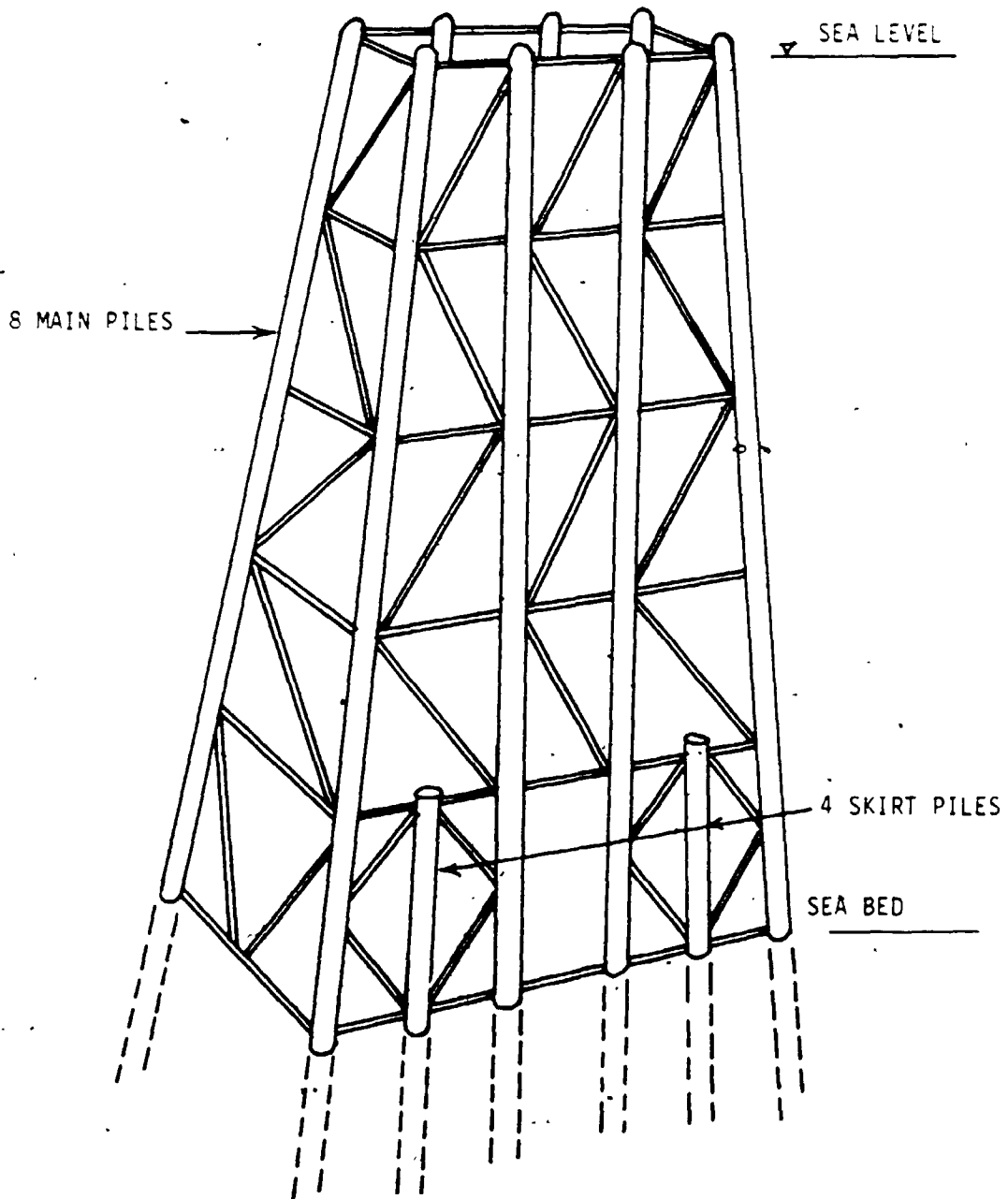
Figure 5-8: Offshore Tower Supported by a Group of Widely Spaced Piles
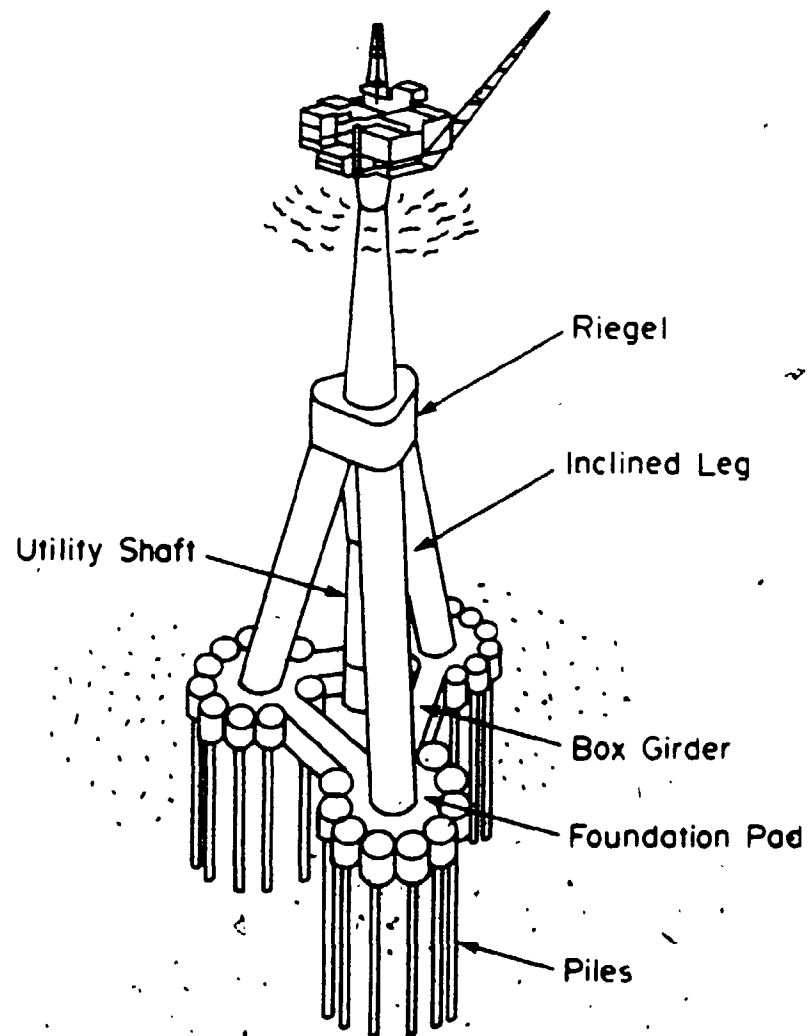
Figure 5-9: Schematic of Gravity Tower Supported by a Group of Pile Clusters

$$(5.22)$$

$$[f]_{v} = \begin{bmatrix} f'_{vv} & \alpha_{11} & & \alpha_{1n} \\ & & \cdot & \\ \alpha_{11} & \cdot & f'_{vv} & \alpha_{1n} \\ & & & \cdot \\ \alpha_{n1} & \cdot & \alpha_{n1} & f'_{vv} \end{bmatrix}$$

where

$$f'_{vv} = f_{vv}/\overline{T}_{vv} \qquad (5.23)$$

In Eq. 5.23, f_{vv} and $\overline{T}_{vv}$ are the single pile vertical dynamic and static flexibility coefficients, respectively and α_{ij} -s are the complex dynamic vertical interaction factors. The boundary conditions in this case are $v_i = 1$, for $i = 1 \cdots n$ and the vertical forces at the pile heads are

$$\{P\}_V = (1/\overline{T}_{vv})[f]_V^{-1}\{1\} \qquad (5:24)$$

Denoting $\overline{K}_{vv} = (1/\overline{T}_{vv})$ and the complex elements of $[f]_V^{-1}$ by ϵ^V, the vertical force P_i acting on pile i is

$$P_i = \overline{K}_{vv}\sum_{j=1}^{n} \epsilon_{ij}^{V} \qquad (5.25)$$

The group stiffness is the sum of the vertical forces at all the pile heads, i.e.

$$K_{vv}^{G} = \overline{K}_{vv}\sum_{i=1}^{n}\sum_{j=1}^{n} \epsilon_{ij}^{V} \qquad (5.26)$$

5.6.2. Horizontal, Rocking and Cross Stiffness of Pile Groups

In cases where only the horizontal stiffness of the pile group is of interest, an equation of the form of Eq. 5.26 can be used to evaluate the horizontal group stiffness. This is achieved by substituting $\overline{K}_{vv}$ and ϵ_{ij}^{V} by the horizontal stiffness

and interaction factors, respectively, for a fixed head or a pinned head pile depending on the nature of piles in the group. When the rocking and cross stiffness of the group are also required, a more general formulation is needed. The compatibility equations for the general case are written as

$$T_{uu}[f]_H\{P\}_H = \{\delta\}_H \qquad (5.27)$$

where T_{uu} is the horizontal static flexibility coefficient for pinned head piles, $\{P\}_H$ is the vector of horizontal forces, H_i, and moments, M_i, at the pile heads, i.e.

$$\{P\}_H = \{H_1 M_1 \ldots H_i M_i \ldots H_n M_n\}^T \qquad (5.28)$$

The vector $\{\delta\}_H$ lists the horizontal translations and rotations at the pile heads

$$\{\delta\}_H = \{u_1 \psi_1 \ldots u_i \psi_i \ldots u_n \psi_n\}^T \qquad (5.29)$$

Finally, $[f]_H$ is the matrix of interaction coefficients for the horizontal translations and rotations. For a group of n piles, the matrix $[f]_H$ comprises $n \times n$ submatrices, i.e.

$$ (5.30) $$

$$[f]_H = \begin{bmatrix} [B]_{11} & [B]_{1i} & [B]_{1n} \\ [B]_{i1} & [B]_{ii} & [B]_{in} \\ [B]_{n1} & [B]_{ni} & [B]_{nn} \end{bmatrix}$$

where each of the submatrices is 2×2 and given by

$$ (5.31) $$

$$[B]_{ii} = \begin{bmatrix} f'_{uu} & f'_{u\psi} \\ f'_{\psi u} & f'_{\psi\psi} \end{bmatrix}$$

and

$$ (5.32) $$

$$[B]_{ij} = \begin{bmatrix} \beta_{ij}^{uu} & \beta_{ij}^{uv} \\ & \\ \beta_{ij}^{vu} & \beta_{ij}^{vv} \end{bmatrix}$$

where

$$f_r' = f_r / T_{uu} \tag{5.33}$$

and

$$\beta_{ij}^r = (T_r / T_{uu}) \alpha_{ij}^r \tag{5.34}$$

In Eqs. 5.33 and 5.34, f_r are the dynamic flexibility coefficients and r stands for uu, vv or uv indicating the horizontal translation, rocking or coupling directions, respectively.

Horizontal Stiffness: The boundary conditions are, ,Fig. 5.10, $u_i = 1$ and $v_i = 0$ for $i = 1 \cdots n$. The horizontal force on pile i is

$$H_i = \overline{k}_{uu} \sum_{j=1}^{n} \epsilon_{2i-1,2j-1}^{H} \tag{5.35}$$

where $\overline{k}_{uu} = 1 / T_{uu}$ is the horizontal static stiffness coefficient for a pinned head pile and ϵ^H are the complex elements of $[f]_{H}^{-1}$; hence the horizontal group stiffness becomes

$$K_{uu}^{G} = \overline{k}_{uu} \sum_{i=1}^{n} \sum_{j=1}^{n} \epsilon_{2i-1,2j-1}^{H} \tag{5.36}$$

In Eq. 5.36, the summation extends over those elements of $[f]_{H}^{-1}$ corresponding to the horizontal forces associated with horizontal displacements, i.e. elements at positions $2i-1, 2j-1$.

Rocking Stiffness: the boundary conditions are, Fig. 5.10, $v_i' = 1$, $v_i = 1 \times r_i$

A) VERTICAL

B) HORIZONTAL

C) ROCKING

D) TORSION
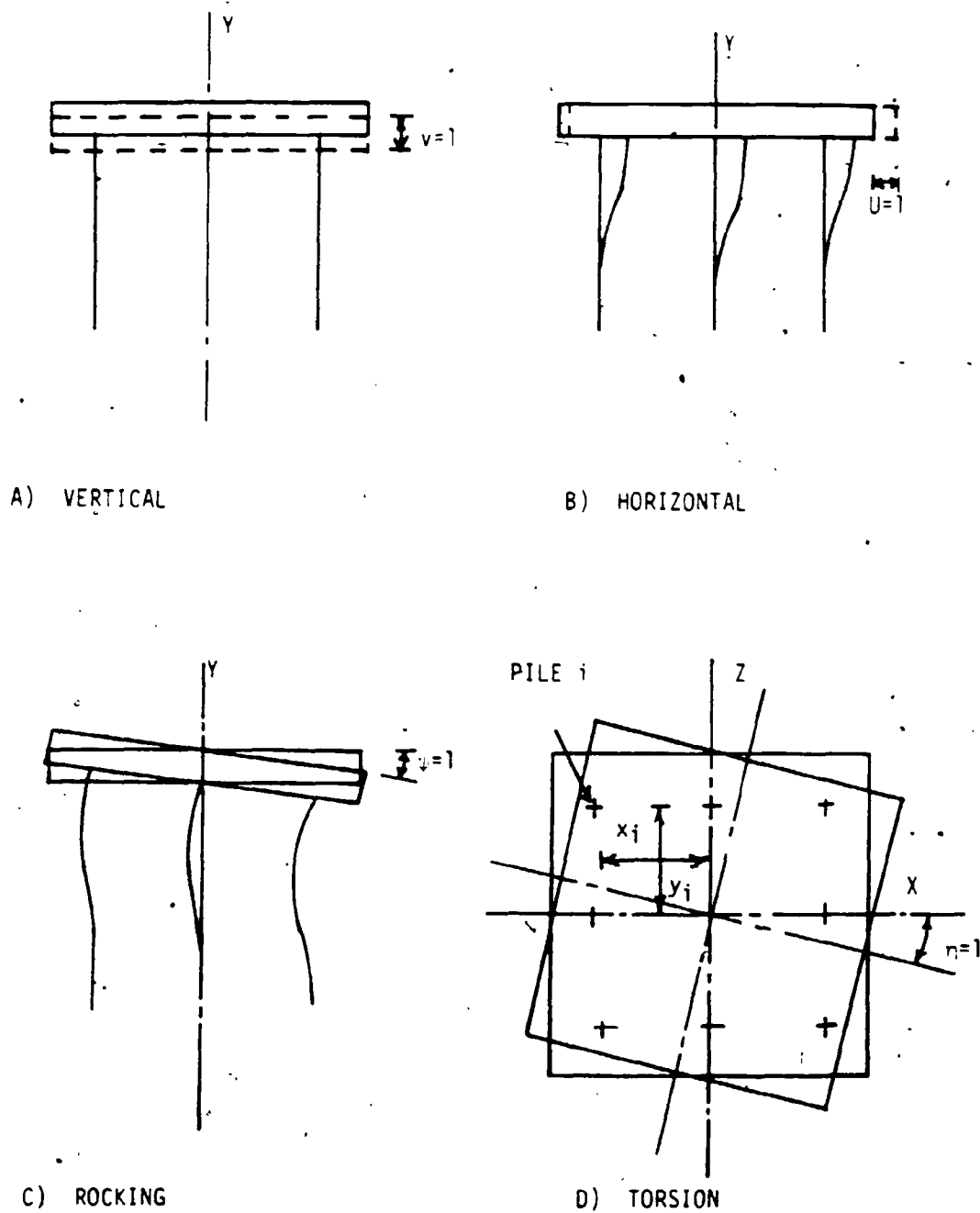
Figure 5-10: Boundary Conditions for Evaluating Pile Group Stiffness Constants

and $u_i=0$ for $i=1 \cdots n$. Rocking stiffness derives from two components: the moments required to produce unit rotations at the pile heads and the moments resulting from the vertical forces. The moments required to produce unit rotations at the pile heads are obtained by applying the boundary conditions pertaining to horizontal translations and rotations to Eq. 5.27 resulting in pile moments

$$(M_i)_1 = \overline{k}_{uu} \sum_{j=1}^{n} \epsilon^{H}_{2i,2j} \tag{5.37}$$

The vertical pile forces are obtained by applying the vertical boundary conditions to Eq. 5.21 and are

$$P_i = \overline{k}_{vv} \sum_{j=1}^{n} \epsilon^{V}_{ij} x_j \tag{5.38}$$

producing a moment

$$(M_i)_2 = \overline{k}_{vv} x_i \sum_{j=1}^{n} \epsilon^{V}_{ij} x_j \tag{5.39}$$

The rocking group stiffness is the sum of both moments over all pile heads, i.e.

$$K^{G}_{\psi\psi} = \overline{k}_{uu} \sum_{i=1}^{n} \sum_{j=1}^{n} \epsilon^{H}_{2i,2j} + \overline{k}_{vv} \sum_{i=1}^{n} \sum_{j=1}^{n} \epsilon^{V}_{ij} x_i x_j \tag{5.40}$$

where ϵ^{H} are the complex elements of $[f]^{-1}_{H}$.

Cross Stiffness: this is obtained by applying unit rotations at the pile heads to Eq. 5.27 and evaluating the associated horizontal forces or applying unit translations at the pile head and evaluating the associated moments. This gives

$$H_i = \overline{k}_{uu} \sum_{j=1}^{n} \epsilon^{H}_{2i-1,2j} \tag{5.41}$$

The group cross stiffness is the sum of all horizontal forces on the pile heads and thus is

$$K_{uu}^{G} = \overline{k}_{uu} \sum^{n} \sum_{j=1}^{n} \epsilon_{2i-1,2j}^{H}$$ (5.42)

5.6.3. Torsional Stiffness

The torque required to twist individual piles is small compared to that resulting from horizontal forces associated with a unit rotation. A unit rotation $\eta=1$ is imposed on the whole pile cap, Fig. 5.10, resulting in the following boundary conditions

$$u_i^x = r_i \sin \theta = z_i \quad ; \quad v_i = 0 \text{ for } i=1 \cdots n$$ (5.43)

and

$$u_i^z = r_i \cos \theta = x_i \quad ; \quad \xi_i = 0 \text{ for } i=1 \cdots n$$ (5.44)

where the superscripts x and z indicate the directions of the superscripted variables. Applying these boundary conditions to Eq. 5.27 for each of the X and Z directions gives the horizontal forces at pile i as

$$H_i^x = \overline{k}_{uu} \sum_{j=1}^{n} (\epsilon_{2i-1,2j-1}^{H})_x z_j$$ (5.45)

and

$$H_i^z = \overline{k}_{uu} \sum_{i=1}^{n} (\epsilon_{2i-1,2j-1}^{H})_z x_j$$ (5.46)

where $(\epsilon_{ij}^{H})_x$ and $(\epsilon_{ij}^{H})_z$ refer to the complex elements of $[f]_{II}^{-1}$ for the X and Z directions respectively. These two horizontal forces produce the moments

$$M_i^x = \overline{k}_{uu} z_i \sum_{j=1}^{n} (\epsilon_{2i-1,2j-1}^{H})_x z_j$$ (5.47)

and

$$M_i^z = \overline{k}_{uu} x_i \sum_{j=1}^{n} (\epsilon_{2i-1,2j-1}^{H})_z x_j$$ (5.48)

The total moment defining the group torsional stiffness results from the summation of moments for all pile heads and thus is

$$K_{\eta\eta}^{G} = \overline{k}_{uu} \sum_{i=1}^{n} \sum_{j=1}^{n} \{ (\epsilon_{2i-1,2j-1}^{H})_{x} z_i z_j + (\epsilon_{2i-1,2j-1}^{H})_{z} x_i x_j \} \tag{5.49}$$

All the formulae for the dynamic group stiffness are analogous to those for static stiffness [117] to which they reduce for $\omega=0$.

5.7. Examples of Group Properties

The influence of dynamic pile-soil-pile interaction on the group stiffness and damping is best illustrated when the results of the analysis are presented in terms of the group efficiency ratio (GER) which is defined for stiffness and damping respectively as

$$GER = \frac{Stiffness\ (damping)\ of\ pile\ group}{n \times Stiffness\ (damping)\ of\ a\ single\ pile}$$

where n is the number of piles in the group. Kaynia and Kausel [49] normalized the pile group stiffness and damping by the static stiffness of a single pile; however, this normalization does not instantly reflect the magnification or reduction in the group properties due to interaction.

The vertical and horizontal GER for both stiffness and damping are calculated for three groups comprising 2, 4 and 10 piles, respectively. Individual piles in the three groups have an outer diameter of 1.45 m, penetration of 72 m, density ratio $\rho_s/\rho_p=0.7$ and stiffness ratio $E_p/E_s=1000$. For a hollow pile, an equivalent density, ρ_{eq} is to be used and is calculated as follows:

$$\rho_{eq} = \frac{\rho_p A_p}{A} \tag{5.50}$$

where ρ_p and A_p are the actual pile density and cross section area, respectively and A is the gross area evaluated assuming a solid cross section.

Fig. 5.11 shows the configuration of the three groups where a rigid massless cap and fixed head piles are assumed. The complex group stiffness is calculated, at different frequencies, using Eq. 5.26 for the vertical direction and Eq. 5.36 for the horizontal direction.

Figs. 5.12 to 5.14 show the variation in group efficiency ratio for both stiffness and damping with frequency for the three groups. The GER for stiffness is mostly less than one except for the smaller groups for which the vertical stiffness can be seen to exceed unity at higher frequencies. GER equal to one indicates no interaction effects while GER less than one indicates reduction in group stiffness or damping. The reduction in group stiffness is particularly large for the group of 10 piles for which it decreases with frequency up to about $A_o=0.35$. For damping, the GER may exceed unity indicating amplification of energy dissipation through pile interaction.

5.8. Conclusions

Dynamic interaction factors for pile-soil separation are evaluated using the dynamic interaction factors produced for fully embedded piles by Kaynia and Kausel. Pile group stiffness constants are formulated for all vibration modes and the group efficiency ratios for the vertical and horizontal vibration of 3 pile groups are calculated at different frequencies. The following conclusions emerge:

1. The effect of pile-soil separation (gapping) on dynamic interaction is to decrease the absolute values of both the real and imaginary parts of the interaction factors.

2. The reduction in interaction factors increase with the pile separation ratio e/d.

3. Dynamic pile-soil-pile interaction reduces the stiffness and increases the damping of pile groups which may have a profound effect on tower response to dynamic loads.

4. Pile group properties vary with frequency more strongly than those of a single pile.

(a) 2 PILES   (b) 4 PILES   (c) 10 PILES
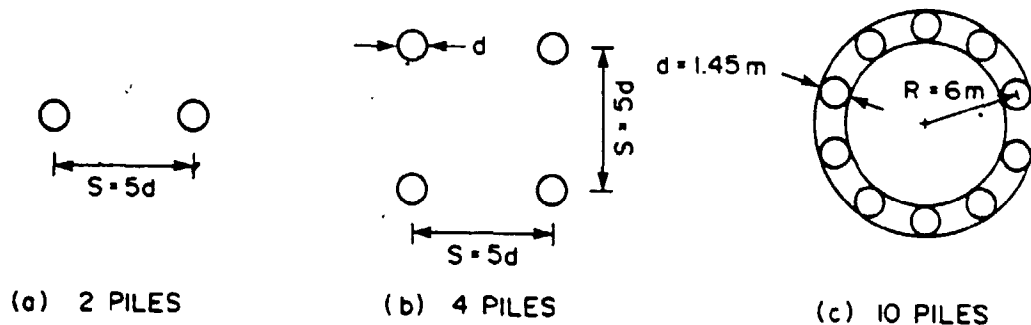
Figure 5-11:   Configuration of the Three Pile Groups Considered
in the Example
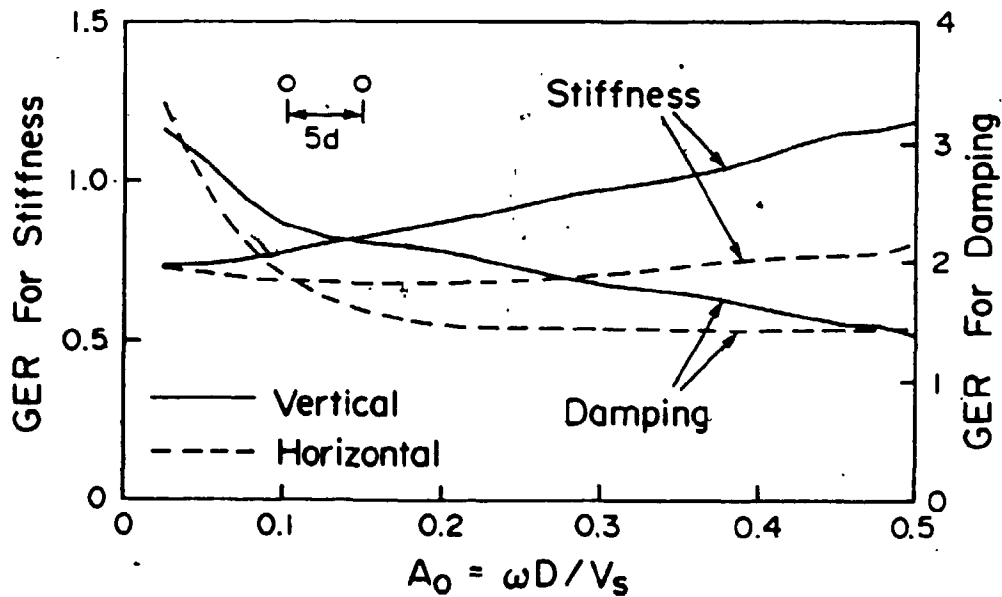
Figure 5-12:   Efficiency Ratio for Stiffness and Damping for
a Group of Two Piles
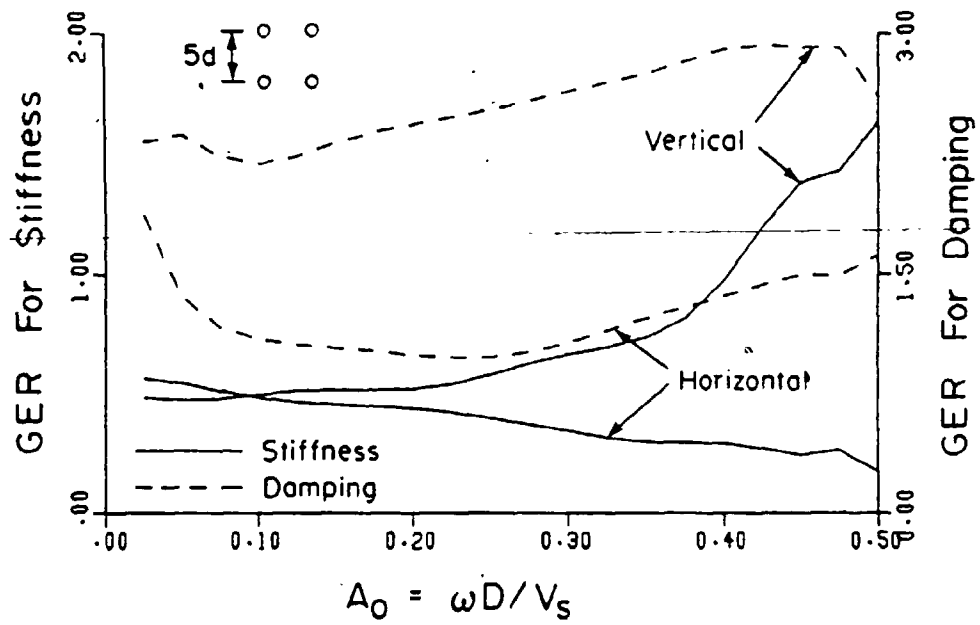
Figure 5-13: Efficiency Ratio for Stiffness and Damping for a Group of Four Piles
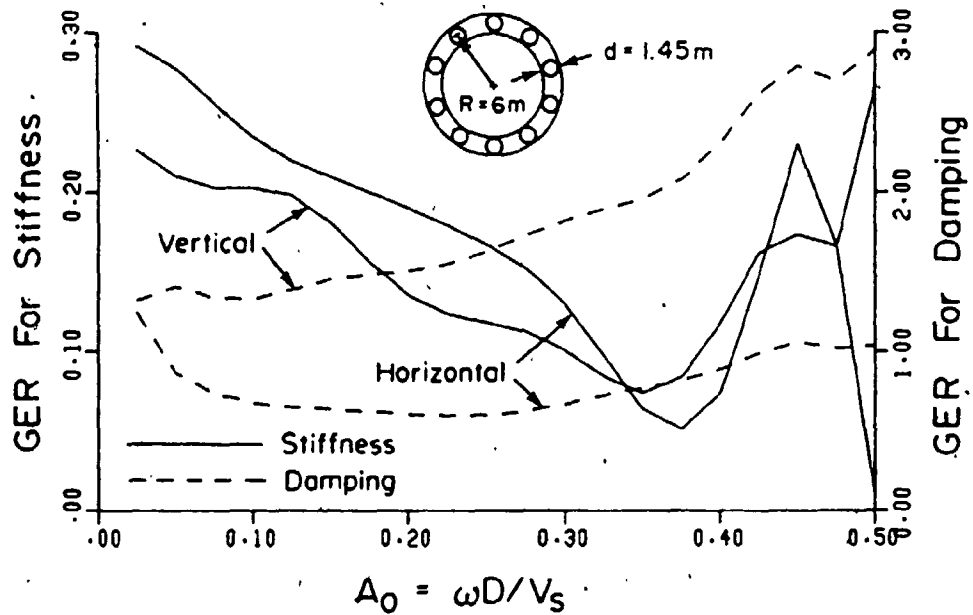
Figure 5-14: Efficiency Ratio for Stiffness and Damping for a Group of Ten Piles

Chapter Six
Wave Forces on Offshore Structures

6.1. Introduction

Estimation of fluid loading on offshore structures due to waves and currents is performed in two main steps. First, the water particle kinematics are evaluated and then using a force theory, wave loads on the specific structure are evaluated.

Early attempts to calculate wave kinematics were based entirely on a regular wave concept. In this approach, the flow kinematics is completely specified, for a given water depth, by the wave height and period. However, real ocean waves are far too irregular to be adequately described by a single progressive wave and a choice is made either to employ a time varying, complex deterministic model with many boundary specifications or to introduce statistical properties into the model. The later approach is more feasible and is implemented by treating the sea surface elevation as a random variable. Wave directionality due to either wind veering or superposition of several storm systems propagating in different directions is accounted for by specifying a directional spectrum for the sea surface elevation.

Methods of estimating wave forces on immersed bodies depend on the size of the body in the incident wave direction (taken as the diameter for cylindrical bodies) relative to the wave length. For small diameter to wave length ratios, Morison's Equation is used to calculate the wave loads, while for large ratios, diffraction effects are important and wave loads have to be calculated using a diffraction theory.

In this chapter, a review of wave loading on offshore structures and the

Important parameters affecting It are given. Effects of wave directionality on the wave force characteristics are examined and an alternative representation of the water particle kinematics spectra is introduced. This alternative representation is based on the use of a coherence function and is thus termed the coherence function model. Wave force estimations obtained using the coherence function model are compared to those obtained using the directional spectrum model to examine the validity of the former approach.

6.2. Review of Wave Loading

Wave theories can be classified into regular and irregular wave theories [118]. *Regular wave theories* describe waves which are periodic in time and space and have a symmetric rigid profile. The main difficulty lies in the nonlinear free surface boundary condition that has to be applied at the instantaneous wave elevation which is initially unknown. The simplest approach is the linear wave theory (Airy theory) in which the free surface boundary condition is linearized by assuming waves of infinitesimal steepness. The resulting wave is a simple harmonic progressive wave with a closed ellipse water particle path. An important feature of the linear wave theory is the dispersion equation which relates the wave phase speed v_c with the spatial and temporal frequencies, κ (wave number) and ω (angular frequency), respectively

$$\omega^2 = g\kappa \, \tanh(\kappa D) \qquad (6.1)$$

or

$$v_c = \frac{g}{\kappa} \, \tanh(\kappa D) \qquad (6.2)$$

where g is the gravity acceleration and D is the water depth, Fig. 6.1. Due to linearity, superposition holds and the linear wave theory links the statistical description of sea surface elevation to sub-surface flow kinematics. The linear wave theory is of fundamental importance in offshore engineering due to its simplicity and validity for all water depth ranges unlike many other wave
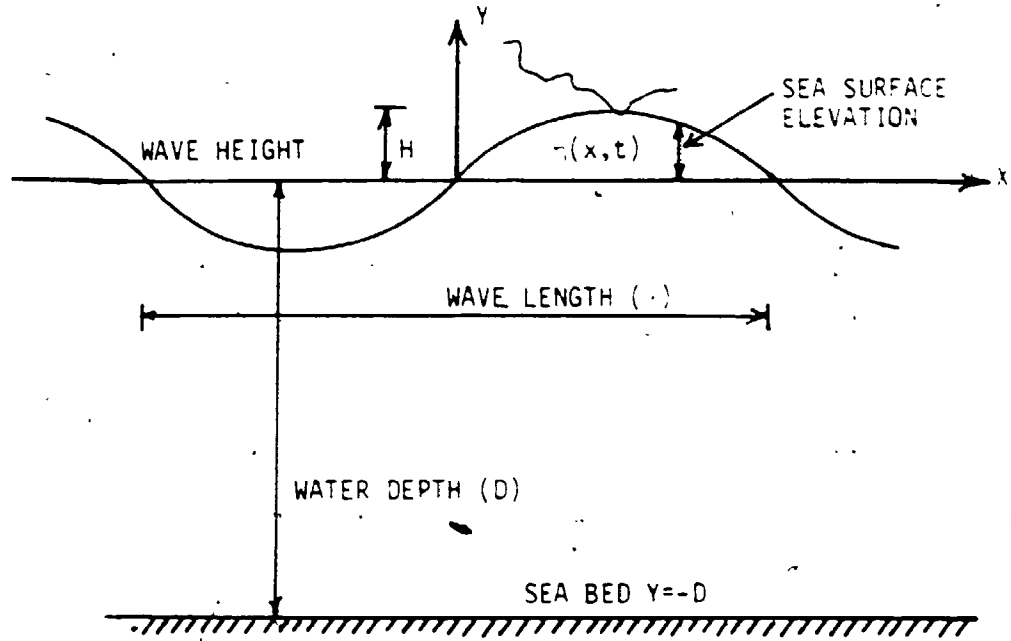
Figure 6-1: Definition Diagram for Wave Parameters
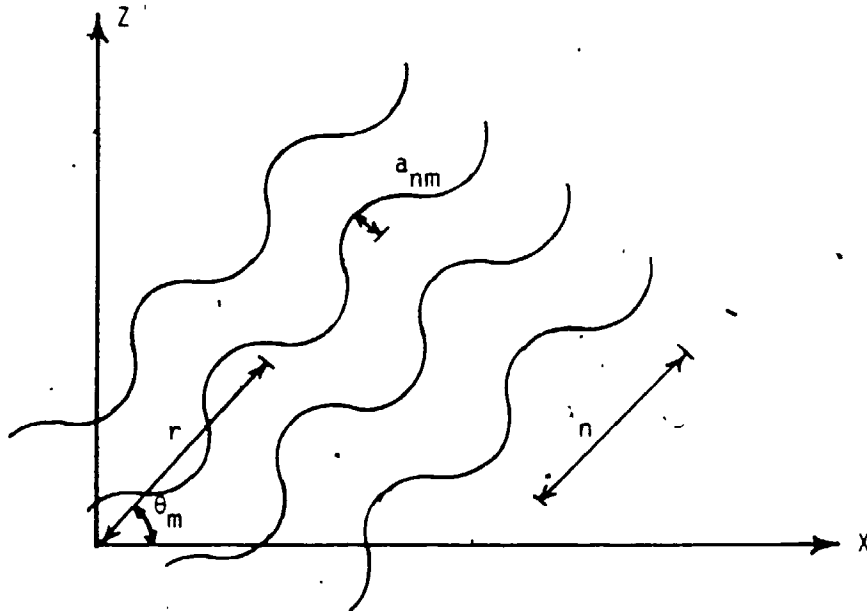
Figure 6-2: Directional Wave System

theories. It is also essential for the investigation of diffraction effects and for the statistical treatment of random waves. Nonlinear approximations have also been adopted, e.g. Stoke's second and fifth order wave theories [119]. Details of the different nonlinear wave theories are given in [120]. Nonlinear wave theories are useful in a pseudo-deterministic analysis of the extreme loading conditions where a design wave with statistically chosen wave height and period is applied to the structure. However, it was shown that application of the regular wave concept in some cases underestimates, while in other cases overestimates the predicted motion of the structure [121].

Irregular wave theories describe irregular waves which are not periodic in time or space. They relate sub-surface kinematics to the completely prescribed surface profile. Linear irregular waves are mainly based on a Fourier analysis of the prescribed surface profile to determine the amplitudes and phases of the harmonic components followed by a linear superposition of a number of linear Airy waves [122]. Examples of nonlinear irregular wave theories are the extended velocity potential theory [123] and the irregular stream function theory [124].

Morison's Equation [125] applies to cylinders of diameter to wave length ratio less than 0.2 ($d/\lambda < 0.2$). This corresponds to the physical assumption that the values of velocities and accelerations are sensibly constant over distances equal to the member diameter [126]. In such cases, both drag and inertia effects are important and the total horizontal fluid force, F, acting on a unit length of a fixed rigid cylinder is given by

$$F = \frac{1}{2}\rho C_D \, d\dot{v}|\dot{v}| + \rho\pi\frac{d^2}{4} C_M \ddot{v} \tag{6.3}$$

where C_D and C_M are the drag and inertia coefficients, ρ is the fluid density and $\dot{v}$ and $\ddot{v}$ are the fluid velocity and acceleration components perpendicular to the cylinder axis, respectively. C_D and C_M depend on Reynolds number

($N_R = \rho \dot{v} d / \mu$ with ρ and μ being the fluid density and viscosity respectively) and Keulegan-Carpenter number ($N_k = \dot{v}_m T / d$ where $\dot{v}_m$ is the mean velocity of the fluid and T is the period of oscillation). Numerous experiments were conducted to estimate the values of C_M and C_D [127-130], however, a wide scatter has been reported by most investigators. A survey of published data for the values of C_D and C_M and their ranges of validity is given in [126]. At high Keulegan-Carpenter numbers, drag forces are more important and the flow is drag dominated while at lower values of N_k, inertia effects are more important and the flow is inertia dominated. The dependency of C_D and C_M on N_k and N_R make them vary with depth and frequency.

For $d/\lambda > 0.2$ the velocity and acceleration of the flow are not constant over a distance equal to the member diameter and the presence of the cylinder causes wave scattering and disturbance of the flow field. *Diffraction analysis* in this case is important where the total force is determined by integrating the pressure evaluated from the superposition of the undisturbed pressure field (Froude-Krylov component) and the pulsating pressure resulting from the disturbance of the flow field [126].

The drag term in Morison's Equation is nonlinear and has to be linearized if the statistical representation of the random wave forces is to be employed. Borgman [131] derived a series representation of the covariance function of the nonlinear drag term. He showed that the series converges quite rapidly and that the error introduced by considering the first term only, which is linear, is quite small [132]. Malhotra and Penzien [133] used the equivalent linearization technique to linearize the drag term and obtained the same expression which results from the first term approximation of Borgman.

Short crested waves observed in ocean wave systems are modeled using the

directional spectrum of sea surface elevation. Recent advances in measuring techniques enabled more data to be gathered and analyzed with the aim of establishing a reliable model for the directional spectrum [134-136]. Use of directional spectrum results in the reduction of along wave forces and allows the prediction of lateral forces [137,138]. For structures comprising a few vertical cylinders, the spectra of wave forces can be obtained by integrating the wave loads over the cylinders [139], however, for structures with several members of different orientations, the member areas and volumes are lumped at the nodes [140].

Vortex excited oscillations, which are particularly important when currents are anticipated, received relatively less attention partly because of the difficulty associated with developing reliable models to estimate such forces. However, studies dealing with this problem indicate that vortex shedding ocurs at a frequency double the wave frequency and, that under lock-in conditions, substantial dynamic amplifications in both, the transverse and the longitudinal directions are produced [141].

In the current study, the linear wave theory is employed to enable the statistical representation of random waves. Wave forces on members of the tower are evaluated using the modified Morison's Equation which accounts for the motion of the cylinder [142]

$$F=\frac{1}{2}\rho C_D d|\dot{v}-\dot{u}|(\dot{v}-\dot{u})+\rho\pi\frac{d^2}{4}[C_M\ddot{v}-(C_M-1)\ddot{u}]$$ (6.4)

where u and u are the acceleration and velocity of the cylinder, respectively. The linearized form of the drag force based on the equivalent linearization technique and employed by many researchers, e.g. [143-145], is used in this study. For a flexible cylinder, the linearized drag force is given by

$$(\dot{v}-\dot{u})|\dot{v}-\dot{u}| = \sqrt{8/\pi}\,\sigma_r(\dot{v}-\dot{u}).$$ (6.5)

where $r = \dot{v} - \dot{u}$ is the relative velocity between the water particle and the cylinder.

6.3. Spectral Density of Water Particle Kinematics

6.3.1. Stationary Gaussian Model of Sea Surface Elevation

In the current study, random waves are represented as a stationary Gaussian process. This model was developed by Rice [146] when studying random noise in electrical circuits and was later applied to ocean waves by several investigators [147-151]. In this model, the sea surface elevation above mean sea level $h(x,t)$ is represented as a sum of many sinusoidal components with different amplitudes and phase angles. For a unidirectional wave system propagating in the X direction, $h(x,t)$ is given by [148]

$$h(x,t) = \sum_{n=1}^{N} a_n \cos(\kappa_n x - \omega_n t + \epsilon_n) \qquad (6.6)$$

where a_n is the amplitude of the nth harmonic component whose frequency and wave number are ω_n and κ_n, respectively, and ϵ_n is the phase angle associated with the nth wave. If ϵ_n is a random variable with a uniform probability density function, i.e.

$$\text{Probability } (\epsilon < \epsilon_n < \epsilon + d\epsilon) = \frac{d\epsilon}{2\pi} \qquad (6.7)$$

and all ϵ_n's are statistically independent, then using the central limit theorem, it can be shown that $h(x,t)$ is a stationary random process and has a Gaussian probability distribution [148].

The mean square value of the nth harmonic component in Eq. 6.6 is $\frac{a_n^2}{2}$ and is also $S_{hh}(\omega_n)\Delta\omega$, where $S_{hh}(\omega_n)$ is the one sided power spectral density of sea surface elevation, accordingly

$$a_n = \sqrt{2S_{hh}(\omega_n)\Delta\omega} \qquad (6.8)$$

and Eq. 6.6 is written as

$$h(x,t) = \sum_{n=1}^{N} \sqrt{2S_{hh}(\omega_n)\Delta\omega}\, \cos(\kappa_n x - \omega_n t + \epsilon_n)$$ (6.9)

If the number of harmonic terms N goes to ∞, $\Delta\omega \to d\omega$, $\omega_n \to \omega$ and $S_{hh}(\omega_n)$ is replaced by the continuous spectrum $S_{hh}(\omega)$ and Eq. 6.9 becomes

$$h(x,t) = \int_0^{\infty} \cos(\kappa x - \omega t + \epsilon)\sqrt{2S_{hh}(\omega)d\omega}$$ (6.10)

Eq. 6.10 represents unidirectional long crested random waves . Such a model is well suited to a swell travelling at some distance from a storm. Within a storm generating area, a more confused sea with short crested waves is more likely to occur. This is accounted for by extending the unidirectional spectrum such that at each frequency, the surface elevation consists of a number of harmonic waves progressing in different directions, Fig. 6.2, and the sea surface elevation is expressed as [148]

$$h(x,z,\theta,t) = \int_{-\pi}^{\pi}\int_0^{\infty} \cos[\kappa(x\cos\theta + z\sin\theta) - \omega t + \epsilon]$$
$$\cdot\sqrt{2S_{hh}(\omega,\theta)d\omega d\theta}$$ (6.11)

In Eq. 6.11, $S_{hh}(\omega,\theta)$ is the sea surface elevation directional spectrum and has the property that the volume $S_{hh}(\omega,\theta)d\omega d\theta$ represents the mean square value of waves progressing in the directions included between θ and $\theta+d\theta$ with frequencies between ω and $\omega+d\omega$.

6.3.2. Power Spectrum of Sea Surface Elevation

When wind blows over a calm sea, waves grow from initial regular long crested waves to irregular short crested ones. This growth takes place either with time (for a fixed fetch) or with fetch (for a fixed time) until a fully developed sea is attained. As waves grow, the wave spectrum also grows and the spectral peak frequency shifts towards successively lower frequencies (longer wave lengths) with the increase in spectral energy [152].

6.3.2.1. Unidirectional Spectrum (Frequency Spectrum)

These are specified for either fully or partially developed seas. Spectra of the first category are expressed in terms of a reference mean wind speed, at 19.5 m above the mean sea level, $\overline{U}$, as the only parameter [153-155]. Spectral forms of the second category account for fetch or fetch and duration [156-158].

- *Pierson-Moskowitz Spectrum* [155]: relates to fully developed seas and is written as

$$S_{hh}(\omega) = \frac{\alpha g^2}{\omega^5} e^{-0.74(\overline{\omega}/\omega)^4} \qquad (6.12)$$

  where $\alpha = 8.1 \times 10^{-3}$ and is termed the Phillips constant, g is the gravity acceleration and $\overline{\omega} = g/\overline{U}$.

- *Bretschneider Spectrum* [156] is given in terms of the significant wave height H_s and the spectral peak frequency ω_o which are in turn obtained from hindcasting relations in terms of the wind speed $\overline{U}$ and fetch and duration of the storm.

- *JONSWAP Spectrum* [157]: provides a modification to the Pierson-Moskowitz spectrum to account for the fetch limited waves and gives a more sharply peaked spectrum.

Other proposed frequency spectra include the six parameter wave spectrum by Ochi and Hubble [158] which is intended to represent almost all stages of development of a sea during a storm.

In this investigation, the Pierson-Moskowitz sea surface elevation spectrum, shown in Fig. 6.3, is used.

6.3.2.2. Directional Spectrum

It is convinient to express the directional spectrum in the form

$$S_{hh}(\omega,\theta) = S_{hh}(\omega)G(\omega,\theta) \qquad (6.13)$$

where $G(\omega,\theta)$ is a directional spread function which represents the distribution of wave energy among waves progressing in different directions. It satisfies the following relationship
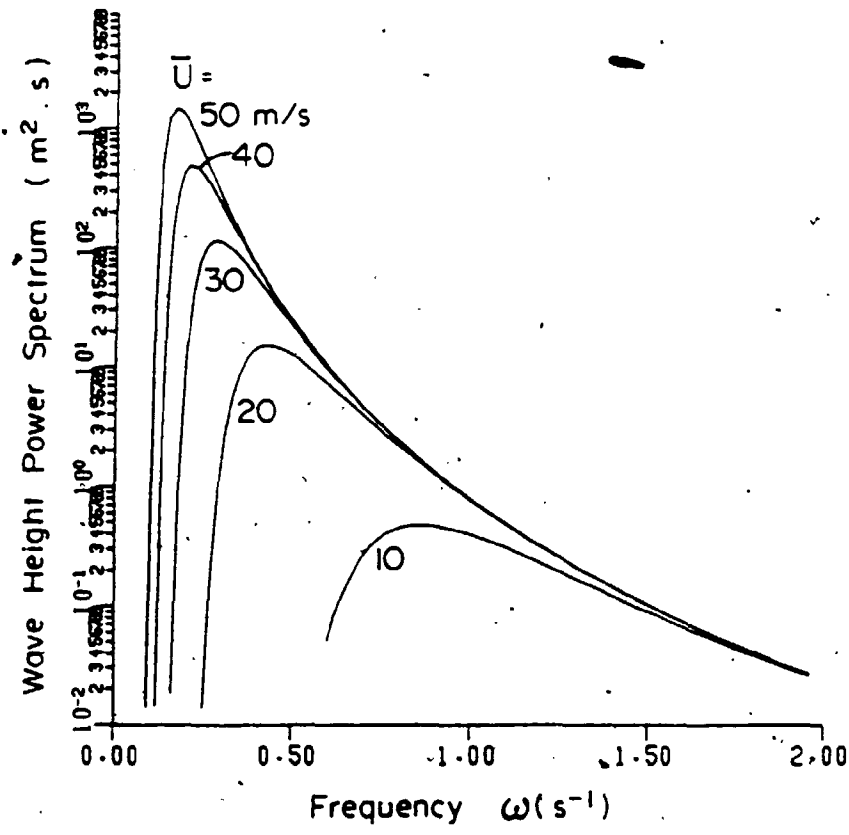
Figure 6-3: Pierson-Moskowitz Spectrum of Sea Surface Elevation

$$(6.14)$$

$$\int_{-\pi}^{\pi} G(\omega,\theta)d\theta = 1$$

The directional spread function is always positive and is symmetric about the mean direction of wave advance $\overline{\theta}$. Various expressions have been suggested for $G(\omega,\theta)$ some of which are described in [159].

- *St. Denis and Pierson* [148]: proposed a cosine squared form given by

$$G(\omega,\theta) = \begin{cases} \dfrac{2}{\pi} & \text{for } |\theta| < \pi/2 \\ 0 & \text{otherwise} \end{cases} \qquad (6.15)$$

where the mean direction of wave advance is $\overline{\theta} = 0$. This form does not provide for variation in concentration about the mean direction.

- *Longuet-Higgins, Cartwright and Smith* [160] suggested a cosine power expression given by

$$G(\theta) = C(S)\cos^{2S}[\tfrac{1}{2}(\theta - \overline{\theta})] \qquad (6.16)$$

In Eq. 6.16, $C(S)$ is a normalized function to ensure that Eq. 6.14 is satisfied, namely

$$C(S) = \frac{1}{2\sqrt{\pi}} \frac{\Gamma(S+1)}{\Gamma(S+1/2)} \qquad (6.17)$$

where Γ is the gamma function and S is a parameter expressing the degree of spread about $\overline{\theta}$

- *Borgman* [159] suggested the wrapped around normal and the circular normal spreading functions. The later was used by Berge [161] to evaluate wave forces on offshore towers. The circular normal directional spreading function is given by

$$G(\theta) = \frac{1}{2\pi I_o(a)} e^{a\cos(\theta - \overline{\theta})} \qquad (6.18)$$

where I_o is the modified Bessel function of the first kind of order zero and a expresses the degree of spread; higher values of a indicate higher concentration about $\overline{\theta}$. Other directional spread functions include a weighted Fourier Series representation [160], given by

$$G(\theta) = \frac{1}{2\pi} + \sum_{n=1}^{N} W_n[a_n\cos(n\theta) + b_n\sin(n\theta)] \qquad (6.19)$$

where W_n are weighting coefficients to enable the use of a limited number of Fourier coefficients instead of the infinite series.

The angular spread is not constant for all frequencies; it is very narrow around the spectral peak frequencies and widens rapidly towards higher and lower frequencies [134]. The spreading functions mentioned above could be made frequency dependent by choosing the parameters S or a to be so. A frequency dependent directional spreading function was proposed by Cote et al. [162].

In this study, the circular normal spread function, Eq. 6.18, is used. The directional spread parameter a is arbitrarily made frequency dependent using the relationship

$$a = \begin{cases} \overline{a}[1 - 0.25(\overline{\omega} - \omega)/\overline{\omega}] & \text{for} \quad 0 < \omega < \overline{\omega} \\ \overline{a}[1 - 0.5(\omega - \overline{\omega})/(\omega_{max} - \overline{\omega})] & \text{for} \quad \overline{\omega} < \omega < \omega_{max} \end{cases} \qquad (6.20)$$

In Eq. 6.20, $\overline{\omega}$ is the spectral peak frequency, ω_{max} is arbitrarily set to a high value at the low energy content of the spectrum. For $\mho = 20$ m/sec, ω_{max} is chosen as 5 rad/sec and $\overline{a}$ is the value of a at $\omega = \overline{\omega}$. The higher the value of $\overline{a}$, the more concentrated the spectrum is around the mean direction of wave advance, $\overline{\theta}$. Shown in Fig. 6.4 is the Circular Normal Directional Distribution function plotted for different values of $\overline{a}$ and at $\omega = \overline{\omega}$.

6.3.3. Water Particle Kinematics Spectra

In the following, spectra of water particles kinematics are derived based on the stationary Gaussian model of random waves discussed in Subsection 6.3.1. Cross spectrum of water particle velocities in the X direction at any 2 points in a directional wave system is derived in detail. A general expression that can be adapted to the cross spectra of other velocity components is then given. Cross
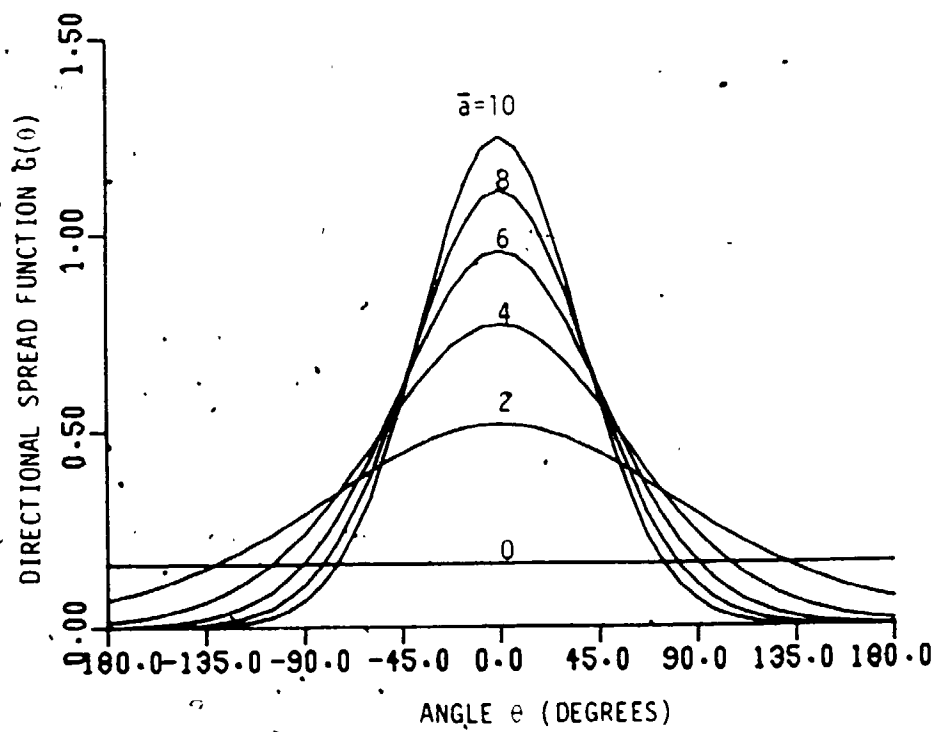
Figure 6-4: Circular Normal Directional Spread Function

spectra for a unidirectional wave system can be similarly derived and only the final expression is given.

An alternative representation of the water particle kinematics based on the use of a coherence function is then introduced. This alternative approach, which is termed the coherence function model, is employed in Section 6.6 to evaluate wave forces on cylindrical members of offshore towers.

6.3.3.1. Directional Spectrum Model

The contribution to sea surface elevation from waves advancing in direction θ_m with frequency ω_n and amplitude a_{nm}, Fig. 6.2, is given by

$$h_{nm} = a_{nm}\cos(\kappa_n r - \omega_n t + \epsilon_{nm}) \tag{6.21}$$

where r is measured in reference to a fixed origin in the direction of wave advance. The mean square value of the sea surface elevation h_{nm} during one cycle is

$$\sigma^2_{h_{nm}} = \frac{a^2_{nm}}{2} = S_{hh}(\omega_n, \theta_m)\Delta\omega\Delta\theta \tag{6.22}$$

therefore a_{nm} is

$$a_{nm} = \sqrt{2S_{hh}(\omega_n, \theta_m)\Delta\omega\Delta\theta} \tag{6.23}$$

The polar coordinate r is expressed in terms of cartesian coordinates as

$$r = x\cos\theta_m + z\sin\theta_m \tag{6.24}$$

From Airy wave theory, the contribution to the horizontal velocity at depth y from such waves is

$$\dot{v}_{nm} = \omega_n\frac{\cosh\kappa_n(y+D)}{\sinh\kappa_n D}h_{nm} \tag{6.25}$$

and the horizontal velocity component in direction x is written as

$$\dot{v}_{nm(x)} = \dot{v}_{nm}\cos\theta_m \tag{6.26}$$

From Eqs. 6.21 and 6.23 to 6.25, Eq. 6.26 is written as

$$\dot{v}_{nm(x)} = \omega_n\frac{\cosh\kappa_n(y+D)}{\sinh\kappa_n D}\sqrt{2S_{hh}(\omega_n, \theta_m)\Delta\omega\Delta\theta} \tag{6.27}$$

$$.\cos[\kappa_n(x\cos\theta_m + z\sin\theta_m) - \omega_n t + \epsilon_{nm}]\cos\theta_m$$

and the total horizontal velocity associated with waves progressing with N different frequencies and from M different directions, at each discrete frequency, is given by

$$\dot{v}_x(t) = \sum_{n=1}^{N} \sum_{m=1}^{M} \omega_n \frac{\cosh \kappa_n(y+D)}{\sinh \kappa_n D} \sqrt{2S_{hh}(\omega_n, \theta_m)\Delta\omega\Delta\theta}$$

$$.\cos[\kappa_n(x\cos\theta_m + z\sin\theta_m) - \omega_n t + \epsilon_{nm}]\cos\theta_m \qquad (6.28)$$

As N and M go to ∞, $\Delta\omega \to d\omega$ and $\Delta\theta \to d\theta$ and Eq. 6.28 becomes

$$\dot{v}_x(t) = \int_0^\infty \int_0^{2\pi} \omega \frac{\cosh \kappa(y+D)}{\sinh \kappa D} \sqrt{2S_{hh}(\omega,\theta)\, d\omega\, d\theta}$$

$$.\cos[\kappa(x\cos\theta + z\sin\theta) - \omega t + \epsilon]\cos\theta \qquad (6.29)$$

To obtain the cross spectrum of water particle velocities at any 2 points, their cross correlation function is first evaluated and then Fourier transformed. The cross correlation function of horizontal velocities in the X direction at any 2 points in the flow field is written as

$$R_{\dot{v}_{x1}\dot{v}_{x2}}(\tau) = \langle \dot{v}_{x1}(t)\dot{v}_{x2}(t+\tau) \rangle \qquad (6.30)$$

where $\langle \ \rangle$ indicates the mean value and τ is the time lag for which the cross correlation function is evaluated, i.e.

$$R_{\dot{v}_{x1}\dot{v}_{x2}}(\tau) = \int_0^\infty \int_0^{2\pi} \omega^2 \frac{\cosh\kappa(y1+D)\cosh\kappa(y2+D)}{\sinh^2\kappa D} \qquad (6.31)$$

$$.2S_{hh}(\omega,\theta) \langle \cos[\kappa(x1\cos\theta + z1\sin\theta) - \omega t + \epsilon]$$

$$.\cos[\kappa(x2\cos\theta + z2\sin\theta) - \omega t - \omega\tau + \epsilon] \rangle \cos^2\theta\ d\theta d\omega$$

where $x1$, $y1$, $z1$ and $x2$, $y2$ and $z2$ are the cartesian coordinates of points 1 and 2, respectively. Using trigonometric identities, and after some manipulations, it can be shown that

$$\langle \cos[\kappa(x1\cos\theta + z1\sin\theta) - \omega t + \epsilon] \qquad (6.32)$$

$$.\cos[\kappa(x2\cos\theta + z2\sin\theta) - \omega t - \omega\tau + \epsilon] \rangle =$$

$$\frac{1}{2}\cos[\kappa(x1-x2)\cos\theta + \kappa(z1-z2)\sin\theta + \omega\tau]$$

In Eq. 6.31, $S_{hh}(\omega,\theta)$ is the one sided spectrum (extending from 0 to ∞) and is related to the two sided spectrum $\overline{S}_{hh}(\omega,\theta)$ by

$$S_{hh}(\omega,\theta) = 2\overline{S}_{hh}(\omega,\theta) \tag{6.33}$$

From Eqs. 6.31 to 6.33, the cross correlation function becomes

$$R_{\dot{v}_{x1}\dot{v}_{x2}}(\tau) = \int_0^\infty \int_0^{2\pi} 2\omega^2 \frac{\cosh \kappa(y1+D)\cosh \kappa(y2+D)}{\sinh^2 \kappa D} \overline{S}_{hh}(\omega,\theta) \tag{6.34}$$
$$\cos[\kappa(x1-x2)\cos\theta + \kappa(z1-z2)\sin\theta + \omega\tau]\cos^2\theta \; d\theta d\omega$$

The limits of the integration in Eq. 6.34 can be extended from $-\infty$ to ∞ because ω^2, cosh, $\sinh^2$, $\overline{S}_{hh}$ and cos are even functions, i.e.

$$R_{\dot{v}_{x1}\dot{v}_{x2}}(\tau) = \int_{-\infty}^\infty \int_0^{2\pi} \omega^2 \frac{\cosh \kappa(y1+D)\cosh \kappa(y2+D)}{\sinh^2 \kappa D} \overline{S}_{hh}(\omega,\theta) \tag{6.35}$$
$$\cos[\kappa(x1-x2)\cos\theta + \kappa(z1-z2)\sin\theta + \omega\tau]\cos^2\theta \; d\theta d\omega$$

Using Euler's formula

$$\cos A = e^{iA} - i\sin A \tag{6.36}$$

Eq. 6.35 can be written as

$$R_{\dot{v}_{x1}\dot{v}_{x2}}(\tau) = \int_{-\infty}^\infty \int_0^{2\pi} \omega^2 \frac{\cosh \kappa(y1+D)\cosh \kappa(y2+D)}{\sinh^2 \kappa D} \overline{S}_{hh}(\omega,\theta) \tag{6.37}$$
$$.\{e^{i[\kappa(x1-x2)\cos\theta + \kappa(z1-z2)\sin\theta + \omega\tau]}$$
$$- i\sin[\kappa(x1-x2)\cos\theta + \kappa(z1-z2)\sin\theta + \omega\tau]\}\cos^2\theta d\theta d\omega$$

since the sine function in Eq. 6.37 is an odd function of ω, the third term in Eq. 6.37 is zero and

$$R_{\dot{v}_{x1}\dot{v}_{x2}}(\tau) = \int_{-\infty}^\infty \{\int_0^{2\pi} \omega^2 \frac{\cosh \kappa(y1+D)\cosh \kappa(y2+D)}{\sinh^2 \kappa D} \overline{S}_{hh}(\omega,\theta) \tag{6.38}$$
$$.e^{i[\kappa(x1-x2)\cos\theta + \kappa(z1-z2)\sin\theta]}\cos^2\theta \; d\theta\} e^{i\omega\tau} d\omega$$

but $R_{\dot{v}_{x1}\dot{v}_{x2}}(\tau) = \int_{-\infty}^\infty S_{\dot{v}_{x1}\dot{v}_{x2}}(\omega)e^{i\omega\tau}d\omega$ and the cross spectral density is given by

$$S_{\dot{v}_{x1}\dot{v}_{x2}}(\omega) = \omega^2 \frac{\cosh \kappa(y1+D)\cosh \kappa(y2+D)}{\sinh^2 \kappa D} \int_0^{2\pi} \overline{S}_{hh}(\omega,\theta) \tag{6.39}$$
$$e^{i\kappa[(x1-x2)\cos\theta + (z1-z2)\sin\theta]}\cos^2\theta d\theta$$

The cross spectra of the other velocity components can be derived similarly and the final formula is given by the general expression

$$S_{\dot{v}_1\dot{v}_2}(\omega) = \omega^2 \frac{\overline{S}_{hh}(\omega)}{\sinh^2\kappa D} HYP1[\kappa(y1+D)] HYP2[\kappa(y2-D)] \tag{6.40}$$

$$\int_{-\pi}^{\pi} G(\omega,\theta) C1(\theta) C2(\theta)$$

$$.e^{i\kappa[(x1-x2)\cos\theta - (z1-z2)\sin\theta]} d\theta$$

where

$$C1(\theta) = \begin{cases} \cos\theta & \text{for } 1 \,//\, X \\ \sin\theta & \text{for } 1 \,//\, Z \\ 1 & \text{for } 1 \,//\, Y \end{cases} \tag{6.41}$$

in which $1 \,//\, X$ indicates velocity component at point 1 to be in the X direction, with similar definitions for $1 \,//\, Y$ and $1 \,//\, Z$. $C2(\theta)$ is similarly defined for velocity component at point 2. Finally,

$$HYP1[\kappa(y1+D)] = \begin{cases} \cosh[\kappa(y1+D)] & \text{for } 1 \,//\, X \text{ or } 1 \,//\, Z \\ -i\sinh[\kappa(y1+D)] & \text{for } 1 \,//\, Y \end{cases} \tag{6.42}$$

and

$$HYP2[\kappa(y2+D)] = \begin{cases} \cosh[\kappa(y2+D)] & \text{for } 2 \,//\, X \text{ or } 2 \,//\, Z \\ i\sinh[\kappa(y2+D)] & \text{for } 2 \,//\, Y \end{cases} \tag{6.43}$$

Cross spectral densities of water particle accelerations can be obtained from those of the velocities, i.e.

$$S_{\dot{v}_1\ddot{v}_2}(\omega) = i\omega S_{\dot{v}_1\dot{v}_2}(\omega) = S_{\ddot{v}_1\dot{v}_2}^{*}(\omega) \tag{6.44}$$

and

$$S_{\ddot{v}_1\ddot{v}_2}(\omega) = \omega^2 S_{\dot{v}_1\dot{v}_2}(\omega) \tag{6.45}$$

in which the asterisk means the complex conjugate. The general expression in Eq. 6.40 is the same as that derived by Berge[161].

Cross spectra of water particle kinematics of unidirectional wave systems can be derived similarly and the formulae are given in [133] and [151]. The general expression for cross spectra of water particle velocities of a unidirectional fully-correlated wave system progressing in a mean direction that makes an angle $\overline{\theta}$ with the X axis is

$$S_{\dot{v}_1 \dot{v}_2}(\omega) = \omega^2 \frac{\overline{S}_{hh}(\omega)}{\sinh^2 \kappa D} C1(\overline{\theta}) C2(\overline{\theta}) \quad (6.46)$$

$$\cdot HYP1[\kappa(y1 + D)] HYP2[\kappa(y2 + D)]$$

$$\cdot e^{i\kappa[(z1 - z2)\cos\overline{\theta} - (z1 - z2)\sin\overline{\theta}]}$$

where $C1(\overline{\theta})$ and $C2(\overline{\theta})$ are given by Eq. 6.41. If θ is substituted by $\overline{\theta}$, and $HYP1[\kappa(y1 + D)]$ and $HYP2[\kappa(y2 + D)]$ are given by Eqs. 6.42 and 6.43, respectively.

6.3.3.2. Coherence Function Model

In the preceding discussion, a confused sea with short crested waves was modeled as a three dimensional stationary Gaussian random process. One of the main features of this model is that the total in-line (along wave) force on any member of the tower is less than that of a unidirectional wave system having the same total energy as part of this total energy produces lateral forces. Another reason for the reduction in the along wave forces is that the wave forces are not in phase along the entire length of the member. This second factor is termed the lack of spatial correlation and has been briefly discussed by Malhotra and Penzien [133] who introduced the spatial cross correlation factor. However, the spatial cross correlation factor of Malhotra and Penzien was derived for a tributary area and not for line members.

The cross spectra of water particle velocity of the unidirectional fully correlated model, employed by several investigators is expressed by Eq. 6.45. For example, in the X direction, Eq. 6.45 takes on the form

$$S_{\dot{v}_{x1} \dot{v}_{x2}}(\omega) = \omega^2 \frac{\cosh \kappa(y1 + D) \cosh \kappa(y2 + D)}{\sinh^2 \kappa D} \overline{S}_{hh}(\omega) \quad (6.47)$$

$$\cdot e^{i\kappa[(z1 - z2)\cos\theta - (z1 - z2)\sin\theta]} \cos^2\theta$$

As can be seen from Eq. 6.47, the cross spectrum of water particle velocity at two

points separated by a distance Δr varies harmonically with a constant amplitude, i.e. with no attenuation. This situation is unrealistic since for short crested waves, the amplitude of the cross spectrum of wave forces attenuates with increased separation. To account for this factor in the present study, lack of spatial correlation is accounted for through a coherence function and the cross-spectrum of water particle velocity is given by

$$S_{\dot{r}_1 \dot{r}_2}(\omega) = \{S_{\dot{r}_1 \dot{r}_2}(\omega)_{fullycorrelated}\} \cdot R \tag{6.48}$$

where R is the square root of the coherence function. Several empirical expressions can be used for the coherence function. In this study, the form analogous to that used for atmospheric turbulence is applied, i.e.

$$R = e^{-c \frac{\Delta r}{\lambda}} \tag{6.49}$$

where c is an exponential decay factor. Δr is the absolute value of the distance between the 2 points and λ is the wave length. The exponential decay factor c is to be determined from laboratory experiments or, preferably, from full scale measurements.

Physically, a wave system whose cross spectrum of water particle velocity is defined by Eq. 6.48 comprises an infinite number of waves each having a different frequency and a random phase angle. All the properties of the unidirectional model are retained except that each wave front is not fully correlated along a line perpendicular to the direction of wave advance.

6.4. Wave Forces on Members of Offshore Towers

With the cross spectral densities of water particle velocities and accelerations defined, the spectra of wave forces on a typical joint of an offshore tower can be formulated.

Consider an offshore tower idealized as a space frame whose coordinate system is shown in Fig. 6.5, where X, Y and Z are the global axes and x, y and z
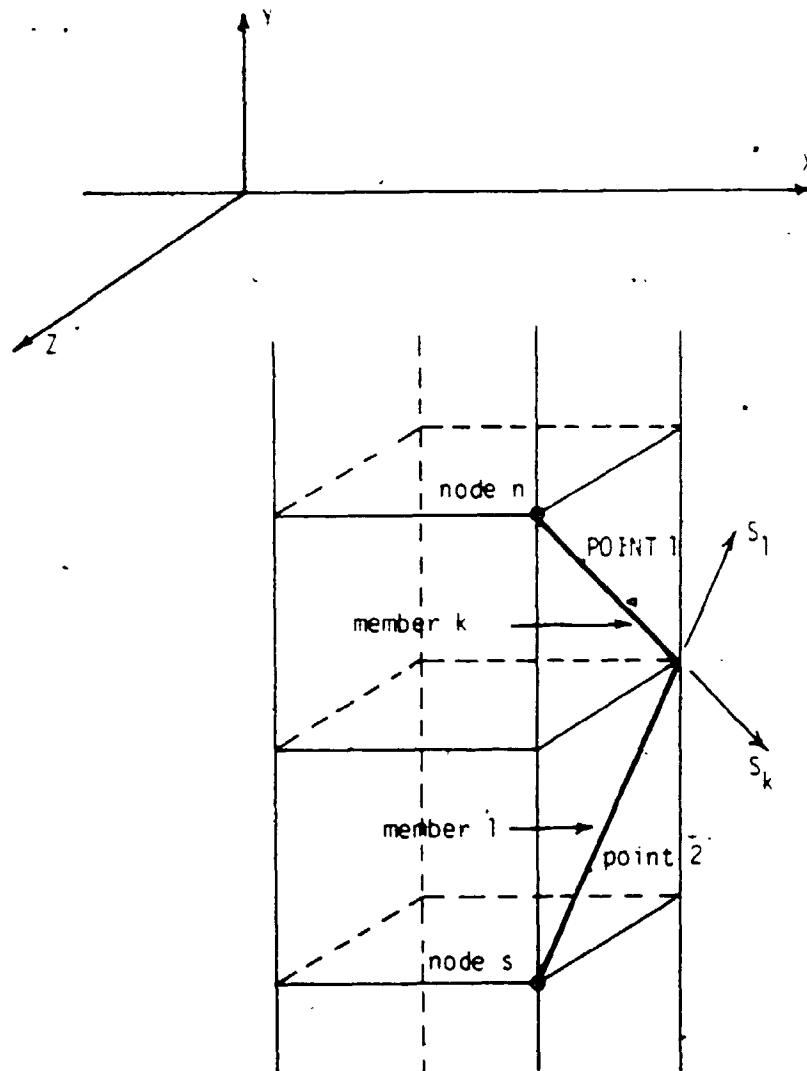
Figure 6-5: Coordinate System for Offshore Tower

are the global coordinates. After static condensation, each joint has 3 translational d.o.f. Let d.o.f. i be positioned at node n at which N_n members meet. Also let p_k, q_k and r_k be the direction cosines of the kth member, which is attached to joint n, with axes X, Y and Z, respectively, and S_k be its element coordinate such that

$$p_k = \frac{x - x_n}{S_k}$$ (6.50)

$$q_k = \frac{y - y_n}{S_k}$$

$$r_k = \frac{z - z_n}{S_k}$$

where x_n, y_n and z_n are the global coordinates of node n. Notice that S_k is always positive and its value for any point on the member represents the distance between that point and the joint. Using the modified Morison's Equation, Eq. 6.4, the wave force $W_i(t)$ acting on the structure, corresponding to d.o.f. i is

$$W_i(t) = \sum_{k=1}^{N_n} \Gamma_k \int_0^{L_k} \{\rho\pi\frac{d_k^2}{4}C_M(S_k)\ddot{v}(S_k,t)$$ (6.51)

$$-\rho\pi\frac{d_k^2}{4}[C_M(S_k)-1]\ddot{u}(S_k,t)$$

$$+\frac{1}{2}\rho d_k C_D(S_k)|\dot{v}(S_k,t)-\dot{u}(S_k,t)|[\dot{v}(S_k,t)-\dot{u}(S_k,t)]\}dS_k$$

where d_k and L_k are the diameter and tributary length of member k, respectively. Finally,

$$\Gamma_k = \sqrt{q_k^2 + r_k^2} \quad \text{for } i//X$$ (6.52)

$$\sqrt{p_k^2 + r_k^2} \quad \text{for } i//Y$$

$$\sqrt{p_k^2 + q_k^2} \quad \text{for } i//Z$$

Since d.o.f. i may be in the X, Y or Z direction, $\dot{u}$, $\ddot{u}$, $\dot{v}$ and $\ddot{v}$ are understood to be the velocity and acceleration components in the same direction as d.o.f. i.

Eq. 6.51 is the general form for wave forces on a typical joint and can be greatly simplified if C_D and C_M are assumed to be constant. To facilitate the evaluation of wave forces, u and $\ddot{u}$ are taken to be constant along the tributary length and equal to their values at the nodes, $\dot{u}_i$ and $\ddot{u}_i$, respectively. For a very long element, additional nodes on the element may be introduced to justify this assumption. For the purpose of evaluating the hydrodynamic damping, the water particle velocity in the third term is taken as constant. With the above assumptions, Eq. 6.51 simplifies to

$$W_i^{\cdot}(t) = \sum_{k=1}^{N_n} \Gamma_k \int_0^{l_k} \{ \rho\pi \frac{d_k^2}{4} C_M \ddot{u}(S_k,t) - \rho\pi \frac{d_k^2}{4}(C_M - 1)\ddot{u}_i(t) \qquad (6.53)$$
$$+ \frac{1}{2}\rho d_k C_D |\dot{v}_i(t) - \dot{u}_i(t)|(\dot{v}_i(t) - \dot{u}_i(t))\} dS_k$$

The drag term is linearized using Eq. 6.5 and Eq. 6.53 becomes

$$W_i^{\cdot}(t) = \sum_{k=1}^{N_n} \Gamma_k [\int_0^{l_k} \{ \rho\pi \frac{d_k^2}{4} C_M \ddot{u}(S_k,t) \qquad\qquad (6.54)$$
$$+ \frac{1}{2}\rho d_k C_D \sqrt{8/\pi}\, \sigma_{r_i} \dot{u}(S_k,t)\} dS_k$$

$$- \rho\pi \frac{d_k^2}{4}(C_M - 1)L_k \ddot{u}_i(t)$$

$$- \frac{1}{2}\rho d_k C_D \sqrt{8/\pi}\, \sigma_{r_i} L_k \dot{u}_i(t)]$$

where σ_{r_i} is the standard deviation of the relative velocity, associated with d.o.f. i, between the water particle and the structure. The third and fourth terms are the added mass and hydrodynamic damping, respectively, and to be transfered to the other side of the equation of motion. Hence, the effective force associated with d.o.f. i, $P_i(t)$, is

$$P_i(t) = \sum_{k=1}^{N_n} \Gamma_k \int_0^{l_k} \{ \alpha_k \ddot{u}(S_k,t) + \beta_k \sigma_{r_i} \dot{u}(S_k,t)\} dS_k \qquad (6.55)$$

where

$$\alpha_k = \rho\pi\frac{d_k^2}{4}C_M \tag{6.56}$$

and

$$\beta_k = \frac{1}{2}\rho d_k C_D\sqrt{8/\pi} \tag{6.57}$$

The cross spectrum of the nodal loads associated with d.o.f i and m, $S_{P_i P_m}(\omega)$, is evaluated as the Fourier transform of their cross correlation function. This process yields

$$S_{P_i P_m}(\omega) = \sum_{k=1}^{N_n}\sum_{l=1}^{N_s}\Gamma_k\Gamma_l\int_0^{l_k}\int_0^{l_l}\{\alpha_k\alpha_l S_{\ddot{r}_1\ddot{r}_2}(S_k,S_l,\omega) \tag{6.58}$$
$$+ \alpha_k\beta_l\sigma_{\dot{r}_m}S_{\ddot{r}_1\dot{r}_2}(S_k,S_l,\omega) + \beta_k\alpha_l\sigma_{\dot{r}_1}S_{\dot{r}_1\ddot{r}_2}(S_k,S_l,\omega)$$
$$+ \beta_k\beta_l\sigma_{\dot{r}_1}\sigma_{\dot{r}_m}S_{\dot{r}_1\dot{r}_2}(S_k,S_l,\omega)\}dS_l dS_k$$

where the subscripts 1 and 2 refer to any two points falling on members k and l, respectively. L_l and S_l are the tributary length and element coordinate, respectively, of the lth member attached to joint s, at which N_s members meet. Γ_l is given by

$$\Gamma_l = \sqrt{q_l^2 + r_l^2} \qquad \text{for } m//X \tag{6.59}$$

$$\sqrt{p_l^2 + r_l^2} \qquad \text{for } m//Y$$

$$\sqrt{p_l^2 + q_l^2} \qquad \text{for } m//Z$$

where p_l, q_l and r_l are the direction cosines of member l with axes X, Y and Z, respectively, and are given by

$$p_l = (x - x_s)/S_l \tag{6.60}$$
$$q_l = (y - y_s)/S_l$$
$$r_l = (z - z_s)/S_l$$

On substituting by Eqs. 6.44 and 6.45, Eq. 6.58 yields

$$S_{P_i P_m} = \sum_{k=1}^{N_n} \sum_{l=1}^{N_s} \Gamma_k \Gamma_l \int_0^{l_k} \int_0^{l_l} \{ \omega^2 \alpha_k \alpha_l S_{\dot{v}_1 \dot{v}_2}(S_k, S_l, \omega)$$

$$+ \alpha_k \beta_l \sigma_{\dot{r}_m} [\iota \omega S_{\dot{v}_1 \dot{v}_2}(S_k, S_l, \omega)]^*$$

$$+ \iota \omega \beta_k \alpha_l \sigma_{\dot{r}_i} S_{\dot{v}_1 \dot{v}_2}(S_k, S_l, \omega)$$

$$+ \beta_k \beta_l \sigma_{\dot{r}_i} \sigma_{\dot{r}_m} S_{\dot{v}_1 \dot{v}_2}(S_k, S_l, \omega) \} dS_l dS_k \qquad (6.61)$$

After rearranging the terms in Eq. 6.61, the cross spectrum of nodal loads can be written as

$$S_{P_i P_m} = \sum_{k=1}^{N_n} \sum_{l=1}^{N_s} \Gamma_k \Gamma_l \{ G_{kl}(\omega) I_{kl} + \alpha_k \beta_l \sigma_{\dot{r}_m} [\iota \omega I_{kl}]^* \} \qquad (6.62)$$

where

$$G_{kl}(\omega) = \alpha_k \alpha_l \omega^2 + \iota \omega \beta_k \alpha_l \sigma_{\dot{r}_i} + \beta_k \beta_l \sigma_{\dot{r}_i} \sigma_{\dot{r}_m} \qquad (6.63)$$

and

$$I_{kl} = \int_0^{l_k} \int_0^{l_l} S_{\dot{v}_1 \dot{v}_2}(S_k, S_l, \omega) dS_l dS_k \qquad (6.64)$$

The standard deviations of the relative velocities, $\sigma_{\dot{r}_i}$ and $\sigma_{\dot{r}_m}$ can not be obtained until the response is evaluated, hence they are evaluated in an iterative procedure. In the first iteration, the structural velocities are assumed to be zero, so that $\dot{r}_i = \dot{v}_i$ and $\dot{r}_m = \dot{v}_m$ and all the variables in Eq. 6.62 are known. The cross spectra of nodal loads, for given values of $\alpha - s$ and $\beta - s$ thus depend on the integrals of the cross spectra of water particle velocities along the members, I_{kl}.

6.5. Directional Spectrum Model

6.5.1. Formulation of Wave Forces

In this model, the spectra of water particle velocities are obtained from the general expression of Eq. 6.40. To evaluate the integrals I_{kl} in Eq. 6.64, the expressions for $S_{\dot{v}_1 \dot{v}_2}(\omega)$ need to be written in terms of the element coordinates S_k and S_l. The coordinates $x1, y1, z1$ and $x2, y2, z2$ are related to S_k and S_l by

$$x1 = x_n + p_k S_k \qquad x2 = x_s + p_l S_l \tag{6.65}$$
$$y1 = y_n + q_k S_k \qquad y2 = y_s + q_l S_l$$
$$z1 = z_n + r_k S_k \qquad z2 = z_s + r_l S_l$$

In this section, the expression for I_{kl} is given only for the case when both velocity components are in the X direction and is termed $I_{k_x l_x}$, i.e.

$$I_{k_x l_x} = I_{kl} \quad \text{for } i//X \text{ and } m//X \tag{6.66}$$

The expressions for all other cases are given in Appendix B. On substitution by Eqs. 6.65 and 6.40, Eq. 6.64 yields

$$I_{k_x l_x} = \omega^2 \frac{\overline{S}_{hh}(\omega)}{4\sinh^2 \kappa D} \int_{-\pi}^{\pi} G(\omega,\theta) e^{i\kappa[(x_n - x_s)\cos\theta + (z_n - z_s)\sin\theta]} \tag{6.67}$$

$$\cdot \left\{ \int_0^{l_k} (e^{\Lambda_n + \kappa S_k(q_k + ip_k\cos\theta + ir_k\sin\theta)} \right.$$

$$+ e^{-\Lambda_n + \kappa S_k(-q_k + ip_k\cos\theta + ir_k\sin\theta)})dS_k \}$$

$$\cdot \left\{ \int_0^{l_l} (e^{\Lambda_s + \kappa S_l(q_l - ip_l\cos\theta - ir_l\sin\theta)} \right.$$

$$+ e^{-\Lambda_s + \kappa S_l(-q_l - ip_l\cos\theta - ir_l\sin\theta)})dS_l \} \cos^2\theta d\theta$$

where

$$\Lambda_n = \kappa(y_n + D) \tag{6.68}$$

and

$$\Lambda_s = \kappa(y_s + D) \tag{6.69}$$

Denote

$$\varsigma = \omega^2 \frac{\overline{S}_{hh}(\omega)}{\sinh^2 \kappa D} \tag{6.70}$$

and

$$R_{ak} = [q_k + i(p_k\cos\theta + r_k\sin\theta)] \tag{6.71}$$
$$R_{bk} = [-q_k + i(p_k\cos\theta + r_k\sin\theta)]$$
$$R_{al} = [q_l - i(p_l\cos\theta + r_l\sin\theta)]$$
$$R_{bl} = [-q_l - i(p_l\cos\theta + r_l\sin\theta)]$$

On carrying out the integrations with respect to S_k and S_l, Eq. 6.67 becomes

$$I_{k_x l_x} = \frac{\varsigma}{4\kappa^2} \int_{-\pi}^{\pi} G(\omega,\theta)\cos^2\theta.1_{n\bar{s}} \tag{6.72}$$

$$\cdot[\frac{1}{R_{ak}}e^{-1}{}_n(e^{R_{ak}\bar{\kappa}}-1)+\frac{1}{R_{bk}}e^{-1}{}_n(e^{R_{bk}\bar{\kappa}}-1)]$$

$$\cdot[\frac{1}{R_{al}}e^{-1}{}_s(e^{R_{al}\bar{\kappa}l_r}-1)+\frac{1}{R_{bl}}e^{-1}{}_s(e^{R_{bl}\bar{\kappa}l_r}-1)]d\theta$$

where

$$\Lambda_{n\bar{s}} = e^{i\kappa\{(x_n-x_s)\cos\theta-(z_n-z_s)\sin\theta\}} \tag{6.73}$$

The dimensionless wave number $\bar{\kappa}$ is defined as

$$\bar{\kappa} = \kappa L_k = 2\pi(L_k/\lambda) \tag{6.74}$$

and

$$L_r = L_l/L_k \tag{6.75}$$

A more general expression for the integrals I_{kl} in all other directions is given in Appendix B.

6.5.2. Parametric Study

A typical cross spectrum of wave forces on two members k and l as given by Eqs. 6.62 and 6.72 depends on C_D and G_M as well as two groups of parameters:

1. *Geometric Parameters and Wind Speed*: $(y_n+D)/L_k$, $(y_s+D)/L_k$, $(x_n-x_s)/L_k$, $(z_n-z_s)/L_k$, D/L_k, L_r direction cosines of both members, the tributary length L_k, d_k and d_l and the mean wind speed $\bar{U}$.

2. *Wave System Parameters*: dimensionless wave number $\bar{\kappa}$, directional spread parameter $\bar{a}$ and mean direction of wave advance $\bar{\theta}$.

The more important parameters are those of the second group and a parametric study is conducted to illustrate the variation of the spectra of wave forces with these parameters for a given set of values for the parameters of the first group.

Spectra of wave forces evaluated using the directional spectrum differ from those evaluated using a unidirectional spectrum in two main aspects:

1. The lateral component of wave force spectrum (normal to the mean direction of wave advance) is present in the case of a directional spectrum.

2. The resultant wave force spectrum on a member is reduced when using a directional spectrum.

These two factors are closely examined together with the approximation involved by considering a constant value of the water particle velocity, which is its value at the node, rather than a varying one along the member. For the parametric study, only one member is assumed to be connected at each of the 2 joints, i.e. $N_n = N_s = 1$. The following values are used for the parameters of the first group, unless otherwise stated:

$$(y_n + D)/L_k = (y_s + D)/L_k = 8, \quad (x_n - x_s)/L_k = (z_n - z_s)/L_k = 0,$$

$$D/L_k = 10, \quad U = 20 \text{ m/sec} \quad L_r = 1, \quad L_k = 10 \, m, \quad d_k = d_l = 1 \, m$$
and $p_k = p_l = q_k = q_l = 0$. C_D and C_M take on the values of
2 and 1.4, respectively.

The orientation of the two members in each case is shown on the plot presenting the results of this case. The spectral peak dimensionless wave number corresponding to a charateristic wind speed of 20 m/s is $\overline{\kappa} = 0.245$.

6.5.2.1. Variation in The Lateral Forces With the Wave System

Parameters

The ratio between the spectra of the horizontal force components in directions Z and X, $R_{zx}(\overline{\kappa})$, defined by

$$R_{zx}(\overline{\kappa}) = |S_{P_z P_z}(\overline{\kappa})/S_{P_x P_x}(\overline{\kappa})| \tag{6.76}$$

measures the relative importance of the two force components. In Eq. 6.76, $S_{P_z P_z}(\overline{\kappa})$ is the cross spectrum of the nodal loads, evaluated using the directional spectrum model, when both degrees of freedom l and m are in the Z direction, i.e.

$$S_{P_z P_z}(\overline{\kappa}) = S_{P_l P_m}(\overline{\kappa}) \quad \text{for } l//Z \text{ and } m//Z \quad . \tag{6.77}$$

similarly,

$$S_{P_x P_x}(\overline{\kappa}) = S_{P_l P_m}(\overline{\kappa}) \quad \text{for } l//X \text{ and } m//X \tag{6.78}$$

The ratio $R_{zx}(\overline{\kappa})$ depends on, among other parameters, the mean direction of wave advance. When evaluated at $\overline{\theta}=0$, $R_{zx}(\overline{\kappa})$ gives the ratio of the spectrum of across wave forces to that of along wave forces.

Fig. 6.6 shows the variation in $R_{zx}(\overline{\kappa})$ with $\overline{\theta}$ for 3 different values of $\overline{a}$ at $\overline{\kappa}=0.3$. The ratio $R_{zx}(\overline{\kappa})$ decreases with the increase in $\overline{a}$ (notice that higher values of $\overline{a}$ indicate a narrower angular spread) for $\overline{\theta} < 45°$. For such angles, the X component is larger than the Z component for any one individual wave and a narrower angular distribution means that a larger percentage of wave energy is contained in waves advancing in directions close to angle $\overline{\theta}$. Conversely, $R_{zx}(\overline{\kappa})$ increases with $\overline{a}$ for $\overline{a} > 45°$. $R_{zx}(\overline{\kappa})$ reaches a maximum value at $\overline{\theta}=90°$, as the mean direction of wave advance lies along the Z axis. It could be seen that at $\overline{\theta}=0°$, $R_{zx}(\overline{\kappa})$ is small for the narrower angular spreads.

Shown in Fig. 6.7 is the variation in $R_{zx}(\overline{\kappa})$ evaluated at $\overline{\theta}=0°$ with the dimensionless wave number $\overline{\kappa}$ for 3 different values of $\overline{a}$. The ratio of across wave forces to along wave forces increases with the increase in $\overline{\kappa}$, i.e. for shorter wave lengths, due to the broader angular spread associated with shorter wave lengths, Eq. 6.20. It can also be noticed that $R_{zx}(\overline{\kappa})$ evaluated at $\overline{\theta}=0°$ decreases for narrower angular distributions (higher values of $\overline{a}$) as expected.

The variation in $R_{zx}(\overline{\kappa})$ with the angular spread parameter $\overline{a}$, for $\overline{\theta}=0°$ and 3 values of $\overline{\kappa}$, is shown in Fig. 6.8. It is noticed that at $\overline{a}=0$, both force
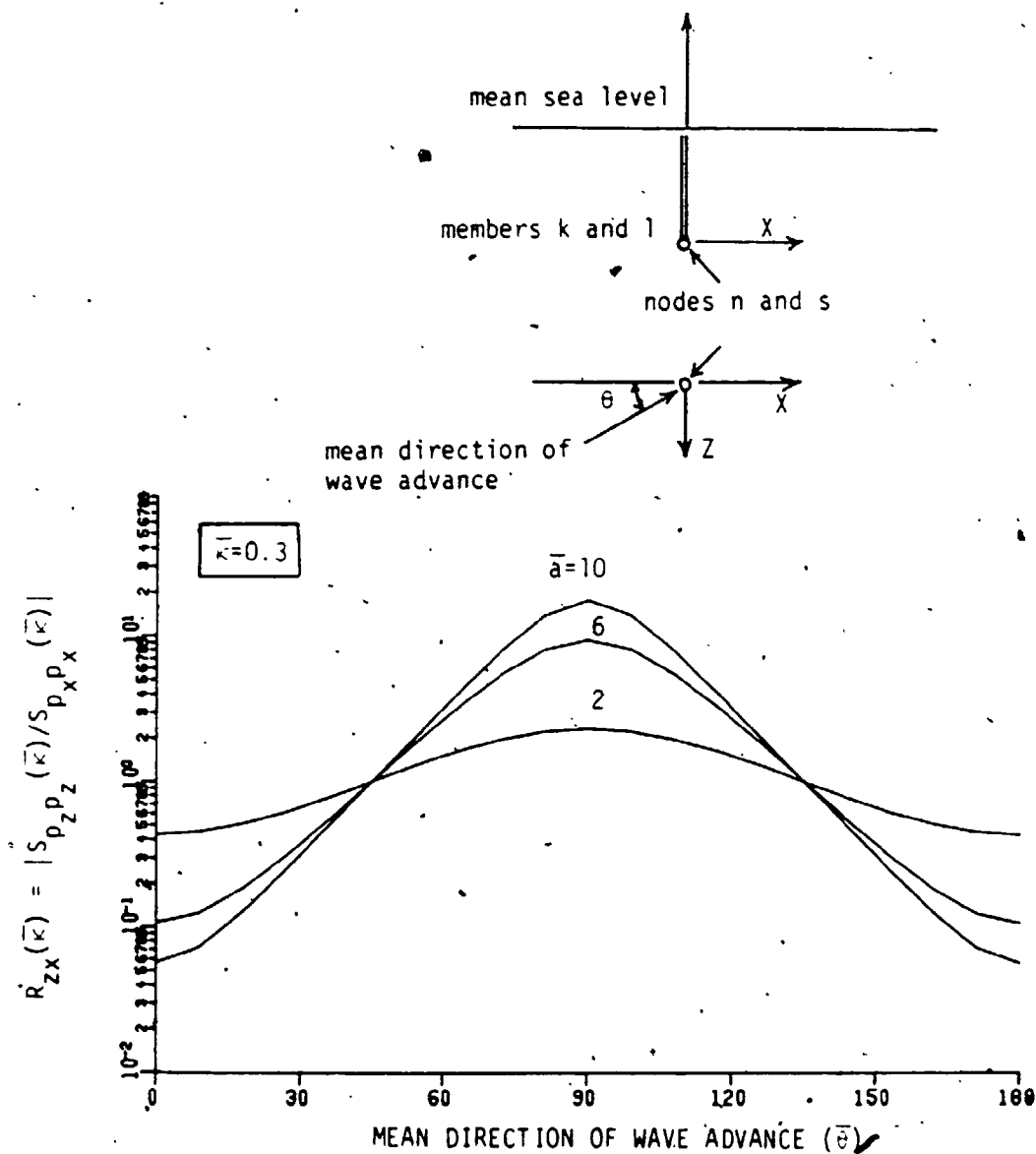
Figure 6-6: Variation in the Ratio of the Spectra of Lateral Force
Components with Mean Direction of Wave Advance
(Directional Spectrum Model)
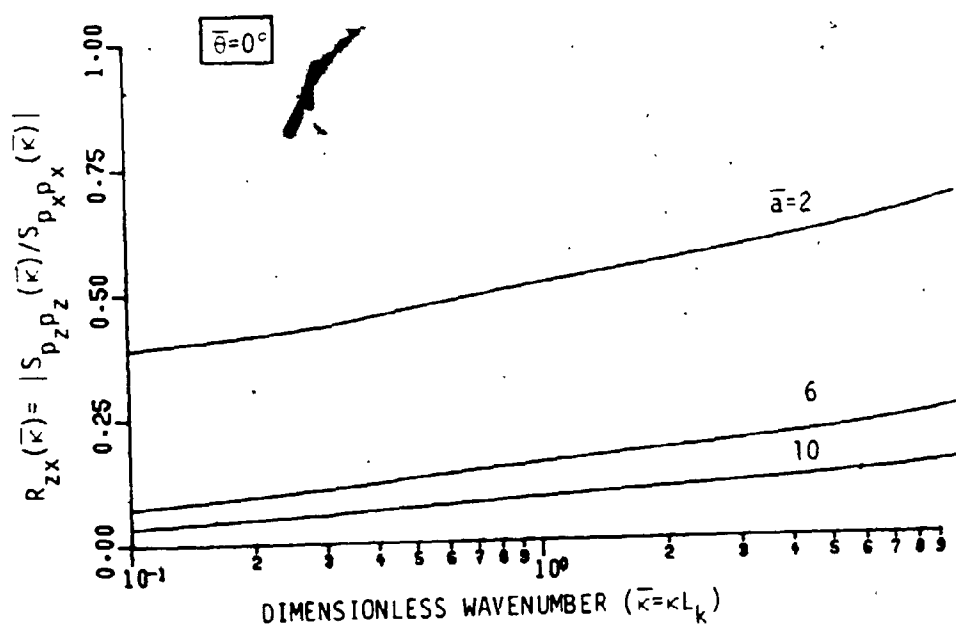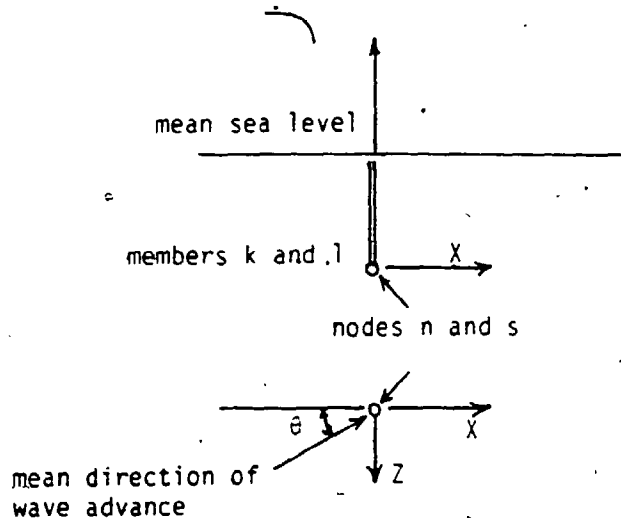
Figure 6-7: Variation in the Ratio of the Spectra of Across Wave to Along
Wave Force Components with Dimensionless Wave Number
(Directional Spectrum Model)

components are equal as the wave energy is distributed equally among all frequencies. The ratio $R_{zz}(\overline{k})$ decreases with the increase in $\overline{a}$. Estimates for the values of $\overline{a}$ based on experimental results of full scale measurements have not yet been reliably established. Berge [161] used values of $\overline{a}$ ranging from $a = 4$, to $a = 100$ to evaluate the response of an offshore tower to three dimensional waves.

Fig. 6.9 shows the variation in $R_{zz}(\overline{k})$ with $\overline{\theta}$, for 3 different values of $\overline{a}$, $\overline{k} = 0.3$ and $\overline{\theta} < 45°$. It is noticed that the narrower the angular spread is (higher values of $\overline{a}$), the less the reduction in wave forces (higher values of $R_z(\overline{k})$). The largest reduction occurs at $\overline{\theta} = 45°$ for all values of $\overline{a}$. This is because at $\overline{\theta} = 45°$, the spectrum of the force component in the X direction at a certain frequency, for both models, contains half the total energy of the wave system at that frequency.

6.5.2.2. Reduction in Along Wave Forces Due to Directional Spread

Spectra of wave forces exerted by a fully correlated unidirectional wave system are formulated similar to those of a directional one and the final general expression is given in Appendix C. The reduction in the wave force spectrum due to directional spread can be measured by the reduction factor $R_z(\overline{k})$ defined as

$$R_z(\overline{\kappa}) = |S_{P_z P_z}(\overline{\kappa})/\overline{S}_{P_z P_z}(\overline{\kappa})| \qquad (6.79)$$

where $S_{P_z P_z(\overline{k})}$ is given by Eq. 6.78 and $\overline{S}_{P_z P_z}(\overline{\kappa})$ is the fully correlated unidirectional model, Eq. C-1. The reduction factor $R_z(\overline{k})$ evaluated at $\overline{\theta} = 0°$ represents the reduction in along wave forces.

In Fig. 6.10, the variation in the reduction factor for along wave forces ($R_z(\overline{k})$ at $\overline{\theta} = 0°$) with dimensionless wave number $\overline{k}$ is plotted for 3 different values of $\overline{a}$. The reduction factor decreases with the increase in angular spread and its variation with the dimensionless frequency is mild.
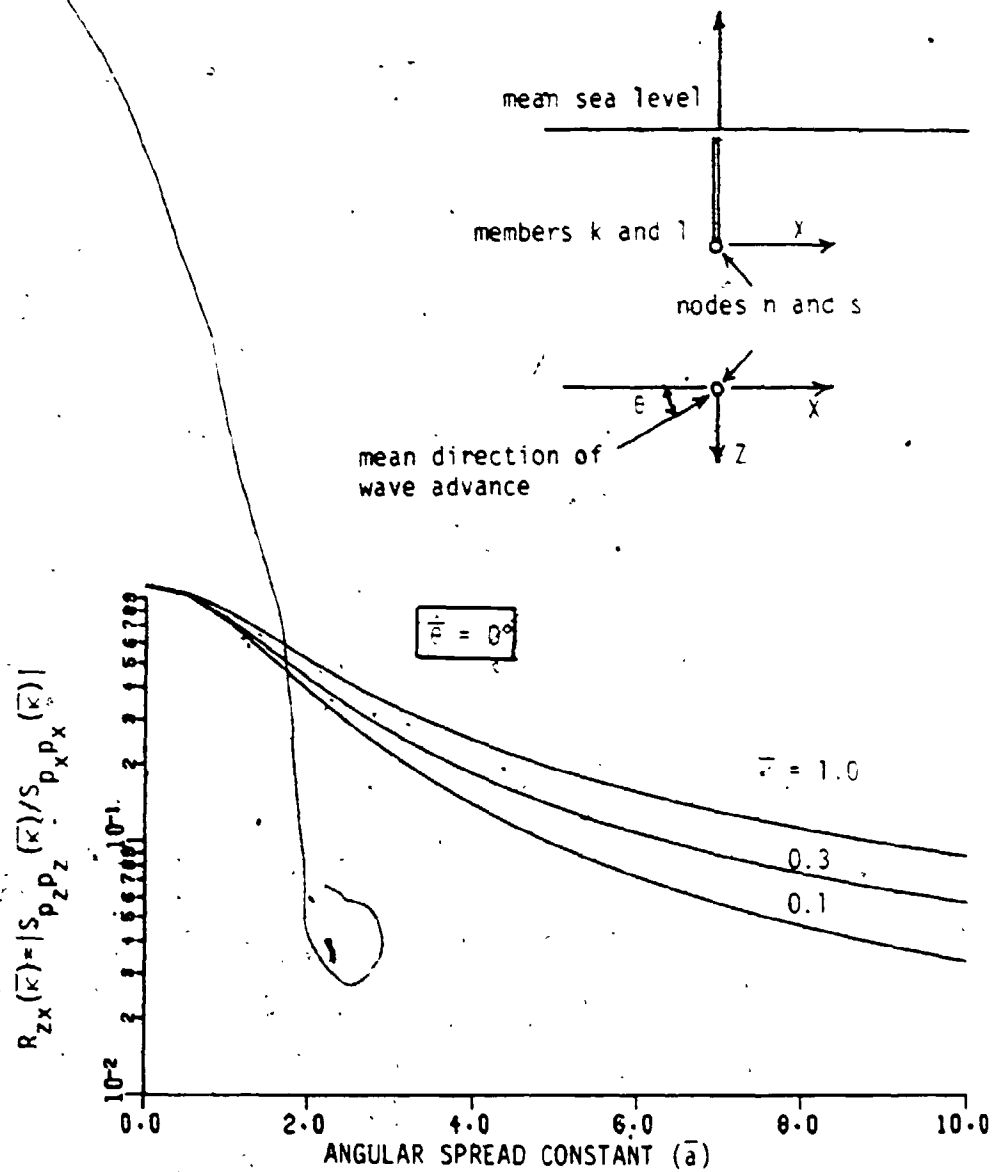
Figure 6-8: Variation in the Ratio of the Spectra of Across Wave to Along Wave Force Components with Angular Spread (Directional Spectrum Model)

150

mean sea level

members k and l

nodes r and s

mean direction of wave advance

ā=10

6

2

ā=0.3

REDUCTION FACTOR $R_x(\cdot)$

1.00
0.75
0.50
0.25
0.00

0.0   7.5   15.0   22.5   30.0   37.5   45.0

MEAN DIRECTION OF WAVE ADVANCE (⁰)
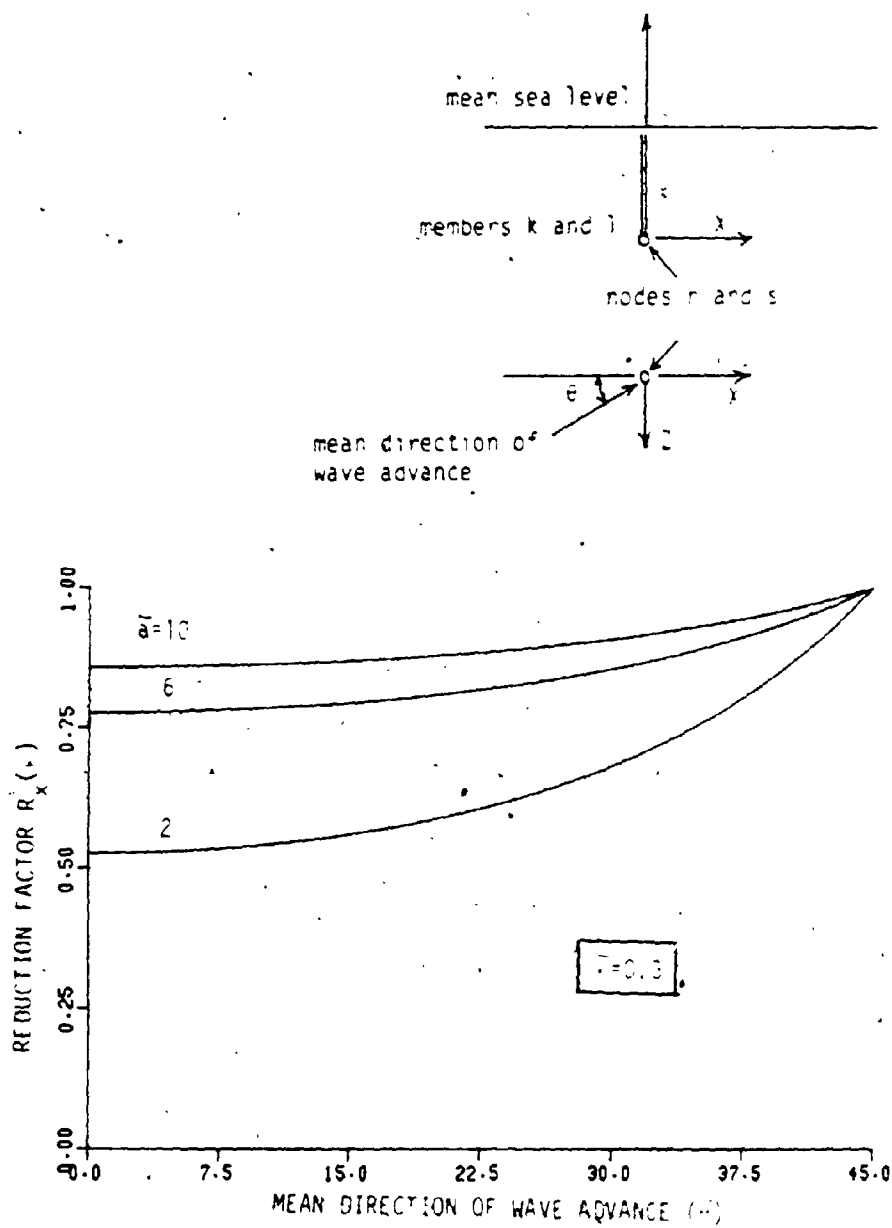
Figure 6-9: Variation in the Reduction of the Spectrum of Force Component in the X Direction with Mean Direction of Wave Advance (Directional Spectrum Model)
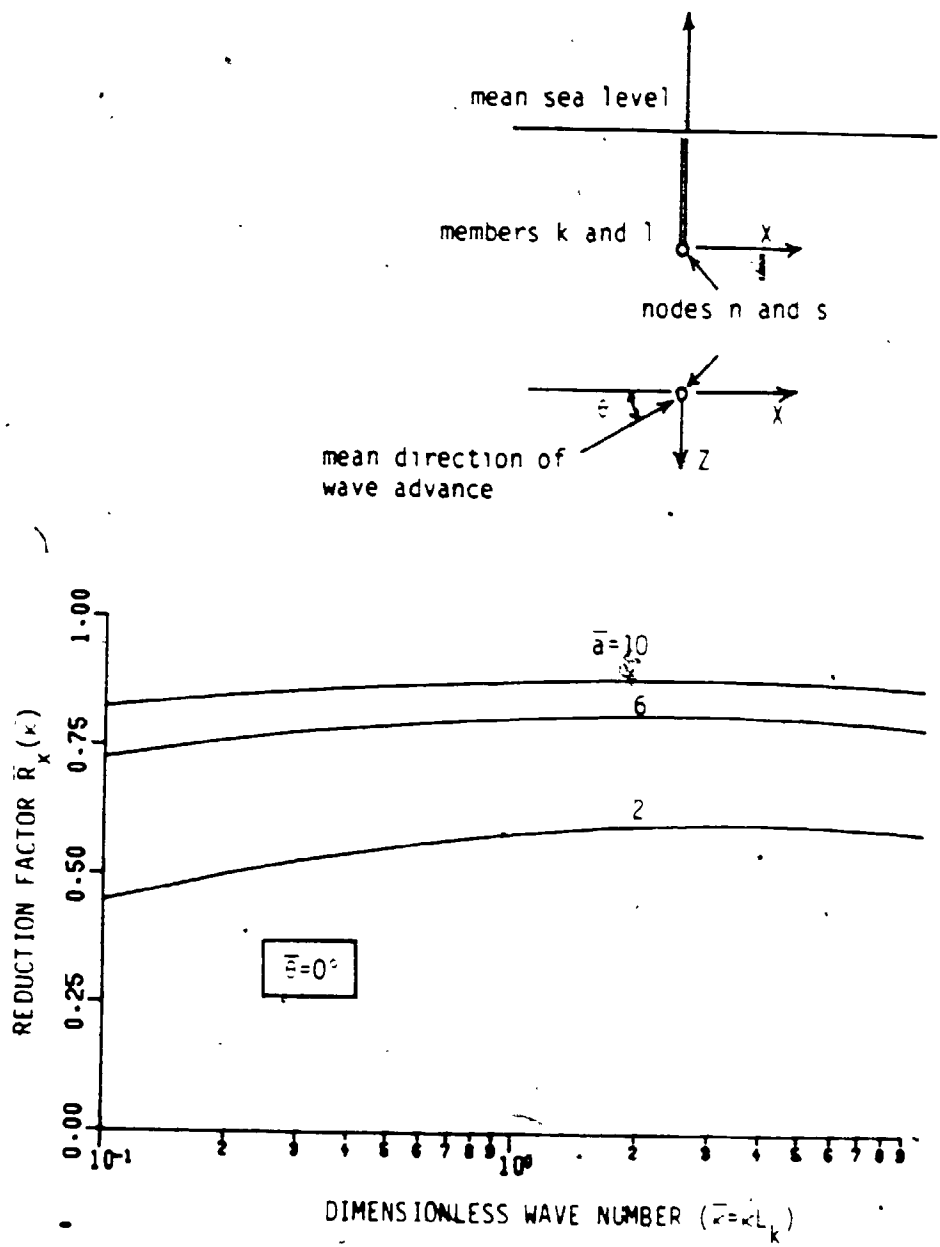
Figure 6-10: Variation in the Reduction of Along Wave Force Spectrum with Dimensionless Wave Number (Directional Spectrum Model)

Shown in Fig. 6.11 is the variation in $\overline{R}_I(\overline{K})$ (at $\overline{\theta} = 0$) with the angular spread parameter $\overline{a}$, for 3 values of $\overline{K}$. $\overline{R}_I(\overline{k})$ increases with the increase in $\overline{a}$ and would reach the upper limit of 1 for $\overline{a} \rightarrow \infty$ indicating that all the wave energy is concentrated at $\theta = \overline{\theta}$. For $\overline{K} = 0.3$, $\overline{R}_I \overline{K}$ has the highest values because the narrowest angular distribution among the three curves is associated with the one for $\overline{R}_I(\overline{K}) = 0.3$.

6.5.2.3. Effect of Lumping the Members at the Nodes

For offshore structures with many members of general orientation, such as the jacket type structures, cross spectra of water particle velocities are usually approximated by their values at the nodes $S_{\dot{v}_1 \dot{v}_2}(\omega)_o$ and the areas and volumes of members connected to a joint are lumped at this joint. In this case, the integrations in Eq. 6.64 are replaced by simple multiplications i.e.

$$I_{kl} = S_{\dot{v}_1 \dot{v}_2}(\omega)_o L_k L_l \qquad (6.80)$$

The expressions for I_{kl} for this case are given in Appendix D for different representations of the wave system. The accuracy of such approximation can be measured by the ratio R_{I_o} given by

$$R_{I_o} = |S_{P_I P_I}(\overline{K})_o / S_{P_I P_I}(\overline{K})| \qquad (6.81)$$

In Eq. 6.81, $S_{P_I P_I}(\overline{K})$ is the cross spectrum of wave forces in the X direction for a directional wave system and $S_{P_I P_I}(\overline{K})_o$ is the cross spectrum of the same quantities calculated for a directional wave system obtained by approximating the velocity along the member by its value at the node.

The ratio R_{I_o} is examined for a vertical member located above nodes n and s. It can be shown that the ratio R_{I_o} for vertical members does not depend on the angular distribution parameter and depends solely on $\overline{K}$. This dependency is shown in Fig. 6.12. For small dimensionless wave numbers (longer wave lengths)
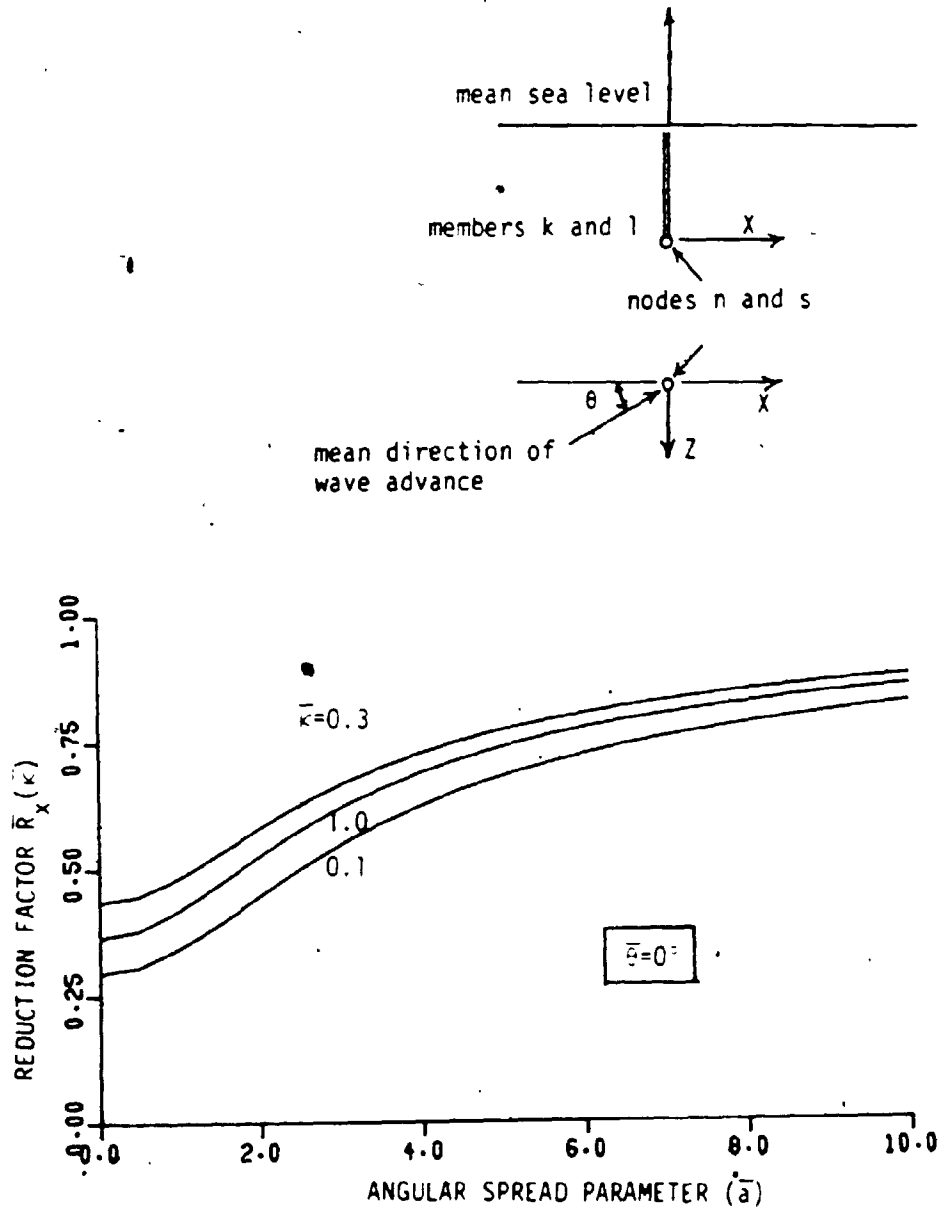
Figure 6-11: Variation in the Reduction of Along Wave Force Spectrum with Directional Spread (Directional Spectrum Model)

154

mean sea level

members k and l

nodes n and s

e

X

Z

mean direction of
wave advance

APPROXIMATION RATIO $R_{x0}(\bar{\kappa})$

any value of $\bar{a}$

$\bar{\theta}=0°$

10^{-1} 10^{0}

DIMENSIONLESS WAVE NUMBER $(\bar{\kappa}=\kappa L_k)$
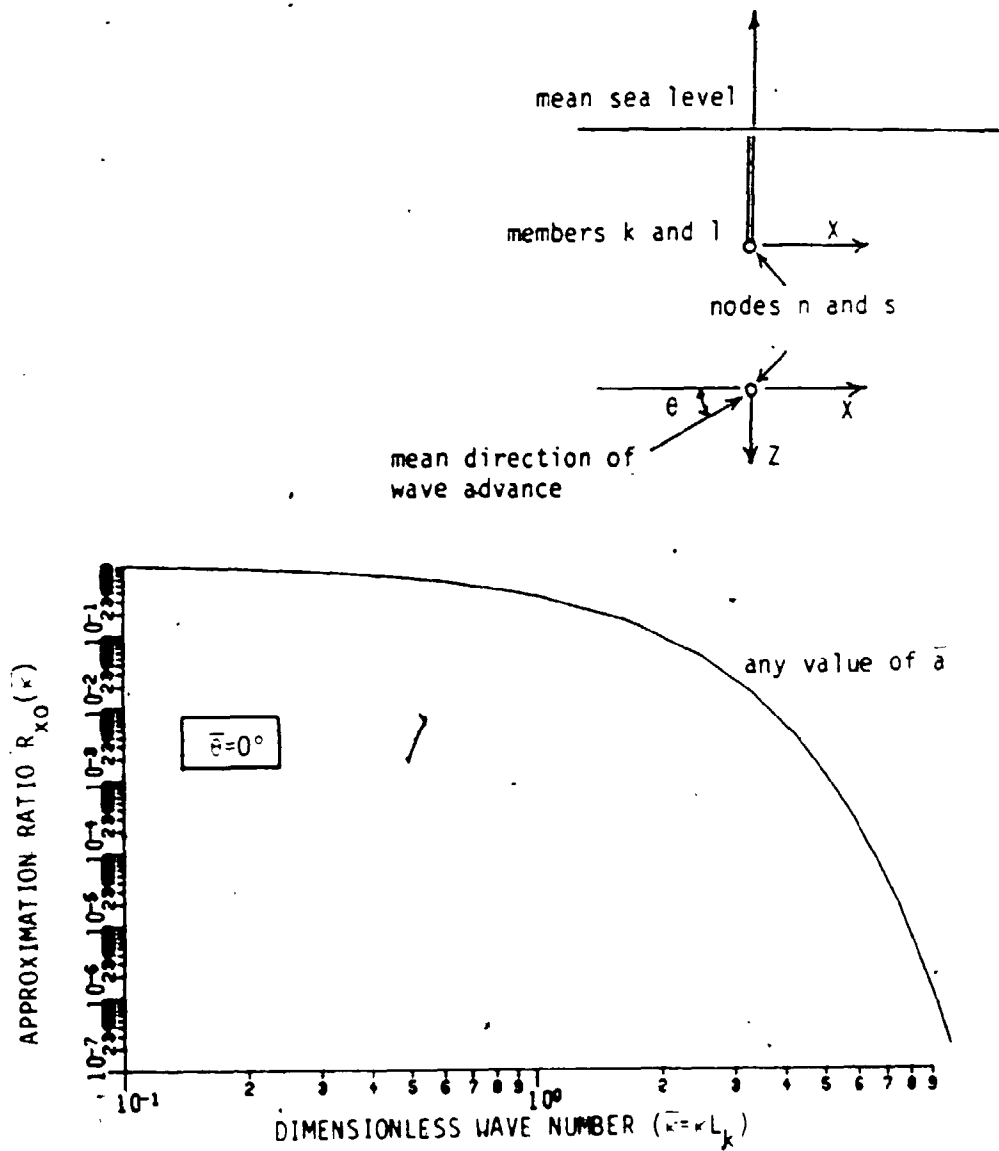
Figure 6-12: Variation in the Approximation Ratio R_{x_o} with
Dimensionless Wave Number (Directional Spectrum Model)

R_{r_o} approaches unity. It decreases moderately with the increase in $\overline{k}$ reaching a value of 0.737 at $\overline{k}=0.3$. For high dimensionless wave numbers, $\overline{k}>1.0$, R decreases rapidly with $\overline{k}$ to reach several orders of magnitude less than unity at $\overline{k}=10.0$. The sharp decrease is explained by the fact that for higher $\overline{k}$ (shorter wave lengths), the deep water approximations hold and the velocity profile varies almost exponentially with depth.

6.6. Coherence Function Model

6.6.1. Formulation

In Section 6.3.2.2, the lack of spatial correlation observed in short crested seas is accounted for by the use of a coherence function and the water particle kinematics spectra are given by Eq. 6.48. The coherence function expressed by Eq. 6.49 is plotted in Fig. 6.43 for different values of the exponential decay parameter c. It can be seen that the coherence decays faster for higher values of c. The value of c may vary with types of waves or direction of separation but it is assumed constant in this study to simplify the analysis.

When points (1) and (2) are in general positions, the coherence function is given by

$$R=e^{\frac{-c}{\lambda}\sqrt{\Delta x^2+\Delta y^2+\Delta z^2}}$$
(6.82)

where

$$\Delta x=|x1-x2|$$
$$\Delta y=|y1-y2|$$
$$\Delta z=|z1-z2|$$
(6.83)

However, if the coherence function given by Eq. 6.82 is used to evaluate the integrals I_{kl} of Eq. 6.64, they do not decouple. A linearized form of the square root in Eq. 6.82 was suggested that allows the integrations to decouple [183]

$$R=e^{-\frac{c}{\lambda}(\Delta x+\Delta y+\Delta z)}$$
(6.84)
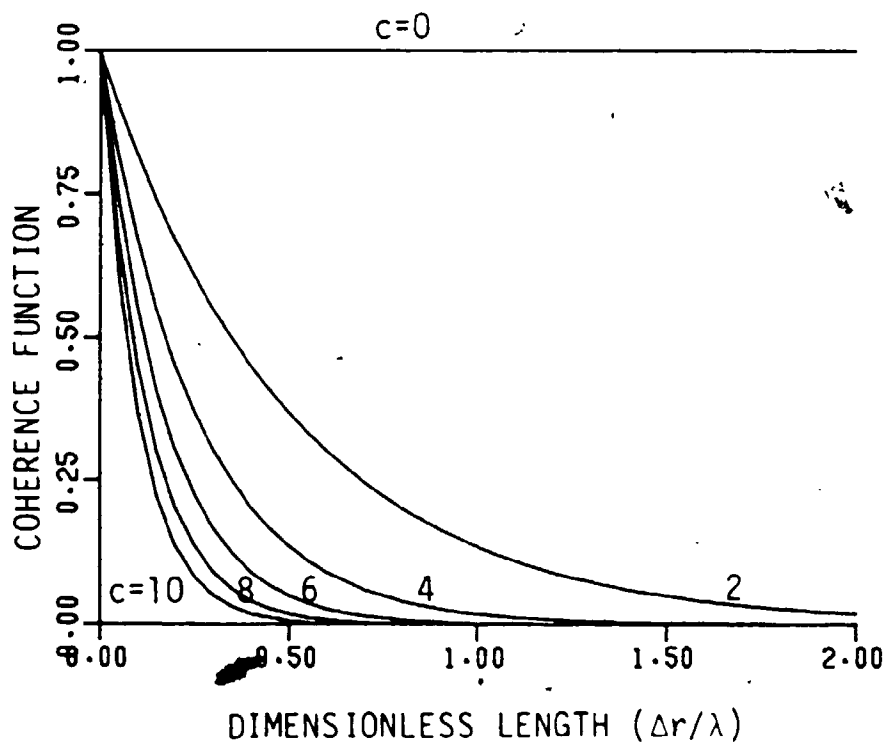
Figure 6-13: Exponential Decay Coherence Function

where γ is a correction factor that depends on the orientation of the line joining the 2 points. If $\Delta x = \Delta y = \Delta z$ then $\gamma = 0.5772$ while if the line joining the 2 points is parallel to any of the three global axes then $\gamma = 1$. For all other orientations γ takes on a value between 0.5772 and 1.

Evaluation of the integrals I_{kl} for the coherence function model is lengthy and only an outline of how the integrations are carried out is given below. The general final expressions for the integrals is given in Appendix E.

Consider a wave system advancing in a mean direction that makes an angle $\overline{\theta}$ with the X axis. From Eqs. 6.46, 6.48 and 6.84, the cross spectral density of water particle velocities follows as

$$S_{\dot{r}_1 \dot{r}_2}(\omega) = \omega^2 \frac{S_{hh}(\omega)}{\sinh^2 \kappa D} C1(\overline{\theta}) C2(\overline{\theta})$$

$$. HYP1[\kappa(y1 + D)] HYP2[\kappa(y2 + D)]$$

$$. e^{i\kappa[(x1 - x2)\cos\overline{\theta} + (z1 - z2)\sin\overline{\theta}]}$$

$$. e^{-\frac{\gamma}{\lambda}(|x1 - x2| + |y1 - y2| + |z1 - z2|)}$$

where $C1(\overline{\theta})$ and $C2(\overline{\theta})$ are given by Eq. 6.41 if θ is substituted by $\overline{\theta}$ and $HYP1[\kappa(y1 + D)]$ and $HYP2[\kappa(y2 + D)]$ are given by Eqs. 6.42 and 6.43, respectively. Noting that $\lambda = 2\pi/\kappa$ and substituting by Eq. 6.65, Eq. 6.85 becomes

$$S_{i_1 i_2}(\omega) = \frac{\varsigma}{4} C1(\bar{\theta}) C2(\bar{\theta}) \Lambda_{ns}$$

(6.86)

$$.exp\{i\kappa[(p_k\cos\bar{\theta} + r_k\sin\bar{\theta})S_k - (p_l\cos\bar{\theta} + r_l\sin\bar{\theta})S_l]\}$$

$$.HYP1[\Lambda_n + \kappa q_k S_k]\, HYP2[\Lambda_s + \kappa q_l S_l]$$

$$.exp\{-c\frac{\kappa\gamma}{2\pi}|p_k S_k - p_l S_l + x_n - x_s|\}$$

$$.exp\{-c\frac{\kappa\gamma}{2\pi}|q_k S_k - q_l S_l + y_n - y_s|\}$$

$$.exp\{-c\frac{\kappa\gamma}{2\pi}|r_k S_k - r_l S_l + z_n - z_s|\}$$

where ς, Λ_n and Λ_s are given by Eqs. 6.70, 6.68 and 6.69, respectively. Λ_{ns} is given by Eq. 6.73 if θ is substituted by $\bar{\theta}$. When carrying out the integrations in Eq. 6.84, the difficulty lies in the exponential terms with the absolute values. The treatment of the absolute value terms is slightly different when the nodes n and s coincide than when they do not and each case will be demonstrated separately.

A)Nodes n and s coincide: A difficulty arises if one or more of the three pairs of direction cosines (p_k and p_l, q_k and q_l and r_k and r_l) have the same sign. In this investigation, the integrations are carried out for the case of only one pair having the same sign. Although it is possible to carry out the integrations for the case of two or three pairs having identical signs, the resulting expressions become extremely lengthy and a reasonable approximation is necessary. For the case of one pair of direction-cosines having identical signs, the integrations have to be performed on two intervals for one of the independent variables.

On the other hand, if each of the three pairs of the direction cosines have different signs, the integrations are carried out on one interval for each of the independent variables.

1)One pair of the direction cosines have the same sign: in this case, the expansion of the absolute value terms is given by

$$|b_k S_k - b_l S_l| = \begin{cases} |b_k| S_k - |b_l| S_l & \text{for } 0 < S_l < b_r S_k \\ |b_l| S_l - |b_k| S_k & \text{for } b_r S_k < S_l < L_l \end{cases} \qquad (6.87)$$

where b_k and b_l refer to the pair of direction cosines with the identical signs and b_r is given by

$$b_r = b_k / b_l \qquad (6.88)$$

Eq. 6.87 gives the expansion for the pair with identical signs, whereas those of the pairs with opposite signs are given by

$$|b_k S_k - b_l S_l| = |b_k| S_k + |b_l| S_l \qquad (6.89)$$

By using Eqs. 6.87 and 6.88, the double integral in Eq. 6.64 is first carried out with respect to S_l on two intervals; $0 \rightarrow b_r S_k$ and $b_r S_k \rightarrow L_l$ and then integrated with respect to S_k from $0 \rightarrow L_k$: Closed form solutions are obtained and no numerical integration is required.

2)Two or three pairs of direction cosines have the same sign: this case arises only when evaluating I_{kk} for a member which is not parallel to any of the global axes. In such case, the integration is approximated by that of an equivalent member that has the same properties but lies parallel to one of the global axes. The direction of the equivalent member is chosen so as to minimize the error introduced by the approximation.

3)Each of the three pairs of direction cosines has opposite signs: the expansion of the absolute value terms is given by Eq. 6.89 and the double integration in Eq. 6.64 is carried out on one interval for each of the independent variables.

B)Nodes n and s Do Not Coincide: two different situations can be distinguished

1)I_{kl} is evaluated on one interval for each variable; this situation arises when each of the three absolute value terms satisfies either of the following conditions:

A) $|\Psi_n - \Psi_s| > 0$: where Ψ refers to any of the global coordinates x, y or z. In this case, the expansion of the absolute value terms is given by

$$|b_k S_k - b_l S_l + \Psi_n - \Psi_s| = \begin{cases} |\Psi_n - \Psi_s| + b_l S_l - b_k S_k \\ \qquad \text{for } \Psi_n < \Psi_s \\ |\Psi_n - \Psi_s| + b_k S_k - b_l S_l \\ \qquad \text{for } \Psi_n > \Psi_s \end{cases} \qquad (6.90)$$

where b_k and b_l are the direction cosines associated with the global coordinate Ψ, i.e if $\Psi \equiv x$ then $b_k \equiv p_k$ and $b_l \equiv p_l$.

B) $|\Psi_n - \Psi_s| = 0$ and b_k and b_l have opposite signs. The expansion of the absolute value terms is given by Eq. 6.89.

2)I_{kl} is evaluated on two intervals for one of the independent variables; this situation arises if any of the three absolute value terms satisfies the following condition:

$|\Psi_n - \Psi_s| = 0$ and b_k and b_l have identical signs

The expansion of the absolute value terms is given by Eq. 6.87.

6.6.2. Parametric Study

The spectra of wave forces evaluated by the coherence function model depend on C_D and C_M as well as two groups of parameters:

1. Geometeric Parameters and Wind Speed: these are the same as for the directional spectrum Section 6.5.2.

2. Wave System Parameters: these are the dimensionless wave number $\overline{K}$, exponential decay parameter c and mean direction of wave advance $\overline{\theta}$.

A parametric study is carried out to examine the variation of the spectra of wave forces estimated using the coherence function model , with each of the parameters of the second group. As in the directional spectrum model, three quantities are examined:

1. The ratio between the two horizontal force components.

2. The reduction of along wave forces due to lack of spatial correlation.

3. The error introduced by assuming the cross spectrum of water particle velocity to be constant and equal to that at the nodes.

Orientation of the members for which the wave forces are evaluated is illustrated on the corresponding figures showing the results of the calculation. The values of the parameters of the first group that are used in the parametric study are the same as those used in Section 6.5.2, unless otherwise stated.

6.6.2.1. Variation in the Ratio Between the Horizontal Force
Components With The Wave System Parameters

Since the coherence function model is essentially a unidirectional model, it may fail to represent the force component normal to the mean direction of wave advance. However, it properly represents the ratio between the 2 horizontal force components. This is illustrated by Fig. 6.14 where the ratio between the horizontal force components, $R_{zx}(\overline{k})$, defined by Eq. 6.76 and evaluated using the coherence function model is plotted for $\overline{\theta} = 0°$ to $180°$. (For a vertical member, $R_{zx}(\overline{k})$ is independent of the exponential decay parameter c). As $\overline{\theta} \rightarrow 0°$, $F_z \rightarrow 0$ and $R_{zx}(\overline{k}) \rightarrow 0$, while as $\overline{\theta} \rightarrow 90°$, $F_x \rightarrow 0$ and $R_{zx}(\overline{k}) \rightarrow \infty$. Nevertheless, for $\overline{\theta} \rightarrow 0$, the F_z force component evaluated by the directional spectrum is already small compared to F_x and as $\overline{\theta}$ increases, $R_{zx}(\overline{k})$ increases showing an increased relative importance of F_z in comparison to F_x, Fig. 6.6. Thus, the ratio $R_{zx}(\overline{k})$ evaluated using the coherence function model, is

mean sea level

members k and l

X

nodes n and s

θ

X

Z

mean direction of
wave advance

any value of c

$R_{zx}(\bar{\kappa}) = |S_{p_z p_z}(\bar{\kappa})/S_{p_x p_x}(\bar{\kappa})|^{1/2}$
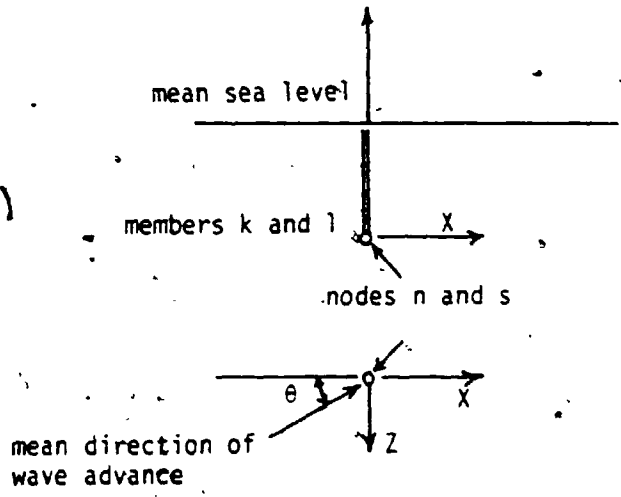
MEAN DIRECTION OF WAVE ADVANCE ($\bar{\theta}$)
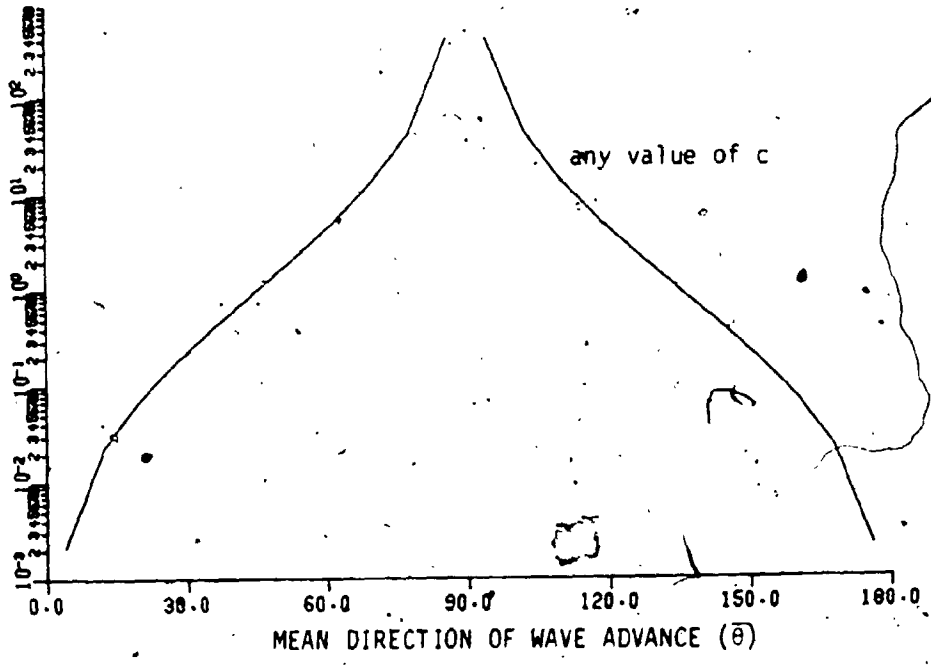
Figure 6-14: Variation in the Ratio of Spectra of the Lateral Force
Components with Mean Direction of Wave Advance (Coherence
Function Model)

improperly represented only at angles where one of the two horizontal force components is small and could be neglected. Fig. 6.15 shows $R_{zx}(\overline{k})$ for both models ($\overline{a}=10$ for the directional spectrum model and any value of c for the coherence function model). It can be noticed that for the range of $\overline{\theta}$ between 15° and 75°, where both components are important both models give close values for $R_{zx}(\overline{k})$.

For vertical members, the ratio $R_{zx}(\overline{k})$ is independent of the parameter c as shown in Fig. 6.16 where $R_{zx}(\overline{k})$ is plotted for 3 different values of $\overline{k}$. It can also be seen that $R_{zx}(\overline{k})$ is smaller for longer wave lengths. In Fig. 6.17, $R_{zx}(\overline{k})$ is plotted for $\overline{\theta}=22.5°$, against the dimensionless wave number $\overline{k}$. The increase in $R_{zx}(\overline{k})$ with $\overline{k}$ is solely due to the increase in the ratio $G'_{k_z l_z}/G_{k_x l_x}$, Eq. 6.62, since $I_{k_z l_z}/I_{k_x l_x}$ for vertical members depend entirely on the angle $\overline{\theta}$.

6.6.2.2. Reduction in Along Wave Forces Due to Lack of Spatial Correlation

As the distance between any 2 points in the wave field increases, the correlation between water particle kinematics at these points decreases and this is characterized by a decrease in their coherency. Consequently, the resultant wave forces decrease and this is represented, for wave forces in the X direction, by the reduction factor $\overline{R}_x(\overline{k})$ defined by Eq. 6.79.

Fig. 6.18 shows the variation in $\overline{R}_x(\overline{k})$ with the constant c for 2 members extending along the vertical axis calculated for $\overline{\theta}=0°$ and 3 different values of $\overline{k}$. The results shown in Fig. 6.18 are for 2 coincident nodes. For smaller values of c, the correlation length is large and even for shorter wave lengths ($\overline{k}=1.0$) is still larger than the member length and the wave forces are well correlated giving values of $\overline{R}_x(\overline{k})$ approaching unity. As c increases, the correlation between forces
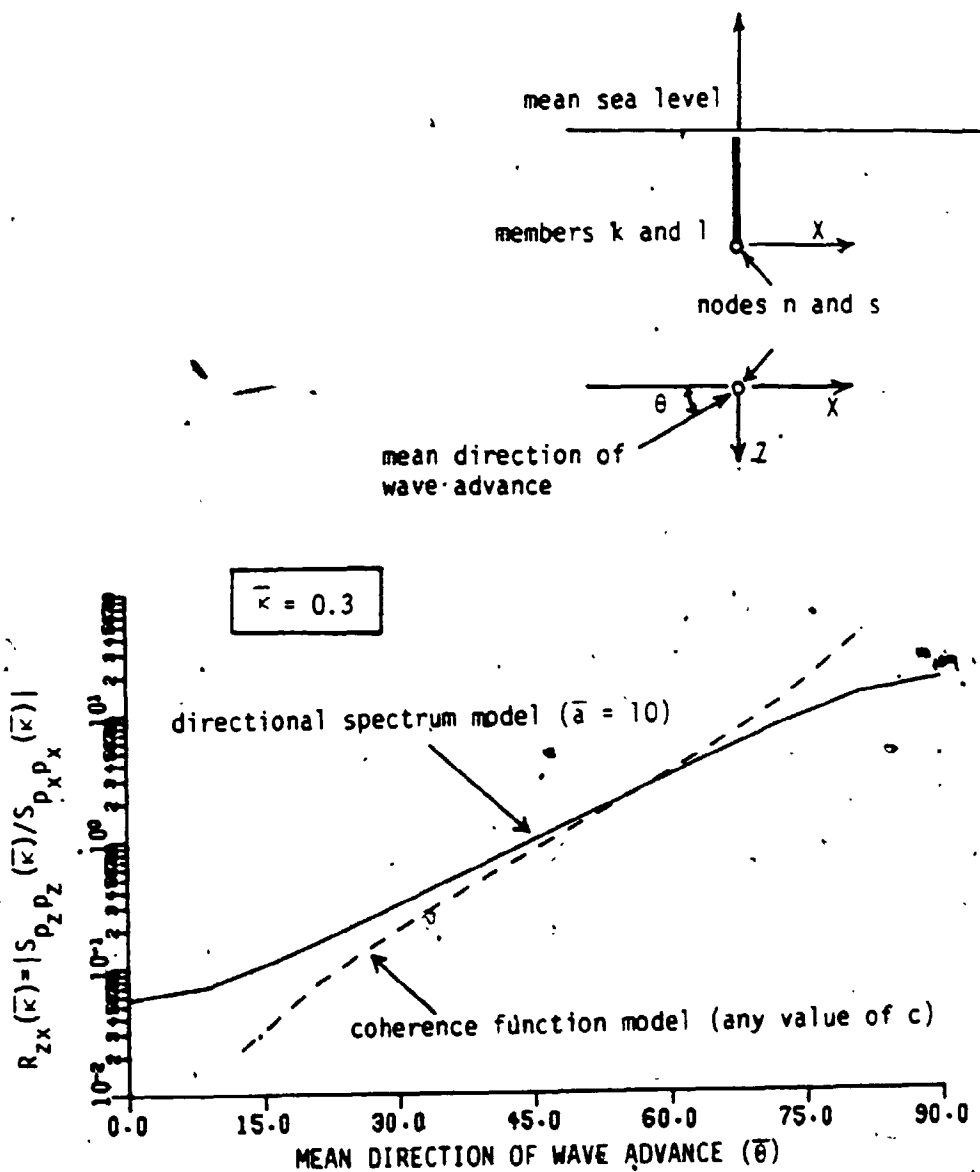
Figure 6-15: Variation in the Ratio of Across to Along Wave Force Spectra with Mean Direction of Wave Advance (Both Models)
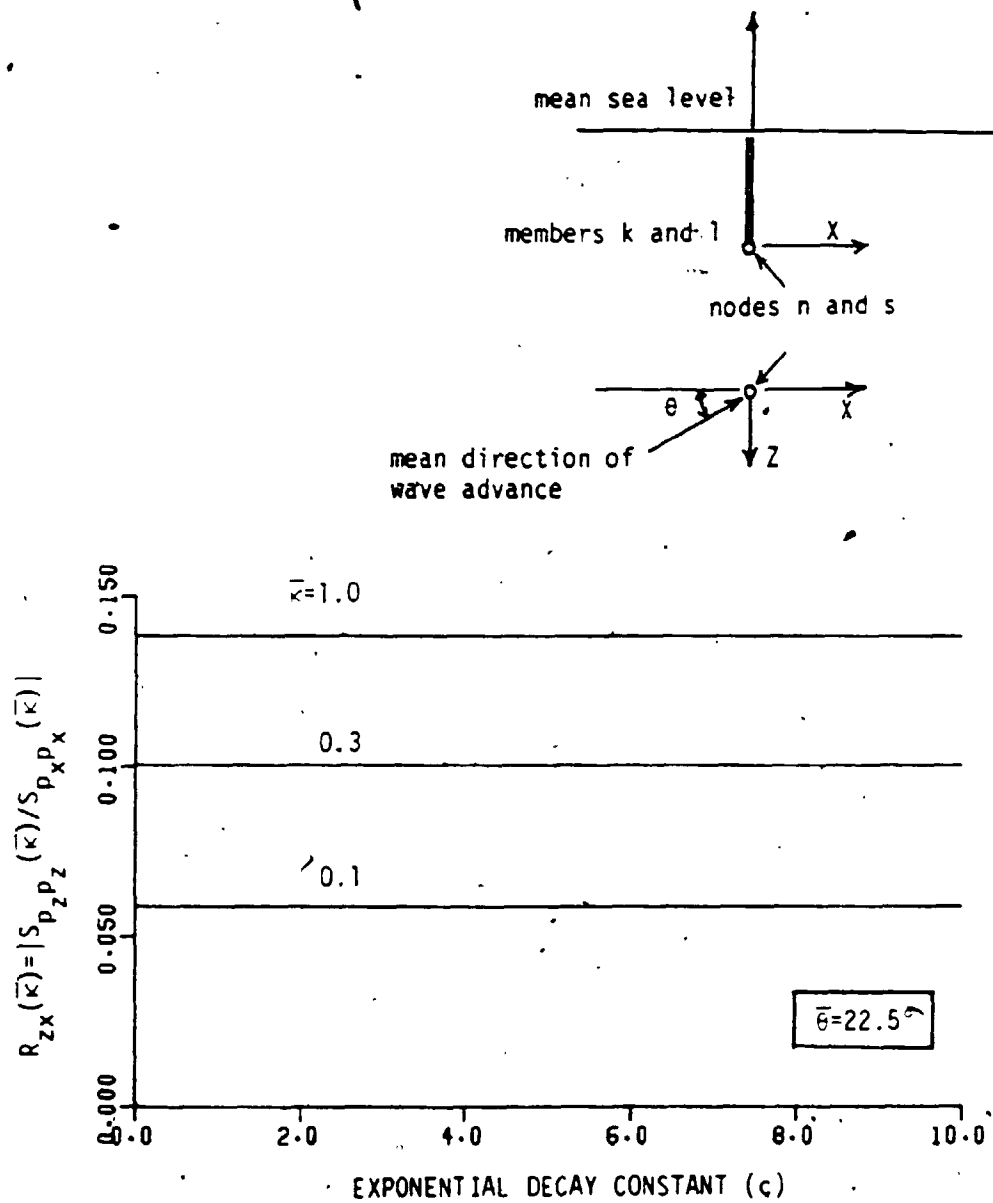
Figure 6-16: Variation in the Ratio of Spectra of the Lateral Force Components with Exponential Decay Constant (Coherence Function Model)
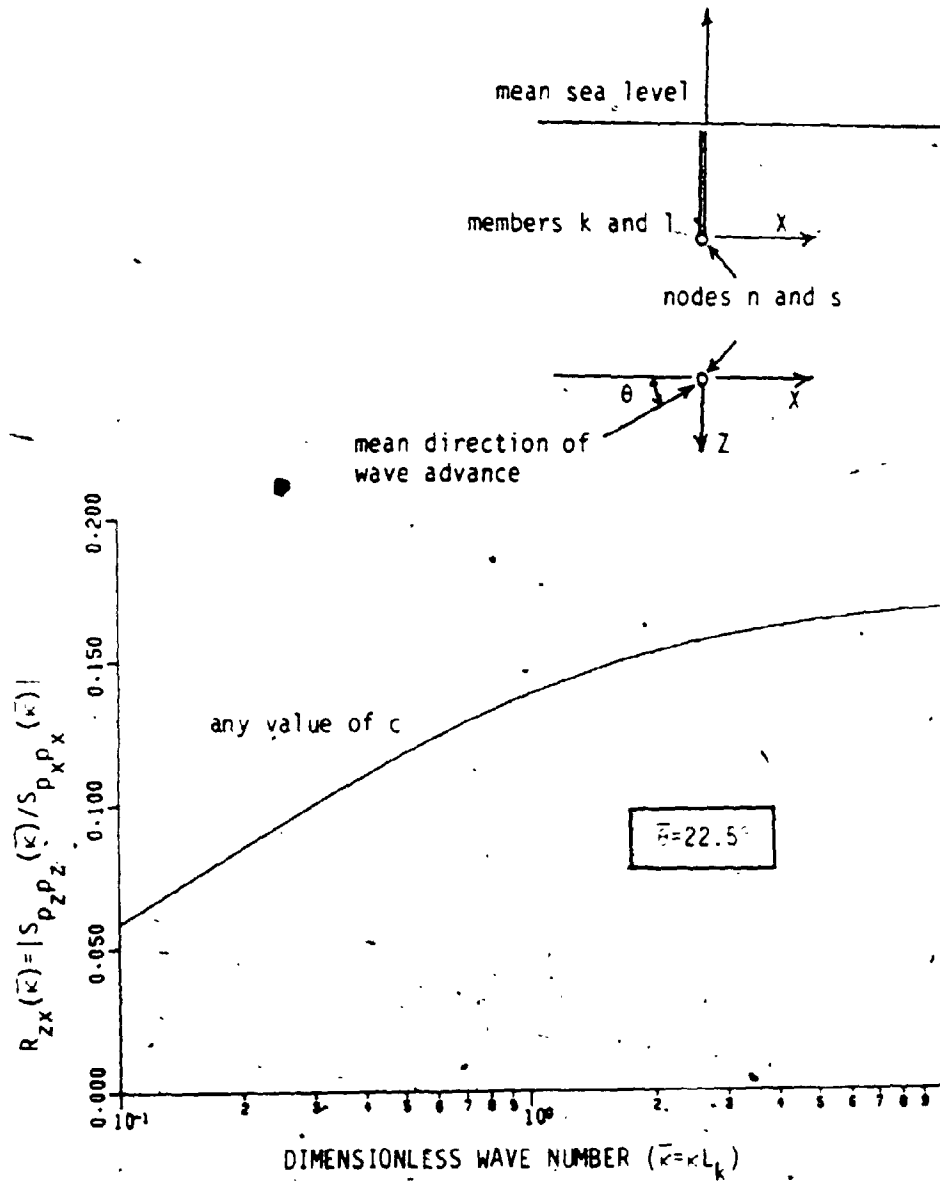
Figure 6-17: Variation.In the Ratio of the Spectra of Lateral Force Components with Dimensionless Wave Number (Coherence Function Model)
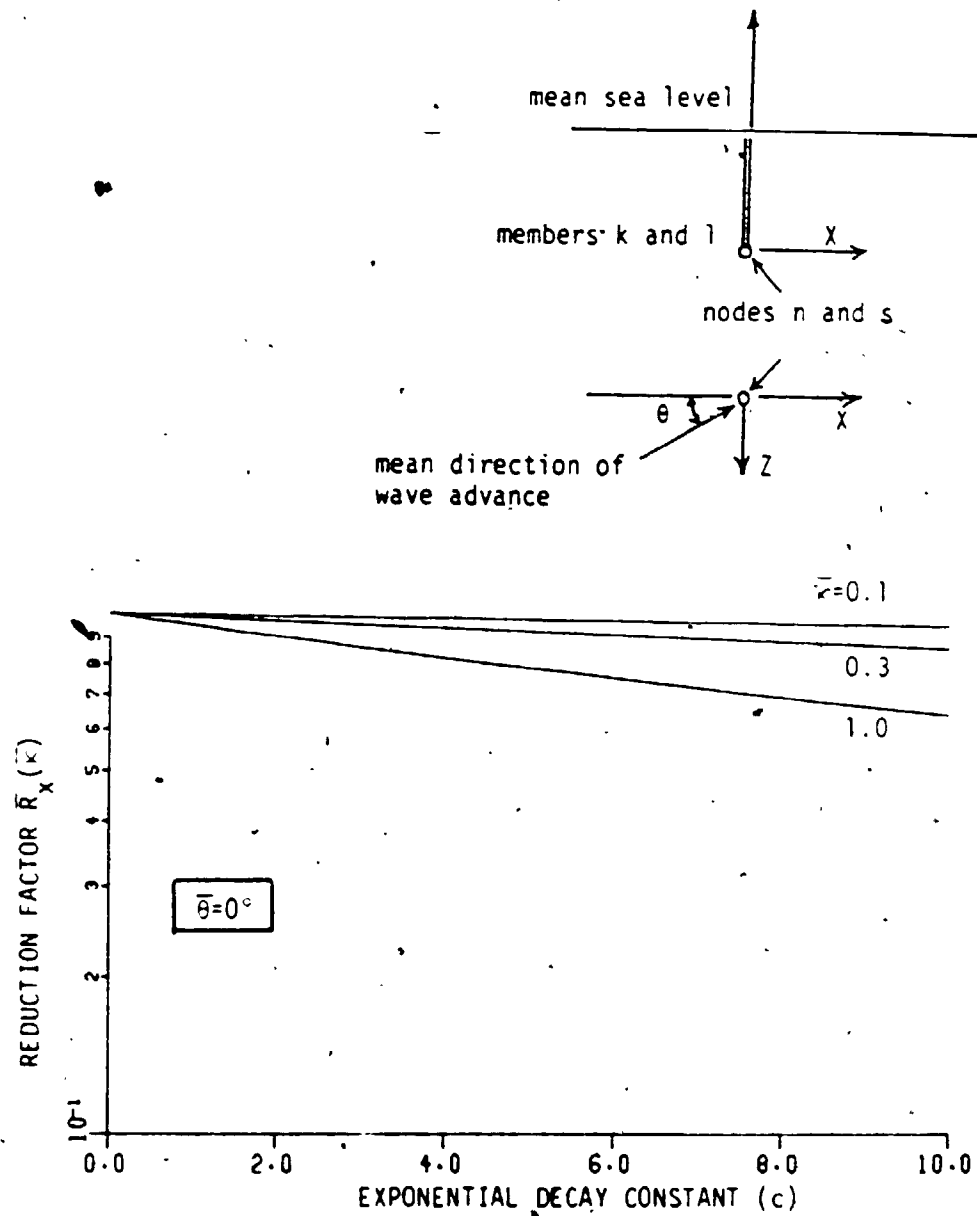
Figure 8-18: Variation in the Reduction of Along Wave Force Spectrum with Exponential Decay Constant (Coherence Function Model)

at any two points on the two-members decreases. The shorter the wavelength, the less the correlation length and consequently $\overline{R}_x(\overline{k})$ decreases for shorter wavelengths (higher values of $\overline{k}$).

For the same 2 members, Fig. 6.19 shows the variation in $\overline{R}_x(\overline{k})$ with $\overline{k}$ for 3 different values of c. The reduction factor shows the same trends mentioned above. In Fig. 6.20, $\overline{R}_x(\overline{k})$ is plotted for the case of n and s are different nodes and are some distance apart. Besides the above mentioned trends, one can notice the substantial decrease in $\overline{R}_x(\overline{k})$ in this case due to the separating distance.

The wave force spectrum on two vertical members separated by a distance Δx is evaluated for different $\Delta x/\lambda$ ratios. Fig. 6.21 shows the variation in the real part of $S_{p'_x p'_x}(\overline{k})$ for the coherence function model for 3 different values of c. The variation with $\Delta x/\lambda$ is periodic with a spatial period of $\Delta x = \lambda$ which reflects the periodic nature of the unidirectional waves. However, the lack of spatial correlation, represented by the coherence function model, leads to the attenuation of the spectral amplitudes as $\Delta x/\lambda$ increases. This attenuation is faster for larger values of c. A shift in the peak of the spectrum is also noticed, i.e. the peaks do not occur exactly at $\Delta x/\lambda = 0, 1, 2$. This is attributed to the participation of both the velocity and acceleration of water particle (which are not in phase) to the total fluid load.

Fig. 6.22 shows the variation in the real part of $S_{p'_x p'_x}(\overline{\kappa})$ for the directional spectrum model with $\Delta x/\lambda$ calculated for 3 different values of $\overline{a}$. It can be noticed that some attenuation occurs for the spectral amplitudes as $\Delta x/\lambda$ increases. The variation of the real parts and absolute values of $S_{p'_x p'_x}(\overline{\kappa})$, evaluated for the unidirectional as well as the directional spectrum model and the coherence function model is shown in Figs. 6.23 and 6.24, respectively. It can be
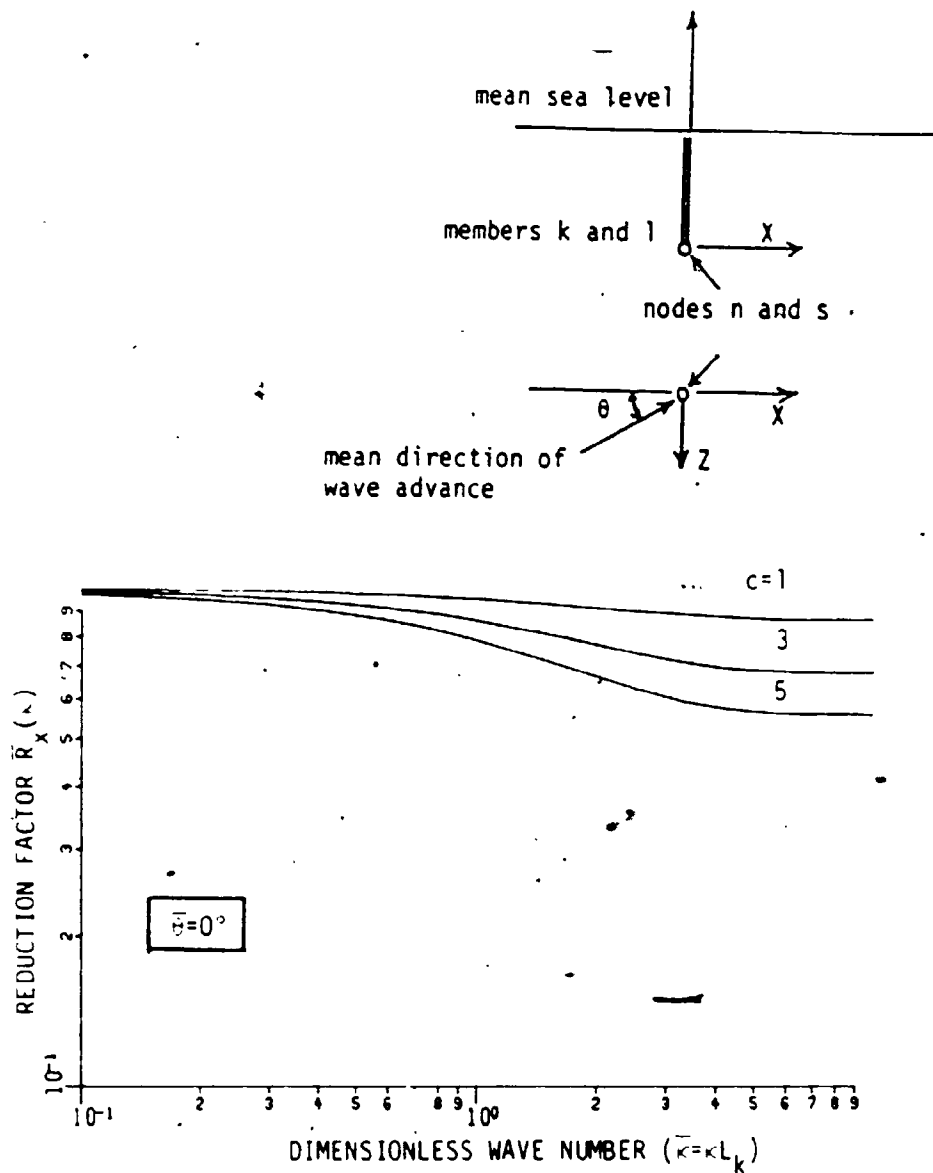
Figure 6-19: Variation in the Reduction of Along Wave Force Spectrum with Dimensionless Wavenumber (Coherence Function Model)
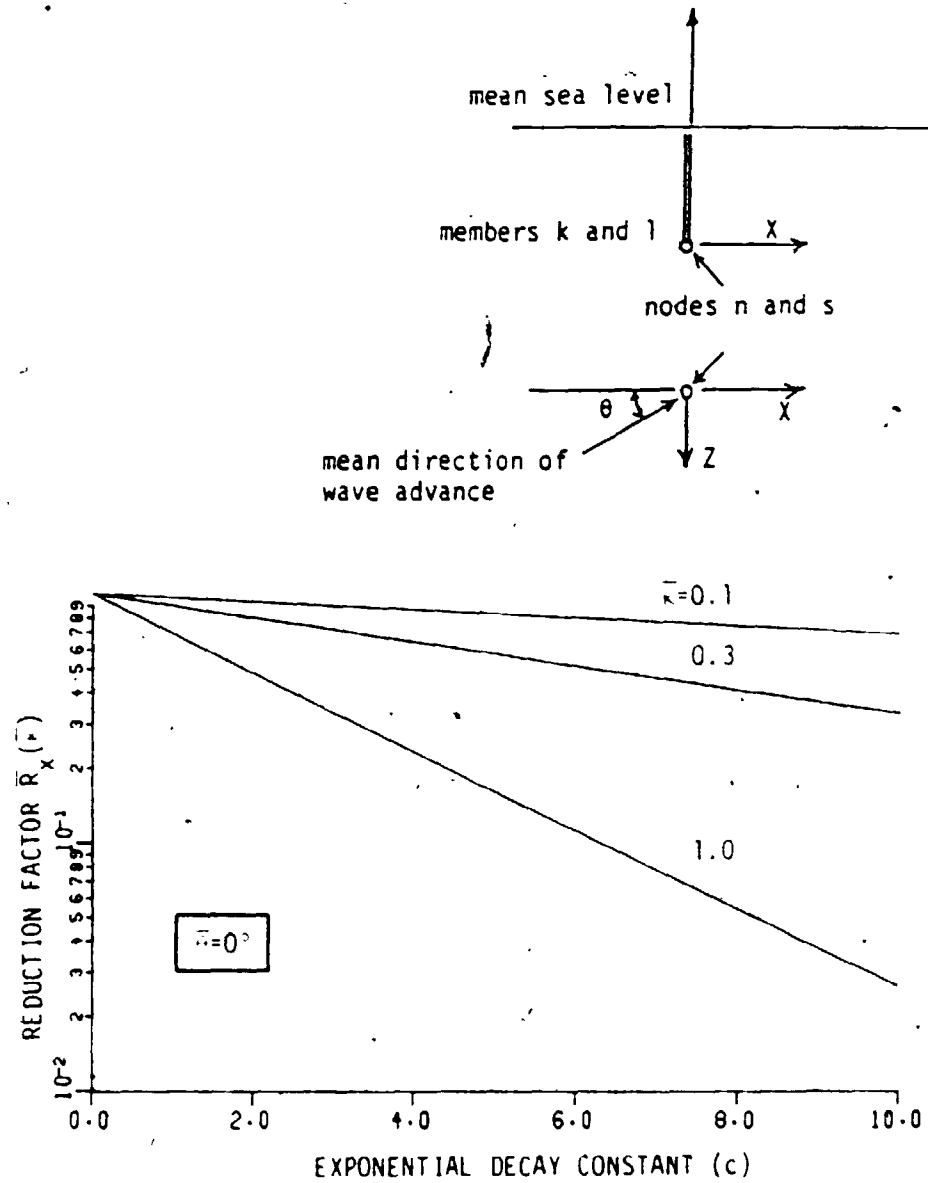
Figure 6-20: Variation in the Reduction of Along Wave Force Spectrum, for Two Vertical Parallel Elements, with Exponential Decay Constant (Coherence Function Model)
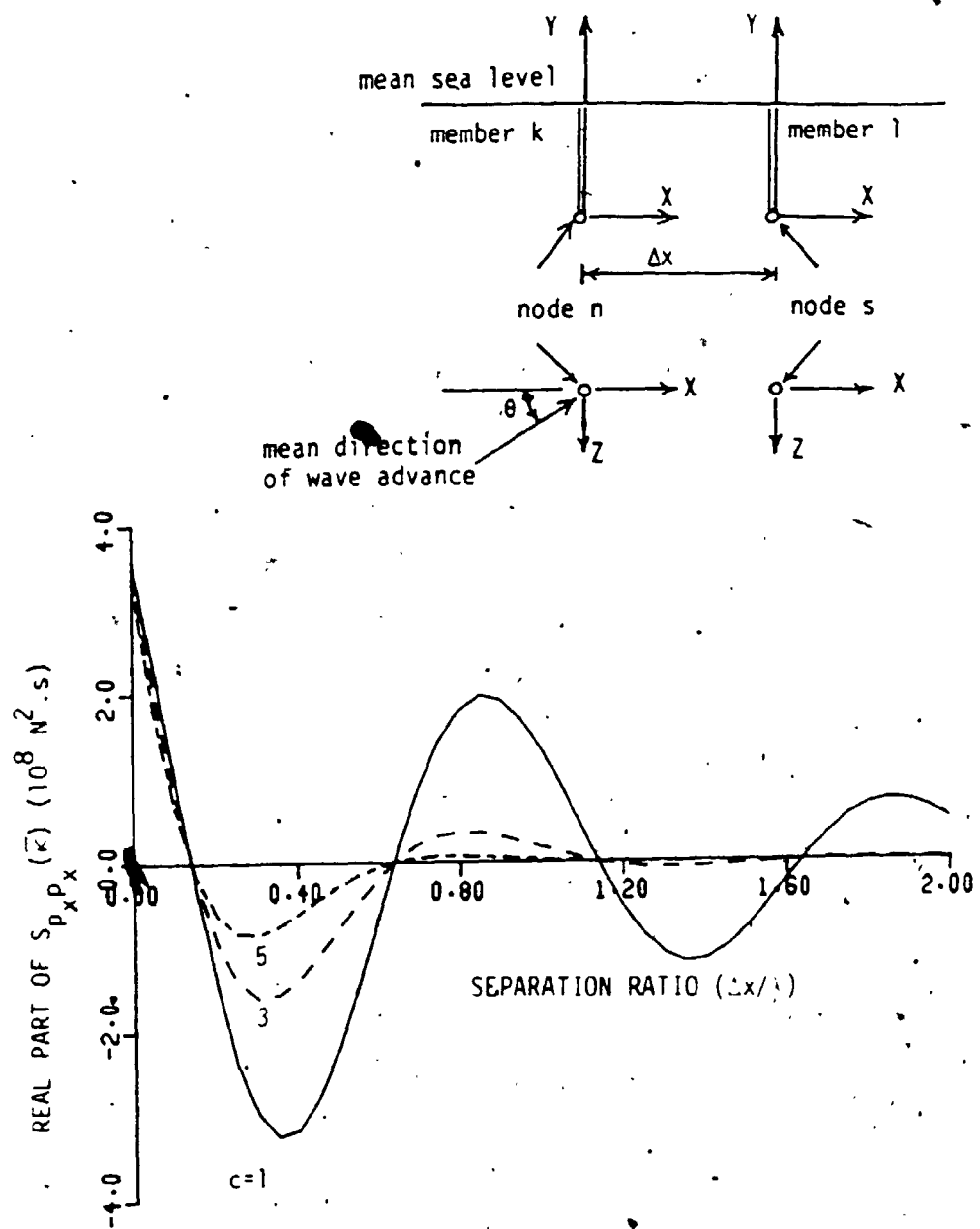
Figure 6-21: Variation in the Real Part of Along Wave Force Spectrum with Separation to Wave Length Ratio (Coherence Function Model)

172
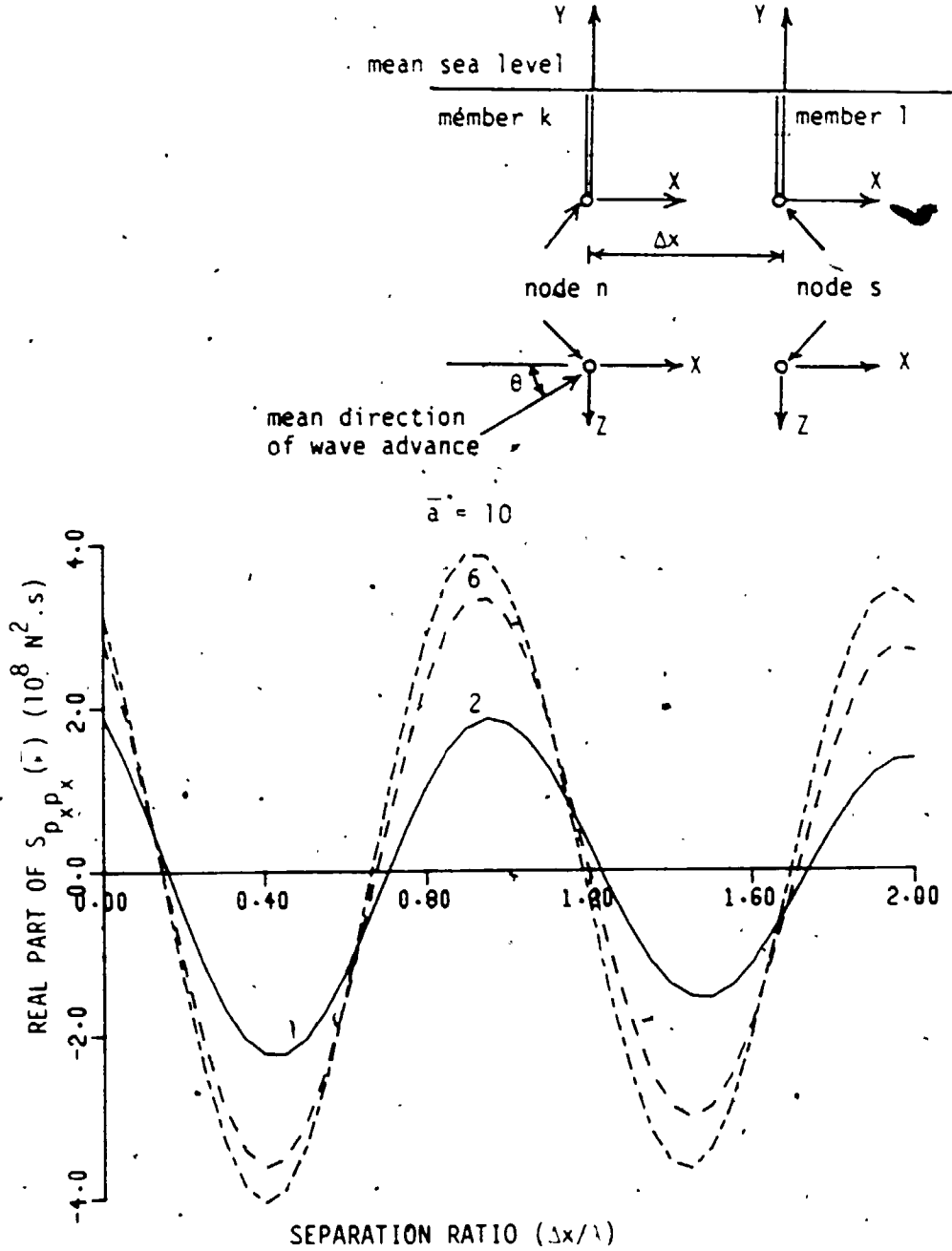
Figure 6-22: Variation in the Real Part of Along Wave Force Spectrum with Separation to Wave Length Ratio (Directional Spectrum Model)

noticed that no attenuation of the spectral amplitudes occur for the fully correlated model. From Figs. 6.21 to 6.24, it can be seen that the attenuation of the spectral amplitudes evaluated using the coherence function model is almost exponential and is sensitive to the value of the constant c. On the other hand, the attenuation obtained using the directional spectrum model is almost linear. The parameters of both models can be chosen such that a similar attenuation is obtained by both models in a certain range of $\Delta x/\lambda$.

6.6.2.3. Effect of Lumping the Members at the Nodes

The reduction factor R_{x_o}, defined by Eq. 6.81, is plotted versus the exponential decay costant c in Fig. 6.25 for 3 different values of $\overline{k}$. Since the member is extending vertically above the node, the ratio R_{x_o} is expected to be less than one for well correlated waves (large wavelengths and smaller values of c). However, R_{x_o} may exceed unity for higher values of c since the approximate velocity values are not reduced by the lack of spatial correlation when the two members coincide. R_{x_o} varies linearly with the constant c and has higher values for longer wave lengths. Shown in Fig. 6.26 is the variation in R_{x_o} with $\overline{k}$ for 3 different values of c at $\overline{\theta}=0°$. R_{x_o} decreases moderately with $\overline{k}$ for longer wave lengths ($\overline{k} \to 0$) and then drops sharply with $\overline{k}$ at higher frequencies due to the exponential velocity profile at these frequencies.

Fig. 6.27 shows the variation in R_{x_o} calculated for the coherence function model ($c=5$) as well as the directional spectrum model (for any value of $\overline{a}$), with $\overline{k}$. Both models give comparable results for R_{x_o} in the range of $\overline{k}=0.1$ to 1.0.
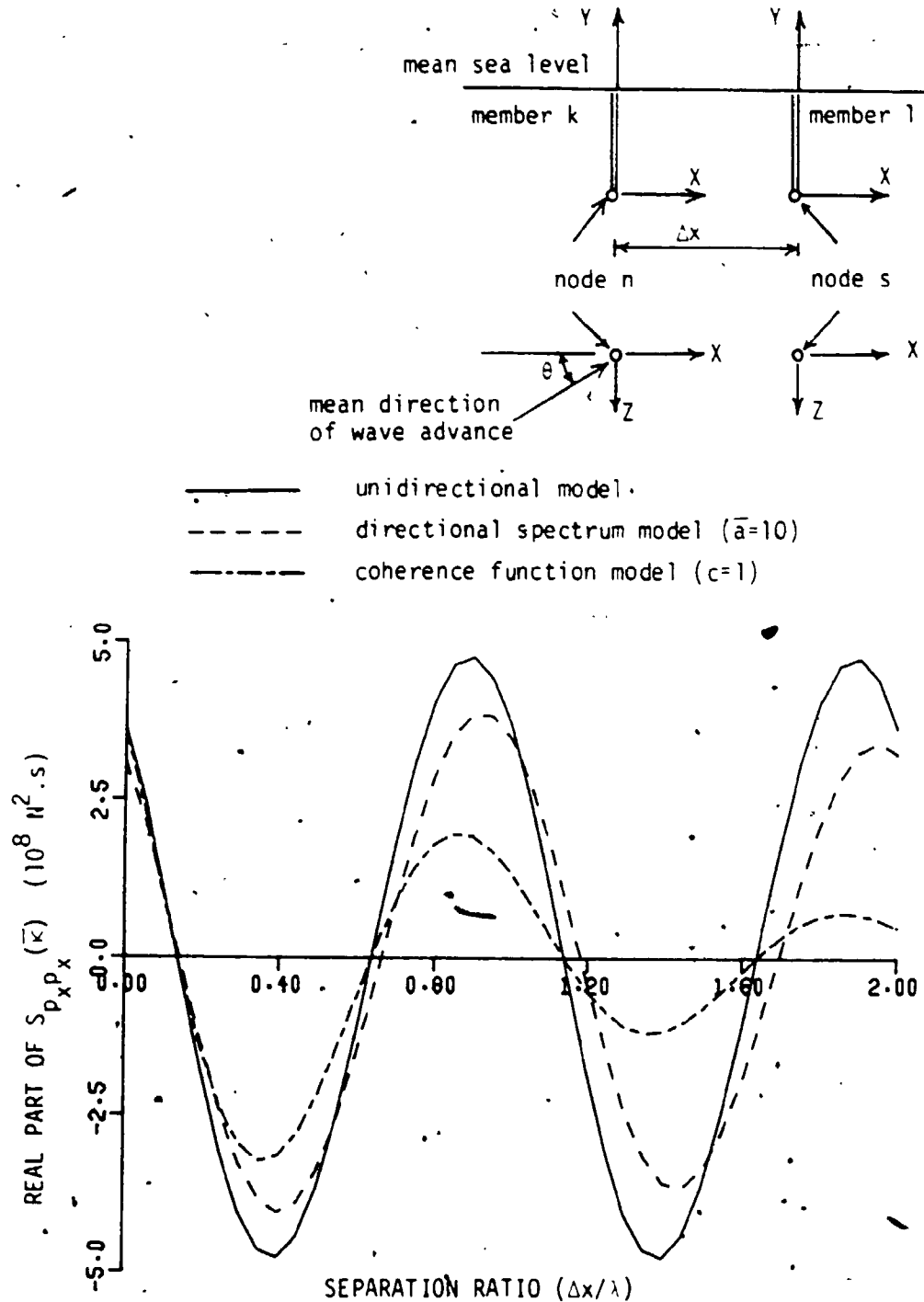
Figure 6-28: Variation in the Real Part of Along Wave Force Spectrum with Separation to Wave Length Ratio (Comparison Between Three Models)
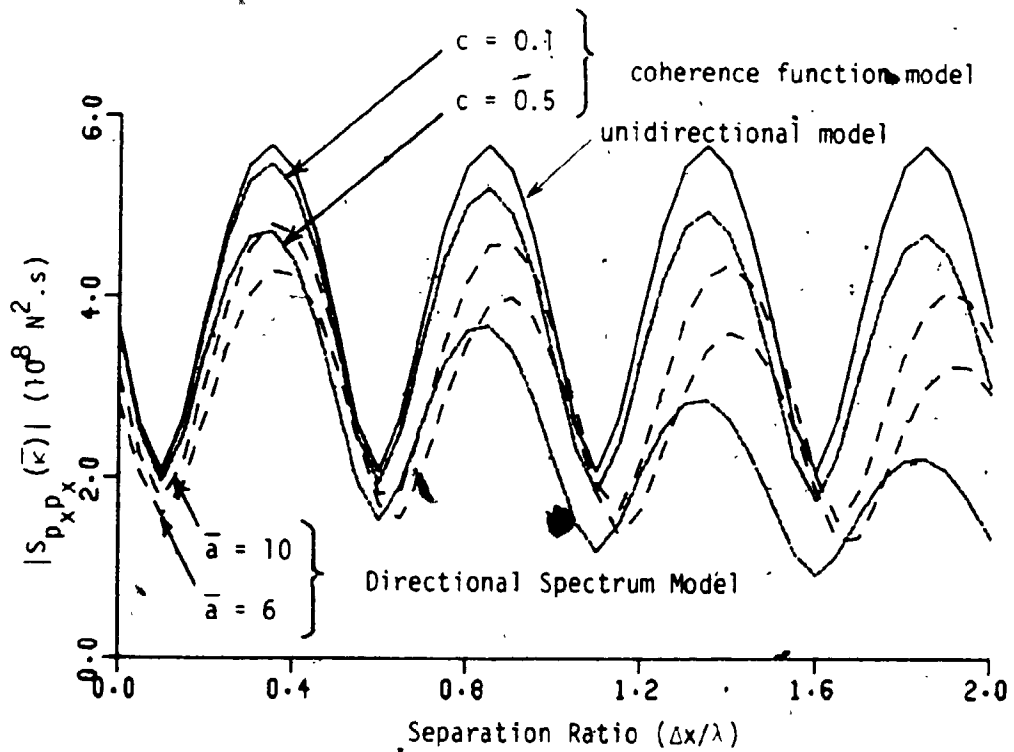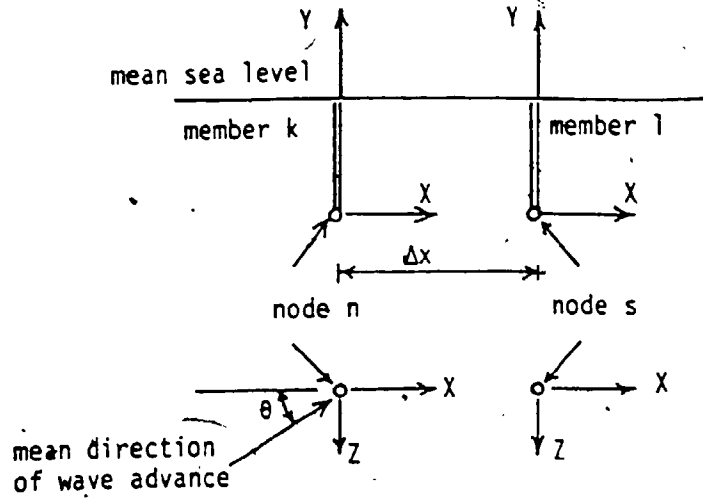
Figure 6-24: Variation in the Absolute Value of Along Wave Force
Spectrum with Separation to Wave Length Ratio (Comparison
Between Three Models)

mean sea level

members k and l

nodes n and s

θ

mean direction of
wave advance

$\bar{\kappa}=0.1$

0.3

1.0

$\bar{\theta}=0°$

APPROXIMATION RATIO $R_{xo}(\bar{\kappa})$

EXPONENTIAL DECAY CONSTANT (ℓ)
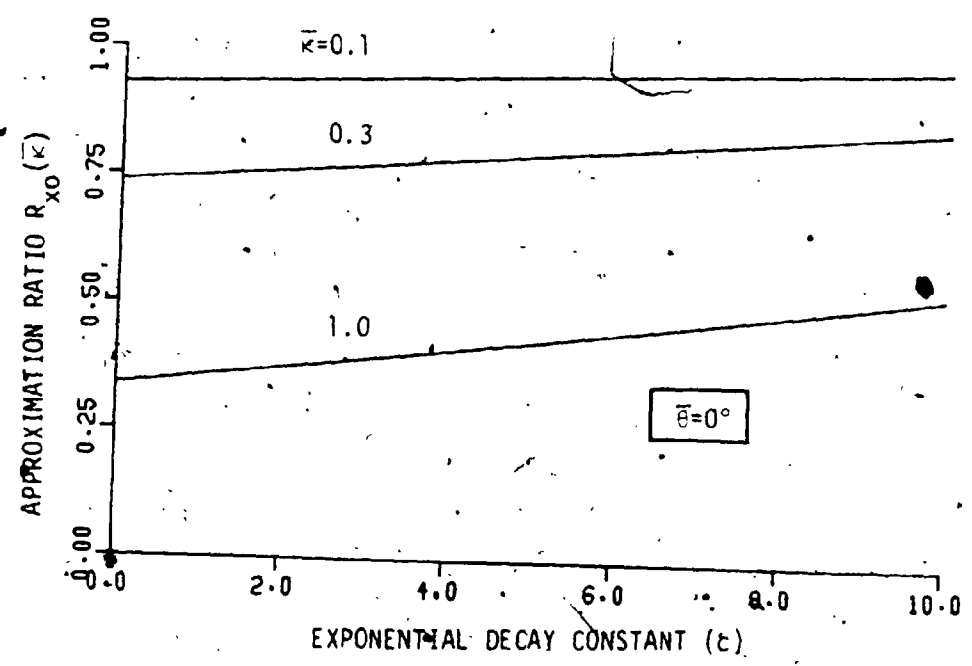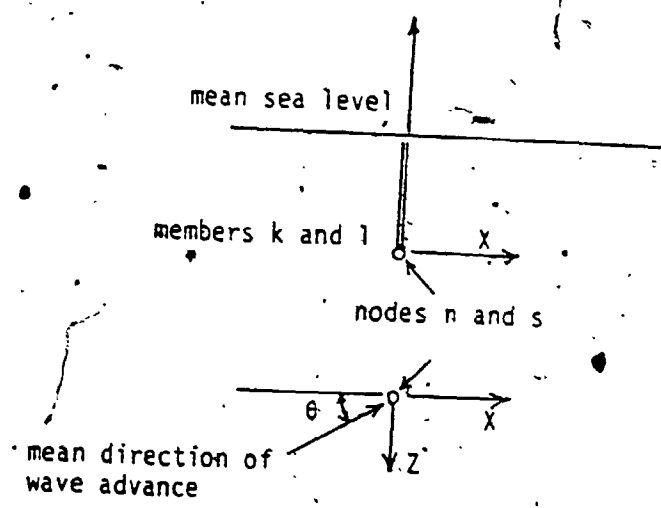
Figure 6-25: Variation in the Approximation Ratio R_{x_o} with Exponential
Decay Constant (Coherence Function Model)

Figure 7-2: Cartesian Coordinate System

mean sea level

members k and l

nodes n and s

θ

X

Z

mean direction of wave advance

c=1

3

5

$\overline{\theta}=0°$

APPROXIMATION RATIO $R_{xo}(\overline{\kappa})$

10^{-1}

2

10^0

2 3 4 5 6 7 8 9
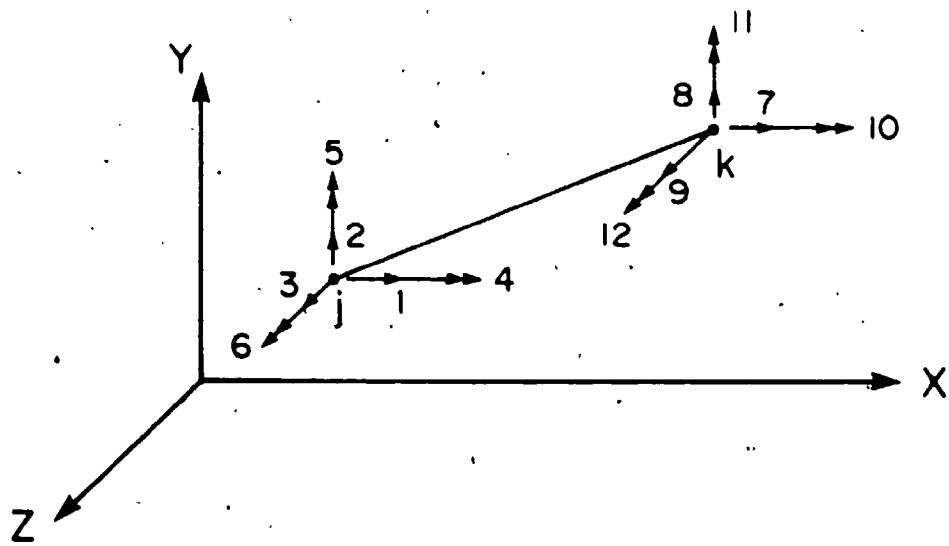
DIMENSIONLESS WAVE NUMBER $(\overline{\kappa}=\kappa L_k)$
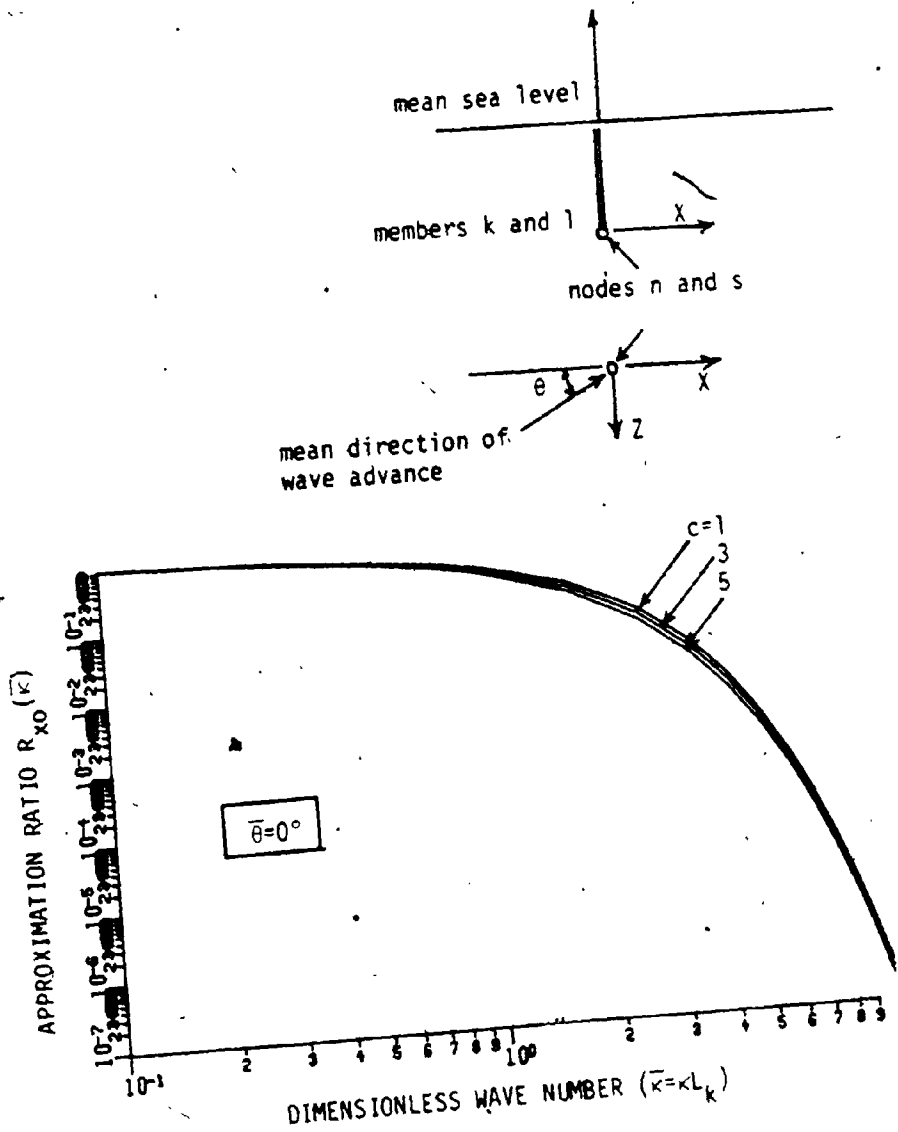
Figure 6-26: Variation in the Approximation Ratio R_{x_o} with Dimensionless Wavenumber (Coherence Function Model)

mean sea level

members k and l

nodes n and s

θ

mean direction of wave advance

APPROXIMATION RATIO $R_{xo}(\bar{\kappa})$

any value of $\bar{a}$

coherence function model (c = 5)

directional spectrum model (any value of $\bar{a}$)

DIMENSIONLESS WAVE NUMBER ($\bar{\kappa} = \kappa L_k$)
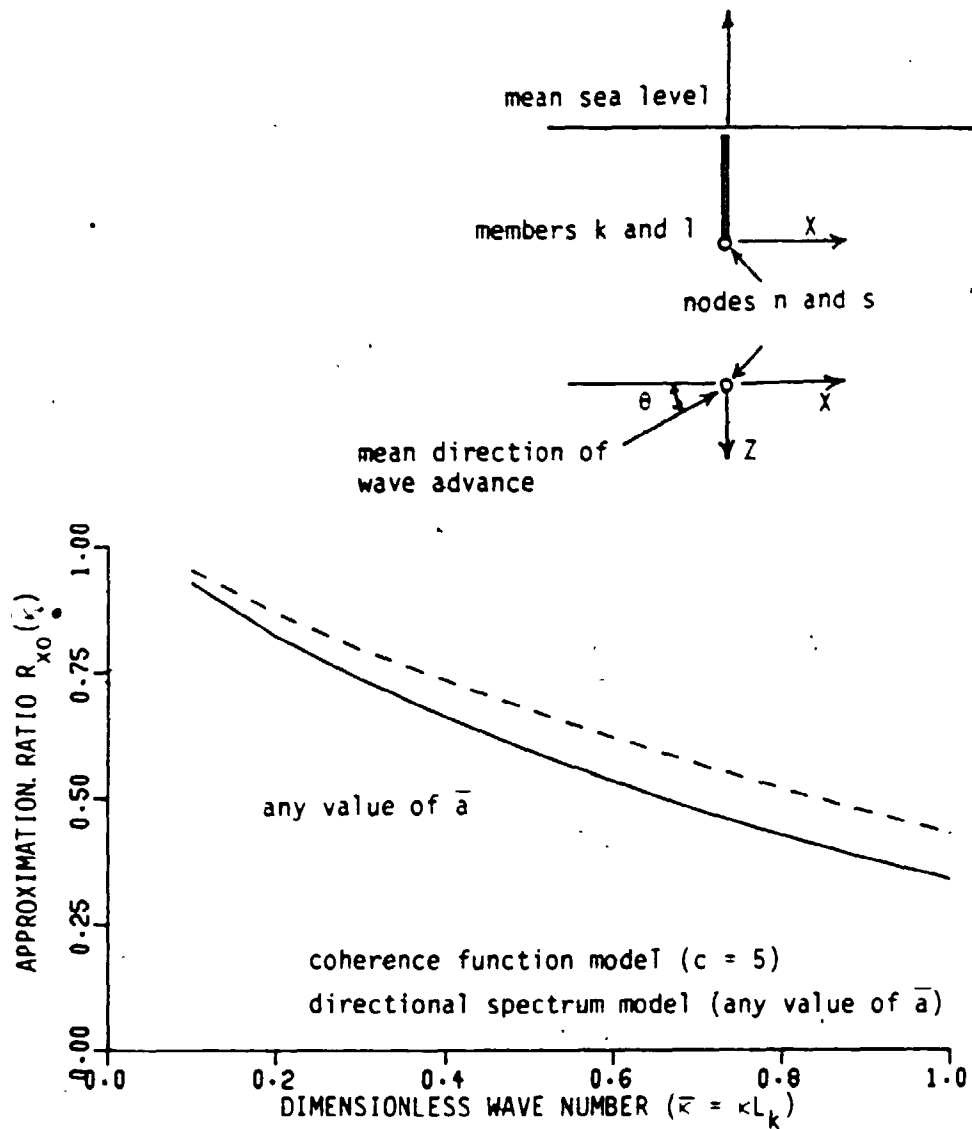
Figure 6-27: Variation in the Approximation Ratio R_{x_o} with Dimensionless Wavenumber (Comparison of Both Models)

6.7. Conclusions

Spectra of wave forces on members of offshore structures are derived considering the cross spectra of water particle kinematics to vary with position along the members. The standard directional spectrum is first utilized to represent the cross spectra of water particle kinematics and the resulting expressions for the spectra of wave forces are hence termed the directional spectrum model. An alternative representation of the cross spectra of water particle kinematics, based on a coherence function, is suggested and the resulting expressions are termed the coherence function model. Three important quantities are evaluated using both models and the results are compared for vertical members which are associated with the largest diameters. A parametric study is carried out to examine the variation of each of these quantities with the independent parameters and the following conclusions emerge:

1. The across wave force component evaluated from the directional spectrum model is generally small, typically about 6 % of the along wave force component. The coherence function model, fails to represent this component.

2. When the mean direction of wave advance makes an angle in the range of 15° to 75° with the X axis, where both force components are important, both models give close values for the ratio between the two horizontal force components.

3. The error introduced in the results of both models by assuming a constant cross spectrum of water particle velocity along the members

    increases with the increase in dimensionless frequency $\bar{F}$. It is mainly due to the rapid decay of the velocity profile with depth at high dimensionless frequencies. This error tends to -be cancelled when evaluating the wave forces for the whole structure as some tributary lengths are above the nodes and some are below the nodes.

4. The values of the exponential decay constant may be established to give a reduction in the along wave forces comparable to that due to directional spread at a specific value of the directional spread constant.

5. While the fully correlated model does not produce an attenuation in the wave forces with the increase in separation to wave length ratio $(\Delta r/\lambda$, both of the directional spread and coherence function models result in some attenuation with the increase in $\Delta r/\lambda$. The degree of this attenuation depends on the chosen values of the model constants.

6. For a certain separation between two members, the attenuation of wave forces is small for the peak waves of the extreme storm conditions and may be neglected. However, for smaller everyday waves which control fatigue life estimation, such attenuation is important and is easier calculated using the coherence function model.

Chapter Seven
Response To Random Wave Forces

7.1. Introduction

Accurate prediction and measurement of natural frequencies, damping ratios and response amplitudes is of particular importance for offshore structures. Monitoring of natural frequencies of the structure allows the detection of damage of the structure and foundation that might have occured. However, to be able to use the monitoring data in a meaningful sense, all the parameters affecting the natural frequencies should be known and their influence well understood. Modal damping ratios are also important since they control the dynamic magnification at the natural frequencies.

Prediction of the above mentioned quantities depends on the accuracy of the input parameters, on the mathematical models used to represent the system and the method employed to solve the governing equations. Due to the large uncertainties associated with many of the input parameters (such as dynamic soil properties, drag and inertia coefficients and description of the sea states) more sophisticated models do not guarantee better results.

In this chapter, the governing equations of motion are formulated and the solution procedure is described. The superstructure is idealized as a space frame, masses are lumped at the structural nodes and structural damping is modeled by equivalent viscous damping. Natural frequencies, damping ratios and mode shapes are obtained by solving the equations of free vibration using the complex eigen value analysis. Spectra of the structural response to wave forces are evaluated using the modal superposition method. The response evaluation is carried out in an iterative procedure due to the dependence of the hydrodynamic damping on the structural displacements.

7.2. Structural Idealization

7.2.1. General

Structural members of an offshore tower behave linearly within a certain deformation range beyond which they behave nonlinearly. Popov et al. [164] examined the inelastic behaviour of fixed offshore towers under severe earthquake excitation and concluded that such an analysis is important to avoid unnecessarily high safety factors. Within the linear elastic range, the structural model has the least uncertainties and using space frame elements, assemblage of the stiffness matrix is straightforward.

For shallow water structures, the number of joints is small and the model nodes may coincide with the structural joints. Some simplification can be brought about for large deep water structures by considering an equivalent beam model where each vertical segment of the structure is replaced by an equivalent beam element. For analysis purposes, such simplifying idealizations have been used [165,166]. Berge et al. [143] assumed a rigid diaphragm at each horizontal level, thus limiting the number of nodes to one at each level. Penzien et al. [167,168] used an equivalent one dimensional model and assigned stiffness coefficients that are typical of real design values. However, these models might fail to account for soil-structure interaction in a realistic way. In particular, one dimensional models require improvements in order to account for pile-soil-pile interaction of flexible foundations.

In this study, the structure is idealized as a space frame as shown in Fig. 7.1. Each node has six degrees of freedom, 3 translations and 3 rotations. The global cartesian axes are X, Y and Z with the positive directions shown in Fig. 7.2.
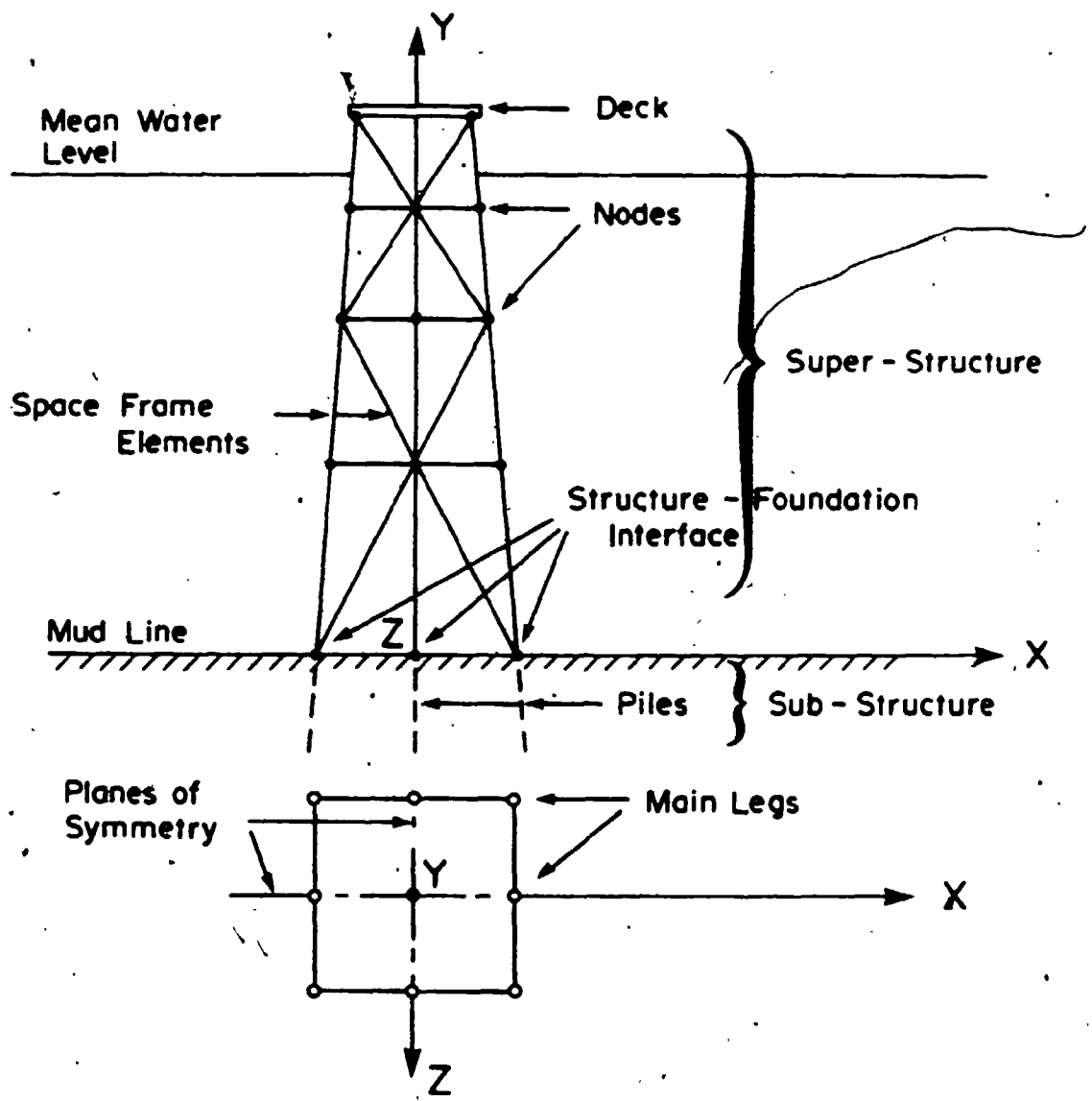
Figure 7-1: Offshore Tower Idealization
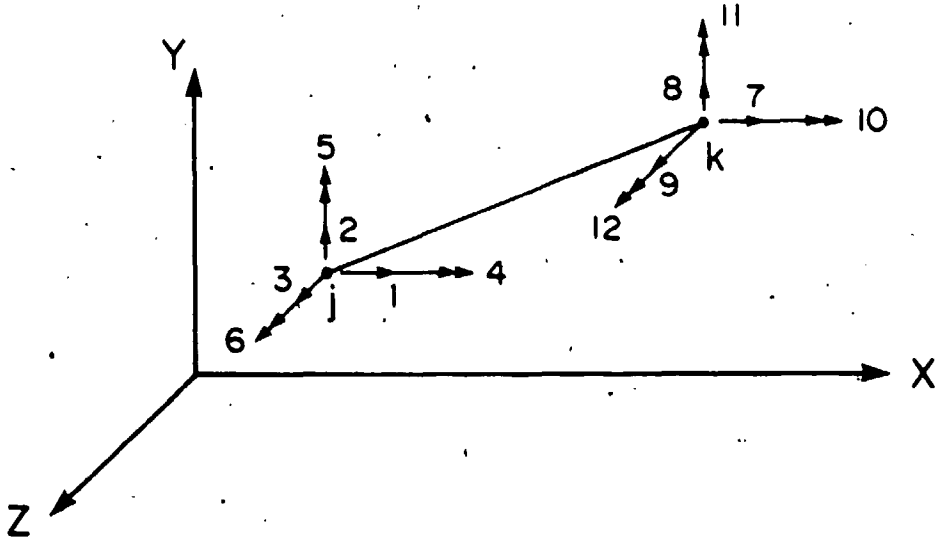
Figure 7-2: Cartesian Coordinate System

7.2.2. Stiffness, Mass and Damping Matrices

Formation of the global stiffness matrix follows the standard displacement method described in many texts, e.g. [169]. Inertia forces of the superstructure are considered through the use of either a lumped mass matrix or a consistent mass matrix. In a lumped mass matrix, masses of individual members are lumped at the nodes and their rotatory inertia ignored. The use of lumped masses tends to lower the natural frequencies as the mass is pushed to the extremeties of the members. A consistent mass matrix, on the other hand, is based on using the same shape functions as those used for evaluating the stiffness matrix [170]. Both methods often yield errors of about the same magnitude in beam problems [171]. An accurate method which takes into account the correct deformed shape under dynamic conditions is the dynamic stiffness method [172]. This method, however, complicates the eigen value analysis.

Extraction of the eigen values and eigen vectors is computationally expensive and a typical offshore tower might have too many degrees of freedom for an economic analysis. Given that only the first few modes are of importance, many of the degrees of freedom can be eliminated or condensed. Success of the condensation relies on the choice of the master degrees of freedom which should be associated with high mass to stiffness ratios and distributed throughout the structure [173].

In this study, the lumped mass matrix is used which is diagonal and the rotatory inertia of individual elements is neglected. Only translational d.o.f. are retained while the rotational ones are eliminated (condensed) except those at the foundation structure interface. These are important since they may be associated with a significant part of the overall flexibility and damping of the foundation especially for large diameter piles and pile clusters. With this idealization, the

mass matrix is readily condensed by omitting the zero rows and columns corresponding to the rotational d.o.f and the stiffness matrix is condensed using static condensation.

Structural damping (material damping) is hysteretic in nature and can be incorporated in the analysis using the complex structural stiffness matrix K_s^* defined by

$$K_s^* = K_s(1 + i2\beta) \tag{7.1}$$

where K_s is the real condensed stiffness matrix of the superstructure and β is the material damping ratio. The imaginary part of Eq. 7.1 represents the material damping. In this study, structural damping is expressed as equivalent viscous damping and the damping matrix of the superstructure C_s is given by

$$[C_s] = \frac{2\beta K_s}{\omega} \tag{7.2}$$

7.2.3. Symmetry

Significant reduction in the storage requirements and computation costs can be achieved in the analysis of structures which possess a symmetric configuration with regard to one or more vertical planes. In these cases, only part of the structure is assembled. For example, if the structure is symmetric with regard to 2 vertical planes, only one quarter is assembled and 4 cases of this model yield all the vibration modes. Two cases for the structure vibrating either symmetrically or antisymmetrically with respect to both planes and two cases for the structure vibrating symmetrically with regard to one plane and antisymmetrically with regard to the other [174].

For the superstructure this is achieved by imposing the appropriate boundary conditions on the d.o.f. falling on planes of symmetry or antisymmetry. Symmetry is taken into account for the foundation stiffness matrix by rewriting the foundation flexibility equation, Eq. 5.17, after equating the appropriate

degrees of freedom according to the vibration mode under consideration. When one of the piles falls on one of the planes of symmetry, its rigidity is halved since only one half of it is considered with the assembled part of the structure In a flexibility formulation this corresponds to doubling its flexibility.

7.3. Governing Equations of Motion

With the foundation model defined in Chapter 5, the hydrodynamic forces formulated in Chapter 6 and the structural idealization illustrated in Section 7.2, the equations of motion of an offshore tower subjected to wave forces are written as

$$[M_a]\{\ddot{u}\} + [C]\{\dot{u}\} + [K]\{u\} = \{W(t)\} \tag{7.3}$$

In Eq. 7.3, $[K]$ is the sum of the stiffness matrices of the structure $[K_a]$ and the foundation $[K_b]$. $[C]$ is the sum of the damping matrices of the structure $[C_a]$ and the foundation $[C_b]$ and $[M_a]$ is the structural lumped mass matrix. $\{u\}$, $\{\dot{u}\}$ and $\{\ddot{u}\}$ are the vectors of structural displacements, velocities and accelerations, respectively. Finally, the vector $\{W(t)\}$ is the vector of wave forces whose individual elements are defined by Eq. 6.49, i.e.

$$W_i(t) = \sum_{k=1}^{N_n} \Gamma_k \int_0^{L_k} \{\rho\pi\frac{d_k^2}{4}C_M(S_k)\ddot{v}(S_k,t) \tag{7.4}$$

$$-\rho\pi\frac{d_k^2}{4}[C_M(S_k)-1]\ddot{u}(S_k,t)$$

$$+\frac{1}{2}\rho d_k C_D(S_k)|\dot{v}(S_k,t)-\dot{u}(S_k,t)|[\dot{v}(S_k,t)-\dot{u}(S_k,t)]\}dS_k$$

In Eq. 7.4, ρ is the water density, d_k, L_k and δ_k are the diameter , tributary length and element coordinate of member k, respectively, and N_n is the number of members attached to joint n at which d.o.f. i is stationed. C_M and C_D are the inertia and drag coefficients which may vary with depth but in this study they are assumed to be constant with the respective values of 1.4 and 2. The projected area factor Γ_k is given by Eq. 6.50.

The drag component of the total wave forces in Eq. 7.4 is nonlinear and has to be linearized for the spectral analysis to be possible. In this study, the linearized drag force is obtained using the equivalent linearization technique discussed in Section 6.2. One method of solving Eq. 7.3 in its nonlinear form is the numerical integration of the equations of motion in the time domain. This has been attempted by Godeau and Deleuil [175], however, in addition to the high computational costs involved, there is some difficulty associated with interpreting the resulting response time histories.

Taylor and Rajagopalan [176] used a random vibration approach and a perturbation technique to examine the effects of the nonlinear drag term on the response spectra. The same authors utilized a narrow band approximation of the response together with the Fokker-Plank equation to obtain estimates of the effective hydrodynamic damping and probability densities of the response quantities [177]. Due to nonlinearity, subharmonic resonances occur at frequencies three times the frequency of the loading function. Most fixed offshore towers have their fundamental frequencies close to these secondary peaks in the force spectra which might lead to an increase in the resonant response. This is particularly important for fatigue life estimation. They also concluded that the hydrodynamic damping evaluated from a linearized analysis is close to that evaluated considering the higher order approximations.

When the drag force is linearized using Eq. 6.5, the linearized nodal load $W_i(t)$ is given by Eq. 6.52 and by transfering the added mass and hydrodynamic damping to the left hand side of the equations of motion, Eq. 7.3 is rewritten as

$$[K]\{u\} + [C]\{\dot{u}\} + [M]\{\ddot{u}\} = \{P(t)\} \qquad (7.5)$$

where $[K]$ is given by

$$[K] = [K_s] + [K_b] \qquad (7.6)$$

and the foundation stiffness matrix is given by Eq. 5.16. The total damping matrix $[C]$ is

$$(7.7)$$

$$[C] = [C_s] + [C_b] + [C_{H}]$$

In which the structural damping matrix $[C_s]$ is given by Eq. 7.2, the foundation damping matrix $[C_b]$ is the equivalent viscous damping of the foundation system, defined as

$$[C_b] = Im\{[F_b]^{-1}\}/\omega \qquad (7.8)$$

where the complex foundation flexibility matrix $[F_b]$ is given by Eq. 5.17 and the hydrodynamic damping matrix $[C_{H}]$ is a diagonal matrix with elements

$$(C_{H})_{ii} = \sum_{k=1}^{N_n} \frac{1}{2}\rho C_D d_k \sqrt{8/\pi}\, \sigma_{r_i} \Gamma_k L_k \qquad (7.9)$$

In Eq. 7.9, σ_{r_i} is the standard deviation of the relative velocity r_i between the structure and the water particles at the position and direction of d.o.f. i. $[M]$ is the total mass matrix which is the sum of the structural diagonal mass matrix and the added mass matrix which is also diagonal, i.e.

$$(M_a)_{ii} = \sum_{k=1}^{N_n} \rho(C_M - 1)\pi\frac{d_k^2}{4}\Gamma_k L_k \qquad (7.10)$$

In Eq. 7.5, the stiffness and damping matrices are frequency dependent as they include the foundation properties. One way of solving Eq. 7.5 is the frequency response method, e.g. [64]. In this method, the time dependent forcing vector is Fourier transformed into a set of discrete harmonic components. The response to each of these components, which is also harmonic, is obtained by solving the resulting set of linear simultaneous algebraic equations giving the frequency responses of different degrees of freedom. Time histories of the responses can be obtained as the inverse Fourier transforms of the frequency response amplitudes of each degree of freedom and the power spectral density of the response is obtained from the standard relationship with the Fourier transform. The frequency response method, which has been employed by Penzien

[67] and by Angelides [166], is suitable for systems with frequency dependent properties. However, when the number of degrees of freedom is large, this method becomes computationally expensive and the modal superposition method is prefered specially when the response is dominated by the first few modes.

Solution of the equations of free vibration is the first step in modal analysis as it provides the natural frequencies, mode shapes and the modal damping ratios. However, due to the non proportionality of damping, classical normal modes do not uncouple the damping matrix. This difficulty has been surpassed by Malhotra and Penzien [133] who assumed a diagonal damping matrix (to uncouple the modes) whose terms are evaluated by optimizing the resulting error using the least square minimization technique. Foster [144] used the nonclassical complex eigen valued modal superposition to uncouple the equations of motion. In this study, the modal superposition method is used and the complex eigen value approach is used to solve the equations of free vibration. Foundation stiffness and damping matrices are evaluated at the first natural frequency which is obtained by iteration starting with undamped system and classical analysis.

7.4. Free Vibration Analysis

Equations of motion for the free vibration are obtained from Eq. 7.5 by setting $\{P(t)\}$ to zero, i.e.

$$[K]\{u\} + [C]\{\dot{u}\} + [M]\{\ddot{u}\} = \{0\} \tag{7.11}$$

The complementary function of the reduced equation, Eq. 7.11, is sought in the form

$$\{u\} = \{\phi\}e^{\lambda t} \tag{7.12}$$

where $\{\phi\}$ is a vector of constants and λ should satisfy the characteristic equation obtained on substituting by Eq. 7.12 into Eq. 7.11, i.e.

$$(\lambda^2[M] + \lambda[C] + [K])\{\phi\} = \{0\} \tag{7.13}$$

Eq. 7.13 is a set of algebraic equations of order N in λ^2 whose solution in this

form is tedious and not amenable to the algorithms developed for solving the standard and the generalized eigen value problems.

A method has been suggested whereby a set of N second order linear differential equations (L.D.E.) is transformed into a set of $2N$ first order L.D.E. [178,179]

$$[A]\{\dot{q}\} + [B]\{q\} = \{0\} \tag{7.14}$$

in which

$$\{q\} = \begin{Bmatrix} \{\dot{u}\} \\ \{u\} \end{Bmatrix} \tag{7.15}$$

and the matrices $[A]$ and $[B]$ are given by

$$[A] = \begin{bmatrix} [0] & [M] \\ [M] & [C] \end{bmatrix} \tag{7.16}$$

and

$$[B] = \begin{bmatrix} -[M] & [0] \\ [0] & [K] \end{bmatrix} \tag{7.17}$$

The solution to Eq. 7.14 is sought in the form

$$\{q\} = \{\Phi\}e^{\mu t} \tag{7.18}$$

Substituting Eq. 7.18 in Eq. 7.14 yields

$$\mu[A]\{\Phi\} + [B]\{\Phi\} = \{0\} \tag{7.19}$$

which is the generalized eigen value problem.

Solution of Eq. 7.19 yields N pairs of complex conjugate eigen values and N pairs of complex conjugate eigen vectors. The complex eigen values can be expressed in the form

$$(\mu_j)_{1,2} = -\varsigma_j \omega_j' \pm \iota \omega_j \sqrt{1 - \varsigma_j^2} \tag{7.20}$$

from which the modal damping is easily extracted [180]. Eq. 7.20 is formally identical to the solution of the free damped vibration of a single degree of freedom system. From Eq. 7.20, the damped frequency ω_j' is given by

$$\omega'_j = \omega_j \sqrt{1-\zeta_j^2} = Im[\mu_j]$$

(7.21)

and the jth modal damping ratio is given by

$$\zeta_j = \frac{-Re[\mu_j]}{|\mu_j|}$$

(7.22)

where Re and Im indicate the real and imaginary parts, respectively. This method has been used in soil-structure interaction problems. e.g. [181,182] and is also used in this study as it establishes the modal damping ratios accurately. More details on this method can be found in [181].

7.5. Response to Wave Forces

With the natural frequencies, modal damping ratios and mode shapes evaluated, the solution proceeds by making a coordinate transformation from the kinematic degrees of freedom to the generalized coordinates.i.e.

$$u_i(t) = \sum_{j=1}^{N} \phi_{ij} \eta_j(t)$$

(7.23)

where ϕ_{ij} is the modal coordinate associated with d.o.f. i in mode j and $\eta_j(t)$ is the generalized coordinate of mode j. Expressed in matrix notation, Eq. 7.23 becomes

$$\{u(t)\} = [\Phi]\{\eta(t)\}$$

(7.24)

where $[\Phi]$ is the modal matrix containing all the mode shapes. If undamped modes are used, in Eq. 7.24, $\{u(t)\}$ is a vector with N elements where N is the total number of unrestrained degrees of freedom. N' depends on the applied boundary conditions according to the specific vibration mode. From the theory of random vibration, the spectral density of the response at d.o.f. i, $S_{u_i u_i}(\omega)$ is

$$S_{u_i u_i}(\omega) = \sum_{j=1}^{N} \sum_{r=1}^{N} \phi_{ij} \phi_{ir} S_{\eta_j \eta_r}(\omega)$$

(7.25)

where $S_{\eta_j \eta_r}(\omega)$ is the cross spectrum of the generalized coordinates $\eta_j(t)$ and $\eta_r(t)$, and is given by

$$S_{\eta_j \eta_r}(\omega) = H_j^*(\iota\omega)H_r(\iota\omega)S_{F_j F_r}(\omega) \qquad (7.26)$$

In Eq. 7.26, $H_j(\iota\omega)$ and $H_r(\iota\omega)$ are the mechanical admittance functions of modes j and r respectively, and $S_{F_j F_r}(\omega)$ is the cross spectrum of the generalized forces $F_j(t)$ and $F_r(t)$, respectively.

For a system with discretized nodal loads, such as the one under consideration, the generalized force in mode j, $F_j(t)$, is

$$F_j(t) = \sum_{i=1}^{N} \phi_{ij} P_i(t) \qquad (7.27)$$

Hence, the cross spectrum of the generalized forces is

$$S_{F_j F_r}(\omega) = \sum_{i=1}^{N} \sum_{m=1}^{N} \phi_{ij} \phi_{mr} S_{P_i P_m}(\omega) \qquad (7.28)$$

In which $S_{P_i P_m}(\omega)$ is the cross spectrum of nodal loads $P_i(t)$ and $P_m(t)$ given by Eq. 6.58, namely

$$
\begin{aligned}
S_{P_i P_m} = \sum_{k=1}^{N_n} \sum_{l=1}^{N_s} \Gamma_k \Gamma_l \int_0^{L_k} \int_0^{l_l} \{ & \omega^2 \alpha_k \alpha_l S_{\dot{v}_1 \dot{v}_2}(S_k, S_l, \omega) \\
& + \alpha_k \beta_l \rho_{\dot{r}_m} [i\omega S_{\dot{v}_1 \dot{v}_2}(\dot{S}_k, S_l, \omega)]^* \\
& + \iota\omega \beta_k \alpha_l \rho_{\dot{r}_i} S_{\dot{v}_1 \dot{v}_2}(S_k, S_l, \omega) \\
& + \beta_k \beta_l \rho_{\dot{r}_i} \sigma_{\dot{r}_m} S_{\dot{v}_1 \dot{v}_2}(S_k, S_l, \omega) \} dS_l dS_k
\end{aligned}
\qquad (7.29)
$$

In Sections 6.5.2.3 and 6.6.2.3, the effects of using a stepwise approximation to the velocity field and lumping the areas and volumes of the members at the nodes on the evaluated force spectra were examined. It was shown that these approximations have little effect for longer waves where most of the wave energy lies and that the canceling effect tends to reduce the error. Adopting these approximations is computationally advantageous, therefore they are used in this study. Consequently, Eq. 6.53 reduces to

$$P_i(t) = \sum_{k=1}^{N_n} \Gamma_k L_k \{\alpha_k \ddot{u}_i(S_k, t) + \beta_k \sigma_{\dot{r}_i} \dot{v}_i(S_k, t)\} \tag{7.30}$$

and Eq. 7.29 reduces to

$$S_{P_i P_m}(\omega) = \sum_{k=1}^{N_n} \sum_{l=1}^{N_s} \Gamma_k \Gamma_l L_k L_l \{(\omega^2 \alpha_k \alpha_l + i\omega \beta_k \alpha_l \rho_{\dot{r}_i} \tag{7.31}$$
$$+ \beta_k \beta_l \rho_{\dot{r}_i} \sigma_{\dot{r}_m}) S_{\dot{v}_i \dot{v}_m}(\omega) + \alpha_k \beta_l \rho_{\dot{r}_m} [i\omega S_{\dot{v}_i \dot{v}_m}(\omega)]^*\}$$

Denote:

$$A_k = \sum_{k=1}^{N_n} \Gamma_k L_k \alpha_k \tag{7.32}$$

$$B_k = \sum_{k=1}^{N_n} \Gamma_k L_k \beta_k \tag{7.33}$$

$$A_l = \sum_{l=1}^{N_s} \Gamma_l L_l \alpha_l \tag{7.34}$$

$$B_l = \sum_{l=1}^{N_s} \Gamma_l L_l \beta_l \tag{7.35}$$

After rearranging the terms and substituting by Eqs. 7.32 to 7.35, Eq. 7.31 becomes

$$S_{P_i P_m}(\omega) = S_{\dot{v}_i \dot{v}_m}(\omega)[\omega^2 A_k A_l + i\omega \sigma_{r_i} B_k A_l + \sigma_{r_i} \sigma_{r_m} B_k B_l] \tag{7.36}$$
$$+ [i\omega S_{\dot{v}_i \dot{v}_m}(\omega)]^* \omega \sigma_{r_m} A_k B_l$$

All the quantities required to evaluate the response spectrum, Eq. 7.25, are now defined except for the standard deviation of the relative velocities. The variance of the relative velocity is obtained from its power spectrum, i.e.

$$\sigma_{\dot{r}_i}^2 = \int_0^\infty S_{\dot{r}_i \dot{r}_i}(\omega)\, d\omega \tag{7.37}$$

As

$$\dot{r}_i(t) = \dot{v}_i(t) - \dot{u}_i(t) \tag{7.38}$$

the power spectral density $S_{\dot{r}_i \dot{r}_i}(\omega)$ is expressed as

$$S_{r_i r_i}(\omega) = S_{v_i v_i}(\omega) + S_{u_i u_i}(\omega) - S_{v_i u_i}(\omega) - S_{u_i v_i}(\omega) \tag{7.39}$$

Noting that

$$S_{\dot{v}_i u_i}(\omega) = i\omega S_{v_i u_i}(\omega) \tag{7.40}$$

$$S_{u_i \dot{v}_i}(\omega) = -i\omega S_{u_i v_i}(\omega) \tag{7.41}$$

$$S_{\dot{u}_i \dot{u}_i}(\omega) = \omega^2 S_{u_i u_i}(\omega) \tag{7.42}$$

$$S_{v_i u_i}(\omega) = S_{u_i v_i}^{*}(\omega) \tag{7.43}$$

Eq. 7.39 can be rewritten as

$$S_{r_i r_i}(\omega) = S_{v_i v_i}(\omega) + \omega^2 S_{u_i u_i}(\omega) - 2\omega Im[S_{u_i v_i}(\omega)] \tag{7.44}$$

The cross spectrum of structural displacements and water particle velocity $S_{u_i v_i}(\omega)$ is given by [19]

$$S_{u_i v_i}(\omega) = \sum_{j=1}^{N} \sum_{l=1}^{N} \phi_{ij} \phi_{lj} H_j^{*}(i\omega) \{ C_M S_{\dot{v}_l v_i}(\omega) \tag{7.45}$$
$$+ \sqrt{8/\pi} C_D \sigma_{r_l} S_{v_l v_i}(\omega) \}$$

From Eqs. 7.37 and 7.44, the variance of the relative velocity is

$$\sigma_{r_i}^2 = \sigma_{\dot{v}_i \dot{v}_i m}^2 + \sigma_{u_i u_i}^2 - 2\omega \int_0^{\infty} Im\{S_{u_i v_i}(\omega)\} d\omega \tag{7.46}$$

7.6. Solution Procedure

The solution starts by assembling the stiffness, damping and mass matrices defined in Eq. 7.5. Solution of the free vibration problem is carried out using the complex eigen value analysis to establish the natural frequencies, mode shapes and modal damping ratios. For free vibration analysis in still water, water particle velocity v is assumed to be zero; then, the drag term is proportional to the square of the structural velocity $\dot{u}^2$ and due to its quadratic nature can be neglected for small amplitudes. However when evaluating the response of the structure to a certain sea state, hydrodynamic damping is considered in the analysis as it constitutes a major source of damping.

To examine the relative importance of the other two sources of damping, the

foundation modal damping ratios ς_{fj} and the structural modal damping ratios ς_{sj} are evaluated separately in the free vibration analysis. This is done by considering only the pertinent damping matrix for each case in Eq. 7.7. The structural modal damping ratios ς'_{sj} obtained in this manner are correct only for the first mode. For higher modes, the corrected structural damping ratios ς_{sj} are obtained from

$$\varsigma_{sj} = \varsigma'_{sj}\omega_1/\omega_j \qquad (7.47)$$

where ω_1 and ω_j are the natural frequencies of the structure at the first and j^{th} mode, respectively. Foundation damping ratios ς_{fj} obtained in this manner do not need this correction as the variation in stiffness and damping properties at low frequencies is very mild. However, the response is usually dominated by the first mode for real structures.

The response analysis proceeds by specifying the sea state (for fully developed seas, the sea state is completely specified by the characteristic wind speed U) and is performed in an iterative procedure. In the first cycle, structural velocities are assumed to be zero; then, $\sigma_{\dot{r}_i} = \sigma_{\dot{v}_i}$ and the hydrodynamic damping matrix $[C_H]$ can be evaluated using Eq. 7.9. A free vibration analysis is carried out to determine the hydrodynamic modal damping ratios ς_{hj}. This is done by setting the foundation and structural damping matrices to zero in Eq. 7.7. During each cycle the system is linear and superposition holds, thus the total modal damping ratio ς_j is the sum of the foundation, structural and hydrodynamic damping ratios, i.e.

$$\varsigma_j = \varsigma_{sj} + \varsigma_{fj} + \varsigma_{hj} \qquad (7.48)$$

Because of the iterative nature of the solution and to avoid excessive computational costs, the classical mode shapes are used in the evaluation of the response spectra, Eqs. 7.25, 7.27 and 7.45. This is a reasonable approximation because the difference between classical and nonclassical mode shapes is

significant only for systems with high damping ratios and for higher modes. After the response spectra are evaluated, new values of the variances of relative velocities are evaluated and another cycle of iteration is carried out. The iteration procedure is terminated when convergence is achieved according to the following criterion

$$\frac{\|\sigma_r^{(k)} - \sigma_r^{(k-1)}\|_2}{\|\sigma_r^{(k)}\|_2} \leq \epsilon \tag{7.49}$$

where ϵ is a specified tolerance, k denotes the iteration number and the vector norm $\|\sigma_r\|$ is defined by

$$\|\sigma_r\|_2 = (\sum_{i=1}^{N} \sigma_r^2)^{0.5} \tag{7.50}$$

The results of this analysis are presented in detail in the next chapter for a jacket type offshore tower.

Chapter Eight
Examples and Parametric Studies

8.1. Introduction

The procedures described in Chapters 5, 6 and 7 are used to analyse a typical offshore tower in order to determine the effect of the system parameters on the response quantities. The tower, shown in Fig. 8.1, is 122 m high and stands in 104 m of water. It is supported by 10 piles, each having an outer diameter of 1.45 m and a penetration depth of 50 m. Six main piles extend through the main legs all the way to the top of the tower and 4 skirt piles are cut off and welded at the level of the first bracing. To save on computational costs, members of the deck section are not idealized individually and their mass and stiffness are lumped and accounted for by assigning high stiffness and mass values to the members at the tower top level.

The tower is symmetric about both axes X and Z and to take advantage of symmetry, only one quarter of the structure is modeled. Figs. 8.2 and 8.3 show the member numbering in the assembled quarter and their properties are shown in Table 8.1. Members 11, 28, 40, 51 and 52 are assigned high stiffness and mass values to account for the unmodeled deck section. Two sets of boundary conditions are applied which give the required mode shapes:

1. X is an axis of symmetry and Z is an axis of antisymmetry; these conditions yield the lowest natural frequency of the structure which is associated with the sway in direction X.

2. Both X and Z are axes of symmetry; these conditions yield the torsional mode.

Sway in the Z direction is obtained by considering Z to be an axis of symmetry and X an axis of antisymmetry. However, sway in the Z direction is
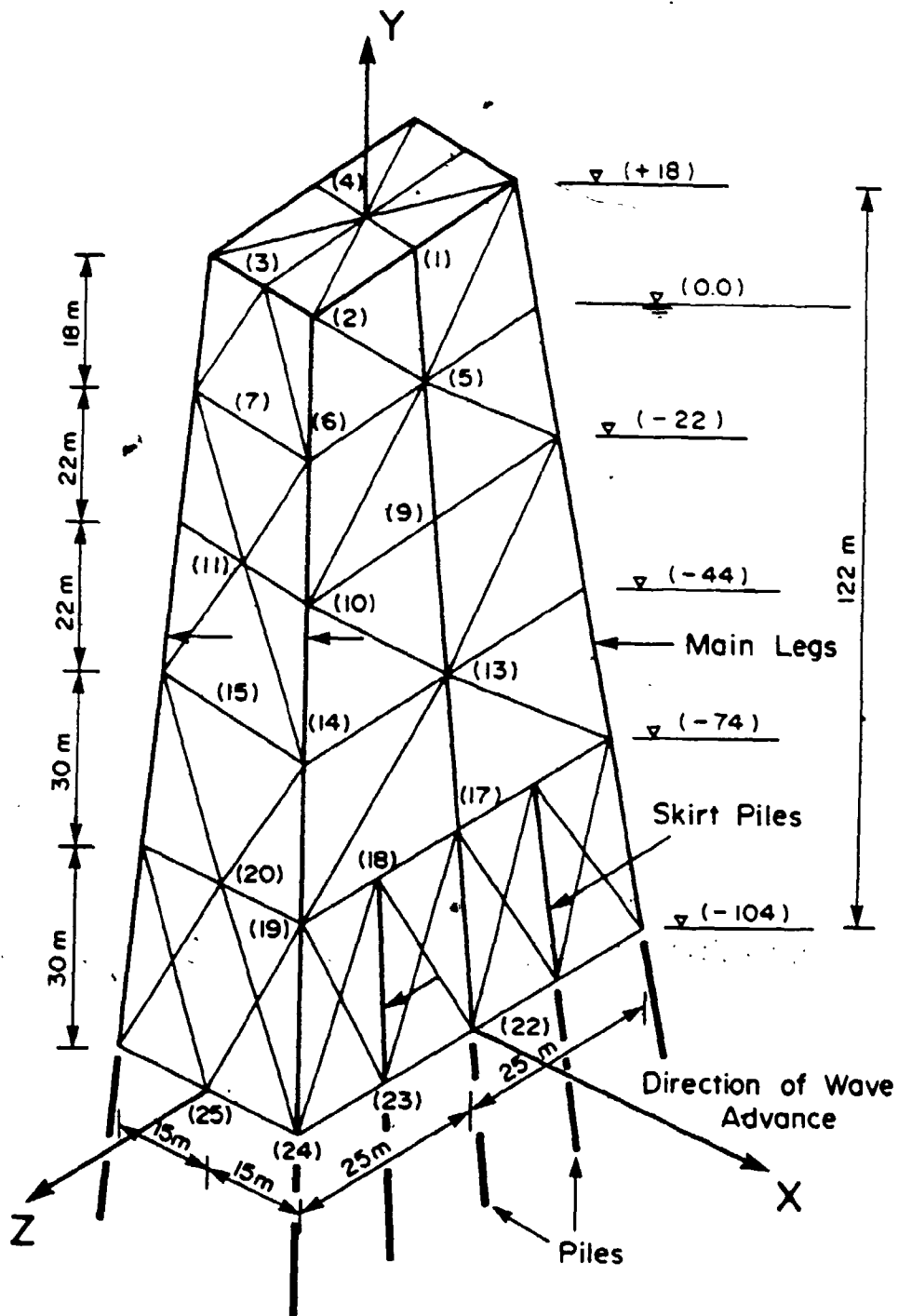
Figure 8-1: Fixed Offshore Tower Used in the Example
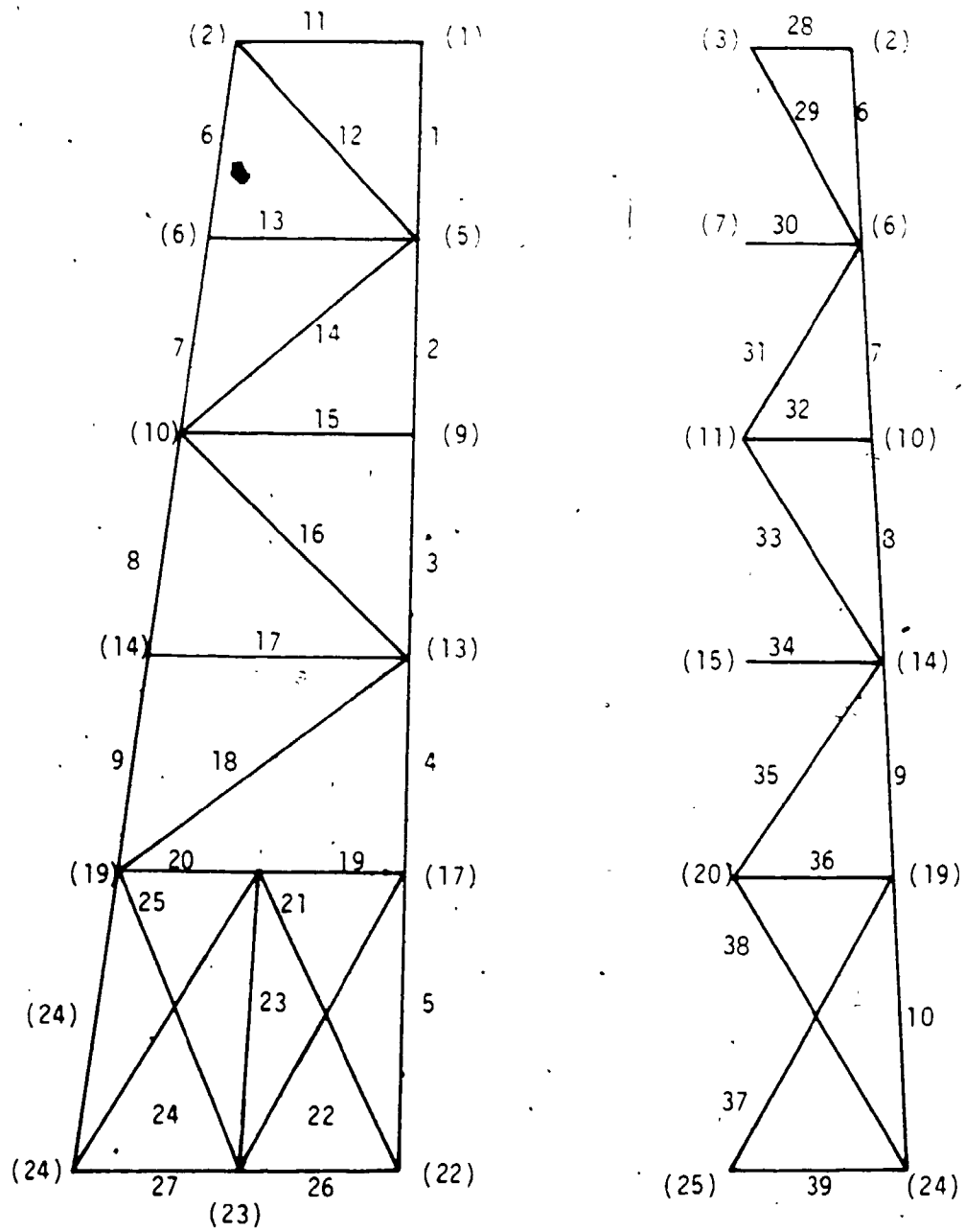
Figure 8-2: Member Numbering of the Tower
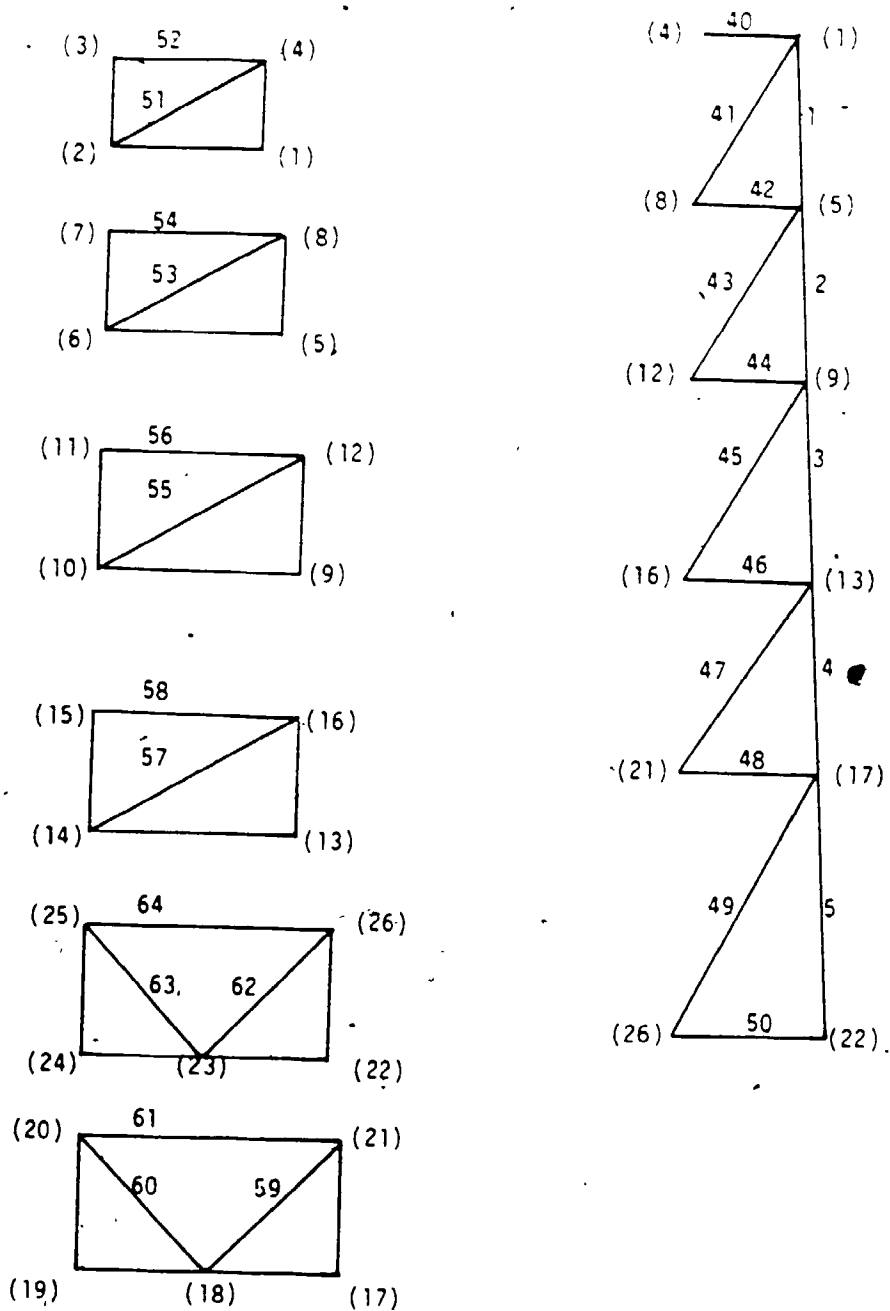
Figure 8-3: Member Numbering of the Tower (Continued)

Member No.	Thickness	Diameter
11-28-40-51-52	0.10	3.0
2-3-4-5-7-8-9-10-23	0.04	1.6
1-6	0.04	1.6
16-18-34-49-50-58-61-64	0.025	1.2
12-13-14-15-17-19-20-21-22-24-25-26-27-30-35-37-38-39-44-45-46-48-54-56-59-60-62-63	0.02	1.0
29-31-32-33-36-41-42-43-47-53-55-57	0.02	0.8
Piles	0.05	1.45

Table 8-1: Structural Properties of the Tower Members

not considered since wave forces are calculated using the coherence function model discussed in Chapter 6 which is a unidirectional model and waves are assumed to progress in the X direction. For the fourth set of boundary conditions, both X and Z axes are considered as axes of symmetry and this gives the vertical vibration modes. These modes, however, are very stiff with high natural frequencies and are not considered in the analysis.

A parametric study is conducted to illustrate the effect of the different parameters, that define the foundation and wave system, on the free vibration as well as the response of the tower. Four main parameters defining the foundation system are considered, i.e. soil shear wave velocity, soil profile, pile-soil-pile interaction and pile separation from the soil. Three different soil profiles are considered in this study which are the constant, parabolic and linear profiles, Fig. 8.4, all considered with or without pile separation. The wave system parameters considered for the parametric study are the characteristic wind speed $\overline{U}$ and the exponential decay parameter c. In addition to the foundation and wave system parameters, the effect of the deck mass on the response quantities is examined. Structural and foundation damping ratios are evaluated separately in order to elucidate their variation with the foundation system parameters independently.

In the parametric study, inertia and drag coefficients are assigned the constant values of 2 and 1.4, respectively. Material damping ratio of the superstructure, β, defined in Eq. 7.1, is assumed to be 1 % which is suitable for materials with low internal damping such as steel. Soil hysteretic damping ratio, is assigned a value of 2.5% which is characteristic of low amplitude strains. The deck mass can be highly variable depending on the type of platform, its production capacity, required topside facilities , stage of completion of the platform and a few other factors [3]. A low value of the deck mass was first
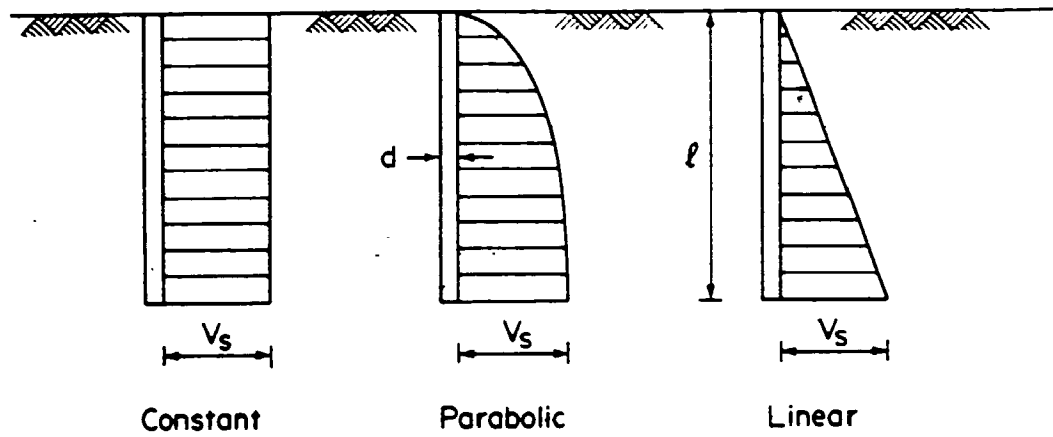
a) Soil profiles with no separation
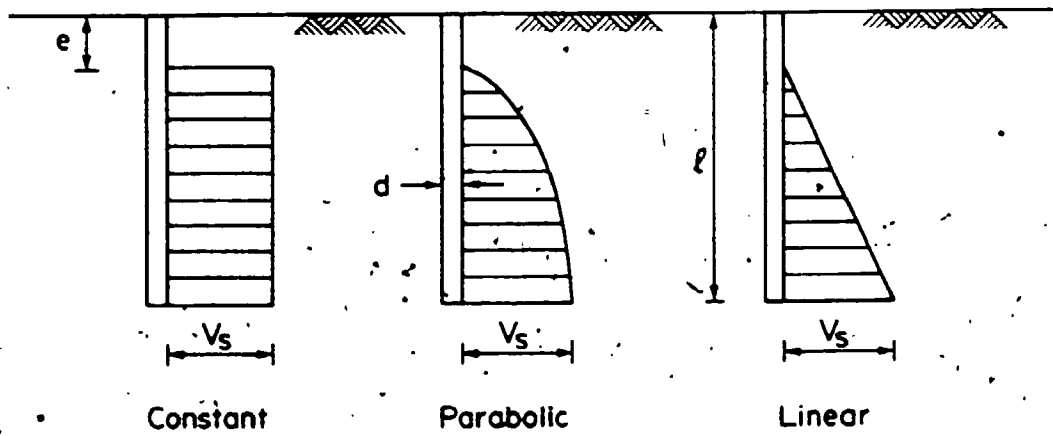
b) Soil Profiles with separation

Figure 8-4: Soil Shear Wave Velocity Profiles

assigned when examining the variation of free vibration characteristics with the foundation parameters. For examining the variation of the response with the system parameters, a higher value of the deck mass was assumed since this brings the natural frequencies closer to the wave energy spectrum peak. However, the variation of the free vibration characteristics as well as the response with the deck mass, expressed as a ratio of the total mass of the superstructure, is also examined. The exponential decay parameter c is assumed to be constant in all directions as discussed in Sec. 6.6.1.

8.2. Variation of Natural Frequencies and Damping Ratios with Foundation Parameters

For all the results presented in this Section, the deck mass is 180 tons, which represents 9.4 % of the total mass, unless otherwise stated.

8.2.1. Effect of Soil Stiffness

The structure is analysed for seven different soil shear wave velocities. For all cases, a parabolic soil profile is assumed, no separation length is considered and dynamic interaction factors are applied. Fig. 8.5a shows the variation in the first two undamped and damped frequencies (obtained for the case of foundation damping only) with soil shear wave velocity at the pile tip. The fixed base structure would correspond to $V_s \rightarrow \infty$. The first natural frequency pertains to the first sway mode and the second natural frequency is associated with the first torsional mode. Natural frequencies drop dramatically with the decrease of shear wave velocity thus approaching the peak region of the wave energy spectrum. It is noticed that most of the damped frequencies are higher than tha undamped ones. This is a consequence of nonproportional damping.

The drop in structural damping ratios with the increase in foundation flexibility is shown in Fig. 8.5b. This is due to the decrease in structural curvature with the increase in soil flexibility. Also shown in Fig. 8.5b is the
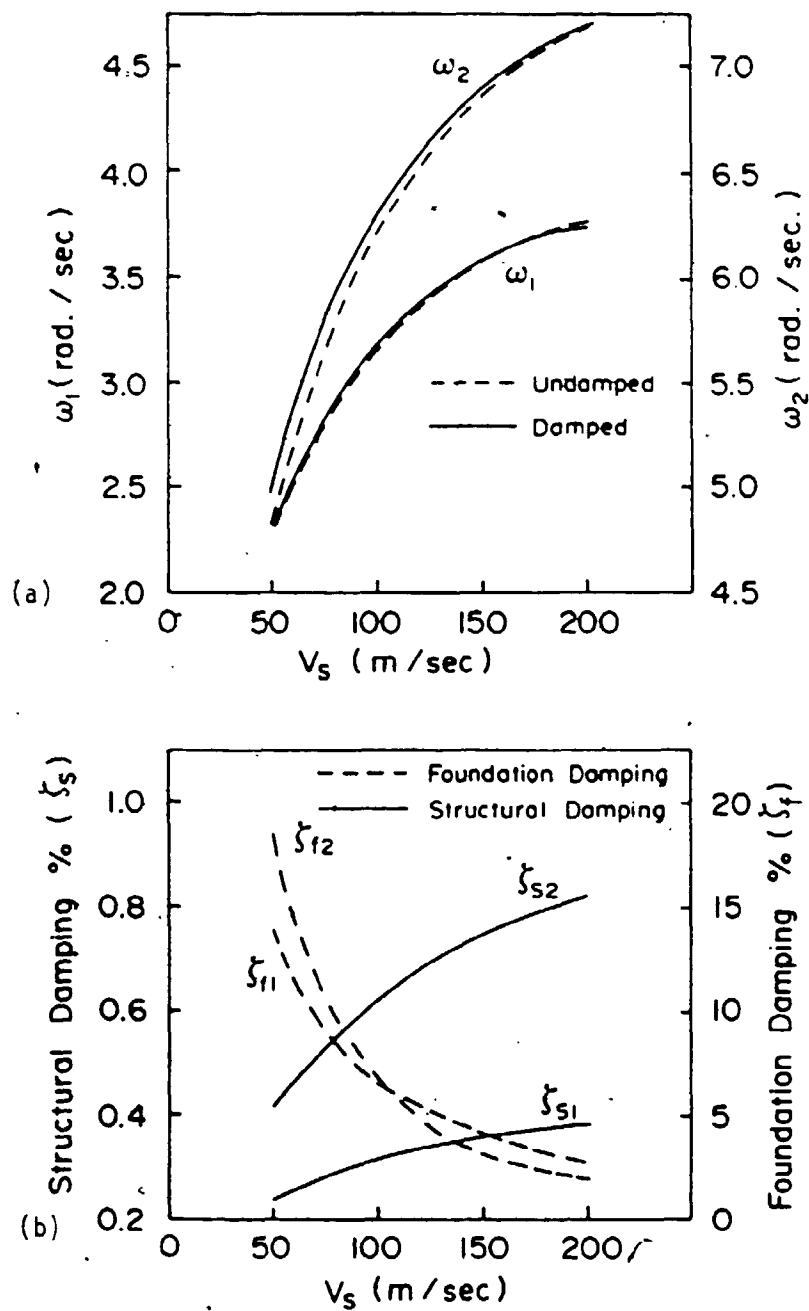
Figure 8-5: Variation in Natural Frequencies and Damping Ratios of the Tower with Soil Shear Wave Velocity

increase in foundation damping ratios with the increase in soil flexibility . It can be noticed that the variation in foundation damping ratio with shear wave velocity is greater for the torsional mode ς_{f2} than it is for the sway mode ς_{f1}.

8.2.2. Effect of Soil Profile

The decrease in soil shear modulus with the decrease in confining pressure can be modeled by assuming a soil shear modulus which varies along the length of the pile in a suitable fashion. Given in Table 8.2a are the first 4 damped and undamped frequencies for the 3 profiles calculated for the following soil conditions; $V_s = 100$ m /sec, no pile separation considered and dynamic interaction factors are applied. Table 8.2b gives the first 4 modal soil and structural damping ratios for the 3 profiles. (It may be mentioned that the soil shear wave velocities are deliberately chosen to be low in order to identify the trends observed in a distinct manner.)

Natural frequencies of the linear and parabolic profiles are lower than those of the constant profile, with those of the linear profile being the lowest. A similar trend is observed for structural damping ratios, with the exception of the fourth mode (second torsional mode) where the structural damping ratio for the linear profile is the highest. Foundation damping ratios show an opposite trend where the damping ratios for linear and parabolic soil profiles are higher than the constant profile with the exception of the fourth mode where the foundation damping ratio of the linear profile is lower than that of the parabolic profile. It can also be seen that the damped frequencies calculated considering structural damping only are closer to the undamped frequencies than those calculated considering foundation damping only. This is because foundation damping ratios are higher than structural damping ratios in this case.

Table 8.3a shows the first 4 undamped and damped frequencies for the 3

a) Undamped and Damped Frequencies

Soil Profile	mode (1)			mode (2)			mode (3)			mode (4)		
	undamp	found	struct	undamp	found	struct	undamp	found	struct	undamp	found	struct
constant	3.64	3.65	3.62	7.32	7.35	7.30	11.3	11.56	11.27	15.14	15.57	15.14
parabolic	3.19	3.21	3.19	6.230	6.29	6.23	9.40	9.94	9.40	13.00	13.28	13.0
linear	2.78	2.80	2.78	5.03	5.1	5.03	7.78	8.26	7.78	11.93	12.02	11.93

b) Foundation and Structural Damping Ratios

Soil Profile	mode (1)		mode (2)		mode (3)		mode (4)	
	Foundation	Structural	Foundation	Structural	Foundation	Structural	Foundation	Structural
constant	4.52	0.61	2.14	0.85	4.18	0.8	5.26	0.78
parabolic	6.31	0.47	6.82	0.62	11.14	0.63	8.73	0.77
linear	8.07	0.38	11.09	0.48	16.34	0.85	6.7	0.82

Table 8-2: Natural Frequencies and Damping Ratios of the Tower Calculated for Three Soil Profiles ($V_s = 100$ m/s, Dynamic Interaction Considered, Pile Separation Neglected)

profiles for $V_s = 100$ m/sec, pile separation ratio $e/d = 2$, and no pile-soil-pile interaction is considered. The soil and structural damping ratios pertaining to these conditions are given in Table 8.3b. The same trends as before are observed with the exception, again, of the fourth mode.

8.2.3. Effect of Pile Separation

During a storm or due to the collision of a ship or an iceberg with the tower, large displacements of the piles occur and the bond between piles and surrounding soil may be lost leading to pile separation from the soil. This was observed in the North sea and in the Bass strait off Australia through monitoring of the natural frequencies [115,116]. Fig. 8.6a shows the variation of damped and undamped natural frequencies with e/d values ranging from $e/d = 0$ (no separation) to $e/d = 2$ for a parabolic soil profile and applying dynamic interaction factors. The variation in natural frequencies is marked but small since the increase in single pile flexibility due to separation is compensated for by the decrease in interaction factors which decreases the flexibility of the foundation system as a whole. Structural and foundation damping ratios for different e/d values are shown in Fig. 8.6b. As can be seen, structural and foundation damping ratios are slightly affected by the increase in separation, as long as the dynamic interaction factors for pile separation are used, with minor peaks and troughs at different e/d values.

To examine the effect of pile separation only, the tower is analysed for the two cases of $e/d = 0$ and 2 neglecting pile-soil-pile interaction. Table 8.4a gives the damped and undamped natural frequencies for these two cases assuming a parabolic soil profile and $V_s = 100$ m/sec. Soil and structural damping ratios, for the same soil conditions, are given in Table 8.4b. Now, that the influence of pile-soil-pile interaction is excluded, the drop in the natural frequencies due to pile separation is larger, the foundation damping ratios are slightly increased for the

a) Undamped and Damped Frequencies

Soil Profile	mode (1) undamp	found	struct	mode (2) undamp	found	struct	mode (3) undamp	found	struct	mode (4) undamp	found	struct
constant	3.64	3.64	3.64	6.87	6.87	6.87	10.35	10.35	10.35	13.99	14.01	13.99
parabolic	3.23	3.23	3.23	5.85	5.87	5.85	8.8	8.85	8.8	12.54	12.56	12.53
linear	2.84	2.85	2.84	4.83	4.86	4.83	7.61	7.68	7.61	11.81	11.83	11.80

b) Foundation and Structural Damping Ratios

Soil Profile	mode (1) Foundation	Structural	mode (2) Foundation	Structural	mode (3) Foundation	Structural	mode (4) Foundation	Structural
constant	1.14	0.64	1.01	0.81	1.83	0.74	2.05	0.70
parabolic	2.19	0.53	4.22	0.61	5.57	0.65	4.1	0.82
linear	3.79	0.44	7.48	0.47	8.8	0.61	4.01	0.88

Table 8-3: Natural Frequencies and Damping Ratios of the Tower Calculated for Three Soil Profiles ($V_s = 100$ m/s, $e/d = 2.0$, Pile-Soil-Pile Interaction Neglected)

211
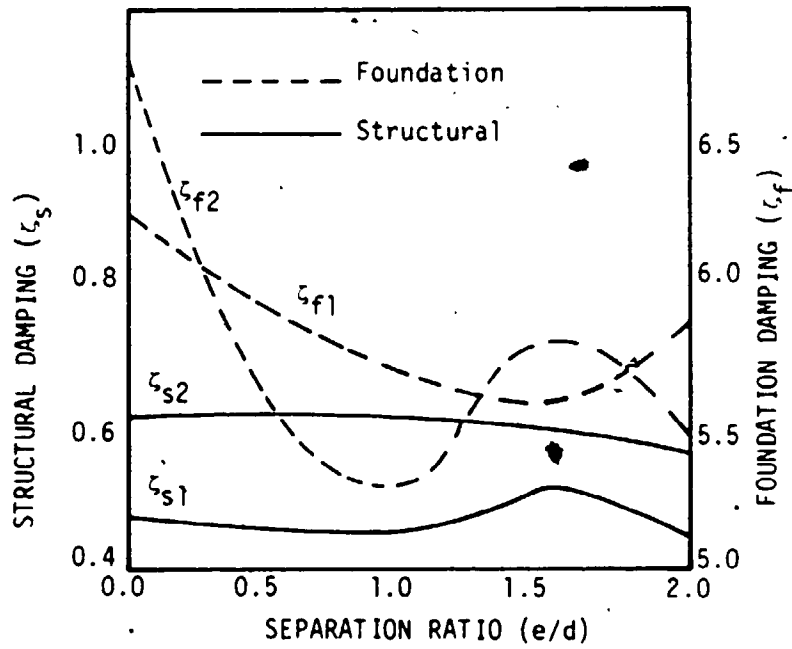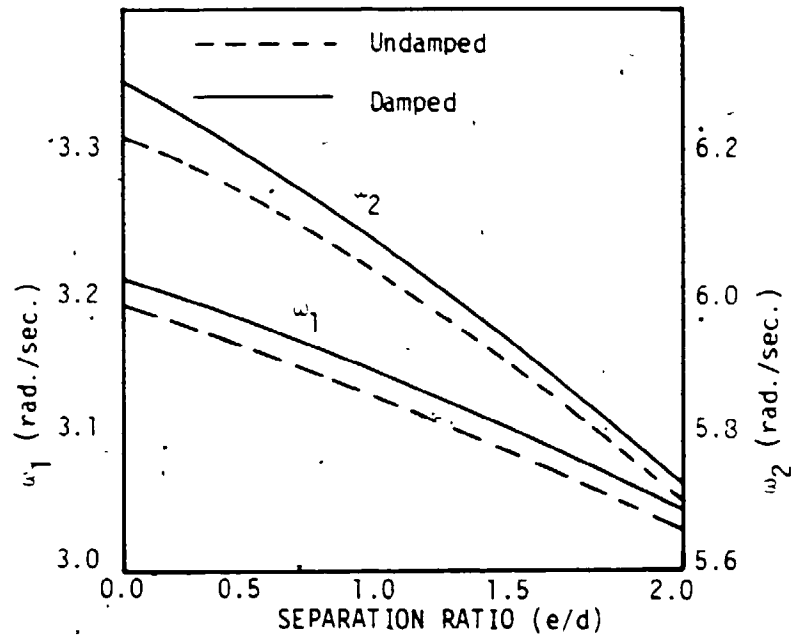
Figure 8-6: Variation in Natural Frequencies and Damping Ratios of the Tower with Pile Separation Ratio e/d

212

a)

Pile Separation Ratios	mode (1)			mode (2)			mode (3)			mode (4)		
	undamp	found	struct	undamp	found	struct	undamp	found	struct	undamp	found	struct
e/d=0.0	3.44	3.44	3.44	6.57	6.61	6.57	9.89	10.0	9.88	13.48	13.59	13.48
e/d=2.0	3.23	3.23	3.23	5.65	5.67	5.65	8.8	8.85	9.8	12.54	12.58	12.53

a) Undamped and Damped Natural Frequencies

b)

	mode (1)		mode (2)		mode (3)		mode (4)	
	Foundation	Structural	Foundation	Structural	Foundation	Structural	Foundation	Structural
e/d=0.0	2.05	0.57	3.56	0.71	6.03	0.69	5.92	0.77
e/d=2.0	2.19	0.53	4.22	0.61	5.57	0.65	4.1	0.82

b) Foundation and Structural Damping Ratios

Table 8-4: Natural Frequencies and Damping Ratios of the Tower Calculated for Two Pile Separation Ratios (V_s=100 m/s, Parabolic Soil Profile, Pile-Soil-Pile Interaction Neglected)

first two natural frequencies and decreased for the next two frequencies. Structural damping ratios follow the usual trend of decreasing with the decrease in natural frequency except for the fourth mode where the damping goes up slightly.

8.2.4. Effect of Pile-Soil-Pile Interaction

Despite the relatively large S/d ratios for this particular tower (the smallest S/d ratio is 8.62), pile-soil-pile interaction has a significant effect on damping ratios and to a smaller extent on natural frequencies. This is shown by comparing the damped and undamped natural frequencies, Table 8.5a, and the soil and structural damping ratios, Table 8.5b, when neglecting and considering dynamic pile-soil-pile interaction. While the natural frequencies drop slightly when the interaction is considered, foundation damping ratios significantly increase for all modes with the greatest increase in the first mode. Structural damping ratios drop slightly when pile-soil-pile intraction is considered, with the exception of the fourth mode where it remains constant. The drop in structural damping ratios is due to the increase in soil flexibility when pile-soil-pile interaction is considered, manifested by the drop in the natural frequencies.

The effect of pile-soil-pile interaction on natural frequencies and damping ratios is examined for the previous soil conditions but considering a pile separation ratio $e/d = 2$. While the percentage decrease in natural frequencies due to pile-soil-pile interaction, Table 8.6a, is about the same as in the previous case, the percentage increase in foundation damping ratios, Table 8.6b, is less than in the previous case. It can also be seen that in this particular case the foundation damping ratios in the sway modes (first and third modes) are more sensitive to pile-soil-pile interaction than are the torsional modes (second and fourth modes). Structural damping ratios slightly decrease in all 4 modes due to the interaction.

a)

	mode (1)			mode (2)			mode (3)			mode(4)		
	undamp	found	struct	undamp	found	struct	undamp	found	struct	undamp	found	struct
no inter- action	3.44	3.44	3.44	6.57	6.61	6.57	9.89	10.0	9.88	13.48	13.59	13.48
inter- action	3.186	3.21	3.19	6.23	6.29	6.23	9.4	9.45	9.4	13.00	17.28	13.0

Undamped and Damped Natural Frequencies

b)

	mode (1)		Mode (2)		mode (3)		mode(4)	
	Foundation	Structural	Foundation	Structural	Foundation	Structural	Foundation	Structural
no inter- action	2.05	0.57	3.56	0.71	6.03	0.69	5.92	0.77
inter- action	6.31	0.47	6.82	0.62	11.16	0.63	8.73	0.77

Foundation and Structural Damping Ratios

Table 8-5: Natural Frequencies and Damping Ratios of the Tower Calculated with and without Interaction ($V_s = 100$ m/s, No Separation, Parabolic Soil Profile)

a)

	mode (1)			Mode (2)			mode (3)			mode(4)		
	undamp	found	struct	undamp	found	struct	undamp	found	struct	undamp	found	struct
no inter-action	3.23	3.23	3.23	5.85	5.87	5.85	8.8	8.85	8.8	12.54	12.58	12.53
inter-action	3.03	3.05	3.03	5.69	5.72	5.69	8.64	8.80	8.64	12.4	12.46	12.4

Undamped and Damped Natural Frequencies

b)

	mode (1)		Mode (2)		mode (3)		mode(4)	
	Foundation	Structural	Foundation	Structural	Foundation	Structural	Foundation	Structural
no inter-action	2.19	0.53	4.22	0.60	5.57	0.65	4.1	0.82
inter-action	5.88	0.45	5.46	0.56	8.07	0.61	8.75	0.82

Foundation and Structural Damping Ratios

Table 8-6: Natural Frequencies and Damping Ratios of the Tower Calculated with and without Interaction ($V_s = 100$ m/s, $e/d = 2.0$, Parabolic Soil Profile)

For structures with very low first natural frequencies. It is sometimes argued that the use of static interaction factors will introduce small errors. To check the validity of this argument, the static interaction factors are used for a parabolic soil profile, $V_s = 100$ m/sec, no separation and the damped and undamped natural frequencies are compared with those obtained using dynamic interaction factors for the same soil conditions in Table 8.7a. Soil and structural damping ratios for both cases are given in Table 8.7b. While the use of static interaction factors gives natural frequencies that are very close to those obtained using the dynamic interaction factors, their use gives foundation damping ratios that are much less than those obtained using the dynamic interaction factors. This suggests that static interaction factors match the real part of the dynamic interaction factors leading to a satisfactory prediction of the natural frequencies (stiffness). But because the imaginary part is missing, the foundation damping derives solely from the damping of single piles. This can be substantiated by comparing the foundation damping ratios obtained using the static interaction factors to those obtained with interaction neglected, Table 8.5b. Thus, if static interaction factors are applied, they should be used only for pile stiffness.

8.2.5. Effect of Deck Mass

For the same platform, deck mass may vary during different operational processes and the variation may reach a factor of 2 [3]. Accordingly, natural frequencies, damping ratios and the tower response are affected. The tower is analysed assuming 4 different values for the deck mass ranging from 9 % to 63% of its total mass. Variation in the first 2 undamped natural frequencies of the tower with the deck mass is shown in Fig. 8.7. As the deck mass increases, natural frequencies of the tower decrease bringing the resonant frequencies closer to the wave energy spectral peak frequency, $\overline{\omega}$. Fig. 8.8 shows the variation in $\overline{\omega}$ with the characteristic wind speed $\overline{C}$ and plotted in the same figure is the first

a)

inter-action		mode (1)			mode (2)			mode (3)			mode (4)		
		undamp	found	struct	undamp	found	struct	undamp	found	struct	undamp	found	struct
Dynamic		3.19	3.21	3.19	6.23	6.29	6.23	9.4	9.94	9.4	13.00	13.28	13.0
Static		3.19	3.19	3.19	6.29	6.31	6.29	9.39	9.44	9.39	13.08	13.13	13.07

a)   Undamped and Damped Natural Frequencies

b)

		mode (1)		Mode (2)		mode (3)		mode (4)	
		Foundation	Structural	Foundation	Structural	Foundation	Structural	Foundation	Structural
Dynamic		6.31	0.48	6.82	0.62	11.14	0.63	8.72	0.77
Static		1.81	0.48	3.58	0.64	5.41	0.63	4.86	0.77

b)   Foundation and Structural Damping Ratios

Table 8-7: Natural Frequencies and Damping Ratios of the Tower Calculated for Static and Dynamic Interaction (V_s=100 m/s, No Pile Separation, Parabolic Soil Profile)
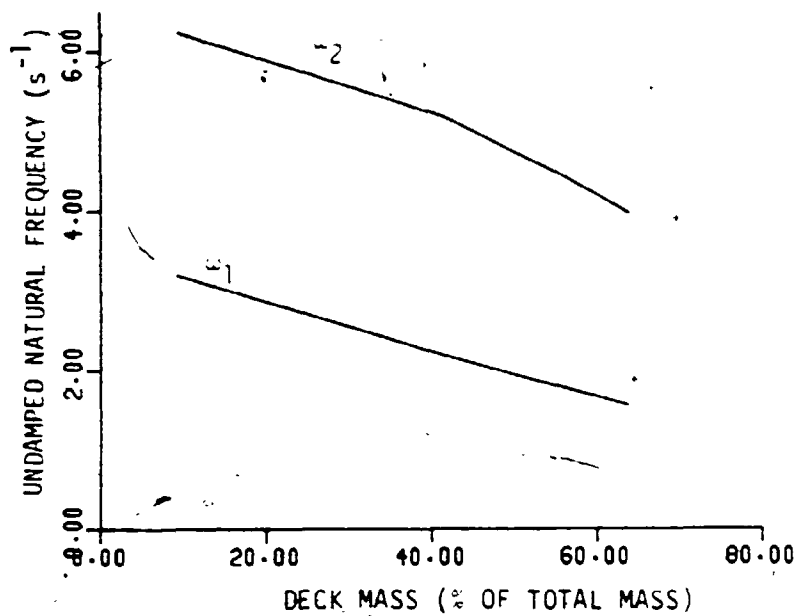
Figure 8-7: Variation in the First Natural Frequency of the Tower with Deck Mass
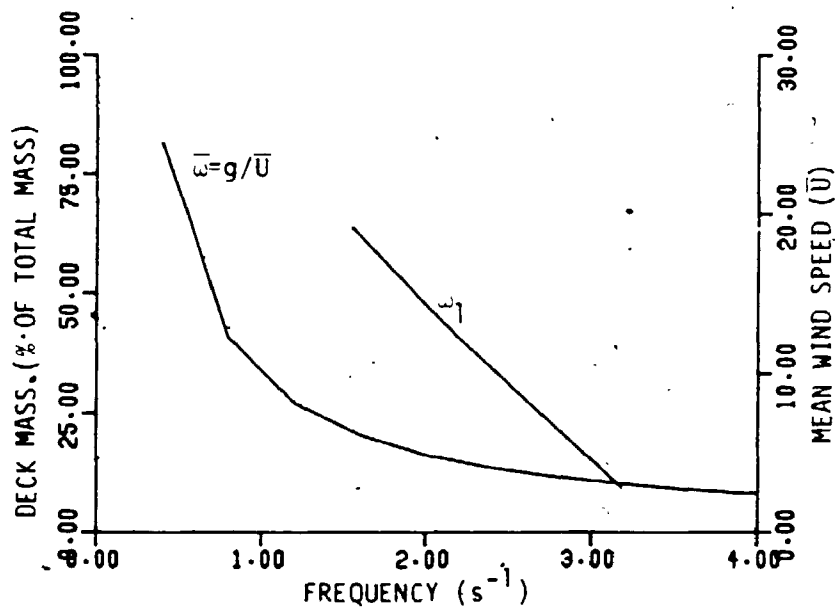
Figure 8-8: Peak Frequencies of Sea Surface Elevation Spectrum and the First Natural Frequencies of the Tower

undamped natural frequency of the tower versus the deck mass. For each value of the deck mass, there is a critical wind speed at which resonance occurs. For this tower, the critical wind speeds corresponding to practical values of the deck mass are very low. However, due to their low values they have a high probability of occurence and consequently are important in fatigue analysis. Total damping ratios of the first 2 modes are plotted versus deck mass in Fig. 8.9 and it can be noticed that modal damping as percentage of the critical damping drops with the increase in mass.

8.3. Variation in Hydrodynamic Damping and Tower Response to Wave Forces With the Different Parameters

For all the results presented in this Section, the dec. mass is assumed to be 63.86% of the total mass and the exponential decay parameter c is assumed to have a value of 1 unless otherwise stated.

8.3.1. Effect of Soil Stiffness

Response of the tower is evaluated for 7 different soil shear wave velocities ranging from 50 to 200 m/sec and 2 different wind speeds, 10 and 40 m/sec. For all cases, a parabolic soil profile is assumed, pile separation is neglected and dynamic pile-soil-pile interaction is considered. Hydrodynamic damping ratios for the different soil shear wave velocities are shown in Fig. 8.10 for $\bar{U} = 10$ and 40 m/sec. As soil shear wave velocity increases, natural frequencies increase, the critical damping increases and damping ratios decrease. This follows the same trend for foundation damping ratios. The variation in standard deviation of the top node deflection in direction X, for the 2 wind speeds, with soil shear wave velocity is shown in Fig. 8.11. At lower wind speeds, the contribution from the resonant part of the response to the total variance is larger than that of the background part. The magnitude of this resonant response is controlled by two
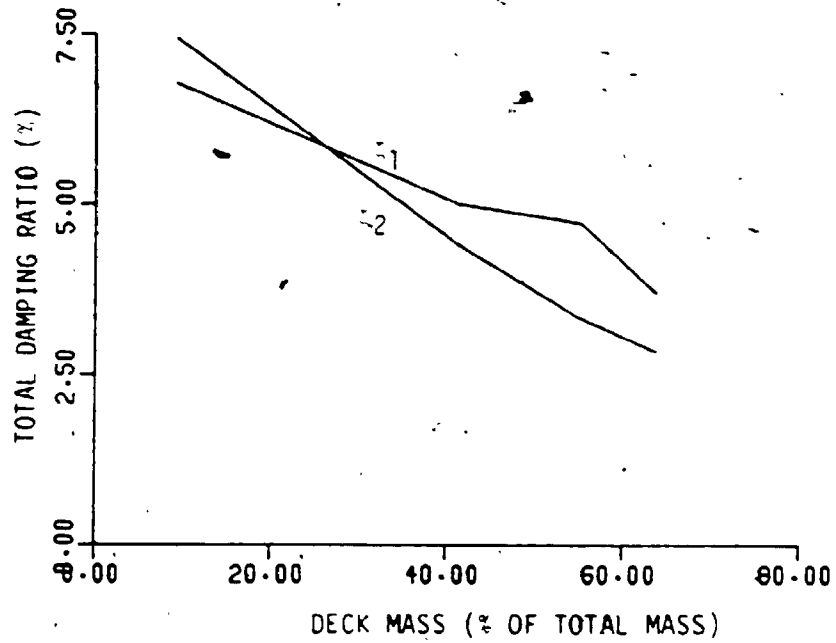
Figure 8-9: Variation in the First Modal Damping Ratio of the Tower with Deck Mass
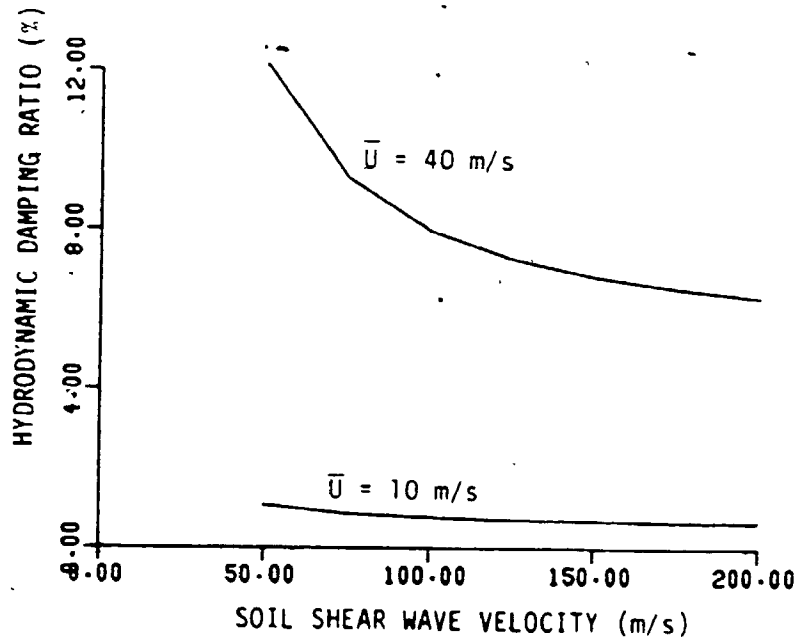
Figure 8-10: Hydrodynamic Damping Ratio for Different Soil Shear Wave Velocities

factors, the proximity of the natural frequencies to the wave energy spectral peak frequency $\bar{\omega}$ and the damping present in the system as fraction of the critical damping. As soil shear wave velocity increases, the natural frequency increases moving away from $\bar{\omega}$ and the damping ratio decreases. These 2 factors have opposite effects on the response spectral amplitudes in the vicinity of the resonance frequency. The net effect of these 2 factors is either to increase or decrease the total response amplitude (standard deviation).

For higher wind speeds, the contribution to the total response from the background component is much higher than that of the resonance component. The background response is quasi-static with little or no dynamic amplification. Thus the magnitude of the background response is controlled by the stiffness of the system. As soil shear wave velocity increases, stiffness of the tower increases, and the tower response decreases.

This is further illustrated by Figs. 8.12 and 8.13 which show the spectra of the top node deflection for two shear wave velocites, 50 and 200 m/sec calculated at $\bar{U} = 10$ and 40 m/sec, respectively. For $\bar{U} = 10$ m/sec, $\bar{\omega} = 0.981$ rad/sec and as can be seen, the tower response with the stiffer soil has little energy at this frequency whereas the tower with $V_s = 50$ m/sec has a pronounced peak. However, due to the closeness of $\bar{\omega}$ and ω_o for $V_s = 50$ m/sec, the response spectrum is somewhat broad banded and the two peaks of the response spectrum can not be distinguished. The resonant peak for $V_s = 200$ m/sec is more pronounced than that for $V_s = 50$ m/sec despite its being further from $\bar{\omega}$ due to the smaller damping ratio associated with the former. For $\bar{U} = 40$ m/sec, Fig. 8.13, the background response dominates the total variance which is much smaller for $V_s = 200$ m/sec than for $V_s = 50$ m/sec.
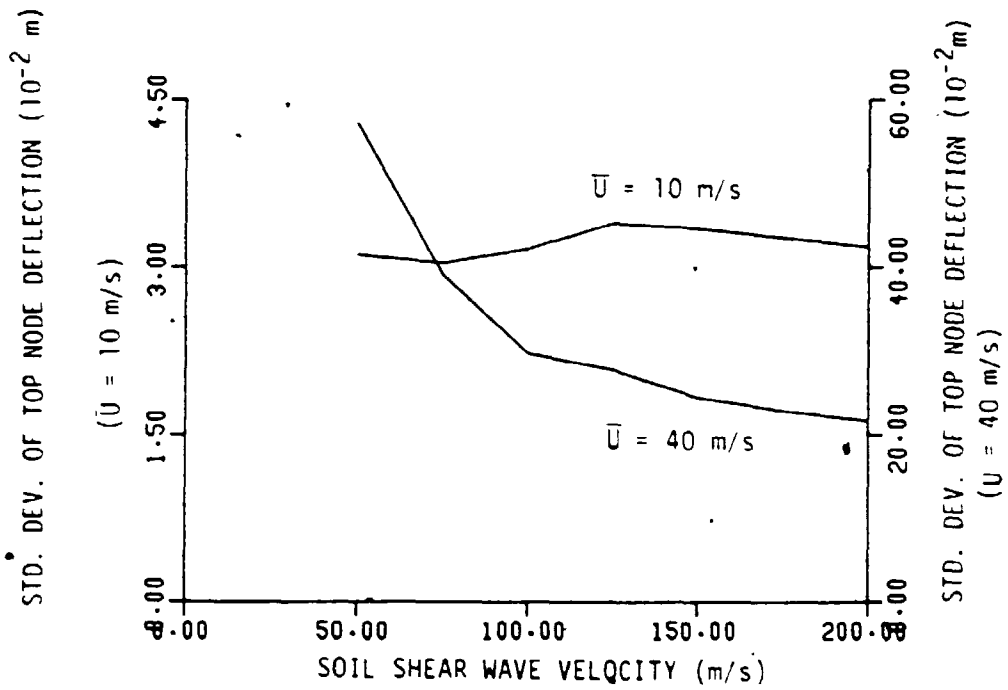
Figure 8-11: Effect of Soil Shear Wave Velocity on Tower Response to Waves
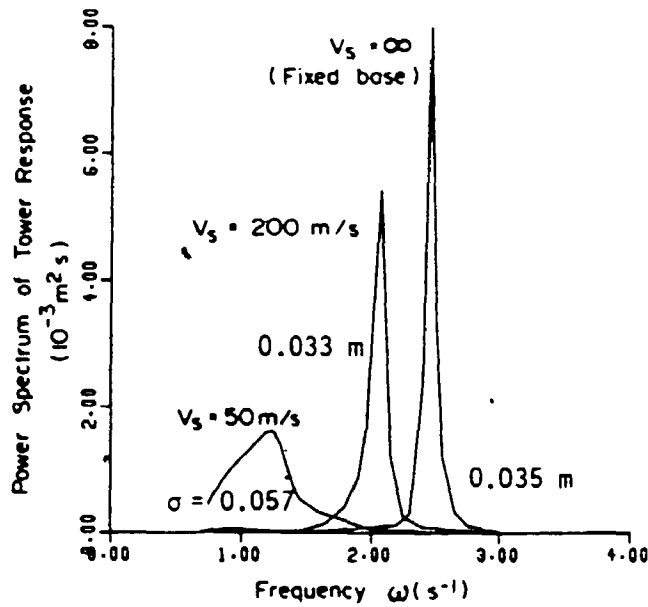
Figure 8-12: Top Node Response Spectra for Three Shear Wave Velocities ($\overline{U}$=10 m/s)
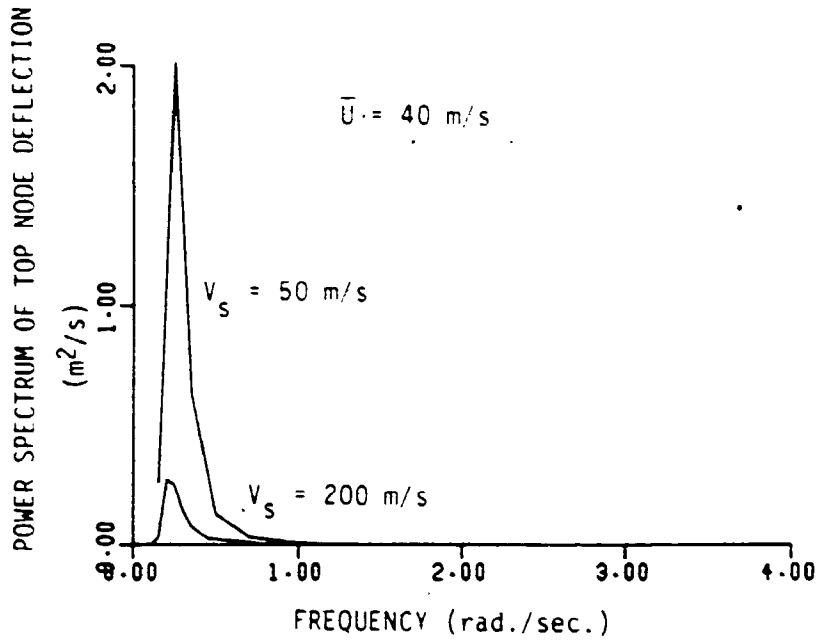
Figure 8-13: Top Node Response Spectra for Two Different Shear Wave Velocities ($\overline{U}$=40 m/s)
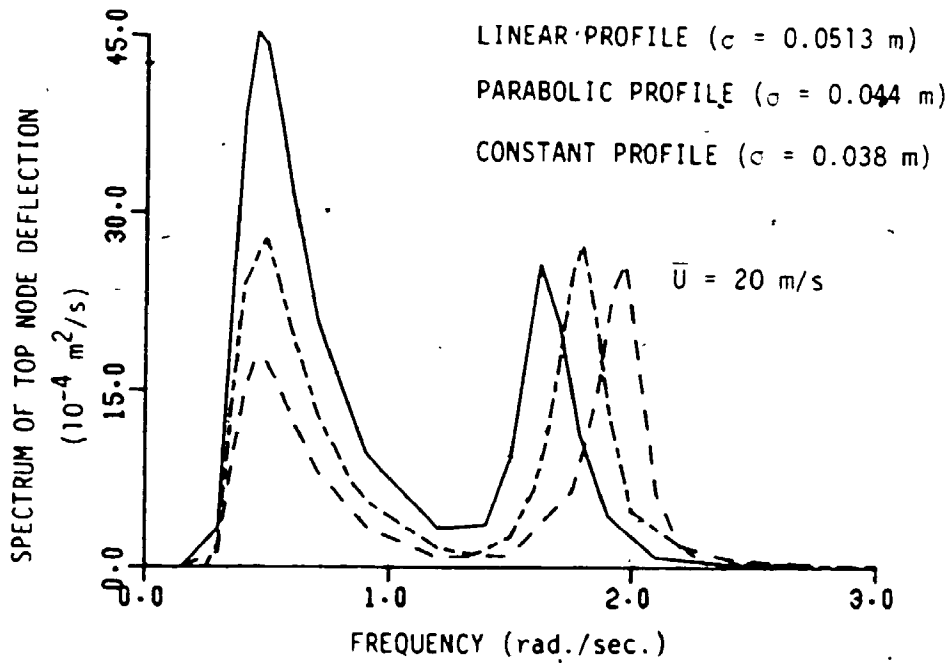
Figure 8-14: Tower Response Spectra for Three Soil Profiles

8.3.2. Effect of Soil Profile

Fig. 8.14 illustrates the effect of soil profile on the tower response. In this figure, the power spectrum of the top node deflection is plotted for the 3 shear wave velocity profiles and $\bar{U}=20$ m/sec. At such an intermediate wind speed, contributions from the background and resonant components to the total variance are both of equal importance. The tower with the linear soil profile has the least stiffness and consequently, the highest response spectral amplitudes in the vicinity of $\bar{\omega}$. The first undamped natural frequencies and the first modal damping ratios of the tower corresponding to the 3 profiles are given in Table 8.8. Although the towers with the linear and parabolic profiles have a higher damping ratios than that with the constant profile , the resonant peaks for the 3 cases are almost equal because the first natural frequencies of the former towers are closer to $\bar{\omega}$ than that of the latter. For this wind speed, the tower with the linear profile has the highest standard deviation and is 35% larger than that of the tower with the constant profile.

8.3.3. Effect of Pile-Soil-Pile Interaction

The tower response is evaluated for three different wind speeds 10, 22 and 30 m/sec with pile-soil-pile interaction neglected and considered. Fig. 8.15 shows the power spectrum of top node deflection for both cases for the 3 wind speeds, respectively. For lower wind speeds, the resonant peak is dominant and when pile-soil-pile interaction is considered, foundation and hydrodynamic damping ratios increase and the resonant peak is suppressed. This leads to a total variance which is less than that when the pile-soil-pile interaction is neglected. At higher wind speeds, the background response peak is dominant and considering pile-soil-pile interaction increases the flexibility of the tower. Consequently, pile-soil-pile interaction increases the total variance of the tower response at higher wind speeds. For intermediate wind speeds, both peaks might

Soil Profile	Natural Frequency ω_1	Damping Ratio ζ_1
Linear.	1.62	0.049
Parabolic	1.79	0.047
Constant	1.97	0.034

Table 8-8: First Natural Frequencies and Modal Damping Ratios Calculated for Three Soil Profiles (V_s=100 m/s. No Pile Separation. Dynamic Pile-Soil-Pile Interaction)

Wind Speed m/s	Pile Inter- action	ζ_h %	$\dfrac{\sigma_b^2}{\sigma^2}$	$\dfrac{\sigma_r^2}{\sigma^2}$	σ_m
10	No	0.72	0.03	0.97	0.047
	Yes	0.77	0.09	0.91	0.032
22	No	2.46	0.50	0.50	0.050
	Yes	2.69	0.68	0.32	0.050
30	No	4.24	0.88	0.12	0.095
	Yes	4.67	0.95	0.05	0.108
40	No	7.22	0.99	0.01	0.269
	Yes	7.98	0.99	0.01	0.316

Table 8-9: Tower Response to Wave Forces and Hydrodynamic Damping Ratios for Different Wind Speeds Calculated Either Neglecting or Considering Pile-Soil-Pile Interaction (V_s=100 m/s. Parabolic Soil Profile)
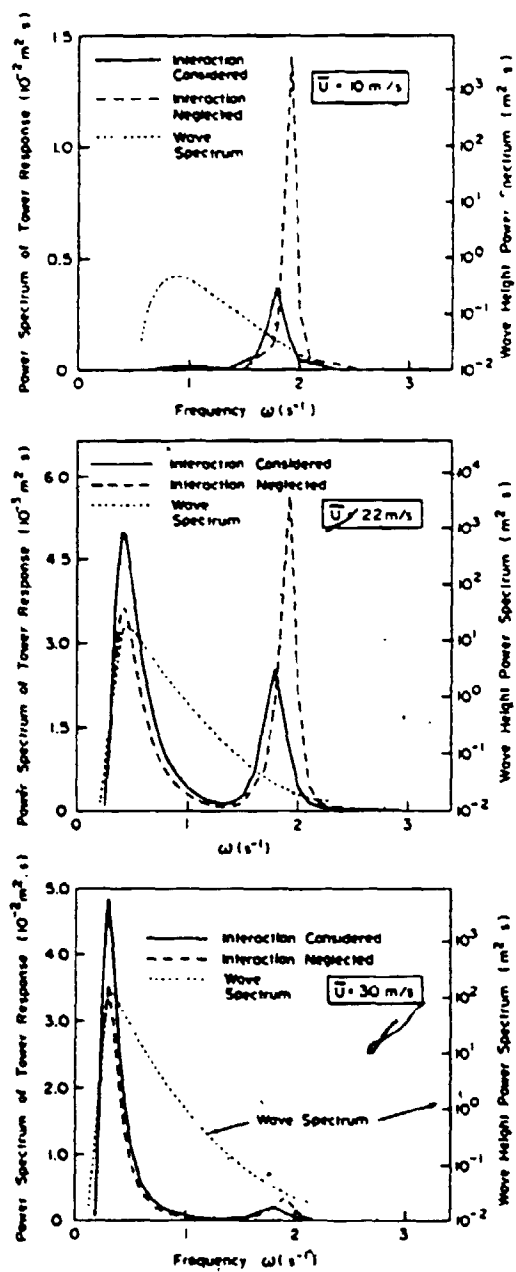
Figure 8-15: Effect of Pile Soil Pile Interaction on Tower
Response Spectrum for Three Different Wind Speeds

227

be of equal importance and considering pile-soil-pile interaction may increase or decrease the total variance.

To illustrate the variation in the contribution to the total variance from the background and resonant components, the total variance σ^2 is split into a background variance σ_b^2 and a resonant variance σ_r^2 and both are expressed as ratios from the total variance. Table 8.9 gives the foundation damping ratios, the hydrodynamic damping ratios, σ_b^2/σ^2, σ_r^2/σ^2, the total variance and the standard deviation of the top node deflection for 4 different wind speeds all either considering or neglecting pile-soil-pile interaction. At $\mathbb{T}=22$ m/sec the increase in background response when considering pile-soil-pile interaction is compensated for by the decrease in the resonant response and the standard deviation of both cases is the same.

Fig. 8.16 shows the variation in hydrodynamic damping ratios with wind speed for $V_s = 100$ m/sec, parabolic soil profile and pile separation neglected, with and without pile-soil-pile interaction. The hydrodynamic damping ratios increase substantially with wind speed and they are greater when considering pile-soil-pile interaction. Fig. 8.17 shows the variation in standard deviation of the tower top node deflection with the characteristic wind speed $\mathbb{T}$ considering and neglecting pile-soil-pile interaction. The reduction in the response at lower wind speeds and the increase in the response at higher wind speeds due to pile-soil-pile interaction is clearly illustrated in this figure.

8.3.4. Effect of Exponential Decay Parameter

Fig. 8.18 shows the variation in standard deviation of top node deflection with values of c ranging from 1 to 10 for $\mathbb{T}=30$ m/sec. The soil profile considered is parabolic with $V_s = 100$ m/sec, pile separation neglected and pile-soil-pile interaction is considered. Standard deviation of the response decreases
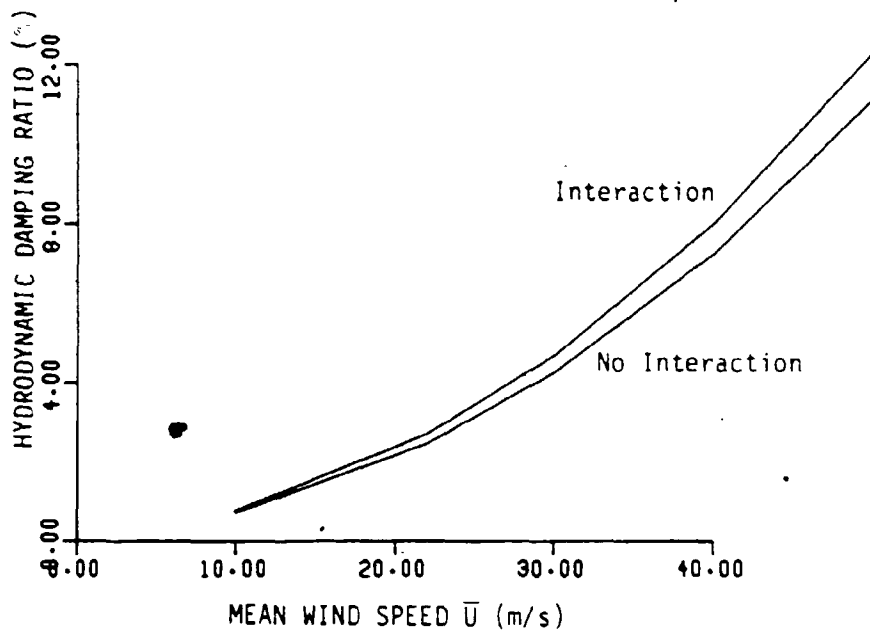
Figure 8-16: Variation in Hydrodynamic Damping Ratio with Mean Wind Speed
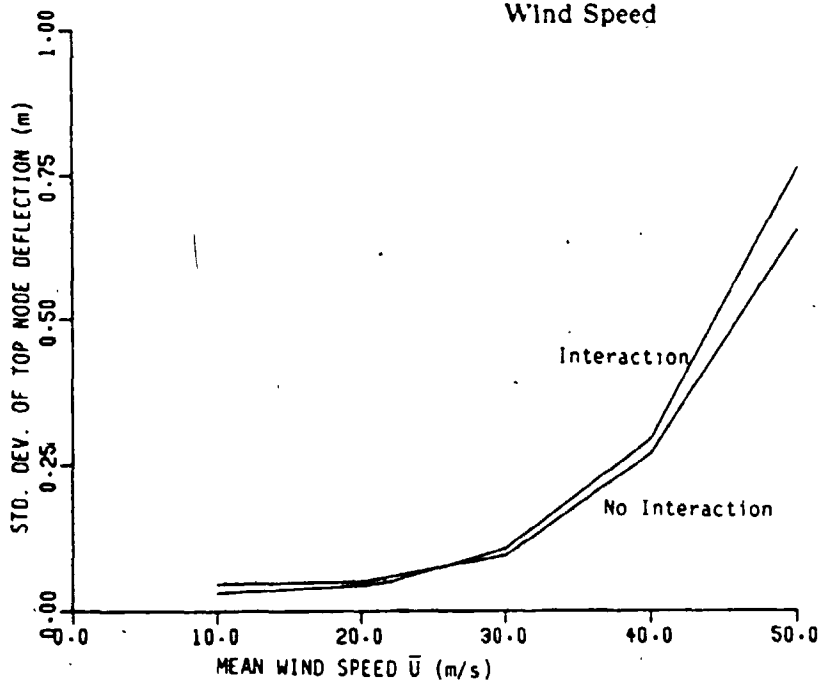
Figure 8-17: Variation in Top Node Response with Mean Wind Speed
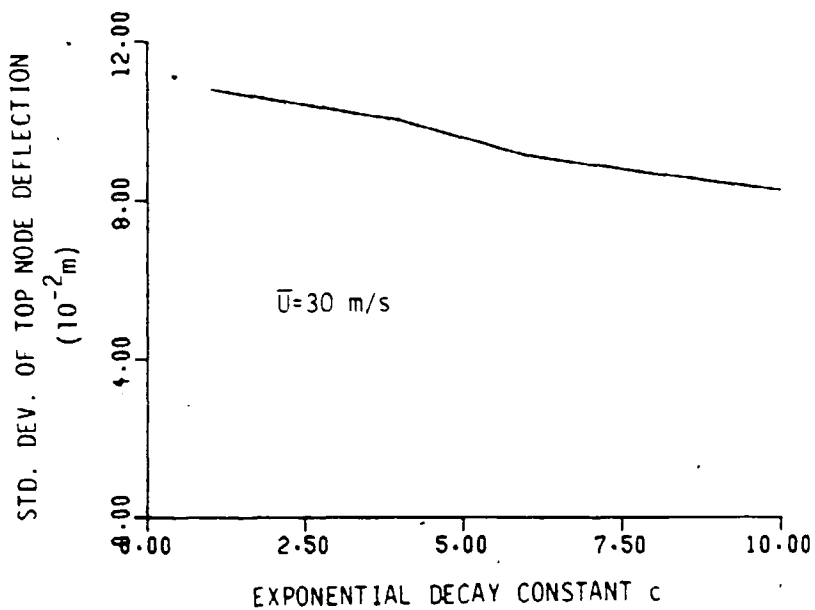
Figure 8-18: Effect of Exponential Decay Parameter on Tower Response
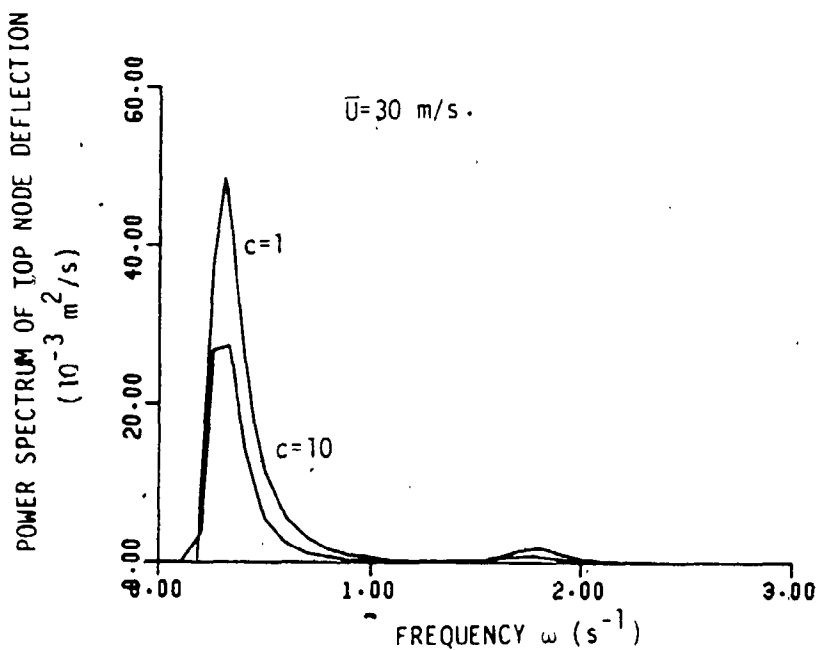
Figure 8-19: Top Node Response Spectra for Two Values of the
Exponential Decay Parameter

by 23% when increasing the value of c from 1 to 10. Shown in Fig. 8.19 are the response spectra evaluated at $\Upsilon = 30$m/sec, $V_s = 100$ m/sec, parabolic soil profile, pile separation neglected and pile-soil-pile interaction considered for $c = 1$ and 10. The decrease in the exponential decay parameter decreases the magnitude of wave forces throughout the whole frequency range with a similar effect on the response spectrum.

8.3.5. Effect of Deck Mass

The variation in the response standard deviation with the deck mass is shown for $\Upsilon = 22$ m/sec in Fig. 8.20. As the deck mass increases, the natural frequencies decrease and get closer to the wave energy spectral peak and the foundation damping ratios also decrease. Thus increasing the mass of the tower increases both the background and resonant responses. An increase in the total mass of the tower by a factor of 2.48 leads to an increase in the standard deviation of the top node deflection by 17%.

8.3.6. Conclusions

A parametric study is carried out to illustrate the effect of the foundation system properties and the wave system parameters on the free vibration characteristics as well as the response of a typical fixed offshore tower. The following conclusions are drawn:

1. Natural frequencies drop dramatically with the increase in soil flexibility.

2. While structural damping ratios drop significantly with the increase in soil flexibility, tower damping derived from soil increases with soil flexibility.

3. Foundation damping ratios are much higher than structural damping ratios in the practical range of soil properties encountered in offshore towers and can not be excluded in any realistic analysis.

4. The drop in structural damping ratios due to soil flexibility is more than compensated for by the increase in foundation damping ratios.
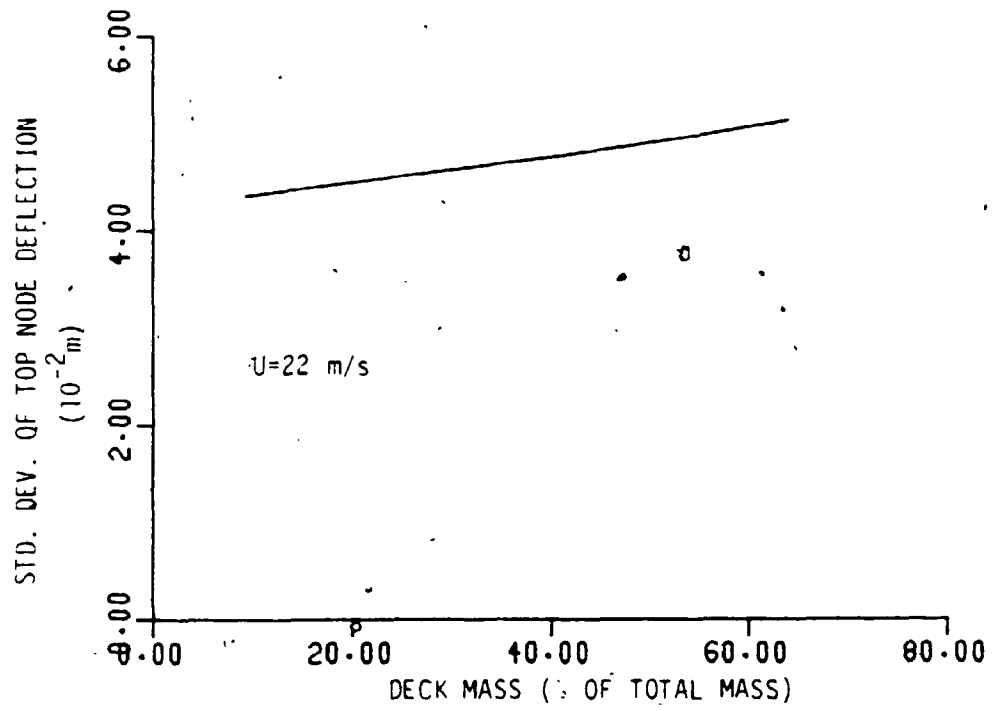
Figure 8-20: Effect of Deck Mass on Tower Response

5. Natural frequencies and structural damping ratios for linear and parabolic soil profiles are lower than those of the constant profile with those of the linear profile being the lowest. Soil damping ratios follow an opposite trend where those of the linear and parabolic soil profiles are higher than those of the constant profile with those of the linear profile being the highest.

6. Pile separation slightly affects natural frequencies and damping ratios if considered simultaneously with pile-soil-pile interaction since the two parameters have opposite effects on the results. Natural frequencies and structural damping ratios decrease slightly with pile separation while foundation damping increases slightly with the separation.

7. When pile separation is considered in absence of pile-soil-pile interaction, the drop in natural frequencies and structural damping ratios increases while the increase in foundation damping ratios is still moderate.

8. Dynamic pile-soil-pile interaction moderately decreases the natural frequencies and structural damping ratios but dramatically increases foundation damping ratios.

9. The use of static interaction factors adequately predicts the natural frequencies and structural damping but grossly underestimates foundation damping ratios.

10. Dynamic pile-soil-pile interaction, usually neglected in design, has a significant effect even with large spacing and should be considered.

11. Hydrodynamic damping ratios decrease with the increase in soil shear wave velocity.

12. The increase in soil shear wave velocity may decrease or increase the tower response at low wind speeds, but it decreases the tower response at high wind speeds.

13. Soil shear wave velocity profile has a significant effect on the tower response. Pile-soil-pile interaction increases the hydrodynamic damping ratios for all wind speeds.

14. The background part of the response increases while the resonant response decreases when considering pile-soil-pile interaction.

15. The total response of the tower to wave forces decreases due to pile-soil-pile interaction at low wind speeds but increases at high wind speeds.

16. For the particular tower analysed, the total response decreases by 23 % when the value of the exponential decay parameter increases from 1 to 10.

17. Increasing the deck mass (and consequently the total mass) of the tower, increases the response of the tower to wave forces.

Chapter Nine
Summary and Conclusions

Three main problem areas are investigated in this study:

1. The analysis of pile driving and prediction of bearing capacity.

2. Evaluating wave force spectrum on members of offshore structures accounting for lack of spatial correlation of random waves.

3. The dynamic response of fixed offshore structures accounting for pile-soil-pile interaction.

9.1. Pile Driving

An improved one dimensional wave equation analysis is developed which accounts for wave propagation in the soil mass. Also a three dimensional finite element analysis of the problem is formulated and its results are compared with the one dimensional model to illustrate the advantages and limitations of both models. The following conclusions emerge:

1. The new soil model for the one dimensional analysis has the advantage of accounting for wave propagation in soil in a way related to fundamental soil properties and may give more realistic results for pile tip displacements and force and velocity time records than the conventional one dimensional model does.

2. The transmitting boundary developed for the finite element analysis can be used for both static and dynamic problems and as its parameters are relatively frequency independent; it can also be used for a time domain analysis.

3. Using a viscous boundary in the pile driving problem creates an artificial offset of the response which may distort the calculated permanent pile set.

4. The finite element analysis is at least two orders of magnitude more expensive than the one dimensional analysis and does not guarantee better results because it also is very sensitive to the input parameters.

5. The extent of the weakened zone around the pile shaft has to be evaluated from comparison with extensive field data.

9.2. Wave Force Spectrum

A model for evaluating spectra of wave forces on members of the jacket type structure is developed which takes into account the lack of spatial correlation associated with random waves (Coherence Function Model. This is incorporated by introducing an exponential decay coherence function in the expressions for wave kinematics spectra. Wave forces calculated using this model are compared with those obtained from a directional representation of the sea surface elevation The following conclusions are drawn:

1. Both, the directional spectrum and coherence function models produce modifications of the same general nature to the wave forces obtained from a one dimensional fully correlated wave model. These are the reduction in the along wave forces and the attenuation of wave forces on two members as the separation increases.

2. The wave forces calculated from both models may be in good agreement if the parameters of both models are properly chosen.

3. The coherence function model fails to represent the ratio between the two horizontal force components only when the mean direction of wave advance is such that one of the two force components is small.

4. The coherence function model appears to be a better model for evaluation of the along wave force component as it incorporates the lack of spatial correlation typical of short crested waves and offers substantial computational advantages.

9.3. Response of Fixed Offshore Towers

The coherence function model and pile-soil-pile interaction are incorporated in the general model for solving the response of the tower to random waves. Pile-soil separation is accounted for. Drag forces are linearized and the analysis is carried out in terms of the theory of random vibration. The effects of both the foundation and wave loading parameters on the dynamic properties as well as the response of the tower are investigated and the following conclusions are drawn:

1. Foundation damping is the major source of damping at low wind speeds while the hydrodynamic damping is the main source at high wind speeds.

2. Dynamic pile-soil-pile interaction, usually neglected in design, has a significant effect even with large pile spacing. It markedly increases the damping derived from the foundation.

3. Dynamic pile-soil-pile interaction increases the background response of the tower but decreases the resonant response.

4. While the total response of the tower increases due to pile-soil-pile interaction at higher wind speeds, it decreases at lower wind speeds.

9.4. Recommendations for Further Research

The nature of pile-soil force transfer mechanism during pile driving is not fully understood and its modelling is basic to the understanding of the driving process. The proposed model parameters should be evaluated in a statistical manner based on a large number of load tests.

Although both of the directional spectrum and coherence function models can yield similar results there is a need to establish the parameters of both models through comparisons with experimental data.

The interaction factors used in this study are based on a linear solution which may exaggerate the effects of pile interaction. A more realistic analysis should include soil nonlinearity.

However, it should be noted that the accuracy of the models presented herein depends on the reliability of the input parameters. With regard to the uncertainties associated with these parameters, particularly with the soil properties, safety of offshore structures should be further studied.

References.

1. Smith, E.A.L., "Pile Driving Analysis by the Wave Equation", ASCE, Transactions, Paper No. 3306, Vol. 127, Part 1., pp. 1145-1170.

2. Bea, R.G., "Dynamic Response of Marine Foundations", Keynote paper for Ocean Structural Dynamics Symposium '84, Sept. 11-13, 1984, Oregon State University.

3. "Planning and Design of Fixed Offshore Platforms", McClelland, B. and Reifel, M.D. (Editors), Van Nostrand Reinhold Company, 1986.

4. Vickery, B.J., "Wind Loads on Compliant Offshore Structures", Proceedings of the Symposium on Ocean Structural Dynamics, Dept. of Civil Engineering, Oregon State University, Corvillas, Oregon, Sept. 8-10, 1982.

5. Strickland, G.E., Brooks, L.D. and Pearce, J.C., "Ice Forces", Chapter 3 in "Planning and Design of Fixed Offshore Platforms", McClelland, B. and Reifel, M.D. (Editors), Van Nostrand Reinhold Company, 1986.

6. Davis, R.O. and Phelan, P.J., "Numerical Approximation in Pile Driving Analysis", Technical Note, International Journal for Numerical and Analytical Methods in Geomechanics, Vol. 2, 1978, pp. 303-310.

7. Matlock, H.M. and Foo., S.C., "Axial Analysis of Piles Using a Hysteretic and Degrading Soil Model", Conference on Numerical Methods in Offshore Piling", Institution of Civil Engineers, London, 1980, pp. 127-133.

8. Holloway, D.M. and Dover, A.R., "Recent Advances in Predicting Pile Drivability", Offshore Technology Conference, Houston, Texas, 1978, OTC 3273.

9. Heerema, E.P. and de Jong, A., "An Advanced Wave Equation Computer Program Which Simulates Dynamic Pile Plugging Through a Coupled Mass Spring System", Numerical Methods in Offshore Piling, Institution of Civil Engineers, London, 1980, pp. 37-42.

10. Goble. G.G. and Hery. P.. "Influence of Residual Forces on Pile Drivability". Second International Conference on the Application of Stress Wave Theory on Piles. Stockholm. Sweden. May 1984.

11. Rausche. F.. Goble. G.G. and Likins. G.E.. Jr.. "Dynamic Determination of Pile Capacity". ASCE. J. of Geotechnical Eng. Div.. Vol. 111. No. 3. March 1985. pp. 367-383.

12. Novak. M.. Nogami. T. and Aboul Ella. F.. "Dynamic Soil Reactions for Plane Strain Case". ASCE. J. Eng. Mechanics Division. Vol. 104 1978. pp. 953-956.

13. Samson. C.H.. Hirsch. T.J. and Lowery. L.L. Jr.. "Computer Study of Dynamic Behaviour of Piling". ASCE. Vol. 89. No. ST4. August. 1963. pp. 413-449.

14. Timoshenko. S. and Goodier. J.M.. "Theory of Elasticity". McGraw Hill Book Co.. Second ed.. 1951.

15. Litkouhi. S. and Poskitt. T.J.. "Damping Constants for Pile Drivability Calculations". Geotechnique. Vol. 30. No. 1. 1980. pp. 77-86.

16. Smith. E.A.L.. "Impact and Longitudinal Wave Transmission". Transactions. ASME. August. 1955. pp. 963-973.

17. Smith. I.M. and Chow. Y.K.. "Three Dimensional Analysis of Pile Drivability". Proc. of the Second International Conference. Numerical Methods in Offshore Piling. Austin. Texas. 1982. pp. 1-19.

18. Chow. Y.K. and Smith. I.M.. "A Numerical Model for the Analysis of Pile Drivability". Second International Conference on the Application of Stress Wave Theory on Piles. Stockholm. Sweden. May 1984.

19. Goble. G.G. and Rausche. F.. "Pile Drivability Predictions by Capwap". Numerical Methods in Offshore Piling. Institution of Civil Engineers. London. 1980. pp. 29-36.

20. Wu. A.K.H.. Kuhlemeyer. R.L. and To. C.W.S.. "Pile Shaft-Soil Model for Wave Equation Analysis: Verification by Dynamic Finite Element Approach". Proc.. Third Canadian Conference on Marine Geotechnical Engineering. St. John's. New Foundland. 1986. pp. 761-778.

21. de Sitter, W.R. and Groep, H.B., "Special Offshore Pile Driving Test", Offshore Technology Conference, May 5-8, 1980, OTC 3828.

22. Vijayverglya, V.N., "Soil Response During Pile Driving", Numerical Methods in Offshore Piling, Institution of Civil Engineers, London, 1980, pp. 53-58.

23. Roy, M., Blanchet, R., Tavenas, F. and La Rochelle, P., "Behaviour of a Sensitive Clay During Pile Driving", Canadian Geotechnical Journal, Vol. 18, 1981, pp. 67-85.

24. Hindy, A. and Novak, M., "Earthquake Response of Buried Insulated Pipes", ASCE, J. of the Eng. Mechanics Div., Vol. 106, No. EM6, December, 1980.

25. Novak, M. and Sheta, M., "Approximate Approach to Contact Effects of Piles", Proc. of Session on Dynamic Response of Pile Foundations: Analytical ASpects, ASCE National Convention, Florida, Oct. 1980, pp. 53-79.

26. Veletsos, A.S. and Verbic, A., "Vibration of Viscoelastic Foundations", Earthquake Engineering and Structural Dynamics, Vol 2, 1973, pp. 87-102.

27. Bossard, A. and Cote, J.F., "Analysis of Pile Response to Impact Loading and Use of Static Soil-Pile Interaction Laws", Second International Conference on the Application of Stress Wave Theory on Piles, Stockholm, Sweden, May 1984.

28. Randolph, M.F. and Simons, H.A., "An Improved Soil Model for One Dimensional Pile Driving Analysis", Third International Conference, Numerical Methods in Offshore Piling, Nantes, France, May 21-22, 1986, pp. 3-17.

29. Corte, J.F. and Lepert, P., "Lateral Resistance During Driving and Dynamic Pile Testing", Third International Conference, Numerical Methods in Offshore Piling, Nantes, France, May 21-22, 1986, pp. 19-33.

30. Rausche, F., Moses, F. and Goble, G.G., "Soil Resistance Predictions from Pile Dynamics", J. of the Soil Mechanics and Foundation Div., ASCE, Vol. 98, No. SM9, Sept. 1972.

31. Rausche, F., "Stress Wave Measuring in Practice", Theme Lecture

and Paper for Second International Conference on the Application of Stress Wave Theory on Piles, Stockholm, Sweden, May 1987.

32. de Sitter, W.R., "Measurement of Local Friction During Driving", Second International Conference on the Application of Stress Wave Theory on Piles, Stockholm, Sweden, May 1984, pp. 25-32.

33. Smith, I.M., To, P. and Willson, S.M., "Plugging of Pipe Piles", Third International Conference, Numerical Methods in Offshore Piling, Nantes, France, May 21-22, 1986, pp. 53-73.

34. Luco, J.E., Hadjian, A.H. and Bos, H.D., "The Dynamic Modeling of the half Plane by Finite Elements", Nuclear Engineering and Design, Vol. 31, 1974.

35. Lysmer, J. and Kuhlemeyer, R.L., "Finite Dynamic Model for Infinite Media", J. of the Engineering Mechanics Div., ASCE, August, 1969.

36. Kuhlemeyer, R.L., "Vertical Vibration of Footings Embedded in Layered Media", Ph.D. Thesis, University of California, Berkeley, California.

37. White, W., Valliappan, S. and Lee, I.K., "Unified Boundary for Finite Dynamic Models", J. of the Engineering Mech. Div., ASCE, pp. 949-964, Oct., 1977.

38. White, W., Valliappan, S. and Lee, I.K., "Energy Absorbing Boundary for Anisotropic Material", Numerical Methods in Geomechanics.

39. Lysmer, J. and Drake, L.A., "A Finite Element Method for Seismology", Methods in Computational Physics, Vol. 11, Bolt, B. (Editor), Academic Press, New York.

40. Kausel, E., Roesset, J.M. and Waas, G., "Dynamic Analysis of Footings on Layered Media", J. of the Engineering Mechanics Div., Vol. 101, No. EM5, Oct. 1975, pp. 679-693.

41. Waas, G., Riggs, H.R. and Werkle, H., "Displacement Solutions for Dynamic Loads in Transversely Isotropic Stratified Media", Earthquake Engineeing and Structural Dynamics, Vol. 13, 1985, pp. 173-193.

42. Veletsos, A.S. and Dotson, K., "Impedances of Soil Layer with Disturbed Boundary Zone", J. of Geotechnical Engineering, Vol. 112, No. 3, March, 1986, pp. 363-368.

43. Lakshmanan, N. and Minai, R., "Dynamic Soil Reactions in Radially Non homogeneous Soil Media", Bulletin of Disaster Prevention Research Institute, Kyoto University, Vol. 31, Part 2, No. 279, 1981.

44. Smith, I.M., "Programming the Finite Element Method", John Wiley & Sons, 1982.

45. Bathe, K.J., "Finite Element Procedures in Engineering Analysis", Prentice- Hall, Inc., 1982.

46. Novak, M. and El-Sharnouby,. B., "Stiffness Constants of Single Piles", J. of Geotechnical Engineering, ASCE, Vol. 109, No. 7, 1983, pp. 961-974.

47. Poulos, H.G. and Davis, E.H., "Pile Foundation Analysis and Design", John Wiley, New York, 1980.

48. Ostadan, F., "Dynamic Analysis of Soil-Pile Structure System", Dissertation Submitted in Partial Satisfaction of the Requirements for the Degree of Doctor of Philosophy, University of California, Berkeley, 1983.

49. Zaman, M.M. and Kuang, S.L., "Influence of Interface Conditions on Dynamic Response of Axially Loaded Piles", International Symposium on Dynamic Soil-Structure Interaction, Minneapolis, Sept. 1984, pp. 75-83

50. Wu, K.H.W., "Pile Shaft-Soil Model for Wave Equation Analysis: Verification by Finite Element Approach", M.Sc. Thesis, University of Calgary, Calgary, Alberta, 1985.

51. Desai, C.S., Zaman, M., Lightner, J.G. and Siriwardane, H.J., "Thin Layer Element For Interface and Joints", International Journal for Numerical and Analytical Methods in Geomechanics, Vol. 8, 1984, pp. 19-43.

52. Goodman, R.E., Taylor, R.L. and Brekke, T.L., "A Model for the Mechanics of Jointed Rock", J. Soil Mechanics and Foundation Division, ASCE, Vol. 94, No. SM3, 1968.

53. Clough, R.W. and Duncan, J.M., "Finite Element Analysis of, Retaining Wall Behaviour", J. of the Soil Mechanics and Foundation Division, ASCE, Vol. 97, No. SM12, 1971, pp. 1657-1673.

54. Zienkiewicz, O.C., Best, B., Dullage, C. and Stagg, K.G., "Analysis of Non-Linear Problems in Rock Mechanics with Particular Reference to Jointed Rock Systems". Proc., Second Congress of the International Society for Rock Mechanics, Belgrade, 1970.

55. Ghaboussi, J., Wilson, E.L. and Isenberg, J., "Finite Element for Rock Joints and Interfaces", J. of the Soil Mechanics and Foundation Division, ASCE, Vol. 99, No. SM10, October, 1973, pp. 833-848.

56. Toki, K., Sato, T. and Miura, F., "Separation and Sliding Between Soil and Structure During Strong Ground Motion", Earthquake Engineering and Structural Dynamics, Vol. 14, 1986, pp. 1-18.

57. Desai, C.S., "Behaviour of Interfaces Between Structural and Geologic Media"; International Conference on Recent Advances in Geotechnical Earthquake Engineering And Soil Dynamics, St. Loui, Mo., 1981, pp.619-638.

58. Desai, C.S.,"Modelling and Implementation of Constitutive Behaviour of Interfaces", International Symposium on Dynamic Soil Structure Interaction, Minneapolis, Sept. 1984, pp. 103-111.

59. Drumm, E.C. and Desai, C.S., "Determination of Parameters for a Model for the Cyclic Behaviour of Interfaces", Earthquake Engineering and Structural Dynamics, Vol. 14, pp. 1-18.

60. Drumm, E.C. and Desai, C.S., "Sand Concrete Interfaces: Cyclic Laboratory Testing and a Constitutive Model", International Symposium on Dynamic Soil Structure Interaction, Minneapolis, Sept. 1984, pp. 125-132.

61. Zaman, M., Desai, C.S. and Drumm, E.C., "Interface Model for Dynamic Soil Structure Interaction", ASCE, J. of Geotechnical Engineering, Vol. 110, No. 9, 1984, pp. 1257-1273.

62. Herrmann, L.R., "Finite Element Analysis in Contact Problems", J. of the Engineering Mechanics Division, ASCE, Vol. 104, No, EM5, 1978, pp. 1043-1057.

63. Zienkiewicz, O.C., Valliapan, S. and King, I.P., "Elasto-Plastic Solutions of Engineering Problems 'Initial Stress', Finite Element Approach", International Journal for Numerical Methods in Engineering, Vol. 1, 1969, pp.75-100.

64. Clough, R.W. and Penzien, J., "Dynamics of Structres", McGraw Hill Book Company, 1975.

65. Kagawa, T., "Soil-Pile Interaction of Offshore Structures During an Earthquake", Twelvth Annual Offshore Technology Conference, Houston, Texas, May 5-8, 1980, OTC 3820.

66. Nogami, T. et al., "Effect of Radiation Damping on Earthquake Response of Pile Supported Offshore Platforms", Earthquake Engineering and Structural Dynamics, Vol. 11, 337-353 (1983).

67. Penzien, J., "Structural Dynamics of Fixed Offshore Structures", Behaviour of Offshore Structures, BOSS 76, The Norwegian Institute of Technology.

68. Wolf, J.P., "Dynamic Soil-Structure Interaction", Prentice-Hall, Inc., 1985.

69. Focht, J.A., Jr. and Kraft, L.M., Jr., "Axial Performance and Capacity of Piles", Chapter 21 in "Planning and Design of Fixed Offshore Platforms", Mclleland,B. and Reifel, M.D., (Editors), 1986, Van Nostrand Reinhold Company.

70. Kriger, G.A., "Modelling of Piled Foundations", Twelvth Annual Offshore Technology Conference, Houston, Texas, May 5-8, 1980, OTC 3748.

71. Melth, R.M., "Force Coupled Structure Foundation Interaction", J. of Waterway, Port, Coastal and Ocean Engineering, Vol. 110, No. 2, May, 1984.

72. Taylor, R.E. and Rajagopalan,A., "Load Spectra for Slender Offshore Structures in Waves and Currents", Earthquake Engineering and Structural Dynamics, Vol. 11, 1983, pp. 831-842.

73. Angelides, D.C., "Stochastic Response of Fixed Offshore Structures in Random Seas", Ph.D. Thesis, Massachusetts Institute of Technology, Department of Civil Engineering, Cambridge, Massachusetts.

74. Clausen, C.J.F., Aas, P.M. and Almeland, I.B., "Analysis of the Pile Foundation System for a North Sea Drilling Platform", Proc. of the Third International Conference, Behaviour of Offshore Structures, MIT, Cambridge, Massachusetts.

75. Randolph, M.F. and Poulos, H.G., "Estimating the Flexibility of Offshore Pile Groups". Proceedings of the Second International Conference on Numerical Methods in Offshore Piling, University of Texas, Austin, Texas, 1982, pp. 313-328.

76. O'Neill, M.W., Ghazzaly,O.I. and Ha, H.B., "Analysis of Three Dimensional Pile Groups with Non-linear Soil Response and Pile-Soil-Pile Interaction". Ninth Annual Offshore Technology Conference, Houston, Texas, May 2-5, 1977, OTC 2838.

77. Hariharan, M. and Kumarasamy, K., "Analysis of Pile Groups Subjected to Lateral Loads", Proc. of the Third International Conference, Behaviour of Offshore Structures (BOSS), MIT, Cambridge, Massachusetts, pp. 383-390.

78. Anagnostopoulos, S.A., "Pile Foundation Modelling for Inelastic Earthquake Analysis of Large Structures", Engineering Structures, Vol. 5, July, 1983.

79. Angelides, D.C. and Roesset, J., "Nonlinear Dynamic Stiffness of Piles", Massachusetts Institute of Technology, Department of Civil Engineering Research Report R 80-13, April, 1980.

80. Poulos, H.G. and Randolph, M.K., "Pile Group Analysis: A Study of Two Methods", J. Geotechnical Engineering, Vol. 109, 1983, pp. 355-372.

81. Nogami, T. and Paulson, S.K., "Transfer Matrix Approach for Nonlinear Pile Group Response Analysis", J. Numerical and Analytical Methods in Geomechanics, Vol. 9, 1985, pp. 299-316.

82. Penzien, J., Scheffley, C.F. and Parmalee, R.A., "Seismic Analysis of Bridges on Long Piles", J. of the Engineering Mechanics Division, Proc. of the ASCE, Vol. 90, No. EM3, June, 1964, pp. 223-253.

83. Penzien, J., "Soil-Pile Interaction", Chapter 14 in Earthquake Engineering, Weigel, R.L. (Editor), Prentice-Hall, 1970.

84. Liou, D.D. and Penzien, J., "Mathematical Modelling of Piled Foundations", Numerical Methods in Offshore Piling, ICE, London, 1980, pp. 69-74.

85. Matlock et al., "Simulation of Lateral Pile Behaviour Under Earthquake Loading", Proc. ASCE, Specialty Conference on

. Earthquake Engineering and Soil Dynamics. Pasadena. California. 1978. pp. 600-619

86. Tajimi. H.."Dynamic Analysis of a Structure Embedded in an Elastic Medium". Proc. of the Fourth World Conference on Earthquake Engineering. Chile. 1969.

87. Nogami. T. and Novak. M. "Soil-Pile Interaction in Vertical Vibration". International J. Earthquake Engineering and Soil Dynamics. 1977. No. 3. pp. 249-261.

88. Novak. M. and Nogami. T.. "Soil-Pile Interaction in Horizontal Vibration". Earthquake Engineering and Structural Dynamics. Vol. 5. 1977. pp. 263-281.

89. Novak.M.. "Dynamic Stiffness and Damping of Piles". Canadian Geotechnical Journal. Vol. 11. No.4. 1974. pp. 574-598.

90. Kobori. T. et al.. "Dynamic Behaviour of a Laterally Loaded Pile". Proc.. Ninth International Conference on Soil Mechanics. Tokyo. 1977.

91. Kuhlemeyer. R.L.. "Vertical Vibration of Piles". J. of the Geotechnical Engineering Division. ASCE. Vol. 105. No. GT2. pp. 371-389.

92. Kuhlemeyer. R.L.. "Static and Dynamic Laterally Loaded Floating Piles". J. Geotechnical Engineering Division. ASCE. Vol. 105.: No. GT2. 1979.

93. Blaney. G.W.. Kausel. E. and Roesset. J.M.. "Dynamic Stiffness of Piles". Proc. Second International Conference on Numerical Methods in Geomechanics. ASCE. New York. 1976. pp. 1001-1012.

94. Angelides, D.C. and Roesset. J.M. "Nonlinear Lateral Dynamic Stiffness of Piles". J. of the Geotechnical Engineering Division. Proc. ASCE. Vol. 107. No. GT11. Nov.. 1981. pp. 1443-1459.

95. Banerjee. P.K. and Butterfield. R.. "Boundary Element Methods in Geomechanics". Chapter 16 in Finite Elements in Geomechanics. Wiley. 1977.

96. Baranov. V.A.. "On the Vibration of an Embedded Foundation". (in Russian). Voprosy. Dinamiki i Prochnosti. No. 14. Polytechnical Institute of Riga. 1967; pp. 195-209.

97. Novak, M., "Vertical Vibration of Floating Piles", J. of the Eng. Mech. Division, ASCE, Vol. 103, No. 103, No. EM1, Feb., 1977, pp.153-168.

98. Novak, M. and Aboul Ella, F., "Impedance Functions of Piles in Layered Media", J. of the Eng. Mech. Division, ASCE, Vol. 104, No EM6, June, 1978, pp. 643-661.

99. Kausel, E., "Forced Vibration of Circular Foundation on Layered Media", Research Report R74-11, Civil Engineering Dept., MIT, Jan., 1974

100. Salinero, I.S. and Roesset, J.M., "Comparison of Analytical Methods to Evaluate Axial and Lateral Dynamic Stiffness of Single Piles", Eighth European Conference on Earthquake Engineering, Lisbon, 1986.

101. Novak, M., Aboul Ella, F. and Sheta, M., "PILAY2-A", Computer Program for Calculation of Stiffness and Damping of Piles in Layered Media, The University of Western Ontario, SACDA, London, Ontario, Canada.

102. El-Sharnouby, B. and Novak, M., "Static and Low Frequency Response of Pile Groups", Canadian Geotechnical Journal, Vol. 22, No. 1, pp. 79-94.

103. Kaynia, A.M. and Kausel, E., "Dynamic Behaviour of Pile Groups", Conference on Numerical Methods in Offshore Piling, University of Texas, Austin, Texas, pp. 509-532.

104. Poulos, H.G., "Analysis and Settlement of Pile Groups", Geotechnique, Vol. 18, pp. 449-471, 1968.

105. Poulos, H.G., "Behaviour of Laterally Loaded Piles -2- Pile Groups", J. Soil Mech. and Foundation Division, Proc. of ASCE, 1971.

106. Poulos, H.G., "Group Factor of Pile Deflection Estimation", J. Geotechnical Eng. Div., ASCE, GT12, 1979, pp.1489-1509.

107. Butterfield, R. and Banerjee, P.K., "The Problem of Pile Group Pile Cap Interaction", Geotechnique, Vol. 21, No.2, 1971, pp. 135-142.

108. Wolf, J.P. and Von Arx, G.A., "Impedance Functions of a Group of Vertical Piles", Proc. ASCE Specialty Conference on Earthquake Eng. and Soil Dynamics, Pasadena, California, 1978, pp. 1024-1041.

109. Wolf. J.P., "Dynamic Stiffness of Group of Battered Piles", J. Geotech. Eng. Division, ASCE, Vol. 106, No. GT2, pp. 198-203. Feb., 1980.

110. Nogami, T., "Dynamic Group Effects of Multiple Piles Under Vertical Vibration", ASCE. Eng. Mech. Spec. Conference. Austin, Texas, 1979, pp. 750-754.

111. Nogami, T., "Dynamic Stiffness and Damping of Pile Groups in Inhomogeneous Soil, "Proc. of Session on Dynamic Response of Pile Foundations: Analytical Aspects, ASCE National Convention, Oct. 1980, pp..31-52.

112. Sheta. M. and Novak, M., "Vertical Vibration of Pile Groups", J. Geotechnical Eng. Division, ASCE, Vol. 108, No. GT4, April, 1982., pp. 570-590.

113. El-Sharnouby, B., "Static and Dynamic Analysis of Pile Foundations", Ph.D. Thesis, University of Western Ontario, London, Canada, 1984.

114. Novak, M. and El-Sharnouby, B., "Pile Groups Under Static and Dynamic Loading", Proc. of the Eleventh International Conference on Soil Mechanics and Foundation Engineering, San Francisco, 1985, Vol. 3, pp. 1449-1454.

115. Private communications with Wotton, R.L., Atkins Research and Development, U.K.

116. Private communications with Howell, J.F., (Vipac, Australia).

117. Novak, M., "Soil-Pile Interaction Under Dynamic Loading", Numerical Methods in Offshore Piling, Institution of Civil Engineers, London, 1980, pp. 59-68.

118. Forristall, G.Z., Ward, E.G., Cardone, V.J. and Borgman, L.E., "The Directional Spectra and Kinematics of Surface Gravity Waves in Tropical Storm Delia", J. of Physical Oceanography, V.8, 1978, pp 888-909.

119. Lamb, H., "Hydrodynamics", Sixth ed., Dover, New York, 1945.

120. Phillps, O.M., "The Dynamics of Upper Ocean", Second ed., Cambridge Univ. Press, 1977.

121. Minkenberg, H.L. and Gie, T.S., "Will The Regular Wave Concept Yield Meaningful Motion Predictions for Offshore Structures". Sixth Annual Offshore Technology Confereence. Houston, Texas, May 1974. OTC 75206.

122. Wheeler, J.D., "Method for Calculating Forces Produced by Irregular Waves". First Annual Offshore Technology Conference. Houston. Texas, May 1969, OTC 1006.

123. Lambrakos, K.F. and Brannon, H.R., "Wave Force Calculations for Stokes and Non Stokes Waves". Proc. Sixth Annual Offshore Technology Conference, Houston, Texas, 1974. OTC 2039

124. Dean, R.G., "Stream Function Representation of Nonlinear Ocean Waves", J. Geophysical Research, V. 70, pp 4561-4572.

125. Morison, J.R., O'Brien, M.P., Johnson, J.W. and Schaaf, S.A., "The Force Exerted by Surface Waves on Piles". Petroleum Transactions. AIME, Vol. 189, 1950, pp. 149-154.

126. Hogben, N., Miller, B.L., Searle, J.W. and Ward, G., "Estimation of Fluid Loading on Offshore Structures". Proc., Institution of Civil Engineers, Part 2, Vol. 63, Sept. 1977, pp. 515-562.

127. Wiegel, R.L., Beebe, K.E. and Moon, J., "Ocean Wave Forces on Circular Cylindrical Piles". Journal of Hydraulics Division. ASCE. Vol. 83, HY2, April, 1957, pp. (1199-1)-(1199-36).

128, Keulegan, G.H. and Carpenter, L.H.,"Forces on Cylinders and Plates in an Oscillating Fluid". J. Res. Nat. Bureau of Standards. Vol 60, 1958, No. 5, May, pp. 423-440.

129. Sarpkaya, T., "In-Line and Tranverse Forces on Cylinders in Oscillatory Flow at High Reynolds Number". Offshore Technology Conference, 1976, OTC 2533.

130. Evans, D.J., "Analysis of Wave Force Data", O.T.C., 1969, Vol. 1. Paper OTC 1005, pp. (I-51)-(I-70).

131. Borgman, L.E., "Statistical Models for Ocean Waves and Wave Forces", Advances in Hydroscience, Vol. 8, 1972, pp. 139-181

132. Borgman, L.E., "Ocean Wave Simulation for Engineering Design". J. of the Waterways and Harbours Div., Proc., ASCE, Vol. 95, No. WW4, Nov. 1969, pp.557-583.

133. Malhotra, A. and Penzien, J., "Non-deterministic Analysis of Offshore Structures", J. Eng. Mech. Div., ASCE, Vol. 96. No. EM6, Dec. 1970, pp. 985-1003.

134. Mitsuyasu, H., Tasai, F., Suhara, T., Mizuno, S., Ohkusu, M., Honda, T. and Rikushi, K., "Observatons of the Directional Spectrum of Ocean Waves Using a Cloverleaf Buoy", J. of Physical Oceanography, Vol. 5, Oct. 1975, pp. 750-760.

135. Mitsuyasu, H. and Mizuno, S., "Directional Spectra of Ocean Surface Waves", Fifteenth Coastal Engineering Conference, Vancouver, 1976.

136. Mobarek, I.E., "Directional Spectra of Laboratory Wind Waves", J of the Waterways and Harbors Div., ASCE, Vol. 91, No WW3, Aug. 1965, pp. 91-119.

137. Dean, R.G. and Borgman, L.E., "Wind and Wave Forces", Chapter 12, Planning and Design of Fixed Offshore Structures, Mclelland,B. and Reifel, M.D. (Editors), 1986, Van Nostrand Reinhold Company.

138. Dean, R.G., "Hybrid Methods of Computing Wave Loading", Proc. Offshore Technology Conference, Houston, May 1977, OTC 3029, pp. 483-492.

139. Borgman, L.E., "Spectral Analysis of Ocean Wave Forces on Piling", J. of the Waterways and Horbors Div., Proc. of the ASCE, Vol. 93, No. WW2, May 1967.

140. Burrows, R., "Probabilistic Description of the Response of Offshore Structures to Random Wave Loading", in Mechanics of Wave Forces on Cylinders, Edited by Shaw, T.L., Pitman, London, 1979, pp. 577-595.

141. Zedan, M.F., Yeung, J.Y., Salena, H.J. and Fischer, F.J., "Dynamic Response of a Cantilever Pile to Vortex Shedding in Regular Waves", Twelvth Annual Offshore Technology Conference, Houston, Texas, May 1980,OTC 3799.

142. Sarpkaya, T. and Isaacson, M., "Mechanics of Wave Forces on Offshore Structures", Chapter 4, Van Nostrand Reinhold Co., 1981.

143. Berge, B. and Penzien, J., "Three Dimensional Stochastic Response of Offshore Towers to Wave Forces", Offshore Technology Conference, May 1974, OTC 2050, pp.173-183.

144. Foster, E.T.. "Model for Nonlinear Dynamics of Offshore Towers". J. Eng. Mech. Div., Proc., ASCE. Vol. 96. No. EM1, Feb. 1970. pp. 41-67.

145. Wu, S.C. and Tung, C.C. "Random Response of Offshore Structures to Wave and Current Forces". Sea Grant Publication UNC-SG-75-22. North Carolina State University, Raleigh. N.C.

146. Rice. S.O.. "Mathematical Analysis of Random Noise". Bell System Tech. J. , Vol. 23, pp. 282-332. Vol. 24, pp. 46-156.

147. Longuet-Higgins, M.S. and Barber. N.F.. "Four Theoretical Notes on the Estimation of Sea Conditions". Report. Admiralty, Res. Lab.. Teddington.

148. StDenis, M. and Pierson, W.J.. "On the Motion of Ships in Confused Seas"..Trans. Soc. Naval Architects and Marine Engineers. New York. 1961. pp.280-357.

149. Pierson, W.J.. "Wind Generated Gravity Waves". Advances in Geophysics. Vol. 2. 1955. pp. 93-178.

150. Neumann, G. and Pierson, W.J.. Chapter 12. Principles of Physical Oceanography. Prentice -Hall Inc., 1966.

151. Kinsman, B.. "Wind Waves. Their Generation and Propagation on the Ocean Surface". Prentice-Hall Inc.. 1965.

152. Mitsuyasu, H.: "Recent Studies on Ocean Wave Spectra". IUTAM. 1985, Elsevier Science Publishers B.V.

153. Darbyshire, J.. "The Generation of Waves by Wind". Proc.. Royal Society, Series A, Vol. 215, pp. 299-328.

154. Neumann, G.. "On Ocean Wave Spectra and a New Method of Forecasting Wind Generated Sea". U.S. Army Corps of Engineers. Beach Erosion Board, Tech. Memo No. 43.

155. Pierson, W.J. and Moskowitz, L.. "A Proposed Spectral Form for Fully Developed Wind Seas Based on the Similarity Theory of S.A. Kitalgorodskii". J. of Geophysical Research. Vol. 69. No. 24. Dec. 15. 1964.

156. Bretschneider, C.L.. "Wave Variability and Wave Spectra for Wind

Generated Gravity Waves", U.S. Army Corps of Engineers, Beach Erosion Board, Tech. Memo. No 118.

157. Hasselmann, K. et. al. "Measurement of Wind Wave Growth and Swell Decay During the Joint North Sea Wave Project (JONSWAP)", Dtsch. Hydrogr. Z., Suppl. A, No. 12, 1973.

158. Ochi, M.K. and Hubble, E.N., "Six Parameter Wave Spectra", Fifteenth Coastal Engineering Conf., Vancouver, 1976, pp 301-328

159. Borgman, L.E., "Directional Spectra Models for Design Use", First Annual Offshore Technology Conference, Houston, Texas, May 1969, OTC 1069.

160. Longuet-Higgins, M.S., Cartwright, D.E. and Smith, N.D., "Observations of the Directional Spectrum of Sea Waves Using the Motion of a Floating Buoy", In: Ocean Wave Spectra, Prentice -Hall, pp. 111-132.

161. Berge, B., "Three Dimensional Stochastic Response of Offshore Towers to Wave Forces", Ph. D. Thesis, University of California, Berkeley, California, 1973.

162. Cote, L.J., Davis, J.O., Marks, W., McGough, R.J., Mehr, E., Pierson, W.J., Ropek, J.F., Stephenson, G. and Vetter, R.C., "Directional Spectrum of a Wind Generated Sea as Determined From Data Obtained by the Stereo Wave Observation Project", Meteorological Papers, Vol. 2, New York University, College of Engineering, pp. 1-88.

163. Davenport, A.G., "Wind Structure and Wind Climate", Paper presented at the International Research Seminar on Safety of Structures Under Dynamic Loading, Trondheim, June 1977.

164. Popov, E.P., Mahin, S.A. and Clough, R.W., "Inelastic Response of Tubular Steel Offshore Towers", J. Structural Division, Proc. ASCE, Vol. 111, No. 10, Oct. 1985, pp. 2240-2258.

165. Sunder, S.S. and Connor, J.J., "Sensitivity Analysis for Steel Jacket Offshore Structures", Progress In Engineering Sciences, Vol. 1, Dynamic Analysis of Offshore Structures, Kirk, C.L. (Editor) CML Publiacations, 1982.

166. Angelides, D.G. and Connor, J.J., "A Probabilistic Model for the Stiffness Degradation of Steel Jacket Structures", Proc. Second

International Conference, Behaviour of Offshore Structures, London, 1979.

167. Penzien, J. and Kaul, M.K., "Response of Offshore Towers to Strong Motion Earthquakes", Earthquake Engineering and Structural Dynamics, Vol. 1, 1972, pp. 55-68.

168. Penzien, J. Kaul, M.K. and Berge, B., "Stochastic Response of Offshore Towers to Random Sea Waves and Strong Motion Earthquakes", Computers and Structures, Vol. 2, 1972, pp. 733-756

169. Weaver, W.J. and Gere, J.M., "Matrix Analysis of Framed Structures", D. Van Nostrand Company, 1980.

170. Archer, J.S., "Consistent Mass Matrix for Distributed Mass Systems", J. Structural Division, ASCE, Vol. 89, No. ST4, 1963, pp. 161-178.

171. Cook, R.D., "Concepts and Applications of Finite Element Analysis", John Wiley, 1974.

172. Kolousek, V., "Dynamics In Engineering Structures", Halsted Press, Division of J. Wiley, 1973.

173. Craig, R.R., "Structural Dynamics: An Introduction to Computer Methods", John Wiley, 1981.

174. Rubinstien, M.F., "Matrix Computer Methods In Structural Analysis", Prentice-Hall, Inc., 1966.

175. Godeau, A.J. and Deleuil, G.E., "Dynamic Response and Fatigue Analysis of Fixed Offshore Structures", Annual Offshore Technology Conference, Houston, Texas, , OTC 2260.

176. Taylor, R.E. and Rajagopalan, A., "Dynamics of Offshore Structures, Part 1, Perturbation Analysis", J. Sound and Vibration, Vol. 83, 1982, pp. 401-416.

177. Rajagopalan, A. and Taylor, R.E., "Dynamics of Offshore Structures, Part 2: Stochastic Averaging Analysis", J. Sound and Vibration, Vol. 83, 1982, pp. 417-431.

178. Frazer, R.A., Duncan, W.J. and Collar, A.R., "Elementary Matrices", Cambridge University Press, London, 1946.

179. Pipes, L.A. and Hovanessian, S.A., "Matrix Computer Methods in Engineering", John Wiley, 1969.

180. El-Hifnawy, L., "Soil-Structure Interaction Under Dynamic Loads", Ph.D. Thesis, The University of Western Ontario, London, Canada, 1984.

181. Novak, M. and El-Hifnawy, L., "Effect of Soil-Structure Interaction on Damping of Structures", J. Earthquake Engineering and Structural Dynamics, Vol. 11, pp. 595-621.

182. Traill-Nash, R.W., "Modal Methods in the Dynamics of Systems With Non-Classical Damping", Earthquake Engineering and Structural Dynamics, Vol. 9, pp. 153-169, 1981.

183. Dawson, T.H., "Offshore Structural Engineering", Prentice-Hall, Inc., 1983.

Appendix A
Stiffness Matrix of Rectangular Axisymmetric Element

The stiffness matrix of the rectangular axisymmetric element shown in Fig 4.5 was rederived from first principles and is given herein.

A.1. Some Basic Constants

$$C11 = E(1-\nu)/(1+\nu)(1 \quad)$$

$$C12 = \nu E/(1+\nu)(1-2\nu)$$

$$C44 = E/2(1+\nu)$$

$$B3A = h$$

$$B5B = r_j^2 \ln(r_j/r_i) - 2(r_j^2 - r_i r_j) + (r_j^2 - r_i^2)/2$$

where r_j and r_i are the outer and inner radii of the element, respectively. h is the element height and E and ν are the Young's modulus and Poisson's ratio of the material, respectively.

$$B6B = r_i^2 \ln(r_j/r_i) + 2(r_i^2 - r_j r_i) + (r_j^2 - r_i^2)/2$$

$$B13B = r_i r_j \ln(r_j/r_i) - (r_j^2 - r_i^2)/2$$

$$B1B = h^3/3$$

$$B10.A = -h^2/2$$

$$B1.A = (r_j^2 - r_i^2)/2$$

$$B3B = r_j^4/12 - (r_j r_i)^2/2 + 2r_j r_i^3/3 - r_i^4/4$$

$$B4B = r_j^4/4 + (r_i r_j^2)/2 - 2r_i r_j^3/3 - r_i^4/12$$

$$B10B = -[(r_j^3 - r_i^2 r_j)/2 - (r_j^3 - r_i^3)/3]$$

$$B11B = (r_j^4 - r_i^4)/12 + (r_i^3 r_j - r_i r_j^3)/6$$

$$B12B = -(r_j^3 - r_i^3)/6 + (r_i r_j^2 - r_i^2 r_j)/2$$

$$B17B = -[(r_i r_j^2 - r_i^3)/2 - (r_j^3 - r_i^3)/3]$$

$$B23.A = (r_j - r_i)^2/2$$

A.2. Terms of the Upper Half of the Stiffness Matrix

$$K(1,1) = \{[(B1A + B5B)C11 - 2\ B23A\ C12]B1B + B3A\ B3B\ C44\}$$

$$K(1,2) = [B10B(C44 + C12) - 2\ B12B\ C12]B10A$$

$$K(1,3) = [(B5B + B1A)C11/2 - B23A\ C12]B1B - B3A\ B3B\ C44$$

$$K(1,4) = [2\ B12B\ C12 + B10B(C44 - C12)]B10A$$

$$K(1,5) = [(-B13B - B1A)B1B\ C11/2 - B3A\ B11B\ C44]$$

$$K(1,6) = [(B12B + B17B)C12 - B10B\ C44]B10A$$

$$K(1,7) = (-B13B - B1A)B1B\ C11 + B3A\ B11B\ C44$$

$$K(1,8) = [(-B12B - B17B)C12 - B10B\ C44]B10A$$

$$K(2,2) = (B3A\ B3B\ C11 + B1A\ B1B\ C44)$$

$$K(2,3) = -K(1,4)$$

$$K(2,4) = (-B3A\ B3B\ C11 + B1A\ B1B\ C44/2)$$

$$K(2,5) = [(-B12B - B10B)C12 + B17B\ C44]B10A$$

$$K(2,6) = (-B3A\ B11B\ C11 - B1A\ B1B\ C44/2)$$

$$K(2,7) = [(-B12B - B10B)C12 - B17B\ C44]B10A$$

$$K(2,8) = (B3A\ B11B\ C11 - B1A\ B1B\ C44)$$

$$K(3,3) = K(1,1) \qquad K(3,4) = -K(1,2)$$

$$K(3,5) = [(-B1A - B13B)B1B\ C11 + B3A\ B11B\ C44]$$

$$K(3,6) = -K(1,8) \qquad K(3,7) = K(1,5)$$

$$K(3,8) = -K(1,6) \qquad K(4,4) = K(2,2)$$

$$K(4,5) = -K(2,7) \qquad K(4,6) = K(2,8)$$

$$K(4,7) = -K(2,5) \qquad K(4,8) = K(2,6)$$

$$K(5,5) = [(B6B + B1A)C11 + 2\ B23A\ C12]B1B + B3A\ B4B\ C44$$

$$K(5,6) = -[B17B(C44 + C12) - 2\ B12B\ C12]B10A$$

$$K(5,7) = [(B6B + B1A)C11 + 2\ B23A\ C12]B1B/2 - B3A\ B4B\ C44$$

$$K(5,8) = -\{[(2\ B12B - B17B)C12 + B17B\ C44]B10A\}$$

$$K(6,6) = (B3A\ B4B\ C11 + B1A\ B1B\ C44)$$

$$K(6,7) = -K(5,8)$$

$$K(6,8) = (-B3A\ B4B\ C11 + B1A\ B1B\ C44/2)$$

$$K(7,7) = K(5,5) \qquad K(7,8) = -K(5,6)$$

$$K(8,8) = k(6,6)$$

Appendix B
Wave Forces for Directional Spectrum Model

The cross spectra of nodal wave forces, $S_{p_l p_m}(\omega)$, could be evaluated once the integrals I_{kl} in Eq. 6.62 are carried out. On substituting by Eqs. 6.63 and 6.39 in Eq. 6.62, the integrals I_{kl} are given by

$$I_{k_1 l_2} = e_1 e_2 \frac{\varsigma}{4\kappa^2} \int_{-\pi}^{\pi} G(\omega,\theta) C1(\theta) C2(\theta) \Lambda_{n s} \tag{B.1}$$
$$\cdot (I_1 + n1\, I_2)(I_3 + n2\, I_4) d\theta$$

where in $I_{k_1 l_2}$, k and l refer to members k and l respectively while 1 and 2 refer to the directions of water particle velocities associated with these members. For example, $I_{k_x l_y}$ is the integral of the cross spectrum of water particle velocity in direction x on member k and the water particle velocity in direction y on member l. In Eq. B.1,

$$e_1 = \begin{cases} 1 & 1//X \text{ or } 1//Z \\ -i & 1//Y \end{cases} \tag{B.2}$$

$$e_2 = \begin{cases} 1 & 2//X \text{ or } 2//Z \\ i & 2//Y \end{cases} \tag{B.3}$$

$$n1 = \begin{cases} 1 & 1//X \text{ or } 1//Z \\ -1 & 1//Y \end{cases} \tag{B.4}$$

$$n2 = \begin{cases} 1 & 2//X \text{ or } 2//Z \\ -1 & 2//Y \end{cases} \tag{B.5}$$

$$\varsigma = \frac{\omega^2 S_{hh}(\omega)}{\sinh^2 \kappa D} \tag{B.6}$$

258

$$A_{n s} = e^{i \kappa (x_n - x_s) \cos \theta - (z_n - z_s) \sin \theta} \tag{B.7}$$

and the direction parameters $C1(\theta)$ and $C2(\theta)$ are given by

$$C1(\theta) = \begin{cases} \cos \theta & 1 // X \\ 1 & 1 // Y \\ \sin \theta & 1 // Z \end{cases} \tag{B.8}$$

and

$$C2(\theta) = \begin{cases} \cos \theta & 2 // X \\ 1 & 2 // Y \\ \sin \theta & 2 // Z \end{cases} \tag{B.9}$$

The terms I_i in Eq. B.1 are given by

$$I_1 = e^{A_n}(e^{R_{ak} \overline{\kappa}} - 1)/R_{ak} \tag{B.10}$$

$$I_2 = e^{-A_n}(e^{R_{bk} \overline{\kappa}} - 1)/R_{bk}$$

$$I_3 = e^{A_s}(e^{R_{al} l_r \overline{\kappa}} - 1)/R_{al}$$

$$I_4 = e^{-A_s}(e^{R_{bl} l_r \overline{\kappa}} - 1)/R_{bl}$$

In Eq. B.10, the terms R_{ak}, R_{bk}, R_{al} and R_{bl} are defined by Eq. 6.69 and A_n and A_s are given by Eqs. 6.66 and 6.67, respectively. The directional spread function $G(\omega, \theta)$ in Eq. B.4 is the Circular Normal directional distribution given by Eq. 6.18.

Appendix C
Wave Forces for Unidirectional Waves

This model is essentially the unidirectional model where the surface elevation is represented by Eq. 6.10 and the water particle velocity spectrum is given by Eq. 6.45, i.e.

$$S_{\dot{v}_1 \dot{v}_2}(\omega) = \varsigma\, C1(\overline{\theta})C2(\overline{\theta}) HYP1[\kappa(Y_1 + D)] HYP2[\kappa(Y_2 + D)] \qquad (C.1)$$

$$.exp\{i\kappa[(x_1 - x_2)\cos\overline{\theta} + (z_1 - z_2)\sin\overline{\theta}]\}$$

where all the terms are defined in Paragraph 6.3.3.1. By expanding the hyperbolic sin and cos terms and substituting by Eq. 6.63. the integrations in Eq. 6.62 are carried out to give

$$I_{kl} = e_1 e_2 C1(\overline{\theta})C2(\overline{\theta})\frac{\varsigma}{4\kappa^2}A_{ns}(I_1 + n_1 I_2)(I_3 + n_2 I_4) \qquad (C.2)$$

where e_1 and e_2, n_1, n_2 and ς are given by Eqs. B.2 to B.6, respectively. $A_{ns}, C1(\overline{\theta})$ and $C2(\overline{\theta})$ are defined by Eqs. B.7 to B.9, respectively. If θ is substituted by $\overline{\theta}$. The terms $I_i, i = 1 \cdots 4$ are given by Eq. B.10 if θ is substituted by $\overline{\theta}$ in the terms R_{ak}, R_{bk}, R_{al} and R_{bl}.

Appendix D
Wave Forces Assuming Constant Velocity

When the velocity is assumed to be constant along the members, the integrals in Eq. 6.62 are written as

$$I_{kl} = L_k L_l S_{\dot{r}_n \dot{r}_s} \qquad (D.1)$$

where L_k and L_l are the tributary lengths of members k and l respectively. $S_{\dot{r}_n \dot{r}_s}$ is the cross spectrum of water particle velocity at nodes nodes n and s. By substituting by the appropriate formulae for the water particle velocity spectra for different models, the following expressions are obtained:

1)Directional Spectrum Model

$$I_{kl} = L_k L_l e_1 e_2 \frac{\varsigma}{4} (e^{A_n} + n_1 e^{-A_n})(e^{A_s} + n_2 e^{-A_s}) \qquad (D.2)$$

$$\int_{-\pi}^{\pi} G(\omega,\theta) C1(\theta) C2(\theta) exp\{\imath \kappa [(x_n - x_s)\cos\theta + (z_n - z_s)\sin\theta]\}$$

where e_1, e_2, n_1, n_2, $g(z)$, A_{ns}, $C1(\overline{\theta})$ and $C2(\overline{\theta})$ are defined by Eqs. E.2 to E.9, respectively and A_n and A_s are defined by Eqs. 6.66 and 6.67, respectively. $G(\omega,\theta)$ is the Circular Normal directional distribution given by Eq. 6.18.

2)Coherence Function Model

$$\qquad (D.3)$$

$$I_{kl} = L_k L_l e_1 e_2 \frac{\varsigma}{4} C1(\theta) C2(\theta) A_{ns} \Delta_{ns}$$
$$(e^{A_n} + n_1 e^{-A_n})(e^{A_s} + n_2 e^{-A_s})$$

where A_{ns}, $C1(\overline{\theta})$ and $C2(\overline{\theta})$ are given by Eqs. B.7 to B.9, respectively, if θ is substituted by $\overline{\theta}$. A_{ns} is given by Eq. E.10.

3)Fully Correlated Unidirectional Model:

$$I_{kl} = L_k L_l e_1 e_2 \frac{\varsigma}{4} C1(\theta) C2(\theta) A_{ns} \qquad (D.4)$$
$$(e^{A_n} + n_1 e^{-A_n})(e^{A_s} + n_2 e^{-A_s})$$

where A_{ns} is given by Eq. B.7 if θ is substituted by $\overline{\theta}$.

Appendix E
Wave Forces for Coherence Function Model

Evaluating the integrals I_{kl} in Eq. 6.62 is necessary to establish the spectral matrix of nodal forces. When the coherence function representation of the water particle velocity spectra, expressed by Eqs. 6.46 and 6.82, is used, the absolute value terms have to be expanded to be able to carry out the integrations. As discussed in Subsection. 6.6.1, 2 different cases are distinguished:

A) Nodes n and s Coincide:

A-1) One pair of the direction cosines have identical signs:

The expansions of the absolute value terms are given by Eqs. 6.85 to 6.87 and carrying out the integrations I_{kl} yields

$$I_{kl} = e_1 e_2 C1(\overline{\theta}) C2(\overline{\theta}) \frac{\varsigma}{4\kappa^2} [\sum_{\iota=1}^{16} (-1)^{n_\iota} I_\iota] \qquad (E.1)$$

where $\overline{\theta}$ is the mean direction of advance of the wave system, e_1 and e_2 are defined by Eqs. B.2 and B.3, respectively, ς is given by Eq. B.6 and $C1(\overline{\theta})$ and $C2(\overline{\theta})$ are defined by Eqs. B.8 and B.9 respectively, if θ is substituted for $\overline{\theta}$. The integer n_ι is given by

$$n_\iota = \begin{cases} \iota + 1 & \\ \quad 1//X \text{ or } 1//Z \text{ and } 2//X \text{ or } 2//Z \\ INT(\iota/2) & \\ \quad 1//X \text{ or } 1//Z \text{ and } 2//Y \\ INT(\frac{5\iota-1}{4} + 1) & \\ \quad 1//Y \text{ and } 2//X \text{ or } 2//Z \\ INT(\iota/2) + INT(\frac{\iota-1}{4})\Upsilon & \\ \quad 1//Y \text{ and } 2//Y \end{cases} \qquad (E.2)$$

where $INT(R)$ is the integer part of the real number R. The terms I_i, $i = 1 \cdots$ 16 are given by

$$I_1 = \frac{e^{2\Lambda_n}[e^{\overline{\kappa}(T_{ak}+b_rT_{l1})}-1]}{T_{l1}(T_{ak}+b_rT_{l1})}$$

(E.3)

$$I_2 = \frac{e^{2\Lambda_n}(e^{\overline{\kappa}T_{ak}}-1)}{T_{l1}T_{ak}}$$

$$I_3 = \frac{[e^{\overline{\kappa}(T_{ak}+b_rT_{l2})}-1]}{T_{l2}(T_{ak}+b_rT_{l2})}$$

$$I_4 = \frac{(e^{\overline{\kappa}T_{ak}}-1)}{T_{ak}T_{l2}}$$

$$I_5 = \frac{[e^{\overline{\kappa}(T_{bk}+b_rT_{l1})}-1]}{T_{l1}(T_{bk}+b_rT_{l1})}$$

$$I_6 = \frac{(e^{\overline{\kappa}T_{bk}}-1)}{T_{bk}T_{l2}}$$

$$I_7 = \frac{e^{-2\Lambda_n}[e^{\overline{\kappa}(T_{bk}+b_rT_{l2})}-1]}{T_{l2}(T_{bk}+b_rT_{l2})}$$

$$I_8 = \frac{e^{-2\Lambda_n}(e^{\overline{\kappa}T_{bk}}-1)}{T_{l2}T_{bk}}$$

$$I_9 = \frac{e^{2\Lambda_n+L_r\overline{\kappa}T_{al}}(e^{\overline{\kappa}T_{k1}}-1)}{T_{al}T_{k1}}$$

$$I_{10} = \frac{e^{2\Lambda_n}[e^{\overline{\kappa}(T_{k1}+b_rT_{al})}-1]}{T_{al}(T_{k1}+b_rT_{al})}$$

$$I_{11} = \frac{e^{L_r\overline{\kappa}T_{bl}}(e^{\overline{\kappa}T_{k1}}-1)}{T_{bl}T_{k1}}$$

$$I_{12} = \frac{[e^{\overline{\kappa}(T_{k1}+b_rT_{bl})}-1]}{T_{bl}(T_{k1}+b_rT_{bl})}$$

$$I_{13} = \frac{e^{\overline{\kappa}L_rT_{al}}(e^{\overline{\kappa}T_{k2}}-1)}{T_{al}T_{k2}}$$

$$I_{11} = \frac{[e^{\bar{\kappa}(T_{k2} + b_r T_{al})} - 1]}{T_{al}(T_{k2} + b_r T_{al})}$$

$$I_{15} = \frac{e^{-2\lambda_n - \bar{\kappa} L_r} T_{bl}(e^{\bar{\kappa} T_{k2}} - 1)}{T_{bl} T_{k2}}$$

$$I_{16} = \frac{e^{-2\lambda_n}[e^{\bar{\kappa}(T_{k2} + b_r T_{bl})} - 1]}{T_{bl}(T_{k2} + b_r T_{bl})}$$

In Eq. E.3,

$$T_{ak} = R_{ak} - \frac{\gamma c}{2\pi}(p_k + q_k + r_k) \qquad (E.4)$$

$$T_{bk} = T_{ak} - 2q_k$$

$$T_{al} = R_{al} - \frac{\gamma c}{2\pi}(p_l + q_l + r_l)$$

$$T_{bl} = T_{al} - 2q_l$$

where R_{ak} and R_{al} are defined by Eq. 6.69 if θ is substituted by $\overline{\theta}$, and

$$T_{k1} = \quad T_{ak} + \frac{\gamma c}{\pi} p_k \qquad \text{if } p_k \text{ and } p_l \text{ have the same sign} \qquad (E.5)$$

$$T_{ak} + \frac{\gamma c}{\pi} q_k \qquad \text{if } q_k \text{ and } q_l \text{ have the same sign}$$

$$T_{ak} + \frac{\gamma c}{\pi} r_k \qquad \text{if } r_k \text{ and } r_l \text{ have the same sign}$$

$$T_{k2} = T_{k1} - 2q_k$$

$$T_{l1} = T_{al} + \frac{\gamma c}{\pi} p_l \quad \text{if } p_k \text{ and } p_l \text{ have the same sign}$$

$$T_{al} + \frac{\gamma c}{\pi} p_l \qquad \text{if } q_k \text{ and } q_a \text{ have the same sign}$$

$$T_{al} + \frac{\gamma c}{\pi} r_l \qquad \text{if } r_k \text{ and } r_l \text{ have the same sign}$$

$$T_{l2} = T_{l1} - 2q_l$$

and

$$b_r = p_k/p_l \qquad \text{if } p_k \text{ and } p_l \text{ have the same sign} . \qquad (E.6)$$

$$q_k/q_l \qquad \text{if } q_k \text{ and } q_l \text{ have the same sign}$$

$$r_k/r_l \qquad \text{if } r_k \text{ and } r_l \text{ have the same sign}$$

In Eq. E.3, λ_η, $\bar{\kappa}$ and L_r are given by Eqs. 6.66, 6.72 and 6.73, respectively.

A-2)Three pairs of direction cosines have opposite signs.

The expansions of the absolute value terms are given by Eq. 6.87 and the integration is carried out on one interval for each of the independent variables. In this case, the integrals I_{kl} are given by

$$I_{kl} = e_1 e_2 C1(\overline{\theta}) C2(\overline{\theta}) \frac{\varsigma}{4\kappa^2} (I_1 + n_1 I_2)(I_3 + n_2 I_4) \qquad (E.7)$$

where e_1, e_2, n_1, n_2 and ς are given by Eqs. B.2 to B.6, respectively and $C1(\theta)$ and $C2(\theta)$ are given by Eqs. B.8 and B.9, respectively. If θ is substituted by $\overline{\theta}$ The terms $I_i, i = 1 \cdots 4$, are given by

$$I_1 = e^{A_n}(e^{\overline{\kappa} T_{ak}} - 1)/T_{ak} \qquad E.8$$

$$I_2 = e^{-A_n}(e^{\overline{\kappa} T_{bk}} - 1)/T_{bk}$$

$$I_3 = e^{A_n}(e^{\overline{\kappa} L_r T_{al}} - 1)/T_{al}$$

$$I_4 = e^{-A_n}(e^{\overline{\kappa} L_r T_{bl}} - 1)/T_{bl}$$

where A_n, $\overline{\kappa}$ and L_r are given by Eqs. 6.66, 6.72 and 6.73, respectively and the terms T_{ak}, T_{bk}, T_{al} and T_{bl} are given by Eq. E.4.

B)Nodes n and s do not coincide:

B-1)I_{kl} is evaluated on one interval for each of the independent variables:

The conditions under which this situation arises were stated in Subsection 6.6.1 and the expansions of the absolute value terms are given by Eqs. 6.87 and 6.88. The integrals I_{kl} are given by

$$I_{kl} = e_1 e_2 \frac{\varsigma}{4\kappa^2} A_{ns} \Delta_{ns} C1(\overline{\theta}) C2(\overline{\theta}) \qquad (E.9)$$
$$(I_1 + n_1 n_2)(I_3 + n_2 I_4)$$

where e_1, e_2, n_1, n_2 and ς are given by Eqs. B.2 to B.6, respectively and A_{ns}, $C1(\overline{\theta})$ and $C2(\overline{\theta})$ are given by Eqs. B.7 to B.9. If θ is substituted by $\overline{\theta}$. Δ_{ns} is given by

$$\Delta_{ns} = exp\{\frac{-c\kappa\gamma}{2\pi}(x_n - x_s + y_n - y_s + z_n - z_s)\} \quad . \tag{E.10}$$

and the terms $I_i, i = 1 \cdots 4$ are given by

$$I_1 = e^{A_n}(e^{B_{ak}\bar{\kappa}} - 1)/B_{ak} \tag{E.11}$$

$$I_2 = e^{-A_n}(e^{B_{bk}\bar{\kappa}} - 1)/B_{bk}$$

$$I_3 = e^{A_s}(e^{B_{al}l_r\bar{\kappa}} - 1)/B_{al}$$

$$I_4 = e^{-A_s}(e^{B_{bl}l_r\bar{\kappa}} - 1)/B_{bl}$$

where

$$B_{ak} = R_{ak} - \frac{\gamma c}{2\pi}(m_1 p_k + m_3 q_k + m_5 r_k) \tag{E.12}$$

$$B_{bk} = B_{ak} - 2q_k$$

$$B_{al} = R_{al} - \frac{\gamma c}{2\pi}(m_2 p_l + m_4 q_l + m_6 r_l)$$

$$B_{bl} = B_{al} - 2q_l$$

in which

$$m_1 = \begin{cases} -p_k/p_k & x_n < x_{_s} \\ 1.0 & x_n = x_{_s} \\ p_k/p_k & x_n > x_{_s} \end{cases}$$

$$\tag{E.13}$$

$$m_2 = \begin{cases} p_l/p_l & x_n < x_{_s} \\ 1.0 & x_n = x_{_s} \\ -p_l/p_l & x_n > x_{_s} \end{cases}$$

$$m_3 = \begin{cases} -q_k/q_k & y_n < y_{_s} \\ 1.0 & y_n = y_{_s} \\ q_k/q_k & y_n > y_{_s} \end{cases}$$

$$m_4 = \begin{cases} q_l/q_l & y_n < y_{_s} \\ 1.0 & y_n = y_{_s} \\ -q_l/q_l & y_n > y_{_s} \end{cases}$$

$$m_5 = \begin{cases} -r_k/r_k & z_n < z_{_s} \\ 1.0 & z_n = z_{_s} \\ r_k/r_k & z_n > z_{_s} \end{cases}$$

$$m_6 = \begin{cases} -r_l/r_l & z_n < z_{_s} \\ 1.0 & z_n = z_{_s} \\ r_l/r_l & z_n > z_{_s} \end{cases}$$

In Eqs. E.11 and E.12, A_n, A_s, $\overline{\kappa}$ and L_r are given by Eqs. 6.66, 6.67, 6.72 and 6.73, respectively and R_{ak} and R_{al} are given by Eq. 6.69. If θ is substituted by $\overline{\theta}$.

B-2)I_{kl} is evaluated on two intervals for one of the independent variables:

The integrals I_{kl} are given by

$$I_{kl} = e_1 e_2 C1(\overline{\theta}) C2(\overline{\theta}) \frac{\varsigma}{4\kappa^2} A_{ns} \Delta_{ns} [\sum_{i=1}^{16} (-1)^{n_i} I_i] \tag{E.14}$$

where $I_i, i = 1 \cdots 16$ are given by

$$I_1 = \frac{e^{A_n + A_s}[e^{\overline{\kappa}(B_{ak} + b_r B_{l1})} - 1]}{B_{l1}(B_{ak} + b_r B_{l1})}$$

(E.15)

$$I_2 = \frac{e^{A_n + A_s}(e^{\overline{\kappa} B_{ak}} - 1)}{B_{l1} B_{ak}}$$

$$I_3 = \frac{e^{A_n - A_s}[e^{\overline{\kappa}(B_{ak} + b_r B_{l2})} - 1]}{B_{l2}(B_{ak} + b_r B_{l2})}$$

$$I_4 = \frac{e^{A_n - A_s}(e^{\overline{\kappa} B_{ak}} - 1)}{B_{ak} B_{l2}}$$

$$I_5 = \frac{e^{-A_n + A_s}[e^{\overline{\kappa}(B_{bk} + b_r B_{l1})} - 1]}{B_{l1}(B_{bk} + b_r B_{l1})}$$

$$I_6 = \frac{e^{-A_n + A_s}(e^{\overline{\kappa} B_{bk}} - 1)}{B_{bk} B_{l2}}$$

$$I_7 = \frac{e^{-A_n - A_s}[e^{\overline{\kappa}(B_{bk} + b_r B_{l2})} - 1]}{B_{l2}(B_{bk} + b_r B_{l2})}$$

$$I_8 = \frac{e^{-A_n - A_s}(e^{\overline{\kappa} B_{bk}} - 1)}{B_{l2} B_{bk}}$$

$$I_9 = \frac{e^{A_n + A_s + b_r \overline{\kappa} B_{al}}(e^{\overline{\kappa} B_{k1}} - 1)}{B_{al} B_{k1}}$$

$$I_{10} = \frac{e^{A_n + A_s}[e^{\overline{\kappa}(B_{k1} + b_r B_{al})} - 1]}{B_{al}(B_{k1} + b_r B_{al})}$$

$$I_{11} = \frac{e^{A_n - A_s + b_r \overline{\kappa} B_{bl}}(e^{\overline{\kappa} B_{k1}} - 1)}{B_{bl} B_{k1}}$$

$$I_{12} = \frac{[e^{A_n - A_s + \overline{\kappa}(B_{k1} + b_r B_{bl})} - 1]}{B_{bl}(B_{k1} + b_r B_{bl})}$$

$$I_{13} = \frac{e^{-A_n + A_s + \overline{\kappa} b_r B_{al}}(e^{\overline{\kappa} B_{k2}} - 1)}{B_{al} B_{k2}}$$

$$I_{14} = \frac{e^{-A_n + A_s}(e^{\overline{\kappa}(B_{k2} + b_r B_{al})} - 1)}{B_{al}(B_{k2} + b_r B_{al})}$$

$$I_{15} = \frac{e^{-A_n - A_s + \overline{\kappa} L_r B_{bl}}(e^{\overline{\kappa} B_{k2}} - 1)}{B_{bl} B_{k2}}$$

$$I_{16} = \frac{e^{-A_n - A_s}[e^{\overline{\kappa}(B_{k2} + b_r B_{bl})} - 1]}{B_{bl}(B_{k2} + b_r B_{bl})}$$

In which

$$
\begin{array}{lll}
B_{k1} = & B_{ak} + \dfrac{c\gamma}{\pi} m_1\, p_k & p_k \text{ and } p_l \text{ have the same sign} \qquad (E.16) \\[2mm]
& B_{ak} + \dfrac{c\gamma}{\pi} m_3\, q_k & q_k \text{ and } q_l \text{ have the same sign} \\[2mm]
& B_{ak} + \dfrac{c\gamma}{\pi} m_5\, r_k & r_k \text{ and } r_l \text{ have the same sign}
\end{array}
$$

$$B_{k2} = B_{k1} - 2q_k$$

$$
\begin{array}{lll}
B_{l1} = & B_{al} + \dfrac{c\gamma}{\pi} m_2\, p_l & p_k \text{ and } p_l \text{ have the same sign} \\[2mm]
& B_{al} + \dfrac{c\gamma}{\pi} m_4\, q_l & q_k \text{ and } q_l \text{ have the same sign} \\[2mm]
& B_{al} + \dfrac{c\gamma}{\pi} m_6\, r_l & r_k \text{ and } r_l \text{ have the same sign}
\end{array}
$$

$$B_{l2} = B_{l1} - 2q_k$$

In Eq. E.16, the m_i terms are defined by Eq. E.13.

Appendix F
Computer Programs Used in the Study

All the necessary computer programs for this study were developed by the author except the subroutines used for equation solving and evaluation of eigenvalues. The name and purpose of each of the computer programs are given below:

SMIT1   Performs the pile driving analysis using the original Smith model.

SMIT2   Performs the pile driving analysis using the proposed soil model.

FEM   Finite element analysis in the frequency domain (implementation and verification of the transmitting boundaries).

PFEM   Finite element analysis for the pile driving in the time domain.

SPECT   Evaluates the spectra of wave forces on members of offshore towers for the three different models.

PGRP   Calculates the pile group stiffness constants taking into account dynamic pile-soil-pile-interaction.

OFFSH   Evaluates the foundation stiffness matrix for the offshore tower.

RESPO   Calculates the response of the tower to random wave forces.

All these programs were developed using the CYBER 835 computer at the University of Western Ontario Computer Center.

Vita

Name: Hisham M. Mitwally

Place of Birth: Ismailia, Egypt

Year of Birth: 1959

Post Secondary Education and Degrees:

    1976-1981, B.Sc. in Civil Engineering, Ain-Shams University, Cairo, Egypt.

    1982-1987; Ph.D., University of Western Ontario.

Scholarships and Awards:

    1976-1981; Egyptian Ministery of Education Scholarship for outstanding students.

    1982-1987; Visa Bursary, University of Western Ontario.

    1983-1987; Special University Scholarship, University of Western Ontario.

Related Work Experience;

    1982-1987; Teaching Assistant at the University of Western Ontario.

    1981-1982; Teaching Assistant at Ain-Shams University, Egypt.

    1981-1982; Design Engineer with Hosni Consultants, Cairo, Egypt.

Publications: *"Pile Driving Analysis"*, Proceedings, Tenth Canadian Congress of Applied Mechanics, London, Ontario, Canada, June 85.

    "Effect of Soil-Structure-Interaction on Damping of Offshore Structures", Proceedings, Third Canadian Conference on Marine Geotechnical Engineering, St. John's, Newfoundland, Canada, June 86.

    "Response of Offshore Towers with Pile Interaction", ASCE, Eng. Mech. Div., (To appear in August 1987).

    "Influence of Pile-Soil-Pile Interaction on Response of Offshore Towers to Wave Forces", Research Report BLWT-1-1986, Fac. of Eng. Science, U.W.O., London, Canada.

END

FIN

30 12 87